

**Engineering mixed surfactant systems to  
template hierarchical nanoporous  
materials**

**A thesis submitted to Cardiff University in  
candidature for the degree of Doctor of  
Philosophy**

**Zaineb Omar H. ET-tarhouni**

**2015**

*Dedicated To*

*The memory of my father who inspired  
scientific thinking in our lives; may Allah  
forgive him and grant him his highest  
paradise (Ameen).*

*I am forever indebted to the greatest women in  
my life, my beloved mother.*

*I owe every bit of my existence to both of  
them.*

*My husband (Naser).*

*My children (Mayar & Maten).*

*We All did it*

## Acknowledgments

In the Name of Allah, the Most Compassionate, the Most Merciful.

This thesis would not be possible without support of many people to whom I am extremely grateful.

I would like to express my deepest gratitude to my supervisors Prof Peter Griffiths and Dr Alison Paul for their excellent guidance, support and patience throughout the duration of my PhD. Thank you very much for every piece of information you gave me. I also would like to thank Prof Karen Wilson for her participation at the beginning stage of the project.

Next I would like to thank all people who helped me in various techniques, Dr Simon Pope (fluorescence), Prof Damien Murphy and Dr Emma Carter (EPR), Dr Ibrahim Salama (surface tension), Mr Omar T. Mansour (PGSE-NMR). And all people in research area who supported me with a single word.

Thanks go to all the people who create such a good atmosphere in the lab throughout years. Thanks to Dr Jamie Hurcom and Dr Glib Meleshko.

I would also like to thank Libyan Ministry of Higher Education and Scientific Research and Tripoli University for fund and giving me such great opportunity.

As my father taught me that education is the best opportunity I've been given, I would like to thank him for being an amazing role model to me and pushing me to be my best, no matter what. I am the person I am today because of you, and I just wanted to tell you thanks and I love you, may Allah bless you with Heaven.

Special thanks go to; my dear husband for all his love, support, encouragement and patience, you have been the rock I have so heavily relied upon for inspiration to be where I am today. A big thanks to my mother for her support, prayer every single day, I couldn't have done it without you. Last but not least special thanks go to my children for inspiring me in their own ways.

## Abstract

The mixing of the hydrocarbon surfactant cetyltrimethyl ammonium bromide (CTAB) and the fluorocarbon surfactant, Zonyl-FSN-100 with the average chemical structure of  $\text{C}_8\text{F}_{17}\text{C}_2\text{H}_4(\text{OC}_2\text{H}_4)_9\text{OH}$ , is quantified. The critical micelle concentration (CMC), the size and shape of the micelles and their composition have been investigated by surface tension, fluorescence, small-angle neutron scattering (SANS), electron paramagnetic resonance (EPR), pulsed-gradient spin-echo NMR spectroscopy (PGSE-NMR),  $^1\text{H}$ -NMR and  $^{19}\text{F}$ -NMR. The pure surfactant aqueous solutions and the mixtures have also been studied in the presence of hydrocarbon oil (hexane) and fluorocarbon oil (perfluorohexane, PFH) in order to investigate the swollen micelle shape and structure. The surfactants mix nonideally except for a degree of ideality at some CTAB mole fraction ( $0.5 > \alpha_{\text{CTAB}} > 0.7$ ). The pure surfactant FSN-100 forms disc-like micelles with a small aggregation number ( $N_{\text{agg.}}$ ) ( $\sim 50$ ) and the CTAB forms globular, charged micelles with a larger aggregation number (135). However, the aggregation number in the mixed micelles is greater than that in the pure surfactant case. The microviscosity of the head group region is sensitive to the number and bulkiness of the headgroups and the degree of hydration, but there is no obvious dependence on the  $N_{\text{agg.}}$ .

In the presence of the fluorocarbon oil (PFH), CTAB and FSN-100 mixed micelles have been used as templates to synthesize nanoporous materials. Different amounts of the oil have been added to the surfactant template in order to investigate the role of oil volume in the synthesis of templated materials. These synthesized materials have been characterized using porosimetry, scanning electron microscopy (SEM), transmission electron microscopy (TEM) and X-ray diffraction (XRD). Some of the materials, at either end of the oil range studied, possess high specific surface areas with bimodal pore size distributions. These materials were explored as potential catalysts and were grafted with sulfonic acid moieties and characterized by TGA and XPS. The catalytic performance in the reaction of palmitic acid conversion, characterized by gas chromatography (GC), approached the level shown in the literature by related materials. Collectively this work has shown some potential in the preparation of novel catalysts, but further refinement is necessary.



## Abbreviations

Al-MCM-41	Mesoporous aluminosilicate
BET	Brunauer-Emmett-Teller
BJH	Barrett-Joyner-Halenda
CMC	Critical Micelle Concentration
CTAB	Cetyltrimethylammonium bromide
CTAC	Cetyltrimethylammonium chloride
DBNMG	Dodecylmalonobis-N-methylglucamide
d-CHCl <sub>3</sub>	Deuterated chloroform
DCM	Dichloromethane
DDAB	Didodecyldimethylammonium bromide
DHE	Dihexylether
16-DSE	16-Doxyl stearic acid methyl ester
EPR	Electron Paramagnetic Resonance
FSN-100	Zonyl FSN-100 fluorocarbon surfactant
FSO-100	Zonyl FSO-100 fluorocarbon surfactant
GC	Gas Chromatography
H	Polarity index
HC/CF	Hydrocarbon/fluorocarbon
HfDePC	1H, 1H, 2H, 2H- perfluorodecylpyridinium chloride
MCM-41	Mobil Composition of Matter No. 41
MPTMS	3-mercaptopropyl trimethoxysilane

$N_{agg}$	Aggregation number
NMR	Nuclear Magnetic Resonance
$^1\text{H}$ -NMR	Proton Nuclear Magnetic Resonance
$^{19}\text{F}$ -NMR	Fluorine (19) Nuclear Magnetic Resonance
PFH	Perfluorohexane
PFD	Perfluorodecalin
PGSE-NMR	Pulsed-Gradient Spin-Echo NMR spectroscopy
$\text{RSO}_3\text{H}$	Alkyl sulfonic acid
RSH	Thiol
SANS	Small-Angle Neutron Scattering
SAXS	Small Angle X-ray Scattering
SBA-15	Santa Barbara Amorphous-15
SDS	Sodium dodecyl sulfate
SEM	Scanning Electron Microscopy
TEM	Transmission Electron Microscopy
TEOS	Tetraethyl orthosilicate
TGA	Thermal Gravimetric Analysis
TPS	Tetrapropoxysilane
Ti-silica	Titanium-silica
TTAB	Tetradecyltrimethylammonium bromide
XPS	X-ray Photoelectron Spectroscopy
XRD	X-ray Diffraction

## List of Figures

### Chapter One: Introduction and Literature Review

- Figure 1.1** The IUPAC classifications of nanoporous material
- Figure 1.2** The cooperative self-assembly pathway
- Figure 1.3** The liquid crystal pathway
- Figure 1.4** Isotherm types based on IUPAC classifications
- Figure 1.5** The types of hysteresis loop
- Figure 1.6** A typical plot of surface tension vs  $\ln$  concentration of a surfactant

### Chapter Two: Materials and Experimental techniques

- Figure 2.1** Chemical structure of the fluorescent probe, pyrene
- Figure 2.2** Pulse sequence for gradient PGSENMR
- Figure 2.3** The three spin states of  $^{14}\text{N}$
- Figure 2.4** A typical EPR spectra
- Figure 2.5** Schematic representations of diffracted beams (Bragg's law)
- Figure 2.6** Schematic representations of X-ray tube, the X-ray detector and the sample
- Figure 2.7** Schematic representations of TGA instrument
- Figure 2.8** The chemical structure of 16-DSE spin probe

## Chapter Three: Phase Behaviour of Mixed Surfactant Systems

**Figure 3.1** Surface tension measurements as a function of total concentration for CTAB (open triangles) and FSN-100 (closed triangles)

**Figure 3.2** Surface tension measurements as a function of total concentration for CTAB (open triangles), FSN-100 (closed triangles), 0.2 CTAB mole fraction (open square), 0.5 CTAB mole fraction (closed squares) and 0.9 CTAB mole fraction (open circles)

**Figure 3.3** Surface tension measurements as a function of total concentration for CTAB (open triangles), FSN-100 (closed triangles), 0.15 CTAB mole fraction (open squares), 0.33 CTAB mole fraction (open diamonds) and 0.8 CTAB mole fraction (open circles)

**Figure 3.4** The critical micelle concentration, CMC, as a function of CTAB solution mole fraction determined by surface tension. The solid line corresponds to the ideal mixing prediction; the dotted line is a guide to the eye

**Figure 3.5** Fluorescence measurements for CTAB aqueous solution. Lines are guide to the eye

**Figure 3.6** Fluorescence measurements for FSN-100 aqueous solution. Lines are guide to the eye

**Figure 3.7** The critical micelle concentration, CMC, as a function of CTAB mole fraction determined by pyrene solubilisation (open circles) and surface tension (closed circles). The dotted lines are guides to the eye. Literature CMC values for the pure surfactants are also plotted, (open triangles)

**Figure 3.8** Small angle neutron scattering of 50mM CTAB aqueous solution (open squares) with fit (solid line)

**Figure 3.9** Small angle neutron scattering of 50mM FSN-100 aqueous solution (open triangles) with fit (solid line)

**Figure 3.10** Small angle neutron scattering of 50mM of 0.2 CTAB mole fraction aqueous solution (closed triangles) with fit (solid line)

**Figure 3.11** Small angle neutron scattering of 50mM of 0.4 CTAB mole fraction aqueous solution (closed squares) with fit (solid line)

**Figure 3.12** Small angle neutron scattering of 50mM of 0.6 CTAB mole fraction aqueous solution (open circles) with fit (solid line)

**Figure 3.13** Small angle neutron scattering of 50mM of 0.8 CTAB mole fraction aqueous solution (star) with fit (solid line).

**Figure 3.14** Small angle neutron scattering as a function of CTAB mole fraction, (open square)  $\alpha_{\text{CTAB}} = 1$ , (open triangle)  $\alpha_{\text{CTAB}} = 0$ , (closed triangle)  $\alpha_{\text{CTAB}} = 0.2$ , (open diamond)  $\alpha_{\text{CTAB}} = 0.4$ , (open circle)  $\alpha_{\text{CTAB}} = 0.6$ , (star)  $\alpha_{\text{CTAB}} = 0.8$ . Fits are included as solid line. Data are offset by a factor of 3 for clarity

**Figure 3.15** Hyperfine coupling constant of CTAB/FSN-100 mixtures, as a function of CTAB solution mole fraction at a total surfactant concentration of 20 mM (open triangles) and 50 mM (open circles). The corresponding volume fraction of water in the headgroup region is indicated on the secondary axis

**Figure 3.16** Rotational correlation time of 16-DSE in CTAB/FSN-100 mixtures, as a function of CTAB solution mole fraction at a total surfactant concentration of 20 mM (open triangles) and 50 mM (open circles). The rotational correlation time corrected using SANS data are over-plotted (closed circles)

**Figure 3.17** Self-diffusion coefficients as a function of CTAB mole fraction, (open squares)  $\alpha_{\text{CTAB}} = 1$ , (open triangles)  $\alpha_{\text{CTAB}} = 0$

**Figure 3.18**  $^1\text{H}$  High resolution-NMR data from 50 mM of CTAB in  $\text{D}_2\text{O}$

**Figure 3.19**  $^1\text{H}$  High resolution-NMR data from 50 mM of FSN-100 in  $\text{D}_2\text{O}$

**Figure 3.20**  $^1\text{H}$  High resolution-NMR data from the mixture of CTAB and FSN-100 in  $\text{D}_2\text{O}$

**Figure 3.21**  $^{19}\text{F}$  High resolution-NMR data from 50 mM of FSN-100 in  $\text{D}_2\text{O}$

**Figure 3.22**  $^{19}\text{F}$  High resolution-NMR data from 50 mM of FSN-100 in  $\text{D}_2\text{O}$  (red) and the mixture of CTAB and FSN-100 in  $\text{D}_2\text{O}$  (blue)

## Chapter Four: The Solution Behaviour of the Oil Swollen Micelles

**Figure 4.1** Surfactant aqueous solutions for both CTAB and FSN-100 before (a), (b) and after adding 2 % of hexane (c)

**Figure 4.2** Surfactant mixture aqueous solutions of 0.2, 0.6 and 0.8 in terms of CTAB mole fraction before (a) and after adding 2 % of hexane (b)

**Figure 4.3**  $^1\text{H}$  High resolution-NMR data from 50 mM of CTAB in  $\text{D}_2\text{O}$  (red) and the lower phase of CTAB/ hexane solution (blue)

**Figure 4.4**  $^1\text{H}$  High resolution-NMR data from 50 mM of CTAB in  $\text{CDCl}_3$  (blue) and the top phase of CTAB/ hexane in  $\text{CDCl}_3$  solution (red)

**Figure 4.5**  $^1\text{H}$  High resolution-NMR data from the top phase of CTAB/ hexane in  $\text{CDCl}_3$  (red) and hexane in  $\text{CDCl}_3$  solution (blue)

**Figure 4.6**  $^1\text{H}$  High resolution-NMR data from the top phase of 50 mM CTAB solution with 2 % PFH in  $\text{D}_2\text{O}$  (red) and the solution of CTAB in  $\text{D}_2\text{O}$  (blue)

**Figure 4.7**  $^1\text{H}$  High resolution-NMR data from the lower phase of 50mM FSN-100 solution with 2% hexane in  $\text{D}_2\text{O}$  (red) and the solution of FSN-100 in  $\text{D}_2\text{O}$  (blue)

**Figure 4.8**  $^1\text{H}$  High resolution-NMR data from the top phase of 50mM FSN-100 solution with 2% PFH in  $\text{D}_2\text{O}$  (red) and the solution of FSN-100 in  $\text{D}_2\text{O}$  (blue)

- Figure 4.9**  $^1\text{H}$  High resolution-NMR data from the lower phase of CTAB/FSN-100 mixture solution with 2 % hexane in  $\text{D}_2\text{O}$  (red) and the solution of CTAB/FSN-100 in  $\text{D}_2\text{O}$  (blue)
- Figure 4.10**  $^1\text{H}$  High resolution-NMR data from the top phase of CTAB/FSN-100 mixture solution with 2 % PFH in  $\text{D}_2\text{O}$  (red) and the solution of CTAB/FSN-100 in  $\text{D}_2\text{O}$  (blue)
- Figure 4.11**  $^{19}\text{F}$  High resolution-NMR data from the lower phase of CTAB solution with 2 % PFH in  $\text{CDCl}_3$  (red) and the solution of PFH in  $\text{CDCl}_3$  (blue)
- Figure 4.12**  $^{19}\text{F}$  High resolution-NMR data from the lower phase of FSN-100 solution with 2 % hexane in  $\text{D}_2\text{O}$  (blue) and the solution of 50 mM FSN-100 in  $\text{D}_2\text{O}$  (red)
- Figure 4.13**  $^{19}\text{F}$  High resolution-NMR data from the top phase of FSN-100 solution with 2 % PFH in  $\text{D}_2\text{O}$  (blue) and the solution of 50 mM FSN-100 in  $\text{D}_2\text{O}$  (red)
- Figure 4.14**  $^{19}\text{F}$  High resolution-NMR data from the lower phase of the CTAB/FSN-100 mixture solution with 2 % hexane in  $\text{D}_2\text{O}$  (red) and the mixture solution of 50 mM CTAB/FSN-100 in  $\text{D}_2\text{O}$  (blue)
- Figure 4.15**  $^{19}\text{F}$  High resolution-NMR data from the top phase of the CTAB/FSN-100 mixture solution with 2 % PFH in  $\text{D}_2\text{O}$  (blue) and the mixture solution of 50 mM the CTAB/FSN-100 in  $\text{D}_2\text{O}$  without PFH (red)
- Figure 4.16** Self-diffusion coefficients of CTAB and FSN-100 and the mixtures with hexane and PFH as a function of CTAB mole fraction.  $\alpha_{\text{CTAB}} = 1$  (open squares),  $\alpha_{\text{CTAB}} = 0$  (open triangles), CTAB/hexane (open blue squares), FSN/hexane (open blue triangles), CTAB/PFH (open red squares), FSN/PFH (open red triangles)
- Figure 4.17** Small angle neutron scattering of 50 mM CTAB aqueous solution (open square) in  $\text{D}_2\text{O}$  and 50 mM CTAB aqueous solution in  $\text{D}_2\text{O}$

saturated with 2 % hexane (closed square)

**Figure 4.18** Small-angle neutron scattering of 50 mM CTAB aqueous solution in D<sub>2</sub>O saturated with 2% hexane (open square) with the fit (solid line)

**Figure 4.19** Small-angle neutron scattering of 50 mM FSN-100 aqueous solution in D<sub>2</sub>O (open triangle), and the solution in D<sub>2</sub>O saturated with 2 % hexane (closed triangle)

**Figure 4.20** Small-angle neutron scattering of 50 mM FSN-100 aqueous solution in D<sub>2</sub>O saturated with 2 % hexane (open triangle) with the fit (solid line)

**Figure 4.21** Small angle neutron scattering of 50 mM CTAB aqueous solution (open square) in D<sub>2</sub>O and 50 mM CTAB aqueous solution in D<sub>2</sub>O saturated with 2 % Perfluorohexane (closed square)

**Figure 4.22** Small-angle neutron scattering of 50 mM CTAB aqueous solution in D<sub>2</sub>O saturated with 2 % PFH (open square) with the fit (solid line)

**Figure 4.23** Small angle neutron scattering of 50 mM FSN-100 aqueous solution (open triangle) with fit (solid line), 50 mM FSN-100 in D<sub>2</sub>O saturated with 2 % perfluorohexane (closed triangle)

**Figure 4.24** Small-angle neutron scattering of 50 mM FSN-100 aqueous solution in D<sub>2</sub>O saturated with 2 % PFH (open triangle) with the fit (solid line)

**Figure 4.25** Small angle neutron scattering as a function of CTAB mole fraction, (open square)  $\alpha_{\text{CTAB}} = 1$ , (open triangle)  $\alpha_{\text{CTAB}} = 0$ , (closed triangle)  $\alpha_{\text{CTAB}} = 0.2$ , (open circle)  $\alpha_{\text{CTAB}} = 0.6$ , (star)  $\alpha_{\text{CTAB}} = 0.8$ , and 2 % Hexane. Fits are included as solid line. Data are offset by a factor of 3 for clarity

**Figure 4.26** Small angle neutron scattering as a function of CTAB mole fraction, (open square)  $\alpha_{\text{CTAB}} = 1$ , (open triangle)  $\alpha_{\text{CTAB}} = 0$ , (closed triangle)  $\alpha_{\text{CTAB}} = 0.2$ , (open circle)  $\alpha_{\text{CTAB}} = 0.6$ , (star)  $\alpha_{\text{CTAB}} = 0.8$ , and 2 % perfluorohexane. Fits are included as solid line. Data are offset by a



factor of 3 for clarity

## **Chapter Five: The Application of Mixed Surfactant Systems to Template Hierarchical Nanoporous Materials**

**Figure 5.1** TEM images (a, b) of the sample FSN/ CTAB/PFH/ hexane

**Figure 5.2** TEM image of the sample FSN/ CTAB/PFH

**Figure 5.3** N<sub>2</sub> adsorption (closed square)-desorption (open square) isotherms and BJH pore size distribution (figure inside) of MCM-41 comparator

**Figure 5.4** Scanning electron microscopy image of MCM-14 comparator

**Figure 5.5** SEM images of the samples, 0 % (a), 20 % (b) and 33 % (c)

**Figure 5.6** TEM images of the samples, 0 % (a), 1 % (b) & (b'), 11 % (c) & (c'), 20 % (d), 27 % (e) and 33 % (f) & (f')

**Figure 5.7** N<sub>2</sub> adsorption (open square)-desorption (closed square) isotherms for 0 % mesoporous sample

**Figure 5.8** N<sub>2</sub> adsorption (open square)-desorption (closed square) isotherms for 1 % mesoporous sample

**Figure 5.9** N<sub>2</sub> adsorption (open square)-desorption (closed square) isotherms for 11 % mesoporous sample

**Figure 5.10** N<sub>2</sub> adsorption (open square)-desorption (closed square) isotherms for 33 % mesoporous sample

**Figure 5.11** BET surface area vs oil volume in the template of samples 0 %, 1 %, 11 %, 20 %, 27 % and 33 %

**Figure 5.12** Pore diameter (closed square) and pore volume (open square) vs oil content in the template of samples 0 %, 1 %, 11 %, 20 %, 27 %

and 33 %

**Figure 5.13** BJH pore size distribution of 0 % sample

**Figure 5.14** BJH pore size distribution of 20 % sample

**Figure 5.15** BJH pore size distribution of 1 % sample

**Figure 5.16** BJH pore size distribution of 33 % sample

**Figure 5.17** XRD patterns of samples 0 % (black), 1 % (red), 11 % (brown), 20 % (green), 27 % (blue) and 33 % (purple)

## Chapter Six: Further Studies and Future Work

**Figure 6.1** A schematic representation of the sulfonic acid functionalization reaction

**Figure 6.2** The thermal analysis curves (TGA) of (a) 0 % (black line), (b) 1 % (red line), (c) 11 % (green line) and (d) 33 % (orange line) sulfonic acid functionalized mesoporous silicas

**Figure 6.3** XPS spectrum (S 2s ) of functionalized 0 % sample showing peaks for sulfur as thiol (228.0 eV) and in the oxidized sulfonic acid form (233.0 eV)

**Figure 6.4** Palmitic acid conversions after 6 h at 60 °C using sulfonic acid functionalized porous silica catalysts of samples 1, 2, 3 and 4 ( 0 %, 1 %, 11 %, and 33 % (open squares) respectively), and the conversion from the literature (sample 5, (closed square))

## List of Tables

- Table 3.1** Values of the CMC, surface tension value at the CMC, maximum surface excess concentration and minimum area per molecule parameters for CTAB, FSN-100, 0.15, 0.2, 0.33, 0.5, 0.6, 0.66, 0.7, 0.75, 0.8, 0.85, and 0.9 CTAB mole fraction solutions,  $n$  for mixtures were calculated as a simple weighted value of CTAB and FSN-100
- Table 3.2** Parameters describing the fits of SANS data from CTAB, FSN-100, 0.2, 0.4, 0.6, 0.8 CTAB mole fraction solutions using a model that describes the micelle as a globular elliptical with some ionic character
- Table 3.3** Experimental values for volume fraction of water in the polar shell ( $\phi_{H_2O}$ ) using EPR, in the single surfactant solutions and mixtures at two different total surfactant concentration.
- Table 3.4** Chemical shifts of  $CH_3$  (CTAB) and  $CH_2$  (FSN-100) signals in the single surfactant solution and the mixture
- Table 4.1** Self-diffusion coefficients of CTAB, FSN-100 and mixtures of 0.2, 0.5, 0.8 CTAB mole fractions in the presence of hexane or PFH at 25 °C
- Table 4.2** Parameters describing the fits of SANS data from CTAB solutions in  $D_2O$  saturated with 2 % hexane and compared to the pure surfactant parameters, using a model that describes the micelle as a globular elliptical with some ionic character
- Table 4.3** Parameters describing the fits of SANS data from FSN-100 solutions in  $D_2O$  saturated with 2 % hexane and compared to the pure surfactant parameters, using a model that describes the micelle as a globular elliptical with some ionic character
- Table 4.4** Parameters describing the fits of SANS data from CTAB solutions in  $D_2O$  saturated with 2 % hexane and compared to the pure

surfactant parameters, using a model that describes the micelle as a globular elliptical with some ionic character

<b>Table 4.5</b>	Parameters describing the fits of SANS data from FSN-100 solutions in D <sub>2</sub> O saturated with 2 % hexane and compared to the pure surfactant parameters, using a model that describes the micelle as a globular elliptical with some ionic character
<b>Table 4.6</b>	Parameters describing the fits of SANS data from the mixtures with hexane of 0.2, 0.6, 0.8 CTAB mole fraction solutions using a model that describes the micelle as a globular elliptical with some ionic character. Parameters between brackets are for the mixtures without oil
<b>Table 4.7</b>	Parameters describing the fits of SANS data from the mixtures with PFH of 0.2, 0.6, 0.8 CTAB mole fraction solutions using a model that describes the micelle as a globular elliptical with some ionic character. Parameters between brackets are for the mixtures without oil
<b>Table 5.1</b>	sample details and abbreviations
<b>Table 5.2</b>	N <sub>2</sub> porosimetry parameters for synthesized materials obtained at different oil volume ratios
<b>Table 5.3</b>	Pore structure parameters from XRD measurements
<b>Table 6.1</b>	The weight percentages of sulfur content of functionalized materials evaluated by TGA technique
<b>Table 6.2</b>	Binding energy and element concentrations from XPS analysis for grafted materials
<b>Table 6.3</b>	Sulfur content in weight percent of functionalized materials evaluated by XPS and TGA techniques

# Table of Contents

Acknowledgment	I
Abstract	II
Abbreviation	III
List of figures	V
List of tables	XIII
Contents	XV
1.1. Hierarchical nanoporous materials	2
1.1.1. Templating with cationic and nonionic surfactants	3
1.1.2. Synthesis mechanisms	3
1.1.2.1. Cooperative self-assembly of surfactants	4
1.1.2.2. Liquid crystal templating	4
1.1.3. Material characterizations	5
1.1.3.1. N <sub>2</sub> adsorption isotherm method	5
1.2. Surfactant phase behaviour	9
1.2.1. Surfactants	9
1.2.2. Surfactants and air-water interfaces	10
1.2.3. Gibbs adsorption equation	10
1.2.4. Mixed surfactant systems	12

1.2.4.1.	Mixed micelle and micelle separation	12
1.3.	Literature review	13
1.3.1.	Nanoporous materials	13
1.3.1.1.	Hydrocarbon surfactant templates	13
1.3.1.2.	Fluorocarbon surfactant templates	14
1.3.1.3.	Mixed micelle templates	16
1.3.2.	Catalytic applications	17
1.3.2.1.	General catalysis reactions	17
1.3.2.2.	Sulfonic acid functionalization reactions	18
1.3.2.3.	Palmitic acid esterification reaction	18
1.3.3.	Surfactant phase behaviour	19
1.3.3.1.	Critical micelle Concentration (CMC) determination	19
1.3.3.2.	Micelle structure determination	22
1.4.	Project Aims	25
1.5.	References	27
2.1.	Introduction	40
2.2.	Experimental techniques and theory	40
2.2.1.	Surface tension	40
2.2.1.1.	Surface tension & surfactant critical micelle concentration (CMC)	40

2.2.1.2.	Drop volume method	39
2.2.1.3.	Surface tension instrument	41
2.2.2.	Fluorescence measurements	41
2.2.2.1.	Fluorescent probes	42
2.2.2.2.	Fluorescence instrument	43
2.2.3.	Small-Angle Neutron Scattering (SANS)	43
2.2.3.1.	Neutrons	43
2.2.3.2.	SANS instrument theory	45
2.2.3.3.	SANS instrument	45
2.2.4.	$^1\text{H}$ -NMR, $^{19}\text{F}$ -NMR and pulsed-gradient spin-echo NMR spectroscopy (PGSE-NMR)	45
2.2.4.1.	Theoretical aspects	45
2.2.4.2.	NMR spectra	45
2.2.4.3.	NMR instruments	47
2.2.5.	Electron paramagnetic resonance spectroscopy (EPR)	48
2.2.5.1.	Theoretical aspects	48
2.2.5.2.	EPR instrument	50
2.2.5.3.	EPR lineshape fitting and analysis	50
2.2.6.	Scanning Electron Microscopy (SEM)	51
2.2.6.1.	Theoretical aspects	51

2.2.6.2. SEM instrument	51
2.2.7. Transmission Electron Microscopy (TEM)	51
2.2.7.1. Theoretical aspects	51
2.2.7.2. TEM instrument	51
2.2.8. X-Ray Diffraction (XRD)	52
2.2.8.1. Theoretical aspects	52
2.2.8.2. XRD instrument	53
2.2.9. Porosimetry (N <sub>2</sub> isotherm)	53
2.2.9.1. Theoretical aspects	53
2.2.9.2. Porosimetry instrument	54
2.2.10. Thermal gravimetric analysis (TGA)	55
2.2.10.1. Theoretical aspects	55
2.2.10.2. TGA instrument	55
2.2.11. X-ray photoelectron spectroscopy (XPS)	56
2.2.11.1. Theoretical aspects	56
2.2.11.2. XPS instrument	57
2.2.12. Gas Chromatography (GC)	57
2.2.12.1. Theoretical aspects	57
2.2.12.2. GC instrument	58



2.3.	Materials	58
2.3.1.	General materials	58
2.3.2.	Surfactants	59
2.3.3.	Materials used in nanoporous silicas synthesis and applications	59
2.4.	Synthesis of nanoporous materials	59
2.4.1.	MCM-41 Comparator	59
2.4.2.	Synthesis of hierarchical nanoporous materials	60
2.4.3.	Post-synthesis grafting reactions	60
2.4.3.1.	Sulfonic acid functionalization	60
2.4.3.2.	Oxidation reaction	60
2.4.4.	Palmitic acid esterification (catalysis tests)	61
2.4.4.1.	Samples for GC	61
2.5.	Sample preparation for characterizations	61
2.5.1.	The choice of solvents	61
2.5.2.	Surface tension	61
2.5.2.1.	CTAB and FSN-100 solutions	61
2.5.2.2.	CTAB/FSN-100 mixtures	62
2.5.3.	Fluorescence	62
2.5.3.1.	Pyrene stock solution	62

2.5.3.2.	Surfactant solution samples	62
2.5.4.	Small angle neutron scattering (SANS)	63
2.5.4.1.	Pure surfactant solutions	63
2.5.4.2.	Surfactant mixture solutions	63
2.5.5.	Pulsed-gradient spin-echo NMR spectroscopy (PGSE-NMR)	63
2.5.5.1.	Pure surfactant solutions	63
2.5.5.2.	Surfactant mixture solutions	63
2.5.6.	Electron paramagnetic resonance spectroscopy (EPR)	64
2.5.6.1.	16-DSE stock solution	64
2.5.6.2.	Surfactant solution samples	64
2.5.7.	Scanning Electron Microscopy (SEM)	64
2.5.8.	Transmission Electron Microscopy (TEM)	64
2.5.9.	X-ray diffraction (XRD)	65
2.5.10.	Nitrogen porosimetry	65
2.5.11.	Thermal gravimetric analysis (TGA)	65
2.5.12.	X-ray photoelectron spectroscopy (XPS)	65
2.6.	References	66
3.1.	Introduction	71
3.2.	Surface tension	71

3.2.1.	Surfactant solutions	71
3.2.2.	Surfactant mixture solutions	73
3.2.3.	CMC determination	74
3.2.4.	Surface area of surfactant per molecule calculations	75
3.3.	Fluorescence	77
3.3.1.	CTAB and FSN-100 single component aqueous solutions	77
3.3.2.	CMC determination	79
3.4.	Small-angle neutron scattering (SANS)	80
3.4.1.	Model used to fit the data	80
3.4.1.1.	CTAB parameters	81
3.4.1.2.	FSN-100 parameters	81
3.4.2.	Surfactant solutions	82
3.4.3.	Surfactant mixture solutions	83
3.5.	Electron paramagnetic resonance spectroscopy (EPR)	88
3.5.1.	The choice of spin-probe	88
3.5.2.	Hyperfine coupling constant	88
3.5.3.	Rotational correlation time	91
3.6.	PGSE- NMR spectroscopy studies	92
3.7.	<sup>1</sup> H-NMR	94

3.7.1.	50 mM CTAB solution	94
3.7.2.	50 mM FSN-100 solution	95
3.7.3.	CTAB/FSN-100 (50 mM, 50 mM) mixture solution	96
3.8.	<sup>19</sup> F-NMR	98
3.8.1.	50 mM FSN-100 and FSN-100/CTAB mixture	98
3.9.	Conclusions	99
3.10.	References	101
4.1.	Introduction	103
4.2.	Phase behaviour of surfactant/oil solutions	104
4.2.1.	Surfactant/W/O systems	104
4.2.2.	Surfactant mixtures/W/O systems	105
4.3.	<sup>1</sup> H-NMR measurements	105
4.3.1.	CTAB/hexane	106
4.3.2.	CTAB/PFH	109
4.3.3.	FSN-100/hexane	110
4.3.4.	FSN-100/PFH	111
4.3.5.	The mixture/hexane	112
4.3.6.	The mixture/PFH	113
4.4.	<sup>19</sup> F-NMR measurements	114

4.4.1.	CTAB/PFH	<b>114</b>
4.4.2.	FSN-100/ hexane	<b>115</b>
4.4.3.	FSN-100/PFH	<b>116</b>
4.4.4.	The surfactant mixture /hexane	<b>117</b>
4.4.5.	The surfactant mixture/PFH	<b>118</b>
4.5.	PGSE- NMR spectroscopy	<b>118</b>
4.5.1.	CTAB with hexane or PFH solutions ( $\alpha_{\text{CTAB}} = 1$ )	<b>119</b>
4.5.2.	FSN-100 with hexane or PFH solutions ( $\alpha_{\text{CTAB}} = 0$ )	<b>120</b>
4.5.3.	Surfactant mixtures with oils	<b>120</b>
4.6.	Small-angle neutron scattering (SANS)	<b>121</b>
4.6.1.	Surfactants with oils	<b>121</b>
4.6.1.1.	CTAB /hexane solutions	<b>121</b>
4.6.1.2.	FSN-100 /hexane solutions	<b>123</b>
4.6.1.3.	CTAB/PFH solutions	<b>125</b>
4.6.1.4.	FSN-100/PFH solutions	<b>128</b>
4.6.2.	Surfactant mixture /oil solutions	<b>130</b>
4.6.2.1.	Mixture/hexane solutions	<b>130</b>
4.6.2.2.	Mixture/PFH solutions	<b>132</b>
4.7.	Conclusions	<b>133</b>

4.8.	References	<b>135</b>
5.1.	Introduction	<b>137</b>
5.2.	System screening experiments	<b>138</b>
5.2.1.	Using CTAB with Zonyl FSO-100 (FSO sample)	<b>138</b>
5.2.2.	Using FSN-100 surfactant (FSN sample)	<b>138</b>
5.2.3.	Using FSN-100 surfactant and PFH (FSN/PFH sample)	<b>138</b>
5.2.4.	Using the template of FSN-100/ CTAB/PFH/hexane	<b>139</b>
5.2.5.	Using the template of FSN-100/CTAB/PFH	<b>139</b>
5.3.	The synthesis of the comparator MCM-41	<b>140</b>
5.4.	CTAB/FSN/PFH based systems	<b>142</b>
5.5.	Scanning electron microscopy (SEM)	<b>143</b>
5.6.	Transmission electron microscopy (TEM)	<b>144</b>
5.7.	Porosimetry characterization	<b>146</b>
5.7.1.	N <sub>2</sub> adsorption- desorption isotherms	<b>146</b>
5.7.1.1.	N <sub>2</sub> isotherm of 0 % sample	<b>148</b>
5.7.1.2.	N <sub>2</sub> isotherm of 1 % sample	<b>149</b>
5.7.1.3.	N <sub>2</sub> isotherm of 11 %, 20 % and 27 % samples	<b>150</b>
5.7.1.4.	N <sub>2</sub> isotherm for 33 % sample	<b>151</b>
5.7.2.	BET specific surface area	<b>152</b>

5.7.3. Pore size determination	<b>153</b>
5.8. X-ray Diffraction (XRD)	<b>158</b>
5.9. Conclusions	<b>159</b>
5.10. References	<b>161</b>
6.1. Introduction	<b>164</b>
6.2. Grafting materials	<b>164</b>
6.2.1. Thermal gravimetric analysis (TGA)	<b>165</b>
6.2.2. X-ray photoelectron spectroscopy (XPS)	<b>167</b>
6.3. Catalytic activity	<b>169</b>
6.3.1. Palmitic acid esterification reaction	<b>169</b>
6.4. Conclusions	<b>171</b>
6.5. References	<b>172</b>
7.1. Project conclusions	<b>174</b>
Appendix	<b>176</b>

## **Chapter One**

### **Introduction and Literature Review**



## 1.1. Hierarchical nanoporous materials

Hierarchical pore structures are attractive materials for traditional ion-exchange, adsorption, and separation applications in terms of having large surface areas, highly ordered nanochannels and uniform pore sizes. The material presents pores on different length scales from 2 nm to 50 nm. Basically, porous materials are classified based on the presence of three types of pores, micropores (<2 nm), mesopores (2-50 nm), and macropores (>50 nm) according to the IUPAC (the International Union of Pure and Applied Chemistry) [1]. Moreover, particular properties such as specific pore structures and reduced materials have a great potential in catalysis, sorption and biomedicine. Current approaches use combined physical templates such as polystyrene spheres to induce porous materials, but there are some difficulties of using the polystyrene templating approach. Polystyrene templating affects the integrity of the produced porous silica, the method is costly and it is a complicated process [2]. Surfactant templating is a good strategy in the synthesis of mesoporous silica as different cationic, anionic and non-ionic surfactants can represent suitable templates to induce bimodal pores. Surfactants also are efficient for templating porous materials since they can be recovered after the templating process. In surfactant templating, the main concept is how to utilize the organic surfactant molecules and the surfactant self-assembly approach to make a framework with other inorganic species in the synthesis of nanoporous solid structures. Figure 1.1 shows the IUPAC classification of nanoporous material based on the pore diameter.

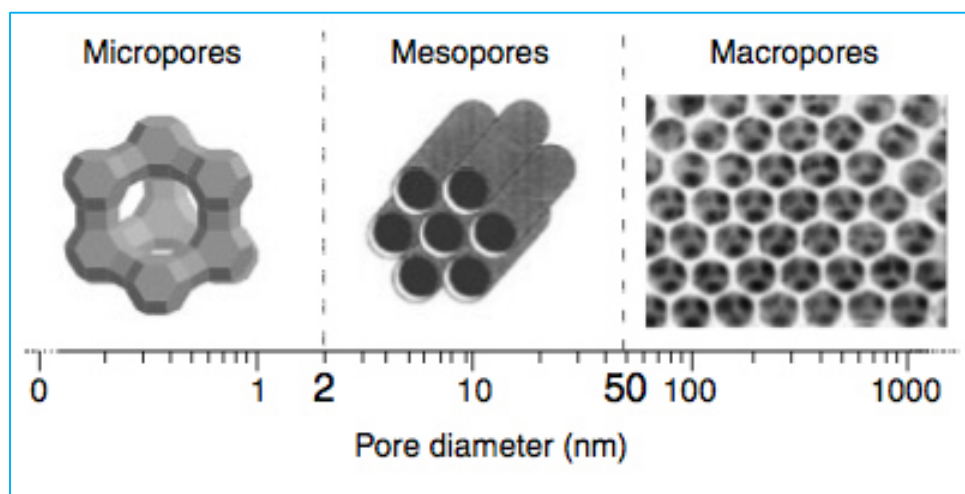


**Figure 1.1 The IUPAC classifications of nanoporous material [3].**

In terms of the applications, nanoporous materials are widely used not only because of their porosity advantages, but also because of their morphology. They also have many

types of possible morphologies such as the thin film, powder and honeycomb [4]. The fabrication of these materials with hierarchical porous structures is the main development of this field. It is possible to combine many benefits from a system with different pore size. For example, high specific surface area can be provided by meso and macroporous structures, whereas increased mass transport and easier accessibility to the active sites through the material can be offered by additional macropores. Hierarchical structures, which have macro and mesopores, have more properties such as superior mass transfer and lower restriction of the diffusion of reactants in the mesopores, compared with single- sized pore structures [4, 5].

In particular, the morphology of nanoporous silicas is controlled by several factors including hydrolysis and condensation of silica precursor around the surfactants, surfactant micelle shapes, and the interaction between micelles, as well as, the other additives such as organic swelling agents and cosolvents. Adjusting these factors provides various morphologies, which are important for a range of applications. For example, films for catalysis and separation, monoliths for optics, and uniform pore sized spheres are suitable for chromatography studies [6].

There are many proposed methods of using surfactants in the synthesis of nanoporous silicas. The most popular and cost effective ways are core-shell templating, self-assembly and microemulsion methods. In the next section, the surfactant self-assembly approach and its suggested pathways will be considered.

### **1.1.1. Templating with cationic and nonionic surfactants**

Cationic surfactants have an excellent solubility and can be used in acidic and basic media. In addition, the cationic quaternary ammonium surfactants  $C_nH_{2n+1}N(CH_3)_3 Br$  ( $n = 8-22$ ), including CTAB were used as structure directing agents in the first reports of mesoporous silicate synthesis [5, 7]. Moreover, the non-ionic surfactants self-assemble to produce mesophases with different geometry and arrangements and they become more popular in the synthesis of mesoporous materials. The fluorinated surfactants form intermediate mesophases easier than hydrocarbon surfactants when assemble into aggregates [8].

### **1.1.2. Synthesis mechanisms**

Many studies have been carried out for the formation of mesostructures, based on the surfactant self-assembly approach. However, two main effective mechanisms are possible in the synthesis of ordered nanoporous materials including cooperative self-assembly and liquid-crystal templating process [7, 9].

### 1.1.2.1. Cooperative self-assembly of surfactants

This mechanism is based on the interactions between the surfactants and silicates to form organic-inorganic mesostructured composites. The formation of hexagonal mesostructure depends on a layered intermediate. Figure 1.2 shows the cooperative surfactant self-assembly pathway [9].

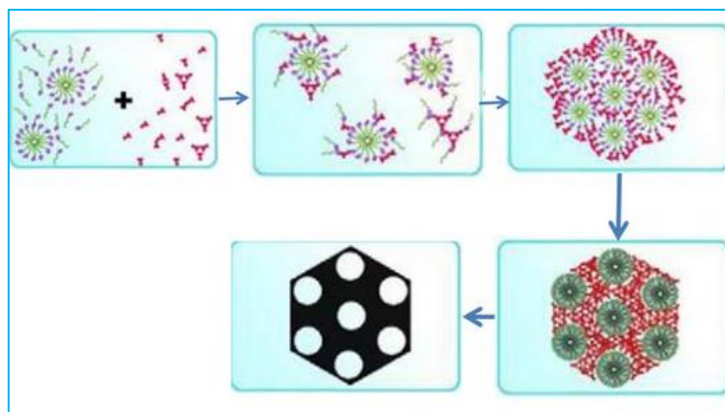


**Figure 1.2 The cooperative self-assembly pathway [9].**

### 1.1.2.2. Liquid crystal templating

In this mechanism, surfactants self-assemble into cylindrical micelles, and form the framework by encapsulating micelles by inorganic materials that balance the micellar surface charge. The liquid-crystal mesophases formed in this surfactant templating assembly process used to form ordered mesoporous materials. The organic template can then be removed by calcination or solvent extraction, etc. to leave a hexagonal arrangement of mesopores. Figure 1.3 shows a schematic representation of liquid crystal template pathway [9].

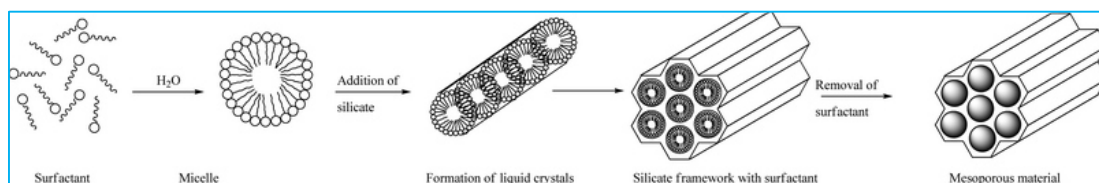


**Figure 1.3 The liquid crystal pathway [9].**

### 1.1.3. Material characterizations

To characterize nanoporous materials, adsorption methods are widely employed. N<sub>2</sub> or Ar adsorption isotherms measured at low temperatures are used to characterize the material porosity to study the surface area and the pore size distribution. In this project N<sub>2</sub> adsorption isotherms have been used to study the porosity systems and determine these key parameters. However, some limitations for these measurements are considered in terms of the expensive automatic equipment, the large amount of sample needed and long-time experiments.

#### 1.1.3.1. N<sub>2</sub> adsorption isotherm method

N<sub>2</sub> isotherm method is one example of gas adsorption technique used to investigate the porous material morphology. The method of N<sub>2</sub> adsorption-desorption is the starting point for the characterization of porous materials particularly mesoporous structures. Nitrogen adsorption-desorption can be applied over a wide range of relative pressure to analyse pore structures, and the multilayer adsorption of nitrogen can occur at liquid nitrogen temperature of 77 K. In the method, the amount adsorbed of nitrogen is evaluated by measuring the change of gas pressure. The operational procedure to determine the adsorption isotherm is by a discontinuous, point-by point procedure or a continuous approach. The discontinuous method is based on introducing different amounts of the adsorptive (N<sub>2</sub>) and at each stage reaching the equilibrium is required. The other approach is more recent and depends on providing a continuous equilibrium isotherm through a slow introducing of the adsorptive. The filling of micropores takes place at lower relative pressures ( $>10^{-4}$ ), whereas mesopores filling occur at higher relative pressure [10].

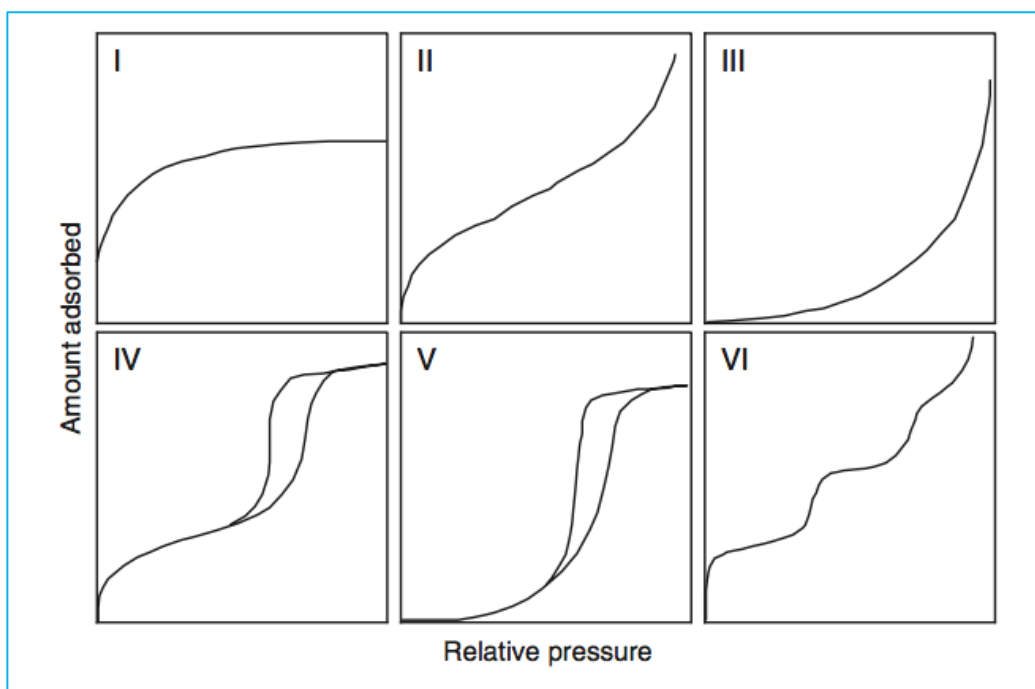


**Figure 1.4 Isotherm types based on IUPAC classifications [10].**

Basically, the gas adsorption starts to form a monolayer on the surface followed by multilayer adsorption and then capillary condensation occurs. Since the temperature is below the critical point of the gas (at or above this point vapour does not liquefy), the gas adsorbed amount increases with increasing the relative pressure. Six main adsorption isotherms are observed based on the plot of adsorbed amount vs the relative pressure. Figure 1.4 shows the IUPAC classification of isotherms [10]. Both types of IV and V have a hysteresis loop, which is related to the mesopore filling by capillary condensation, and emptying by evaporation.

- ***Hysteresis and capillary condensation***

Capillary condensation is the process of filling pores, which have the size range between 2 and 50 nm (mesopores), and it comes after multilayer adsorption on the pore wall. The mesopore spaces become filled with condensed liquid from the gas vapour phase. This phenomenon is the responsible for the hysteresis between the adsorption and desorption branches of the isotherm. The hysteresis loop is dependent of the parameters of the material examined, the temperature and the adsorbate. Thus, at determined parameters the shape of adsorption and desorption branches is strongly associated with the pore size distribution. The hysteresis loop is also classified into four types based on IUPAC classification. Figure 1.5 represents all these types of the hysteresis loop [10].

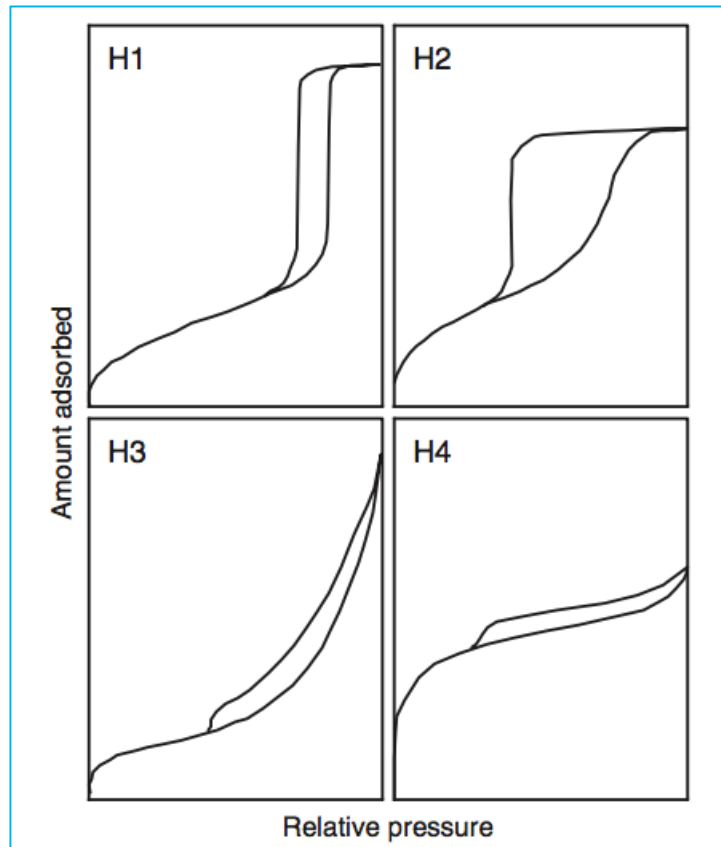


**Figure 1.5 the types of hysteresis loop [10].**

The hysteresis loop shapes are strongly linked to the pore shape. H1 type of hysteresis loop is associated with a narrow and uniform pore size distribution as the pores in MCM-41 (mesoporous silica with cylindrical pores). There is a broad loop with gradual uptake on adsorption and very steep desorption branch in the type H2. This hysteresis is associated with the porous materials, which have interconnected pores of progressive sizes and shapes. H3 and H4 types are continued at high relative pressure

and difficult to define the termination of desorption boundary curve. H3 loop is linked to the solids, which have a coexistence of two types of particles, whereas the H4 is observed in the materials having narrow slit-shaped pores such as activated carbons [10].

- **Pore surface areas and pore size distributions**

The surface area and pore size distributions are the most essential parameters estimated from the adsorption isotherms to characterize the porous materials. The Brunauer, Emmett and Teller model (BET) model [11] determines the specific surface area and the Barrett, Joyner and Halenda (BJH) [12, 13] method is used to obtain the pore size distribution.

- **The Brunauer, Emmett and Teller model (BET)**

The model was adopted to determine the specific surface area of porous materials and established as a standard model for surface area characterization. The model is an extension of the Langmuir model (monolayer condensation) but it takes the formation of multilayers into account [11]. BET equation (1.1) was developed to study the Type II isotherms and reversible part of Type IV isotherms.

$$\frac{P/P_o}{V(1-(P/P_o))} = \frac{1}{V_m C} + \frac{(C-1) \left(\frac{P}{P_o}\right)}{V_m C} \quad (1.1)$$

where,  $V$  is the volume of the adsorbed gas,  $V_m$  is the volume of the monolayer of adsorbed gas,  $P$  is the equilibrium gas pressure,  $P_o$  is the saturation pressure of the adsorbate and  $C$  is the BET constant.

The plot of the  $\frac{P/P_o}{V(1-(P/P_o))}$  vs relative pressure gives a straight line at low relative pressure range of  $0.05 < \frac{P}{P_o} < 0.25$  depending on the sample. The slope =  $(C - 1)/V_m C$  and the intercept is  $\frac{1}{V_m C}$  are used to estimate the specific surface area of the porous material. The linear region of the plot depends on both the adsorbent and adsorptive and the operational temperature. The specific surface area is calculated from the BET monolayer capacity and depends on the average area occupied by each molecule in the completed monolayer.

- **Pore size distribution**

The pore size of mesoporous materials mainly depends on the type and length of the hydrophobic part of surfactants. Larger pore sizes can be formed using cationic

quaternary surfactants with longer alkane chains. For example, the BJH pore diameter of MCM-41 increases from 1.6 to 4.2 nm when increasing the chain length from C<sub>8</sub> to C<sub>12</sub> [14][15].

Using a nitrogen adsorption isotherm for pore size determination is based on the BJH method as a way to estimate the pore size distribution from an appropriate nitrogen isotherm. The analysis of pore size using BJH method is dependent of the application of the Kelvin equation.

- **The Kelvin equation**

The Kelvin equation (1.2) is used to determine the pore radius in porous material using an adsorption porosimetry method. The equation describes the change in the vapour pressure related to the radius of the pore, as the equilibrium vapour pressure is highly dependent on the pore radius [12, 15].

$$\ln \frac{p^\circ}{p} = \frac{2\gamma V_m}{rRT} \quad (1.2)$$

where,  $P$  is the condensation partial pressure of the gas adsorptive,  $p^\circ$  is the saturated partial pressure for a flat surface,  $\gamma$  is the surface tension of liquid nitrogen,  $V_m$  is the liquid molar volume of nitrogen,  $r$  is the pore radius, and  $R$  is the gas constant and  $T$  is the absolute temperature.

## 1.2. Surfactant phase behaviour

Surfactant phase behaviour has been studied in this project for both pure surfactant solutions and mixtures in order to understand the role of the surfactant template in the synthesis of porous materials. To study the surfactant phase behaviour, the critical micelle concentrations (CMC), have been determined using surface tension and fluorescence approaches and from the surface tension study, the surface area per molecule of surfactant has also been investigated. In addition, surfactant micellization has been considered in terms of micelle shape and size, the micelle dynamics and the interaction between surfactant micelles and mixed micelles.

### 1.2.1. Surfactants

Surfactants are organic molecules that have the ability to adsorb at interfaces when dissolved in a solvent, and that changes the interface physical properties. Both surfactant chemical structure (amphiphilic molecules) and the nature of solvent affect the adsorption behaviour. The structure of head and tail groups classifies many



possible types of surfactants. The head groups include charged, natural and polymeric chain with various sizes from small to compact head groups. The tail could be single or double, hydrocarbon, fluorocarbon, and straight or branched. Four main types of surfactants are determined based on the type of head groups (hydrophilic parts) since the head group solubility in water is determined by either hydrogen bonding or ionic interactions. They are anionic, cationic, non-ionic and zwitterionic surfactants. Surfactants used in the project are chosen to be one hydrocarbon surfactant cetyltrimethylammonium bromide (CTAB) as an efficient surfactant for the synthesis of ordered mesoporous materials [16, 17], and the other is fluorocarbon surfactant Zonyl FSN-100 (FSN-100). The hydrocarbon/ fluorocarbon mixed micelle templates are previously considered to provide nanoporous materials with controlled pore size arrangements.

### 1.2.2. Surfactants and air-water interfaces

Water molecules have unequal attraction forces at the air-water surface, and the strong interaction through van der Waals forces and hydrogen bonding pull the molecules to the bulk phase to minimize the contact area with the gas phase in a spontaneous process. Thus, the presence of dissolved surfactant molecules in the bulk phase reduces the surface tension and minimizes the free energy per unit area due to the dual chemical structure of surfactants. At surfactant concentrations below the CMC, there is a dynamic equilibrium between the surfactant molecules arriving at the surface and those leaving the surface to the bulk. At the CMC, the surface is at maximum coverage of surfactant molecules in order to minimize the free energy, and surfactant aggregations start to form in the bulk phase. Above the CMC, surfactant monomolecular layer is adsorbed and the bulk includes free monomers and micellised surfactants.

### 1.2.3. Gibbs adsorption equation

At the air-water interface, surfactants adsorbed reduce the solution surface tension until reaching a constant value at concentrations above the surfactant CMC creating a break point in the plot of surface tension vs log concentration. In this case, the Gibbs adsorption equation for surface excess (equation 1.3) can be used to determine the Gibbs surface excess of the surfactant relative to water at any concentration up to the CMC, since the reduction of the surface tension has changing slope until reaching a maximum value at the CMC and then becomes zero above the CMC. The reduction of surface tension region in the plot represents the surfactant saturation of the interface and that can be used to estimate the area per molecule of the surfactant [18, 19].

$$\Gamma = -(\partial\gamma/\partial\ln C)/nRT \quad (1.3)$$

Where  $\Gamma$  is the surface excess of the surfactant,  $n$  is the number of species formed by surfactant dissociation (e.g. for non- ionic surfactants  $n = 1$ ),  $(\partial\gamma/\partial\ln C)$  is the slope of line B (figure 1.6),  $R$  is the gas constant and  $T$  is the temperature.

The surface area per molecule at the air/water interface has traditionally been calculated through applying the Gibbs equation. As the interface is saturated in the Gibbs region, the Gibbs approach predicted a continued linear decline. Thus, the surface area per molecule can be calculated from equation 1.4, [20, 21].

$$A_{min} = 10^{20} / N \cdot \Gamma \quad (1.4)$$

Where  $N$  is Avogadro's number and  $A_{min}$  is expressed in  $\text{\AA}^2/\text{molecule}$

Figure 1.6 shows a typical decay of surface tension of water and an increase of surface excess of surfactant vs the surfactant concentrations. In this figure Gibbs equation is used to quantify the adsorption at the surface. A reduction in the surface tension is observed with small changes in the concentration of the surfactant in the bulk phase. The gradual decrease in the surface tension with an increase in surface excess of surfactant is observed in region A. In addition, at higher surfactant concentration near to the CMC, a limited value of adsorption is reached and the surface tension curve becomes more linear, whereas in most cases the region of the concentrations below the CMC is curved.

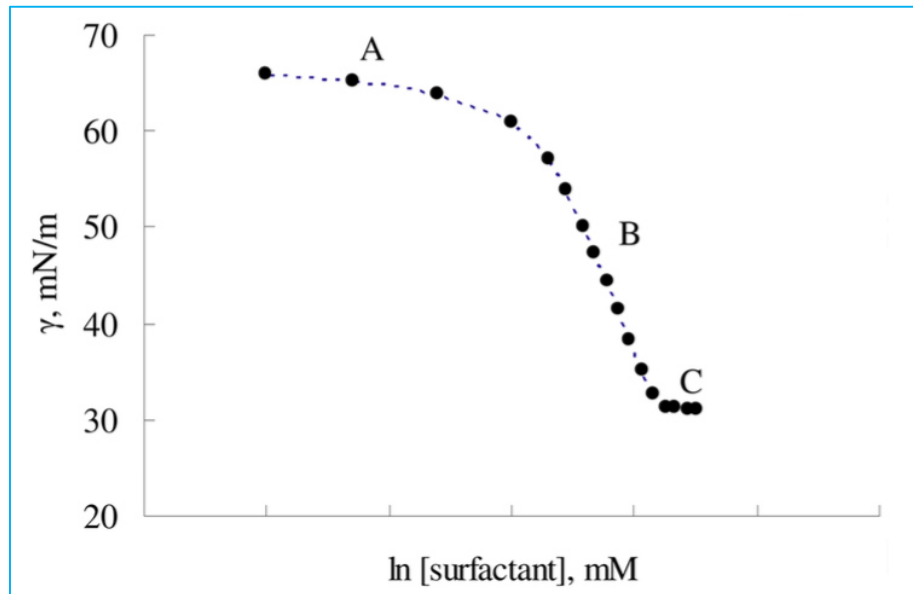


**Figure 1.6 A typical plot of surface tension vs ln concentration of a surfactant [20].**

### 1.2.4. Mixed surfactant systems

Typically, industrial surfactant systems are mixtures of different species, such as ionic, nonionic, and electrolytes. The mixed species provides the ability to control the ionic strength, pH and viscosity as well as other physiochemical properties of the system [22, 23]. Thus adjusting the composition of these systems can provide desirable surface properties for many applications. However, to select a suitable surfactant system, the interaction between molecules adsorbed at the interface and the adsorption phenomena of this surfactant must be known [24].

There have been many studies considered the adsorption and micelles in binary surfactant mixtures [25-31]. In particular, many fluorocarbon surfactants have growing interest in medical and environmental applications [32, 33]. The main discussion in mixed surfactant micelles is the degree of the ideality. It is well known that the interactions between fluorocarbon surfactants and hydrocarbon surfactants in the mixtures are nonideal [34, 35]. The nonideal mixing between these types of surfactants indicates the significant difference in the hydrophobicity.

#### 1.2.4.1. Mixed micelle and micelle separation

The formation of micelles in surfactant aqueous solutions affects the physical properties of the solution such as surface tension and light scattering, and the CMC can be measured when these changes occur. In mixed surfactant solutions, micelles contain two or more surfactant components in equilibrium with monomers. In this case the pseudo-phase separation models can be applied to study the mixed micellization in binary surfactant mixtures [36-38]. The assumption of these models is that surfactants mix ideally and the CMC of the mixture can be estimated as a function of the overall composition of the surfactant mixture and the CMCs of the pure surfactants [39]. The pseudo-phase separation approach has been used to predict the behaviour of binary nonionic surfactant mixtures as well as binary ionic surfactant mixtures particularly in the case when the hydrophilic groups are the same in both surfactants. In the case of ionic-nonionic surfactant mixtures, a deviation from ideality are often observed and that has led to develop the phase separation model to include the nonideal mixing in surfactants by treating micelles using regular solution approximations [39].

- ***Clint phase separation model***

The micellization of mixed surfactants has been studied by this theory in a simple phase separation model. It assumes that the micellar composition and the concentration of monomer of each component can be calculated as a function of total

concentration by using the CMC of the pure surfactant and the mole fraction in the mixture. Thus, the CMC of the mixture in this case is calculated by means of the ideal mixing theory and assuming the simple phase separation model (equation 1.5) [40]. In the surface tension studies, at the air-water interfaces the surface tension is calculated by assuming that the mixed monolayer to be in equilibrium with the monomers in the solution. The curve of the surface tension vs the concentration (log C) in such a system is predicted to have a minimum [38] .

$$\frac{1}{C_M} = \frac{\alpha}{C_{M1}} + \frac{1-\alpha}{C_{M2}} \quad (1.5)$$

Where,  $C_M$  is the CMC of the mixture,  $C_{M1}$  and  $C_{M2}$  is the CMC of the surfactants 1 and 2 respectively,  $\alpha$  is the mole fraction of the surfactant in the mixture. The activity coefficient of free monomers in the equation is assumed equal to unity.

### 1.3. Literature review

The literature review is split into three main sections in terms of studying the synthesis of porous materials, their properties as catalyst support materials, and the phase behaviour of surfactant solutions.

#### 1.3.1. Nanoporous materials

The formation of hollow spherical materials has been described in many papers with many of them focussed upon silica materials. Most of the reported systems in this field were generally based on sol-gel/emulsion techniques and self-assembly processes. However, a variety of inorganic materials such as iron oxide, titanium, and zeolites have been used to fabricate many hollow particles with pore diameter ranging from 2 to 100 nm [1, 5, 41]. A large number of surfactants have been used to template nanoporous materials and bimodal pores can be produced by choosing suitable surfactant mixtures [42-44]. However, mixing two different templates does not necessarily provide favourable bimodal fabricated materials. In this section we review nanoporous material formation using hydrocarbon surfactants, fluorocarbon surfactants and mixed surfactant templating, for which many different surfactants have been used in many different experimental approaches.

##### 1.3.1.1. Hydrocarbon surfactant templates

Well-ordered hexagonal mesoporous silica (SBA-15) with uniform pore sizes (up to 300 Å) has been synthesized by Zhao et al. Poly (alkylene oxide) triblock copolymers have been used as organic structure-directing agents in a self-assembly process. The

synthesis has been presented in acidic media to induce highly ordered materials with two-dimensional hexagonal mesophases [45].

Based on emulsion chemistry applications, stable hollow silica microspheres have been synthesised by Li et al. A sol-gel method of tetraethyl orthosilicate (TEOS) in non-ionic W/O emulsion has been used. In this work, the synthesized microspheres are thermally stable, have high specific surface area, and do not collapse even after calcination at 700 °C for 8 h [46].

However, in a single step synthesis, hollow silica spheres with high uniformity in size and multilamellar structure have been produced by Sun et al. They used PEO-PPO-PEO) ABA block copolymer based emulsion and combined with sodium silicate [47].

In terms of the applications of such materials, the synthesis of functional hollow pores has attracted much attention. For example, Titanium-silica (Ti-silica) hollow spheres with a mesoporous shell have synthesized by Li et al. They used an inverse multiple oil/water/oil emulsion to template the material with controlled shell thickness by changing the concentration of the silica source [48].

By using CTAB surfactant, Grun et al. have introduced two novel synthesis pathways for the preparation of mesoporous materials MCM-41. Both methods include tetra-n-alkoxysilanes TEOS or tetra-n-propoxysilane (TPS) as silica sources, represent short reaction times, easy preparation and excellent reproducibility [17].

In a different procedure, Dhainaut et al. have studied dual-templating routes to synthesize hierarchical macroporous-mesoporous SBA-15 silicas. They employed liquid crystalline surfactants and polystyrene beads. The templated materials present high surface areas, well-defined macro and mesopore network and narrow size distributions around 300 nm [49].

#### **1.3.1.2. Fluorocarbon surfactant templates**

Many of cationic and nonionic fluorocarbon surfactants have been used as templates for porous materials [8]. The ability of a fluorinated surfactant to form ordered mesoporous materials has been investigated by Blin and Stebe. Their report represents the first example of mesoporous silica formed with only fluorinated surfactants. They also studied the phase behavior of the template in the synthesis in order to investigate the properties of the molecular sieves. Moreover, to enlarge the pore size they either used perfluorodecalin (PFD) as swelling agent or increased the surfactant weight percent in water. So, this study provides a better understand of the swelling mechanism of mesoporous materials [50].

Fluorinated surfactants also have the ability to form novel intermediate mesophases more easily than hydrocarbon surfactants when assembled into aggregates. Tan et al. have reported a comprehensive investigation of using cationic fluorinated surfactants to template nanoporous materials. In this study, perfluoroalkylpyridinium chloride surfactants with different tail lengths have been used in aqueous solutions to prepare different pore structures. The same series of materials have been prepared again in aqueous-ethanol mixtures to avoid the initial immiscibility of the silica source. In both cases the pore size increase with increasing the tail length of the surfactant and that agrees with using the hydrocarbon surfactants. However, in the fluorinated surfactant case the pore architecture includes both a mesh phase and a bilayer structure as the chain length increase. So in this study, a significant work on the cationic fluorinated surfactants has been shown not only as templates to control the pore size but also to develop ceramic materials with novel pore network [8].

In terms of studying the effect of fluorocarbon addition on the structure of mesoporous materials prepared with fluorinated surfactants, Blin and Stebe have incorporated perfluoroheptane and perfluorodecalin oils as expanders into the fluorocarbon micellar solution. Material pore diameters and pore arrangements have been changed due to this addition. The pore size increased from 4.0 to 6.8 nm on adding perfluoroheptane whereas adding perfluorooctane had no effect on the structure or the pore sizes [51].

The concentration of surfactants also greatly influences the porosity of fabricated materials. Large and small-nanoporous silica has been synthesized using a cationic partially fluorinated surfactant with a short tail. Tan et al. have reported this study and they employed 1-(3, 3, 4, 4, 4-pentafluorobutyl) pyridinium chloride surfactant as a directing agent in the synthesis. Unusually large porous silica with uniform foam was produced at low surfactant concentration whereas at higher concentration more typical wormhole like pores were structured [52].

The synthesis conditions including pH also affected the material porosity. In a similar study, Esqena et al. have reported the aqueous phase behavior and the synthesis of mesoporous silica in nonionic fluorinated surfactant solutions. A self-assembly precipitation method has been carried out to prepare the material. In addition, at higher HCl concentrations, hexagonal ordered mesopores were formed, while lower concentrations of HCl directed the synthesis to form disordered worm-like mesopores. Further, at very small surfactant concentrations, the materials possess high specific surface areas ( $\sim 1000\text{m}^2/\text{g}$ ) [53].

### 1.3.1.3. Mixed micelle templates

The synthesis of hierarchical porous materials using a mixed micelle template approach has been considered by Gao Hu et al. They estimated that the phase separation of mixed micelles was the key point in the synthesis process. They also combined the pseudophase separation theory for the critical micelle concentration with the Flory-Huggins theory for the chain molecular mixture in order to consider the properties of mixed surfactant solutions and how that effects pore size arrangements in the materials [41].

Various block copolymers such as the Pluronic of F127, P123 and SE (PS-co-PEO) have been combined with the surfactant of CTAB by Sel et al. They considered using surfactant mixtures and nanocasting procedure to form hierarchical bimodal mesoporous materials [54].

Relatively small particles with high surface areas have been synthesized using water-in-oil mixed surfactant microemulsion systems. Bumajdad et al. have synthesized metal oxide nanoparticles from the template of aqueous-in-heptane microemulsions which were stabilized by mixed surfactant solutions contain the didodecyldimethylammonium bromide (DDAB) and the nonionic surfactant Brij®35 ( $C_{12}E_{23}$ ). The system was used to synthesize iron oxide ( $\alpha\text{-Fe}_2\text{O}_3$ ) and cerium oxide ( $\text{CeO}_2$ ) nanoparticles using the precipitant of ammonia, the range of the nanoparticle size was 30-60 Å [55].

Hydrocarbon/fluorocarbon cationic surfactant templating of mesoporous silica has been studied by Xing et al. The study considered the coassembly behaviour of mixed cetyltrimethylammoniumchloride (CTAC) and 1H, 1H, 2H, 2H- perfluorodecylpyridinium chloride (HFDePC) with silica. The structure and pore size distributions are controlled by changing some parameters such as the molar ratio of CTAC to HFDePC [56].

Mixed micellar phases have also been studied by Groenewolt et al. Fluorinated nonionic surfactants Fluowet OTN<sup>TM</sup> and Fluowet OTL<sup>TM</sup> have been used with two hydrocarbon block copolymer surfactants to prepare highly organized mesoporous silica. From this study two different situations in the solution can be identified, demixed or mixed micelles. This identification provides a good way to know the resulting porous system from hydrocarbon/fluorocarbon mixtures with controlled pore size distribution [57].

By using mixed micellar template aspects, Yang et al. have also developed mesoporous silica vesicles with hierarchical structures. They used triblock copolymer Pluronic P103 and SDS as a co-surfactant in the presence of NaF. The anionic-

nonionic surfactant molar ratio (SDS/Pluronic P103) can be adjusted to vary the particle size and vesicle cavity diameter. The resulted materials have great potential as practical catalyst, drug delivery systems and bimolecular applications [58].

Hierarchically bimodal porous structures have also been obtained by templating silica microparticles with surfactant micelle/ microemulsion mixture solutions. Carroll et al. have reported this synthesis process using the aqueous solution of CTAB and the oil phase of polyether-polysiloxane/dimethicone copolyol surfactant (ABIL EM 90) in hexadecane. They confirmed that tuning the phase state and adjusting the surfactant composition and concentration can control the structure of resultant material [59].

Multimodal porous networks using mixed micellar solutions have been reviewed by Yang et al. Different methods have been used including supramolecular assemble of amphiphilic polymers or surfactants with other surfactant systems or macrotemplates such as liquid drops and solid particles. They also discuss other physical or chemical methods, phase separation aspects and template replication, which are combined with using surfactants in the synthesis of multiporous materials [60].

### **1.3.2. Catalytic applications**

Porous material properties including high surface area, controllable pore size and narrow pore size distribution, and thermal stability are interesting in a wide variety of potential applications where molecular recognition is required [61, 62]. Palmitic acid esterification reaction is one example as an application to show the importance of developing these materials in several branches of the chemical industry [61].

The next few examples of the catalytic approaches represent the importance of such materials and their characterization in order to determine their ability and efficiency for catalysis applications.

#### **1.3.2.1. General catalysis reactions**

Self-assembled systems have been used in catalysis applications. For example, many researchers have used dispersion colloids to precipitate nanoparticles such as nanoceria ( $\text{CeO}_2$ ) [63-67]. In particular, different types of cationic quaternary ammonium surfactants (e.g. CTAB) were used for this purpose, also to control the particle size and the surface area of the nanoparticles [68-70].

Mesoporous silicas have been extensively studied as catalysts and catalyst supports. For example, functionalized SBA-15 mesoporous silica has been investigated by Cheng et al. as a catalyst. Good crystallographic order, high surface area and large



uniform pore size have been obtained. The synthesized material also has a high catalytic efficiency [71].

Zhang et al. have used the hydrolysis of aluminum tri-sec-butoxide in O/W microemulsion solution in the presence of CTAB to synthesis large mesoporous aluminas. They have obtained a disordered mesostructure with large mesopores and it exhibited high performance as catalyst support. Generally, due to the higher hydrolytic stability, mesoporous aluminas are superior to silica in the catalyst support approaches. However, most researchers focused mainly on using mesoporous silica in such applications [72].

Rigby et al. have studied the characterization of mesoporous materials as catalyst supports. Gas sorption and mercury porosimetry techniques have been used to assess the homogeneity of templated materials and their pore size distribution [73].

#### **1.3.2.2. Sulfonic acid functionalization reactions**

Sulfonic acid functionalization as post-synthesis reactions of porous materials has been considered in many studies. For example, Morales et al. have worked on mesoporous silica materials to correlate the difference in hydrophobic/hydrophilic character of the surface of propyl- and arene- sulfonic acid mesoporous supports, with the catalytic properties of modified silica for aqueous sensitive reaction sites. The higher catalytic activity of these materials was affected by the increased hydrophobicity near the sulfonic acid moieties [74].

In addition, sulfonic acid functionalized honeycomb silica has been synthesized by Satoh et al. They succeeded in attaching sulfonic acid groups to silica microhoneycomb structures with an average of macropore size about 27 micrometer and observed high stability in catalytic activity for 24 h in a flow reactor [75].

In terms of studying the quantitative oxidation of thiol groups in sulfonic acid-functionalized silica, Cano-Serrano et al. have developed a simple procedure for the synthesis. They have prepared amorphous mesoporous silica with attached thiol groups to make strong acid sites in the esterification reaction of acetic acid by methanol [76].

#### **1.3.2.3. Palmitic acid esterification reaction**

The hierarchical macro- mesoporous SBA15 silica synthesized by Dhainaut et al. was also subsequently functionalized with propylsulfonic acid to yield a macro-mesoporous solid acid catalyst. This bi-modal solid acid architecture gives significant rates of the

transesterification of bulky glyceryl trioctanoate and long chain palmitic acid esterification reaction [49].

The esterification reaction of palmitic acid has also been studied by Carmo et al. They have used mesoporous aluminosilicate Al-MCM-41 in the presence of methanol, ethanol and isopropanol. Different ratios of Si/Al have been used to prepare the catalyst at room temperature and then characterized in terms of its structural, morphological and thermal aspects. The concentration of acidic sites on the produced catalyst and the amount of incorporated metal influenced the reaction in a fixed atmosphere [61].

### 1.3.3. Surfactant phase behaviour

Recently, surfactant solution systems have been a subject of many investigations [26, 27, 29, 31, 77]. These materials self-assemble in aqueous solutions to make a wide variety of aggregated structures. To study the composition of these aggregates, many techniques have been used and most of them based on determining the structure, shape-size, critical micelle concentration and the interaction between micelles in the solution. In this part of the literature review, many features of surfactant solutions will be highlighted by the various techniques used to study surfactant phase behaviour.

#### 1.3.3.1. Critical micelle Concentration (CMC) determination

Critical micelle concentrations (CMC) have been studied for many surfactants in the pure surfactant solutions as well as the mixtures. The properties of micelles have been extensively studied using various experimental methods. Some of these measurements are, static and dynamic light scattering [78-80], small angle X-ray scattering (SAXS) [81, 82], neutron scattering (SANS) [83, 84], electron paramagnetic resonance (EPR) [83, 85], nuclear magnetic resonance (NMR) [86, 87], and different method of dynamics of micellization [88, 89]

- **Hydrocarbon surfactants**

A considerable effort has been made to determine CMC values of surfactants. Among various methods, fluorescence, surface tension measurements and electron spin resonance (ESR) techniques have been widely used. Bahri et al. have studied the hydrocarbon surfactants CTAB, DTAB and SDS systems in order to relate the obtained CMC values and measured microviscosity for each surfactant [77, 90].

The CMC of different hydrocarbon surfactants including nonionic, anionic and cationic surfactants have been determined using the pyrene 1:3 ratio approach. In this study,

Aguiar et al. have determined the CMC of the surfactants SDS, DTAB, TTAB, CTAB, TX-100,  $C_{12}E_8$  and  $C_{12}E_4$  [90]. For example the CMC of CTAB obtained by the conductance method was 0.98 mM.

The micellar behavior of the cationic hydrocarbon surfactants CTAB and TTAB has been studied in water organic solvent mixed media [91]. The techniques used in this study are the surface tension and conductivity at 303 K. The CMC value, the minimum area per molecule and the maximum surface excess concentration have been compared over a range of different organic solvents used in the water mixed media.

The CMC of mixed surfactant solutions have also been determined [92-94]. For example, the CMC values of binary mixtures of ionic hydrocarbon surfactants have been determined in many studies [29-31], and they generally fall in the range between the individual pure components. A linear relationship between the CMC and the surfactant molar ratio indicates that the chain moieties in such mixtures exhibit ideal mixing behavior [25].

In addition, determining the CMC of mixed surfactant systems is essential since using mixing thermodynamic models requires the knowledge of the CMC over a range of compositions. Anton et al. have studied the determination of the CMC for mixed surfactant systems [95].

A very large number of surfactant mixture reports were for systems of micelles composed of normal hydrocarbon surfactants and they have been largely studied and well characterized. However, limited studies are available on the mixed fluorinated and partially fluorocarbon/hydrocarbon surfactant micelles. Interestingly, some unique features of fluorinated surfactants have been reported in terms of studying their surface activity, hydrophobicity and miscibility with hydrocarbon surfactants [96].

- ***Fluorinated surfactants***

The micellization of fluorinated surfactants differs from the hydrocarbon surfactants since they have different surface activity and hydrophobicity. Lower CMC values are strongly related to the fluorinated surfactants and even one single chain amphiphiles can form bilayer aggregates [97].

One of the most studied techniques to investigate fluorinated surfactant solution behavior is fluorescence analysis. Generally, fluorescence probe methods including pyrene as a probe are used to characterize micelles from fluorocarbon surfactant solutions. For example, Kalyanasundaram has used pyrene fluorescence to probe fluorocarbon surfactant micelles and the micelles in the mixtures with hydrocarbon

surfactants [98]. The study has shown that the solubility of pyrene in perfluorocarbon micelles is very limited but the analysis can still determine the CMC values on the possible compositions of mixed surfactant micelles.

To consider surfactant phase behavior in the monolayer at the water-air interface and in the bulk phase, Szymczyk has studied Zonyl FSN-100 and Zonyl FSO-100 as examples of fluorocarbon surfactants. Such systems exhibit different behaviors in aqueous solution as two apparent CMC values can be recorded. The two CMC values have been determined as a result of either the coexistence of different micelle sizes or pre-association and micellization processes [99].

In order to determine the critical micelle concentration of the nonionic fluorocarbon surfactant Zonyl FSN-100 in aqueous solutions, Skvarla et al. have confirmed the two break points in the surface tension curve. These two-CMC values of FSN-100 aqueous solution may indicate the presence of the surfactant with different chain length in solution, which causes a gradual transition from unimers to micelles [100].

- ***Fluorocarbon-hydrocarbon surfactant mixtures***

In terms of fluorocarbon surfactant applications, one fluorinated surfactant does not possess all the expected properties due to its oleophobic features. However, to achieve the required properties, mixed hydrocarbon- fluorocarbon systems can be used. Barthelemy et al have studied fluorocarbon-hydrocarbon nonionic surfactant mixtures and their phase behavior has been examined by  $^{19}\text{F}$ -NMR spectroscopy and UV-visible spectroscopy. The system also showed two CMC values as a function of surfactant concentration. Above the second CMC two kinds of micelles have shown to coexist due to the incompatibility between the two different surfactants [101].

Mixed cationic surfactants have also been studied by Dubey to investigate the aggregation behavior and properties of such mixtures using different techniques. Tetradecyltrimethylammonium bromide (TTAB), CTAB, and hexadecyltriphenylphosphonium bromide (HTPB) and their mixtures in aqueous solutions have been investigated in this study using NMR, fluorescence and conductance techniques [102]

The ideality of binary mixtures is the main interest in these systems and it is well known that mixed hydrocarbon/fluorocarbon surfactants are nonideal [103]. The fluorinated materials also exhibit limited miscibility with hydrocarbon amphiphiles [35, 104]. However, in the first report studied by Mukerjee and Yang [35], on the hydrocarbon surfactant SDS and the fluorocarbon surfactant sodium perfluorooctate, they investigate that both surfactants cannot form mixed micelles. They suggest that the two

surfactants may form their own micelles or partially mixed micelles in water. The study also examined the magnitude of nonideality based on calculating the CMC values of the mixed systems assuming the extreme case of complete demixing of micelles.

The micellar microenvironment fluorocarbon/ hydrocarbon surfactant mixtures have also been studied by Asakawa et al. The study reported that using a fluorescence probe and  $^1\text{H}$  NMR and  $^{13}\text{C}$  NMR chemical shifts the second CMC values could be determined. These values confirm the coexistence of two kinds of mixed micelles [102, 105].

To investigate the nonideality and immiscibility of hydrocarbon (CH) /fluorocarbon (CF) surfactant mixtures. Long et al. have reviewed a number of CH/CF systems. Completely different phase behavior and self-assembly aggregation processes can be observed from such mixtures which confirms the repulsion between the two hydrophobic chains [106].

The nonideality behavior of the fluorocarbon-hydrocarbon surfactant mixture has been studied by Mukerjee and Handa [107]. The fluorocarbon and hydrocarbon nonideality in air-water, perfluorohexane-water and hexane-water interfaces effects the free energy of adsorption based on the difference in the affinity of the surfactant for the interface and the maximum possible adsorption before forming micelles.

### 1.3.3.2. Micelle structure determination

Many techniques have been used to estimate the micelle structure such as light scattering, fluorescence, electron paramagnetic resonance spectra (EPR), PGSE-NMR and small-angle neutron scattering (SANS) [108-117]. Moreover, to characterize the micellar structures, many literatures rely on individual methods [118-120]. However, most details obtained through combination of different methods. For example, the Soft Matter Group in Cardiff university combine the EPR, PGSE-NMR, and SANS methods in much of their research [83] [110].

Generally, surfactant aggregates can be formed in various shapes depending on many parameters including head group size, surfactant charge, length of tails, and concentration and temperature. These shapes include spherical and wormlike micelles, vesicles and lipid bilayers [109].

- ***Small-Angle neutron scattering (SANS)***

To explain the effect of the architecture of the surfactant molecule in the structure (shape-size) of the micelle, different surfactants have been studied. For example,

Goyal and Aswal have applied SANS experiments on the micellar solutions, and investigated the relationship between the molecular architecture and the shape and size of micelles such as CTAB as a single tail/ single head group molecule, and Gemini surfactants which include two tails and two head groups attached to a spacer [113].

The correlation between the surfactant structure and the aggregation behavior in aqueous solutions have been also studied using SANS technique. For example, the ionic surfactant CTAB has been studied in terms of the micelle shape and size in aqueous solution. The aggregation number of CTAB micelles has been estimated in different CTAB concentrations [121].

Micelle aggregation process has also been evaluated using SANS by Griffiths et al. A series of aqueous solutions including the nonionic surfactant SDS, the cationic surfactant dodecyltrimethylammonium bromide (DTAB) and dodecyltrimethylammonium chloride (DTAC) have been studied in the presence of sodium bromide and sodium chloride [83].

SANS has also been used to characterize the mixed surfactant micelles in terms of the comparison of the micelle shape and size between the pure surfactant and the mixed micelles. For example, the ionic surfactant SDS and the nonionic sugar-based surfactant dodecylmalono-bis-methylglucamide (DBNMG) mixed micelle system has been investigated by Bales, et.al. A classical model of a hydrocarbon core surrounded by a polar shell has been considered to fit the SANS [122]

SANS analysis has also been used by Das et al to determine shape and size of highly concentrated micelles in CTAB/NaSal solutions. They studied the effect of temperature on micellar shape and found that large micelles are formed at low temperatures and with increasing temperature micelles start to break up to form smaller micelles [112].

In order to determine shape and size of the nonionic fluorocarbon surfactant Zonyl FSN-100 in aqueous solutions, Skvarla et al. have used NMR spectroscopy and light and small angle X-ray scattering. Small angle X-ray scattering analysis was used to confirm the assumption of forming spherical core-shell micelles from FSN-100. The compact core formed by the fluorocarbon chains and the swollen shell formed by the hydrated part of the surfactant [100].

- ***Electron paramagnetic resonance NMR spectra (EPR)***

Bales et al. have studied micelle shape and size using EPR analysis to investigate the sodium dodecylsulfate (SDS) micelles. From the estimated hyperfine-coupling constant of the indicator, the polarity of SDS micelles decreases linearly with micelle size,

whereas the microviscosity which is estimated from the rotational correlation time of the used indicator, increases with the size [115].

In order to measure the polarity of surfactant head-group region in a mixture, EPR has been used by Griffiths et al. The ionic surfactant sodiumdodecylsulfate (SDS) has been mixed with the sugar-based nonionic surfactant (tetradecylmalono) bis (N-methylglucamide) (C<sub>14</sub>BNMG). At low SDS mole fraction, the majority of the head group region has been occupied by the sugar head- group and from the rotational correlation time of the spin-probe, the microviscosity increases with decreasing SDS mole fraction [114].

Investigating surfactant micelles using EPR technique has also been reported by Griffiths et al. They have aimed to compare the aggregation process in three different systems, SDS, DTAB and DTAC in the presence of sodium bromide and sodium chloride. Different hydration degrees of the micelle surface have been calculated from the hyperfine coupling constant values [83].

- ***Pulsed gradient spin-echo NMR spectroscopy (PGSE-NMR)***

In terms of studying the structure of CTAB micelles, Giustini et al. have used pulsed-gradient spin-echo NMR technique to investigate the microemulsion solution of CTAB/water/n-pentanol/n-hexane. From the analysis of n-pentanol self-diffusion coefficient, they determine the composition of the continuous organic phase and of the interfacial phase. From the CTAB self-diffusion coefficient, the size of reverse micellar has been estimated [111].

CTAB micelles have been also studied by Mills et al to investigate the size, shape and composition of reverse micelles in the mixture of CTAB/pentanol/water microemulsion. They used pulsed gradient stimulated echo nuclear magnetic resonance technique. The study indicates that both CTAB and pentanol molecules are in different environments within the microemulsion. The distribution of CTAB and pentanol between reverse micelles interphase and continuous phase has been determined by measuring the diffusion coefficient for the mixture at short and long times [109].

Palazzo et al. in a different study have considered the system of water-in-oil CTAB/n-pentanol/n-hexane/water microemulsion. This time, they evaluated the average head group area of CTAB, the alcohol fraction in the micelles and the amount of water in the organic bulk using different techniques such as PGSE-NMR spectroscopy, conductivity and near infrared absorption spectroscopy [108].

PGSE-NMR, is a powerful method to probe the compositions of mixed micelles. For example, the interaction between the nonionic surfactant (dodecylmalonobis(N-methylglucamide)) (DBNMG) and the anionic surfactant (sodium dodecyl sulfate) (SDS) has been studied by Griffiths et.al. In the study, over a range of compositions both surfactants showed an ideal mixing behaviour [123].

## 1.4. Project Aims

The purpose of this project is to explore the use of mixed surfactant systems to template and design hierarchical porous structures. Chapter One can be concluded in the context of studying the fluorocarbon surfactant FSN-100 and the hydrocarbon surfactant CTAB. Thus, FSN-100 and CTAB form the templated framework in a self-assembly process by incorporation of their micelles. In the project, mixtures of CTAB and FSN-100 in the presence of an oil phase (perfluorohexane) as an expander has been used to template the nanoporous silica. The key point is varying the amount of oil in the template to investigate how that affects the morphology of the resulted materials in terms of the material surface area, the type of porosity and the pore size distribution.

In addition, there have been summarized that one technique is not enough to study fluorocarbon/hydrocarbon surfactant mixtures and multiple techniques are strongly needed to obtain the whole picture of mixed micelle systems. From the literature review, the hydrocarbon surfactant CTAB has been extensively studied but there are few papers were about the fluorocarbon surfactant FSN-100. Many studies have considered CTAB mixtures with other hydrocarbon and fluorocarbon surfactants. However, FSN-100 mixtures either with CTAB or other surfactants have less attention over the past few years. In terms of using surfactants as templates for the synthesis of nanoparticles, the cationic quaternary ammonium surfactants  $C_nH_{2n+1}N(CH_3)_3 Br$  ( $n = 8-22$ ), particularly CTAB are the most surfactant forms were used in the very beginning reports of templating mesoporous silicate (MCM-41) as well as the recent studies of these materials.

The combination of CTAB and FSN-100 therefore represents a new area of research in the context of silica based material templating.



To conclude, the main aims of the project are to:

- study the structure of fluorocarbon (FSN-100)/hydrocarbon (CTAB) mixed surfactant micelles.
- study the phase behaviour of these mixed micelles in the presence of hydrocarbon oil (hexane) and fluorocarbon oil (perfluorohexane).
- explore the use of swollen mixed micelles as templates to synthesize nanoporous materials.
- characterize the porosity in these materials as potential precursor catalyst.
- functionalize through alkyl sulfonic acid surface grafting.
- quantify the ability to convert palmitic acid into palmitate.

## 1.5. References

1. Parlett, C.M.A., K. Wilson, and A.F. Lee, Hierarchical porous materials: catalytic applications. *Chemical Society Reviews*, 2013. **42**(9): p. 3876-3893.
2. Liu, C., et al., Synthesis of porous hollow silica spheres using functionalized polystyrene latex spheres as templates. *Korean Journal of Chemical Engineering*, 2011. **28**(6): p. 1458-1463.
3. Wang, X., Bu, X. and Feng, P. , Porous Inorganic Materials. , in *Encyclopedia of Inorganic Chemistry*. . 2006. p. 1-21.
4. Yuan, Z.Y. and B.L. Su, Insights into hierarchically meso-macroporous structured materials. *Journal of Materials Chemistry*, 2006. **16**(7): p. 663-677.
5. Lopez-Orozco, S., et al., Zeolitic Materials with Hierarchical Porous Structures. *Advanced Materials*, 2011. **23**(22-23): p. 2602-2615.
6. Wu, T., et al., New Zeolitic Imidazolate Frameworks: From Unprecedented Assembly of Cubic Clusters to Ordered Cooperative Organization of Complementary Ligands. *Chemistry of Materials*, 2008. **20**(24): p. 7377-7382.
7. Wan, Y. and D. Zhao, On the controllable soft-templating approach to mesoporous silicates. *Chemical Reviews*, 2007. **107**(7): p. 2821-2860.
8. Tan, B., et al., Controlling nanopore size and shape by fluorosurfactant templating of silica. *Chemistry of Materials*, 2005. **17**(4): p. 916-925.
9. Pal, N. and A. Bhaumik, Soft templating strategies for the synthesis of mesoporous materials: Inorganic, organic-inorganic hybrid and purely organic solids. *Advances in Colloid and Interface Science*, 2013. **189**: p. 21-41.
10. Horikawa, T., D.D. Do, and D. Nicholson, Capillary condensation of adsorbates in porous materials. *Advances in Colloid and Interface Science*, 2011. **169**(1): p. 40-58.
11. Ladavos, A.K., et al., The BET equation, the inflection points of N<sub>2</sub> adsorption isotherms and the estimation of specific surface area of porous solids. *Microporous and Mesoporous Materials*, 2012. **151**: p. 126-133.
12. Barrett, E.P., L.G. Joyner, and P.P. Halenda, The Determination of Pore Volume and Area Distributions in Porous Substances .1. Computations from

- Nitrogen Isotherms. Journal of the American Chemical Society, 1951. **73**(1): p. 373-380.
13. Joyner, L.G., E.P. Barrett, and R. Skold, The Determination of Pore Volume and Area Distributions in Porous Substances .2. Comparison between Nitrogen Isotherm and Mercury Porosimeter Methods. Journal of the American Chemical Society, 1951. **73**(7): p. 3155-3158.
  14. Jana, S.K., A. Mochizuki, and S. Namba, Progress in pore-size control of mesoporous MCM-41 molecular sieve using surfactant having different alkyl chain lengths and various organic auxiliary chemicals. Catalysis Surveys from Asia, 2004. **8**(1): p. 1-13.
  15. Makowski, W. and P. Kustrowski, Probing pore structure of microporous and mesoporous molecular sieves by quasi-equilibrated temperature programmed desorption and adsorption of n-nonane. Microporous and Mesoporous Materials, 2007. **102**(1-3): p. 283-289.
  16. Hu, J., et al., One-step synthesis of micro/mesoporous material templated by CTAB and imidazole ionic liquid in aqueous solution. Microporous and Mesoporous Materials, 2011. **142**(1): p. 268-275.
  17. Grun, M., et al., Novel pathways for the preparation of mesoporous MCM-41 materials: control of porosity and morphology. Microporous and Mesoporous Materials, 1999. **27**(2-3): p. 207-216.
  18. A.M. Ovrutsky, A.S.P., M.S. Rasshchupkyna, 5 – Adsorption. The Gibbs Adsorption Equation. Surfaces, Interfaces, Crystallization, 2014: p. 127-149.
  19. Bermudez-Salguero, C. and J. Gracia-Fadrique, Analysis of Gibbs adsorption equation and thermodynamic relation between Gibbs standard energies of adsorption and micellization through a surface equation of state. Journal of Colloid and Interface Science, 2011. **355**(2): p. 518-519.
  20. Menger, F.M., L. Shi, and S.A.A. Rizvi, Re-evaluating the Gibbs Analysis of Surface Tension at the Air/Water Interface. Journal of the American Chemical Society, 2009. **131**(30): p. 10380-+.
  21. Menger, F.M., L. Shi, and S.A.A. Rizvi, Additional Support for a Revised Gibbs Analysis. Langmuir, 2010. **26**(3): p. 1588-1589.

22. Ali Khana, E.F.M., Synergism and polymorphism in mixed surfactant systems. *Current Opinion in Colloid & Interface Science*, 2000. **4**: p. 402-410.
23. Hines, J.D., et al., A study of the interactions in a ternary surfactant system in micelles and adsorbed layers. *Journal of Physical Chemistry B*, 1998. **102**(48): p. 9708-9713.
24. Negm, N.A., M.R. Mishrif, and D.E. Mohamed, Vanillin based cationic surfactants mixed systems: Micellization and interfacial interaction behaviors in presence of nonionic conventional surfactant. *Colloids and Surfaces a- Physicochemical and Engineering Aspects*, 2015. **480**: p. 122-129.
25. Mysels, K.J. and R.J. Otter, Thermodynamic Aspects of Mixed Michelles - Application to an Empirically Established Equilibrium. *Journal of Colloid Science*, 1961. **16**(5): p. 474-&.
26. Tokiwa, F. and K. Ohki, Thermodynamic Studies of Micellization and Micellar Solubilization of a Nonionic-Cationic Surfactant. *Kolloid-Zeitschrift and Zeitschrift Fur Polymere*, 1968. **223**(2): p. 138-&.
27. Tokiwa, F. and K. Ohki, A Consideration of Micelle Formation of an Ionic-Nonionic Surfactant through Its Ionization Energy. *Bulletin of the Chemical Society of Japan*, 1968. **41**(6): p. 1447-+.
28. Tokiwa, F., K. Ohki, and I. Kokubo, Gel Filtration of Mixtures of Surfactants on Sephadex. *Bulletin of the Chemical Society of Japan*, 1968. **41**(12): p. 2845-+.
29. Moroi, Y., K. Motomura, and R. Matuura, Critical Micelle Concentration of Sodium Dodecyl Sulfate-Bivalent Metal Dodecyl-Sulfate Mixtures in Aqueous-Solutions. *Journal of Colloid and Interface Science*, 1974. **46**(1): p. 111-117.
30. Nishikid.N, et al., Effect of Alcohols on Micelle Formation of Nonionic Surfactants in Aqueous-Solutions. *Bulletin of the Chemical Society of Japan*, 1974. **47**(11): p. 2634-2638.
31. Mysels, K.J. and R.J. Otter, Conductivity of Mixed Sodium Decyl and Dodecyl Sulfates - Composition of Mixed Micelles. *Journal of Colloid Science*, 1961. **16**(5): p. 462-&.
32. Krafft, M.P., Fluorocarbons and fluorinated amphiphiles in drug delivery and biomedical research. *Advanced Drug Delivery Reviews*, 2001. **47**(2-3): p. 209-228.

33. Moody, C.A. and J.A. Field, Perfluorinated surfactants and the environmental implications of their use in fire-fighting foams. *Environmental Science & Technology*, 2000. **34**(18): p. 3864-3870.
34. Mukerjee, P., Fluorocarbon-Hydrocarbon Interactions in Interfacial and Micellar Systems. *Journal of the American Oil Chemists Society*, 1982. **59**(4): p. A297-A297.
35. Mukerjee, P. and A.Y.S. Yang, Nonideality of Mixing of Micelles of Fluorocarbon and Hydrocarbon Surfactants and Evidence of Partial Miscibility from Differential Conductance Data. *Journal of Physical Chemistry*, 1976. **80**(12): p. 1388-1390.
36. Shinoda, K., The Critical Micelle Concentration of Soap Mixtures (2-Component Mixture). *Journal of Physical Chemistry*, 1954. **58**(7): p. 541-544.
37. Lange, H. and K.H. Beck, Micelle Formation in Mixed Solutions of Homologous and Non-Homologous Surface-Active Agents. *Kolloid-Zeitschrift and Zeitschrift Fur Polymere*, 1973. **251**(6): p. 424-431.
38. Clint, J.H. and T. Walker, Thermodynamics of Micellization of Nonionic Surface-Active Agents. *Abstracts of Papers of the American Chemical Society*, 1974: p. 104-104.
39. Holland, P.M. and D.N. Rubingh, Nonideal Multicomponent Mixed Micelle Model. *Journal of Physical Chemistry*, 1983. **87**(11): p. 1984-1990.
40. Motomura, K., M. Yamanaka, and M. Aratono, Thermodynamic Consideration of the Mixed Micelle of Surfactants. *Colloid and Polymer Science*, 1984. **262**(12): p. 948-955.
41. Gao, F., et al., Phase Separation of Mixed Micelles and Synthesis of Hierarchical Porous Materials. *Langmuir*, 2014. **30**(38): p. 11284-11291.
42. Huo, Q.S., et al., Generalized Synthesis of Periodic Surfactant Inorganic Composite-Materials. *Nature*, 1994. **368**(6469): p. 317-321.
43. Tan, B., et al., Elongated silica nanoparticles with a mesh phase mesopore structure by fluorosurfactant templating. *Langmuir*, 2004. **20**(17): p. 6981-6984.
44. Sakamoto, Y., et al., Direct imaging of the pores and cages of three-dimensional mesoporous materials. *Nature*, 2000. **408**(6811): p. 449-453.

45. Zhao, D.Y., et al., Triblock copolymer syntheses of mesoporous silica with periodic 50 to 300 angstrom pores. *Science*, 1998. **279**(5350): p. 548-552.
46. Li, W.J., et al., Synthesis of stable hollow silica microspheres with mesoporous shell in nonionic W/O emulsion. *Chemical Communications*, 2002(20): p. 2434-2435.
47. Sun, Q., et al., The Formation of Well-Defined Hollow Silica Spheres with Multilamellar Shell Structure. *Adv. Mater*, 2003. **15**: p. 1097-1100.
48. Li, W.J. and Coppins, M.O. Synthesis and characterization of stable hollow Ti-silica microspheres with a mesoporous shell. *Chemistry of Materials*, 2005. **17**(9): p. 2241-2246.
49. Dhainaut, J., et al., Hierarchical macroporous-mesoporous SBA-15 sulfonic acid catalysts for biodiesel synthesis. *Green Chemistry*, 2010. **12**(2): p. 296-303.
50. Blin, J.L. and M.J. Stebe, Preparation of mesostructured silica using a nonionic fluorinated surfactant: Relation between mesoporous characteristics and surfactant phase behavior. *Nanoporous Materials Iv*, 2005. **156**: p. 97-104.
51. Blin, J.L. and M.J. Stebe, Effect of fluorocarbon addition on the structure and pore diameter of mesoporous materials prepared with a fluorinated surfactant. *Microporous and Mesoporous Materials*, 2005. **87**(1): p. 67-76.
52. Tan, B., et al., Large- and small-nanopore silica prepared with a short-chain cationic fluorinated surfactant. *Nanotechnology*, 2005. **16**(7): p. S502-S507.
53. Esquena, J., et al., Formation of mesostructured silica in nonionic fluorinated surfactant systems. *Microporous and Mesoporous Materials*, 2006. **92**(1-3): p. 212-219.
54. Sel, O., et al., Principles of hierarchical meso- and macropore architectures by liquid crystalline and polymer colloid templating. *Langmuir*, 2006. **22**(5): p. 2311-2322.
55. Bumajdad, A., et al., Generation of metal oxide nanoparticles in optimised microemulsions. *Journal of Colloid and Interface Science*, 2007. **312**(1): p. 68-75.
56. Xing, R., et al., Demixed Micelle Morphology Control in Hydrocarbon/Huorocarbon Cationic Surfactant Templating of Mesoporous Silica. *Journal of Physical Chemistry C*, 2010. **114**(41): p. 17390-17400.

57. Groenewolt, M., M. Antonietti, and S. Polarz, Mixed micellar phases of nonmiscible surfactants: Mesoporous silica with bimodal pore size distribution via the nanocasting process. *Langmuir*, 2004. **20**(18): p. 7811-7819.
58. Yang, B., et al., Assembly of nonionic-anionic co-surfactants to template mesoporous silica vesicles with hierarchical structures. *Microporous and Mesoporous Materials*, 2010. **131**(1-3): p. 21-27.
59. Carroll, N.J., et al., Microparticles with Bimodal Nanoporosity Derived by Microemulsion Templating. *Langmuir*, 2009. **25**(23): p. 13540-13544.
60. Yang, X.-Y., et al., Hierarchically structured functional materials: Synthesis strategies for multimodal porous networks. *Pure and Applied Chemistry*, 2009. **81**(12).
61. Carmo, A.C., et al., Production of biodiesel by esterification of palmitic acid over mesoporous aluminosilicate Al-MCM-41. *Fuel*, 2009. **88**(3): p. 461-468.
62. Jermy, B.R. and A. Pandurangan, Al-MCM-41 as an efficient heterogeneous catalyst in the acetalization of cyclohexanone with methanol, ethylene glycol and pentaerythritol. *Journal of Molecular Catalysis a-Chemical*, 2006. **256**(1-2): p. 184-192.
63. Duran, P., et al., Cerium (IV) oxide synthesis and sinterable powders prepared by the polymeric organic complex solution method. *Journal of the European Ceramic Society*, 2002. **22**(9-10): p. 1711-1721.
64. Brezesinski, T., et al., The generation of mesoporous CeO<sub>2</sub> with crystalline pore walls using novel block copolymer templates. *Nanoporous Materials* Iv, 2005. **156**: p. 243-248.
65. Brezesinski, T., et al., Self-assembly and crystallization Behavior of mesoporous, crystalline HfO<sub>2</sub> thin films: A model system for the generation of mesostructured transition-metal oxides. *Small*, 2005. **1**(8-9): p. 889-898.
66. Rangari, V.K., D.N. Srivastava, and A. Gedanken, Preparation of ceria nanoparticles embedded in PMMA using sonochemical technique. *Materials Letters*, 2006. **60**(29-30): p. 3766-3768.
67. Pappas, G.S., et al., Synthesis and characterization of new SiO<sub>2</sub>-CaO hollow nanospheres by sol-gel method: Bioactivity of the new system. *Journal of Non-Crystalline Solids*, 2008. **354**(2-9): p. 755-760.

68. Terribile, D., et al., The synthesis and characterization of mesoporous high-surface area ceria prepared using a hybrid organic/inorganic route. *Journal of Catalysis*, 1998. **178**(1): p. 299-308.
69. Wu, Z.H., et al., Structure and chemical transformation in cerium oxide nanoparticles coated by surfactant cetyltrimethylammonium bromide (CTAB): An x-ray absorption spectroscopic study. *Journal of Physical Chemistry B*, 2002. **106**(18): p. 4569-4577.
70. Laosiripojana, N., W. Sutthisripok, and S. Assabumrungrat, Reactivity of high surface area CeO<sub>2</sub> synthesized by surfactant-assisted method to ethanol decomposition with and without steam. *Chemical Engineering Journal*, 2007. **127**(1-3): p. 31-38.
71. Wang, X.G., et al., Direct synthesis and catalytic applications of ordered large pore aminopropyl-functionalized SBA-15 mesoporous materials. *Journal of Physical Chemistry B*, 2005. **109**(5): p. 1763-1769.
72. Zhang, X., F. Zhang, and K.Y. Chan, The synthesis of large mesopores alumina by microemulsion templating, their characterization and properties as catalyst support. *Materials Letters*, 2004. **58**(22-23): p. 2872-2877.
73. Rigby, S.P., et al., Nanocasting of novel, designer-structured catalyst supports. *Chemical Engineering Science*, 2004. **59**(22-23): p. 5113-5120.
74. Morales, G., et al., Aqueous-sensitive reaction sites in sulfonic acid-functionalized mesoporous silicas. *Journal of Catalysis*, 2008. **254**(2): p. 205-217.
75. Satoh, Y., et al., Synthesis of Sulfonic Acid Functionalized Silica Honeycombs. *Industrial & Engineering Chemistry Research*, 2013. **52**(44): p. 15293-15297.
76. Cano-Serrano, E., et al., Sulfonic acid-functionalized silica through quantitative oxidation of thiol groups. *Chemical Communications*, 2003(2): p. 246-247.
77. Bahri, M.A., et al., Investigation of SDS, DTAB and CTAB micelle microviscosities by electron spin resonance. *Colloids and Surfaces a-Physicochemical and Engineering Aspects*, 2006. **290**(1-3): p. 206-212.
78. Christov, N.C., et al., Synergistic sphere-to-rod micelle transition in mixed solutions of sodium dodecyl sulfate and cocoamidopropyl betaine. *Langmuir*, 2004. **20**(3): p. 565-571.



79. Alargova, R., et al., Light-Scattering Study of Sodium Dodecyl Polyoxyethylene-2-Sulfate Micelles in the Presence of Multivalent Counterions. *Langmuir*, 1995. **11**(5): p. 1530-1536.
80. Shiloach, A. and D. Blankschtein, Measurement and prediction of ionic/nonionic mixed micelle formation and growth. *Langmuir*, 1998. **14**(25): p. 7166-7182.
81. Reiss-Husson, F.L., V, The structure of the micellar solution of some amphiphilic compounds in pure water as determined by absolute small-angle X-ray scattering techniques. *J. Phys. Chem*, 1964. **68**: p. 3504-11.
82. Lang, P. and O. Glatter, Small-angle X-ray scattering from aqueous solutions of tetra(oxyethylene)-n-octyl ether. *Langmuir*, 1996. **12**(5): p. 1193-1198.
83. Griffiths, P.C., et al., Role of counterion concentration in determining micelle aggregation: Evaluation of the combination of constraints from small-angle neutron scattering, electron paramagnetic resonance, and time-resolved fluorescence quenching. *Journal of Physical Chemistry B*, 2004. **108**(12): p. 3810-3816.
84. Petkov, J.T., et al., The Impact of Multivalent Counterions,  $Al^{3+}$ , on the Surface Adsorption and Self-Assembly of the Anionic Surfactant Alkylpolyoxyethylene Sulfate and Anionic/Nonionic Surfactant Mixtures. *Langmuir*, 2010. **26**(22): p. 16699-16709.
85. Bales, B.L., et al., Precision relative aggregation number determinations of SDS micelles using a spin probe. A model of micelle surface hydration. *Journal of Physical Chemistry B*, 1998. **102**(50): p. 10347-10358.
86. Tornblom, M., U. Henriksson, and M. Ginley, A Field-Dependent H-2 Nuclear Magnetic-Relaxation Study of the Aggregation Behavior in Micellar Solutions of Ctab and Sds. *Journal of Physical Chemistry*, 1994. **98**(28): p. 7041-7051.
87. Colafemmina, G., et al., Lauric Acid-Induced Formation of a Lyotropic Nematic Phase of Disk-Shaped Micelles. *Journal of Physical Chemistry B*, 2010. **114**(21): p. 7250-7260.
88. Aniansson, E.A.G., et al., Theory of Kinetics of Micellar Equilibria and Quantitative Interpretation of Chemical Relaxation Studies of Micellar Solutions of Ionic Surfactants. *Journal of Physical Chemistry*, 1976. **80**(9): p. 905-922.

89. Zana, R., Dynamics of surfactant self-assemblies: micelles, microemulsions, vesicles and lyotropic phases. Vol. 125. 2005: CRC press.
90. Aguiar, J., et al., On the determination of the critical micelle concentration by the pyrene 1 : 3 ratio method. *Journal of Colloid and Interface Science*, 2003. **258**(1): p. 116-122.
91. Naorem, H.e.a., Conductometric and surface tension studies on the micellization of some cationic surfactants in water-organic solvent media. *J. Surface Sci. Technol.*, 2006. **22**(3-4): p. 89-100.
92. Turro, N.J., et al., Surface and Bulk Interactions of Ionic and Nonionic Surfactants. *Journal of Physical Chemistry*, 1986. **90**(2): p. 288-291.
93. Lei, X.G., et al., Microenvironmental Control of Photochemical-Reactions .3. Additive Effects on Micellar Structure and Properties of Tx-100. *Langmuir*, 1991. **7**(12): p. 2872-2876.
94. Zana, R., et al., Mixed micellization of cetyltrimethylammonium bromide and an anionic dimeric (gemini) surfactant in aqueous solution. *Langmuir*, 1997. **13**(3): p. 402-408.
95. Anton, R.E., et al., Surfactant-Oil-Water Systems near the Affinity Inversion .9. Optimum Formulation and Phase-Behavior of Mixed Anionic-Cationic Systems. *Journal of Dispersion Science and Technology*, 1993. **14**(4): p. 401-416.
96. Mukerjee, P., Fluorocarbon-Hydrocarbon Interactions in Interfacial and Micellar Systems. *Journal of the American Oil Chemists Society*, 1982. **59**(12): p. 573-578.
97. Matsuoka, K. and Y. Moroi, Micellization of fluorinated amphiphiles. *Current Opinion in Colloid & Interface Science*, 2003. **8**(3): p. 227-235.
98. Kalyanasundaram, K., Pyrene Fluorescence as a Probe of Fluorocarbon Micelles and Their Mixed Micelles with Hydrocarbon Surfactants. *Langmuir*, 1988. **4**(4): p. 942-945.
99. Szymczyk, K., Behaviour of the fluorocarbon surfactants in the monolayer at the water-air interface and in the bulk phase. *Journal of Fluorine Chemistry*, 2013. **150**: p. 109-116.

100. Skvarla, J., et al., Micellization of Zonyl FSN-100 fluorosurfactant in aqueous solutions. *Colloids and Surfaces a-Physicochemical and Engineering Aspects*, 2014. **443**: p. 209-215.
101. Barthelemy, P., et al., Fluorocarbon - Hydrocarbon nonionic surfactants mixtures: A study of their miscibility. *Langmuir*, 2002. **18**(7).
102. Dubey, N., Studies of mixing behavior of cationic surfactants. *Fluid Phase Equilibria*, 2014. **368**: p. 51-57.
103. Mukerjee, P., Fluorocarbon Hydrocarbon Interactions in Micelles and Other Lipid Assemblies, at Interfaces, and in Solutions. *Colloids and Surfaces A-Physicochemical and Engineering Aspects*, 1994. **84**(1): p. 1-10.
104. Elbert, R., T. Folda, and H. Ringsdorf, Saturated and Polymerizable Amphiphiles with Fluorocarbon Chains - Investigation in Monolayers and Liposomes. *Journal of the American Chemical Society*, 1984. **106**(25): p. 7687-7692.
105. Asakawa, T., et al., Probe Methods for the 2nd Cmc of Fluorocarbon and Hydrocarbon Surfactant Mixtures. *Langmuir*, 1989. **5**(2): p. 343-348.
106. Long, P.F. and J.C. Hao, Phase behavior and self-assembly aggregation of hydrocarbon and fluorocarbon surfactant mixtures in aqueous solution. *Advances in Colloid and Interface Science*, 2012. **171**: p. 66-76.
107. Mukerjee, P. and T. Handa, Adsorption of Fluorocarbon and Hydrocarbon Surfactants to Air-Water, Hexane-Water, and Perfluorohexane-Water Interfaces - Relative Affinities and Fluorocarbon-Hydrocarbon Nonideality Effects. *Journal of Physical Chemistry*, 1981. **85**(15): p. 2298-2303.
108. Palazzo, G., et al., Role of the cosurfactant in the CTAB/water/n-pentanol/n-hexane water-in-oil microemulsion. 1. Pentanol effect on the microstructure. *Journal of Physical Chemistry B*, 2003. **107**(8): p. 1924-1931.
109. Mills, A.J. et al., NMR and Molecular Dynamics Study of the Size, Shape, and Composition of Reverse Micelles in a Cetyltrimethylammonium Bromide (CTAB)/n-Hexane/Pentanol/Water Microemulsion. *Journal of Physical Chemistry B*, 2014. **118**(36): p. 10767-10775.
110. Griffiths, P.C., et al., Small-angle neutron scattering, electron paramagnetic resonance, electrophoretic NMR, and time-resolved fluorescence quenching

- studies of sodium dodecyl sulfate and tetra(ethylene oxide) dodecyl ether mixed surfactant micelles. *Journal of Physical Chemistry B*, 2004. **108**(4): p. 1351-1356.
111. Giustini, M., et al., Microstructure and dynamics of the water-in-oil CTAB/n-pentanol/n-hexane/water microemulsion: A spectroscopic and conductivity study. *Journal of Physical Chemistry*, 1996. **100**(8): p. 3190-3198.
112. Das, N.C., et al., Shape and Size of Highly Concentrated Micelles in CTAB/NaSal Solutions by Small Angle Neutron Scattering (SANS). *Langmuir*, 2012. **28**(33): p. 11962-11968.
113. Goyal, P.S. and V.K. Aswal, Micellar structure and inter-micelle interactions in micellar solutions: Results of small angle neutron scattering studies. *Current Science*, 2001. **80**(8): p. 972-979.
114. Griffiths, P.C., et al., Electron paramagnetic resonance and small-angle neutron scattering studies of mixed sodium dodecyl sulfate and (tetradecylmalono)bis(N-methylglucamide) surfactant micelles. *Langmuir*, 2002. **18**(4): p. 1065-1072.
115. Bales, B.L. and C. Stenland, Statistical Distributions and Collision Rates of Additive Molecules in Compartmentalized Liquids Studied by Epr Spectroscopy .1. Sodium Dodecyl-Sulfate Micelles, 5-Doxylstearic Acid Ester, and Cobalt(II). *Journal of Physical Chemistry*, 1993. **97**(13): p. 3418-3433.
116. Goyal, P.S., et al., Role of Van-Der-Waals Forces on Small-Angle Neutron-Scattering from Ionic Micellar Solutions. *Chemical Physics Letters*, 1993. **211**(6): p. 559-563.
117. Eastoe, J., et al., Micelles of asymmetric chain catanionic surfactants. *Colloids and Surfaces a-Physicochemical and Engineering Aspects*, 1996. **117**(3): p. 215-225.
118. Brito, R.M.M. and W.L.C. Vaz, Determination of the Critical Micelle Concentration of Surfactants Using the Fluorescent-Probe N-Phenyl-1-Naphthylamine. *Analytical Biochemistry*, 1986. **152**(2): p. 250-255.
119. Huibers, P.D.T., et al., Prediction of critical micelle concentration using a quantitative structure-property relationship approach .1. Nonionic surfactants. *Langmuir*, 1996. **12**(6): p. 1462-1470.

120. Mazer, N.A., G.B. Benedek, and M.C. Carey, Investigation of Micellar Phase of Sodium Dodecyl-Sulfate in Aqueous Sodium-Chloride Solutions Using Quasi-Elastic Light-Scattering Spectroscopy. *Journal of Physical Chemistry*, 1976. **80**(10): p. 1075-1085.
121. Haldar, J., et al., Molecular modulation of surfactant aggregation in water: Effect of the incorporation of multiple headgroups on micellar properties. *Angewandte Chemie-International Edition*, 2001. **40**(7): p. 1228-+.
122. Bales, B.L., R. Ranganathan, and P.C. Griffiths, Characterization of mixed micelles of SDS and a sugar-based nonionic surfactant as a variable reaction medium. *Journal of Physical Chemistry B*, 2001. **105**(31): p. 7465-7473.
123. Griffiths, P.C., et al., FT-PGSE NMR study of mixed micellization of an anionic and a sugar-based nonionic surfactant. *Journal of Physical Chemistry B*, 1997. **101**(6): p. 915-918.

## **Chapter Two**

### **Materials & Experimental Techniques**

## 2.1. Introduction

This chapter will include the theory of the experimental techniques used in the project, a description of the materials used in this work and sample preparations as well as the synthetic element of the nanoporous material synthesis.

## 2.2. Experimental techniques and theory

The section includes techniques used for characterization in the project including those used in phase behaviour study, porous material synthesis and applications.

### 2.2.1. Surface tension

Molecules at the liquid solution surface have a different behaviour from those in the bulk. Equal forces of attraction in all directions affect molecules located in the bulk, whereas molecules at the surface of the liquid solution have only one-direction forces due to the unbalanced attractive forces [1].

Basically, surface tension values strongly relate to the nature of the substances, which are used to form the surface. Water as a polar liquid has high surface tension ( $\sim 72.0 \text{ mNm}^{-1}$ ) due to the strong intermolecular interactions. Thus, decreasing the strength of the molecular interactions leads lowering of surface tensions.

#### 2.2.1.1. Surface tension & surfactant critical micelle concentration (CMC)

Surface tension measurements have been used to determine the critical micelle concentration (CMC) of surfactants as well as their surface area per molecule.

Due to the ability of surfactants to decrease the surface tension even at low surfactant concentrations, surface tension is used in surfactant solution studies. Typically, increasing the surfactant concentration shows a rapid decrease in the surface tension, until a concentration at which the surface tension curve levels off. This concentration is the critical micelle concentration of the surfactant, and micelles start to be formed above this point. After this concentration, the surface tension curve becomes largely independent of the concentration due to the thermodynamic basis in the preferential formation of micelles [2, 3].

### 2.2.1.2. Drop volume method

In this project, the drop volume method has been used to investigate all studied samples.

Drop volume method is based on measuring the volume of a drop, which is formed from a metal capillary. By increasing the volume of the drop, its weight is increased until it reaches a critical value when it cannot be balanced by the surface tension. The volume of a drop at the end of the glass syringe is related to the surface tension using equation (2.1) [4].

$$\sigma = \frac{F V g \Delta \rho}{2 \pi r_{cap}} \quad (2.1)$$

where  $\sigma$  = surface tension,  $V$  = drop volume,  $g$  = acceleration gravity constant,  $\Delta \rho$  = difference of the densities of both aqueous solution and air,  $F$  = correction factor which corrects the directly measured volume, and  $r_{cap}$  = the radius of the capillary tip.

### 2.2.1.3. Surface tension instrument

Surface tension measurements were carried out at room temperature using a LAUDA Drop Volume Tensiometer (TVT1).

## 2.2.2. Fluorescence measurements

Fluorescence phenomenon is strongly related to the absorption by molecules to the energy in the form of photons of visible or ultraviolet light.

The energies of photons from visible and ultraviolet light are enough to move an electron in a molecule from the ground state to an excited state. Thus, a molecule can absorb photons when the energy provided by the photon  $E_{photon}$  equals the energy needed to transfer an electron from the ground state orbital to a higher energy orbital ( $\Delta E_{transition}$ ). Since the molecule in both ground and excited states has different vibrational and rotational energy levels, the photon absorption can promote the molecule to any of the vibrational or rotational substates of the excited level [5].

The energy change in each possible transition is different which indicates that each one corresponds to a different wavelength  $\lambda$ , and thus peak in the spectra based on equation 2.2.

$$\lambda = hc / \Delta E_{transition} \quad (2.2)$$

where,  $h$  is the Planck's constant and  $c$  is the speed of light.



The molecule then loses any excess of vibrational energy when the absorbed energy reaches one of the higher vibrational levels of the excited state. The loss of energy is because of collision and the electron falls to the lowest vibrational level of the excited state. This process is continual until the lowest vibrational level of the first excited state is reached. At this level, the molecule can emit energy in a form of fluorescence, when return to one of the ground state vibrational levels [5].

### 2.2.2.1. Fluorescent probes

Some fluorescent probes such as pyrene and naphthalene mainly consist of conjugated molecules. The conjugated carbon-carbon double bond in the molecule absorbs the radiation and an electron excited from a  $\pi$  orbital to a  $\pi^*$  antibonding orbital. This transition requires less energy, as the molecular orbitals are closer than that in un-conjugated molecules. In this case the carbon-carbon double bond performs as a chromophore, which is a term to describe chemical groups that have specific optical absorptions and colour [6].

Figure 2.1 shows the chemical structure of pyrene ( $C_{16}H_{10}$ ) as one of the polycyclic aromatic hydrocarbon compounds, which has five predominant vibronic peaks from 1 to 5 based on the shorter to longer wavelength. The micropolarity around pyrene molecules can be indicated by the intensity ratio of  $I_1/I_3$ , which is considered to estimate the polarity level of its environment [6].

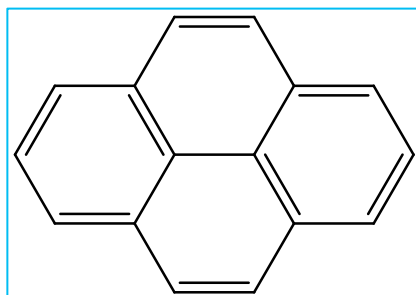


**Figure 2.1 Chemical structure of the fluorescent probe, pyrene.**

At room temperature the fine structure of pyrene monomer fluorescence is strongly dependent on the solvent polarity. The greatest difference in the fluorescence spectrum is at the 373 and 384 nm peaks. However, in nonpolar environments, the most intense peak is the 384 nm whereas at higher polarity, the peak of 373 nm is the most intense. The ratio of  $I_{373}/I_{384}$  values can be used to obtain a sensitive parameter of solution polarity [6]. To estimate the surfactant CMC, pyrene  $I_1/I_3$  ratio is plotted as a function of the total surfactant concentration and that show a typical decrease up to the CMC of the surfactant.  $I_1/I_3$  ratio values correspond to a polar environment below the

CMC of the surfactant, so when the surfactant concentration increases, the ratio decreases rapidly to indicate a more hydrophobic environment. However, the ratio reaches a constant value above the CMC as the pyrene incorporates into the hydrophobic region of the micelles [7, 8].

#### 2.2.2.2. Fluorescence instrument

Photophysical data were obtained on a JobinYvon–Horiba Fluorolog spectrometer fitted with a JY TBX photodetection module. All spectra were recorded using an excitation wavelength of 340 nm. All samples have been measured at room temperature. CMCs were determined by the breakpoints in the concentration dependent ratio of the third to first vibronic peak, known as the  $I_3/I_1$  ratio.

#### 2.2.3. Small-Angle Neutron Scattering (SANS)

Studying colloidal systems requires the determination of the molecular organization in order to relate the physical properties and molecular structure. Quantitative information on size, shape and structure of colloidal particles can be obtained using scattering techniques. These techniques mainly depend on interactions between incident radiations (neutrons or X-ray) and the particles. Since micelles or other colloidal dispersions have a range of size between 10 to  $10^4$  Å, the incident wavelength must fall within this range to get valuable information [9]. Using the Bragg equation (equation 2.3) [10].

$$n \lambda = 2 d \sin \theta \quad (2.3)$$

where,  $\theta$  is the angle of diffraction of radiation,  $\lambda$  is the wavelength and  $d$  is the separation of lattice planes which is the distance between atomic layers, and  $n$  is an integer (1, 2, 3 etc.).

Therefore, small particles such as microemulsion droplets, which are in nanometer of size, scatter at small angles, and small angle neutron scattering (SANS) is the appropriate way to study these systems [9, 11].

##### 2.2.3.1. Neutrons

Neutrons are uncharged subatomic particles that can be scattered by strong nuclear forces and can penetrate the material bulk and interact with the nuclei of investigated material [9]. Their scattering differs from electrons and traditional electromagnetic methods as scattering is by the interaction with the electron clouds. The neutron mass is  $1.675 \times 10^{-27}$  Kg, (1.839 times that of the electron) and they are stable when linked

to atomic nucleus, whereas they have a lifetime of 1000 s as a free particle. The neutron wavelength  $\lambda$  depends on its velocity based on the Broglie equation (2.4), so the time-of-flight technique is used to select a specific neutron wavelength.

$$\lambda = h/mv \quad (2.4)$$

where,  $h$  is the Planck's constant,  $v$  the particle velocity and  $m$  is the neutron mass.

Neutron scattering of an atom does not relate to the atomic number as the interaction is with the nuclei which differ from the X-rays and electrons since the scattering power is strongly relates to the atomic number. Neutrons also have lower possibility to degrade investigated samples as they have lower energy than X-ray for the same wavelength [9].

The sources of neutrons for research are produced in two ways, the nuclear fission of radioactive material in reactor-based sources or by spallation in accelerator based neutron sources. In the reactor-based sources, neutrons are produced as a product of the nuclear fission of heavy nuclides (uranium-235 nuclei) in reactors. The U-235 is split into fragments and generates a very high energy (MeV). The thermalized high-energy neutrons cause emitting beams with a broad band of wavelengths. A thermal equilibrium of neutrons with a hot source will help to shift the energy of neutrons to higher energies (shorter wavelengths). To select the targeted wavelength, Bragg scattering approach using a crystal monochromator or velocity selection through a mechanical chopper could be used. By this way, high-flux neutron beams with high quality and narrow wavelengths distributions are produced for experimental purposes.

In the other method, the spallation at accelerator based pulsed neutron sources; neutrons are released by using high-energy particles ( $H^+$ ) from higher power accelerator to collide a heavy metal target (U, Ta). In this method, useful neutrons with less heat are released compared to those produced from fission. Between 1-30 neutrons per proton are produced by these collisions. Neutrons here also need to be slowed by passage through moderating materials in order to have the right wavelength (energy) to be used in experimental purposes.

In both ways, neutrons interact with the investigated particle in an elastic or inelastic fashion. The energy of neutrons is not changed in the elastic interaction whereas the inelastic one includes loss of energy from the molecular motion of the scattering atom. That might also be a coherent (scattering from ordered nuclei produces patterns of constructive and destructive interference) or incoherent (scattering from random events involving dynamic information). However, only coherent elastic scattering is considered

in a SANS experiment, and incoherent scattering that occur in background can be measured from the total scattering [12].

### 2.2.3.2. SANS instrument theory

Generally, SANS instruments count the number of scattered neutrons as a function of wave vector and that depends on the scattering angle  $\theta$  and the wavelength  $\lambda$  based on equation (2.5).

$$Q = 4\pi/\lambda \sin (\theta /2) \quad (2.5)$$

$Q$  value therefore relates to the size of the object, meaning that smaller objects scatter at high  $Q$  values, whereas larger objects scatter at low  $Q$  values.

### 2.2.3.3. SANS instrument

The SANS measurements were performed as detailed previously [13] on the fixed-geometry, time-of-flight LOQ diffractometer (ISIS Spallation Neutron Source, Oxfordshire, UK). All measurements were carried out at 25 °C. Experimental measuring times were between 40 and 80 minutes. All scattering data were normalised for the sample transmission and incident wavelength distribution, corrected for instrumental and sample backgrounds using an empty quartz cell, and for the linearity and efficiency of the detector response. The data were put onto an absolute scale using a well-characterised partially-deuterated polystyrene-blend standard sample.

The data-fitting model used for both surfactant solutions and the mixtures are described along with the results in Chapter Three.

### 2.2.4. $^1\text{H}$ -NMR, $^{19}\text{F}$ -NMR and pulsed-gradient spin-echo NMR spectroscopy (PGSE-NMR)

Nuclear magnetic resonance is the used technique to elucidate the chemical structures and observing the interaction between molecules. The common elements to possess a magnetic moment in NMR spectroscopy are  $^1\text{H}$  and  $^{13}\text{C}$  nuclei, which are in most of surfactant molecules, and  $^{19}\text{F}$  to study the fluorocarbon surfactants.

$^1\text{H}$ -NMR,  $^{19}\text{F}$ -NMR and PGSE-NMR are the complementary techniques that have been used to study the surfactant aqueous solutions as well as the surfactant/oil solutions.

#### 2.2.4.1. Theoretical aspects

Pulsed-gradient spin-echo NMR is a suitable technique to measure diffusion coefficients. The technique is a valuable tool to study mixture separation analysis

based on the molecular size approach. The technique is similar to all nuclear magnetic resonance techniques in terms of the advantages when studying multicomponent systems as non-destructive tools, but the most important feature of PGSE-NMR is the ability to identify and analyse each component in the mixture in a single experiment.

Self-diffusion coefficient ( $D_s$ ) is a term to express both the rotational and transitional motion of molecules in solutions [14]. The value of  $D_s$  is obtained by the Stokes-Einstein equation (2.6) [14].

$$D_s = K T / 6 \pi \eta R_H \quad (2.6)$$

where,  $K$  is the Boltzmann constant,  $T$  is the temperature,  $\eta$  is the solvent viscosity and  $R_H$  is the hydrodynamic radius.

The equation is strictly valid for a spherical particle with a  $R_H$  radius but also may use to determine the size of molecules. In a defined amount of time  $t$  (s), the distance  $z$ , which a molecule travels in a single direction, is obtained by equation 2.7.

$$z = (2 D t)^{1/2} \quad (2.7)$$

#### 2.2.4.2. NMR spectra

In the  $^1\text{H}$ -NMR spectrum, basically starting to pulse a magnetic field at  $90^\circ$  and then detecting what was pulsed to produce the peaks in the frequency domain. However, in the diffusion spectrum, what the spin-Echo does is refocusing the magnetization with a  $90^\circ$  pulse then dispersed using a magnetic field gradient (figure 2.2). After some time another pulse is focused again at  $180^\circ$ . The magnetization builds up into an echo after the same time of the  $90^\circ$  pulses. So the total is basically  $2\tau$ .

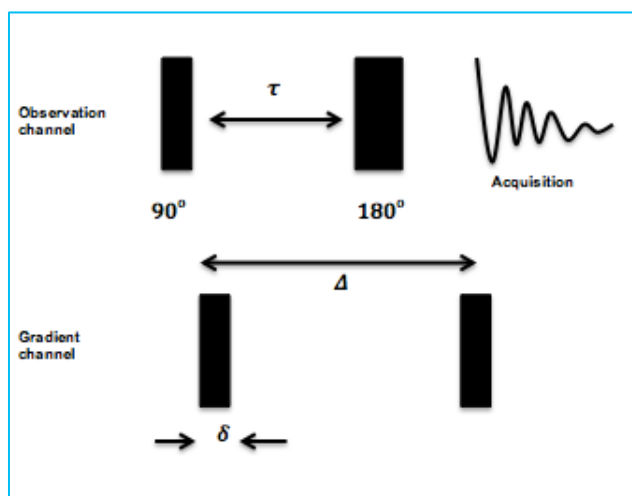


Figure 2.2 Pulse sequence for gradient PGSE-NMR.

Interestingly, if the time is varied to make  $\tau$  longer and longer, the peaks get smaller intensities and the reason they do is because longer time allows relaxing the sample so if the intensity is plotted versus the time the signal decreases exponentially and then the relaxation time can be measured. In the gradient channel, a gradient is pulsed and adjusted the time of each gradient to put small delta  $\delta$  for each gradient and the time between this is the big delta  $\Delta$ . The first gradient dephases the magnetization and the other one rephases it. Further, if the molecules have diffused in that time big delta then it is not able to rephase the magnetization and again the peak intensity decreases upon this echo when the gradient plotted versus the intensity. The decay depends on the parameters of  $\Delta$ ,  $\delta$ ,  $\lambda$ . These NMR parameters should be set in the experiment, as constants and then the  $D_s$  can be determined.

### 2.2.4.3. NMR instruments

Pulsed-Gradient Spin-Echo (PGSE-) NMR measurements were performed on a Bruker AMX400 NMR spectrometer operating at 400 MHz ( $^1\text{H}$ ) using a stimulated echo sequence. All the experiments were run at 25 °C using the standard heating/cooling system of the spectrometer to an accuracy of  $\pm 0.3$  °C.

The self-diffusion coefficient,  $D_s$ , was deduced by fitting the attenuation of the integral for a chosen peak to equation 2.8.

$$A(\delta, G, \Delta) = A_0 \exp(-k D_s) \quad (2.8)$$

where  $A$  is the signal intensity in the presence and absence (0) of the field gradients, and  $k = -\gamma^2 G^2 \delta^2 (\Delta - \frac{\delta}{3})$ .

where  $\gamma$  is the magnetogyric ratio of the nucleus under observation, in this case protons,  $\Delta$  the diffusion time,  $\delta$  the gradient pulse length, and  $\sigma$  the ramp time, and  $G$  is the gradient field strength [15].

The analysis of the self-diffusion coefficients  $D_s$  solves the association and complexation processes. The methylene resonance associated to  $-(\text{CH}_2)_x-$  of the inner part of the hydrocarbon chains related to the broad peak between  $\delta = 1.11 - 1.20$  ppm in case of micellization studies, is related to the attenuation function observed in the  $^1\text{H}$  NMR spectra. That reflects the time-average population-weighted average mobility of the monomeric and micellized surfactant.

In case of complexation, the attenuation function was recorded from the peak corresponding to the methylene in the spacer used in the experiment (singlet at  $\delta =$

5.36 ppm) and again, reflected the time-average population-weighted average mobility of monomeric and micellised surfactant.

### 2.2.5. Electron paramagnetic resonance spectroscopy (EPR)

Electron paramagnetic resonance is the most sensitive tool for characterization of solutions containing stable free radicals. The paramagnetic substance is defined as the material that acquires a resultant magnetic moment in the direction of an applied external magnetic field. The resultant moment of the substance is partially due to the induced dipole possessed from the change in the motion of the electrons of the atom or ion [16-18].

#### 2.2.5.1. Theoretical aspects

The spectral line fitting of the EPR spectra reveals information about the polarity and the rotational correlation time, since the radical spectrum is sensitive to the rate of molecular motion. In the micellar environments, studying these two parameters provides a description of the size of micelles and the polarity around micelles.

- **Rotational correlation time**

Rotational correlation time  $\tau_i$  is a parameter to describe the average time for a molecule to move in any direction.

For fast molecular motion ( $10^{-11} < \tau_i < 10^{-9}$ ) s the rotational correlation time can be estimated by equation 2.9.

$$\tau_i = 6.5 \times 10^{-10} \Delta H_0 \left( \sqrt{\frac{H_0}{H_{-1}}} - 1 \right) \quad (2.9)$$

where,  $\Delta H_0$  is linewidth of the central peak and  $H_0$  and  $H_{-1}$  are the intensities of the central and high field peaks respectively.

- **Hyperfine coupling constant**

As a polarity determination index, the hyperfine-coupling constant is sensitive to the amount of water in the surrounding of the nitroxide, and it results from magnetic interaction between the electron and nuclear spins of atomic neighbours. Three possible spin states ( $m = -1, 0, +1$ ) for the  $^{14}\text{N}$  as aminoxyl radicals (figure 2.3), which cause three lines in its EPR spectrum (figure 2.4). In the figure, form 1 is stabilized in the presence of polar solvents which can provide H bonding and that increase the hyperfine-coupling constant.

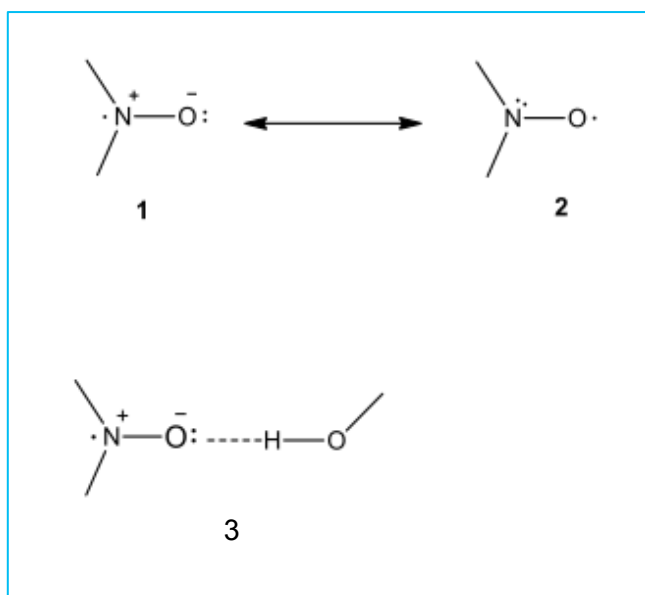


**Figure 2.3 The three spin states of  $^{14}\text{N}$ .**

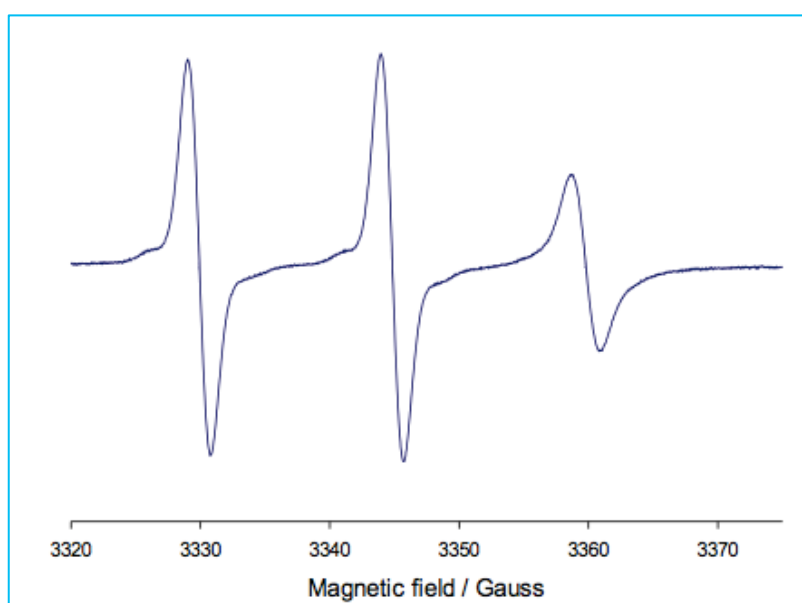


**Figure 2.4 A typical EPR spectra.**

The hyperfine-coupling constant is directly related to the distance between peaks in the EPR spectrum and indicates the extent of delocalization of the unpaired electron over the molecule. It is obtained by measuring the half of the separation of the two outermost lines in the spectrum. This parameter varies with the local polarity around the aminoxyl group, which may help to investigate micellar environments from studying the polarity of the location of the used spin probe.



### 2.2.5.2. EPR instrument

Five EPR spectra were recorded on a Bruker ESP-300 spectrometer. The experimental details measurements are identical to those described previously [19]. The non-degassed samples were sealed with a gas-oxygen torch into melting point capillaries, which were housed within quartz EPR tube for the measurements. A Bruker Variable Temperature Unit (BVT 2000) has been used to control the temperature to  $\pm 0.2$  K.

### 2.2.5.3. EPR lineshape fitting and analysis

The EPR spectra have been analysed in terms of the rotational correlation time ( $\tau_i$ ), which was estimated using the formula in equation (2.9).

The rotational correlation time and hyperfine-coupling constant were calculated by fitting the values using (WinEPR, Bruker) software.

The line shapes have been fitted to a Voigt approximation in order to separate the Gaussian and Lorentzian components of the spectral lines and to locate the resonance fields of the three EPR lines, which have been built by the nitroxide radical to a precision of few mG. Rotational correlation times are computed from the overall linewidth of the centre line and the peak-to-peak heights of the three lines and corrected for inhomogeneous broadening using the procedure outlined by Bales [13, 19].

From EPR outcomes, the separation  $A+$  of the low and centre lines ( $M_I=+1$  and  $M_I=0$ ) is directly related to the polarity index  $H$  (25°C), defined as the molar ratio of OH groups in a given volume relative to water (equation 2.10).  $H$  (25°C) therefore corresponds to the volume fraction of water in the polar shell,  $\phi_{water}$ , and may be used to constrain the SANS fitting.

$$H (25^\circ\text{C}) = (A+ - 14.21) / 1.52 \quad (2.10)$$

### 2.2.6. Scanning Electron Microscopy (SEM)

The surface of solid materials can be studied by using SEM techniques. A high-energy electron beam is focused on the sample to generate a variety of signals at the surface of the sample. External morphology, chemical composition and crystalline structure can be estimated using SEM technique [20].

#### 2.2.6.1. Theoretical aspects

Scanning electron microscopy uses electrons instead of light to form an image for the material surfaces. SEM can determine the morphology of the sample and the crystal size. An electron beam is produced by an electron gun in the instrument, and then passed through the microscope in a vertical path connected within the vacuum. Through an electromagnetic field, the beam travels and passes the lenses to be focused down toward a sufficiently thin specimen. Once the beam hits the sample, electrons and X-ray are ejected and then converted to a signal after collected using a detector [20, 21].

#### 2.2.6.2. SEM instrument

SEM was performed using Hitachi S-4300LV microscope equipped with a Schottky field emission gun.

### 2.2.7. Transmission Electron Microscopy (TEM)

Detailed morphological and compositional information of the investigated sample can be provided by TEM.

#### 2.2.7.1. Theoretical aspects

TEM is a microscopy technique that uses a beam of electrons transmitted through the sample. The image is formed as a result of the interaction between the electrons and the sample and then magnified and focused onto an imaging device [22].

#### 2.2.7.2. TEM instrument

TEM was performed using high-resolution transmission electron microscope (HRTEM) system JEOL 2100 (LaB6). The instrument is equipped with high-resolution Gatan digital camera (  $2\text{ k}\times 2\text{ k}$  ) providing resolution of 0.2 Å. To provide excellent compositional contrast, a dark field (HAADF/Z-contrast) detector was used.

### 2.2.8. X-Ray Diffraction (XRD)

X-ray powder diffraction is used for phase identification of a crystalline material and characterizes the unit cell dimensions. In nonporous materials, this technique is commonly used to determine some of their properties such as  $d$ -spacing, pore spacing ( $a$ ) and lattice parameters. By this technique, a solid sample can be classified in terms of its structure to be crystalline phase or amorphous.

#### 2.2.8.1. Theoretical aspects

In XRD, the incident beam is reflected by a set of material planes, to produce the diffraction XRD pattern, which is plotted based on the intensity of reflected beams (figure 2.5). The reflected X-ray from the surface of the sample travels less distance than the X-ray reflected from a plane of atoms in the crystal. X-ray penetrated the surface sample, travels down to the internal layer and then reflects to travel back over the same distance before getting back at the surface. The total distance depends on the separation between layers and the angle ( $\theta$ ) of the incident beam. Bragg has developed this study and expressed the equation 2.11, to explain why the crystal faces appear to reflect X-ray beams at certain angles ( $\theta$ ) of the incident beams [10].

$$n \lambda = 2 d \sin \theta \quad (2.11)$$

where  $d$  is the distance between atomic layers in a crystal (interplanar  $d$ -spacing) and  $\lambda$  is the wavelength of the beam, and  $n$  is an integer (1, 2, 3 etc.).

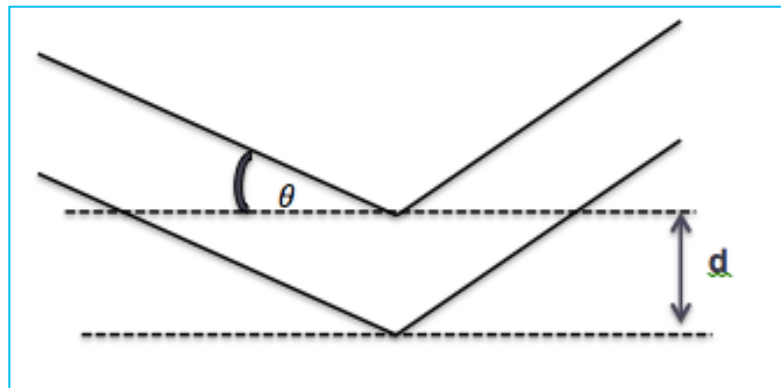


**Figure 2.5 Schematic representations of diffracted beams based on Bragg's law.**

The reflected waves from the layers need to travel a whole number of wavelengths inside the materials to be in phase with the wave reflected from the surface, and then a very strong signal can be detected from the reflection, when the reflected waves from different layers are in phase with each other (figure 2.6).

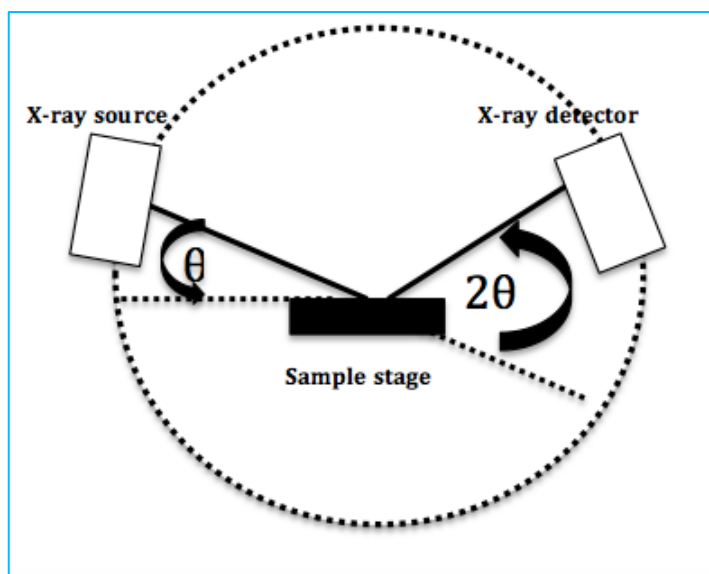


**Figure 2.6** Schematic representations of X-ray tube, the X-ray detector and the sample.

#### **2.2.8.2. XRD instrument**

Low angle powder XRD patterns were recorded on a Panalytical X'pert Pro diffractometer fitted with an X'celerator detector and Cu Ka ( $\lambda = 1.54 \text{ \AA}$ ) radiation source. The spectrometer was calibrated periodically using silicon, which has well known, well-defined and strong diffraction peaks. Low angle patterns were recorded for  $2\theta = 0.3 - 8^\circ$  with a step size of  $0.01^\circ$ .

#### **2.2.9. Porosimetry ( $N_2$ isotherm)**

For nanoporous materials, it is essential to focus on the porosity system in terms of studying the pore size distribution and the surface area of the material.  $N_2$  adsorption porosimetry has been used as a valuable technique for this purpose.

##### **2.2.9.1. Theoretical aspects**

Traditionally, the pore size distribution is obtained from the Barrett, Joyner and Halenda (BJH) adsorption method, whereas, the specific surface area is estimated by the Brunauer, Emmett and Teller model (BET) [23, 24], both methods are strongly related to the assumption of converting the  $N_2$  isotherm into valuable information.

In  $N_2$  isotherm, the sample is treated with a small amount of nitrogen to reach equilibrium with the surrounding vessel. At the equilibrium, the pressure of the vessel represents the volume of the gas based on the ideal gas equation. Once the

equilibrium achieved, nitrogen will continued to be added until the pressure is saturated. Thus, the isotherm is built by plotting the adsorbed volume versus partial pressure. Six types of adsorption isotherms have been classified by IUPAC (see section 1.3.1 in Chapter one).

The BET method is the standard model for surface area estimation, and is based on the concept of determining the surface area related to the gas adsorbed. The adsorbed gas is usually N<sub>2</sub> at temperature of 77K. BET theory has described the amount of gas adsorbed as given in equation 2.12.

$$\frac{P/P_0}{V(1-(P/P_0))} = \frac{1}{V_m C} + \frac{(C-1) (\frac{P}{P_0})}{V_m C} \quad (2.12)$$

where,  $V$  is the volume of the adsorbed gas,  $V_m$  is the volume of the monolayer of adsorbed gas,  $P$  is the equilibrium gas pressure,  $P_0$  is the saturation pressure of the adsorbate and  $C$  is the BET constant.

At given pressure, the amount of gas adsorbed can be used to estimate the number of adsorbed molecules that will be needed to make a monolayer on the surface of the material, and then the surface area can be easily calculated [23].

BJH method is proposed to assess the pore size using the classical Kelvin equation, which relates the pressure of the capillary condensation or evaporation to the material pore size. The method is based on the model of adsorbent as a collection of cylindrical pores and represents the capillary condensation in the pores [23, 25].

#### 2.2.9.2. Porosimetry instrument

Nitrogen physisorption was undertaken on a Quantachrome Nova 2000e porosimeter and analysed using NOVWin software version 11.

Specific BET surface areas were calculated over the relative pressure range 0.05–0.25, where a linear relationship was maintained. Pore diameters and volumes were calculated using the BJH method to the desorption isotherm for relative pressures >0.35.

### 2.2.10. Thermal gravimetric analysis (TGA)

Thermogravimetric analyzer (TGA) is an important technique used for material characterization. It studies the material mass as a function of temperature or time in a controlled atmosphere.

#### 2.2.10.1. Theoretical aspects

TGA is performed by a gradual increase (heating) or decrease (cooling) of the sample temperature in a furnace after measuring its weight on a balance outside the furnace. Due to increasing temperatures, a gradual mass loss is observed, related to the loss of each volatile component in a material decomposition. The weight of the sample at each temperature is plotted vs temperature in a TGA curve [26]. Figure 2.7 shows a schematic representation of TGA instrument.

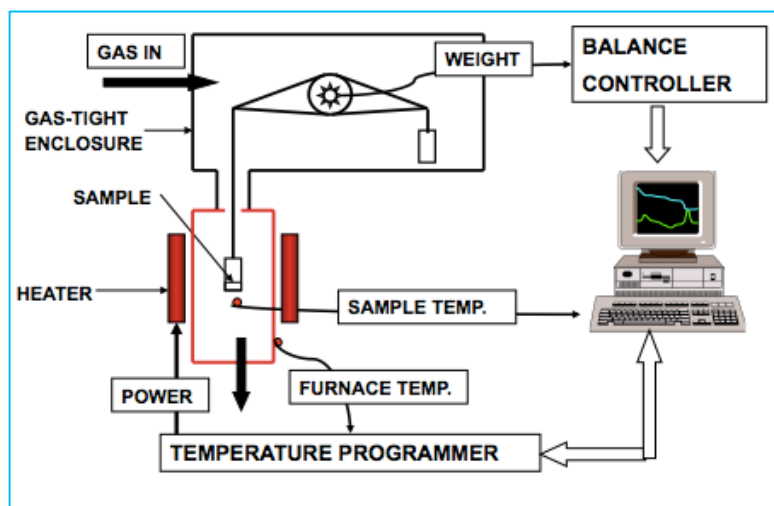


Figure 2.7 Schematic representations of TGA instrument [26].

#### 2.2.10.2. TGA instrument

TGA was performed using a Stanton Redcroft STA780 thermal analyser on 10–20 mg samples under a 10 V% of O<sub>2</sub> /He mixtures (20 cm<sup>3</sup> min<sup>-1</sup> total flow) during heating at 20 °C min<sup>-1</sup> in order to study the decomposition of organic moieties in the sample.

### 2.2.11. X-ray photoelectron spectroscopy (XPS)

It is essential to study the changes of the catalyst surfaces in the reactions based on active sites of the catalyst. These changes include the surface electronic, chemical and structural properties through a specific process.

#### 2.2.11.1. Theoretical aspects

XPS is one of the analytical techniques are used to study material surface changes. The technique is suitable to determine the quantitative elemental compositions (atomic %) of elements on the surface of the sample. Hydrogen and Helium are the two elements, which cannot be detected by XPS as they have atomic number of 1 and 2 respectively and that is not applicable to be analyzed by XPS [27, 28].

High-energy photons (in KeV) hit the material with photoelectrons. Einstein's law, (equation 2.13), measures the kinetic energy  $E_k$  of the photoelectron.

$$E_k = h\nu - E_b \quad (2.13)$$

where,  $h\nu$  is the incident radiation energy,  $E_b$  is the electron binding energy in a particular level (equation 2.14).

$$E_b = E_i - E_f \quad (2.14)$$

where  $E_i$  is the initial (ground) atomic state, and  $E_f$  is the final (ionized) state.

When the incident photon flux with sufficient energy (typically >1200 eV) [29, 30] and hit the sample levels, materials can be ionized and photoelectrons are ejected from atom core levels. Due to the photoelectron effect, spectra are produced to display all energy levels as a distribution of the kinetic energy of emitted photoelectrons based on equation 2.13. The binding energy of the electron for each energy level can also be calculated by equation 2.14. The quantum number of each level classify and label each photoelectron peaks in the spectra [30], since the electron at that level is described by a total momentum number  $j = l + s$ , where  $l$  is the orbital momentum number and  $s$  is the spin momentum number (-1/2 or +1/2).

Identification of the elements at the surface of materials is the main target of using XPS for characterization approaches, since each element has a unique set of binding energies. The typical XPS spectrum involves the plot of electron counts versus binding energy (eV). Element oxidation states can also be determined by XPS analysis as the binding energy shifts with the screening effects of the electron in different orbitals.

The emitted electron from the sample leaves the core hole, which is immediately filled by another electron from the lower energy level. The difference of energies between the two levels can be expressed in either two ways. The first is the emission of a photon with an appropriate energy in the form of X-ray fluorescence. The other way is that the photon transferred to a third electron (Auger electron), and this electron is able to be emitted and escape with certain energy and it also has an independent kinetic energy that different from the photon energy, which used to irradiate the sample.

#### **2.2.11.2. XPS instrument**

XPS instrument consists of four main components, which are the X-ray source, the electron detector, the electron energy analyser and high vacuum pumping system.

The principle of the technique is based on the photoelectric effect. If an atom absorbs a photon of energy greater than the work function of the atom, the electron can be ejected with the excess energy as kinetic energy.

The sample is irradiated with monoenergetic soft X-rays under UHV (ultra-high vacuum). The X-ray source is Mg or Al. Photons have limited penetration in the solid within the distance of 1-10  $\mu\text{m}$ , so atoms can emit photoelectrons in this region by the photoelectric effect, and that makes the technique is useful for surface investigations of materials.

In this project, XPS measurement were carried out by Dr David Morgan using a Kratos Axis Ultra-DLD XPS system with a monochromated Al Ka source and analysed using Casa XPS software.

#### **2.2.12. Gas Chromatography (GC)**

Gas chromatography has been used to characterize palmitic acid esterification reaction.

##### **2.2.12.1. Theoretical aspects**

GC is the one of the most widely used technique to analyse hydrocarbon mixtures since the technique involves a wide range of measurements from ppm to 100%, the ability to detect a wide range of components and the advantage of measurement repeatability. All gas chromatographs compose from the same functional components including the sample handling system, the column and the chromatograph oven.

The function of the sample handling system is to control the sample pressure and remove liquids and solid from the sample to ensure a clean and dry sample is injected



to the chromatograph [31].

The main analytical components of GC chromatograph are the column, the valve and detector, which are enclosed in a heated oven. The change of the temperature can affect the performance and response of the column and detectors, so the oven is designed to isolate the other component from the temperature changes, and keep the internal temperature is very stable. Using a temperature control of  $\pm 0.3$  °C.

The column in GC is to separate a gas mixture into its individual components by material physical properties such as boiling point, molecular size or polarity differences.

The GC column includes the stationary and moving phases by packing tube with column packing material. Inside the column, materials placed and filtered at one of the column ends, and then the sample gas is carried through the column using the carrier gas that is not measured. This phase between the sample and the carrier gas is the moving phase. The carrier gas could be helium for the application of hydrogen, and hydrogen, nitrogen or argon and that depends on the application [31, 32].

When the sample moves inside the column, the lower boiling point components move slowly than the higher boiling point components. The difference of their speed cause the separation and that depends on the column temperature. The amount of component separation is strongly dependent on the length of the column [29].

#### **2.2.12.2. GC instrument**

The GC measurements were carried out by Mr Thomas Williams, using a Waters GC 6890N gas chromatograph with a 30 m 5% phenyl 95% methyl column with a 0.1  $\mu$ m diameter. The temperature program is initial temperature 40 °C held for 5 minutes and then ramped up to 300 °C at 8.0 °C/min, It is then held for 5 minutes. The inlet was 200 °C and with a split of 20 %.

### **2.3. Materials**

The materials section has been divided into three parts, first is general materials, which includes those used in different experiments such as preparing stock solutions. Second, surfactants, and then thirdly, the materials used in nanoporous silicas and their applications.

#### **2.3.1 General materials**

Perfluorohexane (PFH) was purchased from Fluorochem. Hexane, D<sub>2</sub>O, d-chloroform, 16-doxyl stearic acid methyl ester (16-DSE) (EPR spin-probe) and pyrene (fluorescent

probe) were purchased from Sigma-Aldrich and used as received. Distilled water was used for preparation of the aqueous solutions. Acetone and ethanol have been used as solvents and were purchased from Sigma-Aldrich.

### 2.3.2. Surfactants

Zonyl FSN-100 with an average chemical structure of  $C_8F_{17}C_2H_4(OC_2H_4)_9OH$  (MW= 950 g mol<sup>-1</sup>), Zonyl FSO-100 ( $CF_3(CF_2)_n(EO)_n$ ) and cetyltrimethylammonium bromide (CTAB, 364.45 g mol<sup>-1</sup>) were purchased from Sigma-Aldrich and used as received.

### 2.3.3. Materials used in nanoporous silicas synthesis and applications

Palmitic acid, aqueous ammonia (35 wt %), tetraethoxysilane (TEOS, 98%) as silica precursor, were purchased from Sigma-Aldrich and used as received. Methanol, toluene, dihexylether, hydrogen peroxide (H<sub>2</sub>O<sub>2</sub>), 3-mercaptopropyl trimethoxysilane (MPTMS), and dichloromethane (DCM) were purchased from Fisher.

## 2.4. Synthesis of nanoporous materials

This section includes the preparation method of the nanoporous materials, the grafting reaction on the surface of materials, and the esterification reaction of palmitic acid. It also includes the synthesis of MCM-14 as a comparator for the synthesized materials.

### 2.4.1. MCM-41 Comparator

MCM-41 (Mobil Composition of Matter No. 41) is a form of mesoporous silicate, which has hexagonal arrays of a regular pore system [33]. The synthesis of MCM-41 has been studied using n-alkyltrimethylammonium bromide of various alkyl chain lengths from C<sub>12</sub> to C<sub>20</sub>, as a template [34]. In this project, MCM-41 has been prepared using Hexadecyltrimethylammonium bromide (CTAB (C<sub>16</sub>)) based on the same pathway to use it as a comparator for the targeted materials.

MCM-41 was synthesized by adding TEOS (98%, 0.008 mol) slowly to the CTAB solution (0.055 mol L<sup>-1</sup>) over a period of 15 min, in the presence of 9.0 g of aqueous ammonia (35%). The mixture was stirred for one hour, after which white precipitate was filtered, washed with deionized water and dried at 90 °C. To remove the organic template, the resultant material was calcined at 550 °C in air (1 K min<sup>-1</sup>) for 5 h.

Results obtained are discussed in Chapter 5 and were in a good agreement with the literature values [34]. Based on these results, the MCM-41 synthesis pathway [34] has

been adjusted to include the fluorocarbon surfactant FSN-100 and perfluorohexane as an oil phase in order to create an additional type of pores in a hierarchical material pore structure as will be described in the next section.

### 2.4.2. Synthesis of hierarchical nanoporous materials

0.4 g CTAB was dissolved in 20 ml deionized water to yield a  $0.055 \text{ mol L}^{-1}$  solution. Different amounts of perfluorohexane were added to the aqueous FSN-100 stock solution (0.4g FSN100 in 20 ml  $\text{H}_2\text{O}$ ,  $0.021 \text{ mol L}^{-1}$ ) to prepare six samples with different volume percentages of the oil in the surfactant mixture solution (0 %, 1 %, 11 %, 20 %, 27 % and 33 %). Aqueous ammonia (35 wt %, 2.216 g) was added to the mixture. While stirring, tetraethoxysilane TEOS (98 %, 0.008 mol) was added slowly to the surfactant mixture solution over 15 min. The mixture was stirred for one hour at room temperature, and then the resultant white precipitate was filtered and washed with approximately 70 ml of deionized water. After drying at 80-90 °C for about 12 h, samples were calcined at 550 °C with the rate of  $1 \text{ K min}^{-1}$  in air and kept at this temperature for 5 h to remove the template.

### 2.4.3. Post-synthesis grafting reactions

The grafting reaction of sulfonic acid to the synthesized materials was performed through a post synthesis method following a procedure described previously [35]. The reaction includes two main steps, sulfonic acid functionalization followed by oxidation reaction to convert thiol groups (RSH) into sulfonic acid ( $\text{RSO}_3\text{H}$ ).

#### 2.4.3.1. Sulfonic acid functionalization

Grafting synthesized nanoporous materials to yield sulfonic acid functionalization was achieved through the post synthesis method [35]. Typically, 0.2247g of the prepared mesoporous material was added to 30 ml toluene and mixed for 50 minutes, before 0.25 ml of 3-mercaptopropyl trimethoxysilane (MPTMS) was added to the mixture. The mixture was refluxed at 130 °C for 24 h and then the resultant solid filtered and washed with methanol before drying at 80 °C overnight.

#### 2.4.3.2. Oxidation reaction

To convert thus attached thiol group to sulfonic acid, 30 ml  $\text{H}_2\text{O}_2$  was mixed with the sample at room temperature for 24 h. The sample was then filtered and washed with methanol three times before again drying at 80 °C overnight.

#### 2.4.4. Palmitic acid esterification (catalysis tests)

Catalytic tests were performed following a procedure reported by Lee et al [35]. A typical palmitic acid esterification was performed by mixing 1.282 g of palmitic acid, 6.25 ml methanol and 0.24 g dihexylether (DHE) in a reaction tube at 60 °C under refluxing for 10 minutes. After taking the first sample to be measured by GC, the catalyst (25 mg) was added to the mixture, before the mixture was regularly sampled over 24 h by withdrawing 0.1 ml and analysing by GC.

##### 2.4.4.1. Samples for GC

0.1 ml of the sample was added to 50 ml of dichloromethane (DCM) for dilution and then 1.0 ml of the diluted solution kept in GC tubes to be analysed by gas chromatography to determine the amount of methyl palmitate or the conversion rate of palmitic acid to palmitate reaction.

### 2.5. Sample preparation for characterization

Samples have been prepared in different ways based on both targeted characterization and the requirements of each used technique. Some techniques such as XRD, SEM and XPS need solid samples, but samples have to be dissolved for other techniques.

#### 2.5.1. The choice of solvents

The solvent was D<sub>2</sub>O in small-angle neutron scattering (SANS), pulse gradient spin echo NMR spectroscopy (PGSE-NMR), <sup>19</sup>F-NMR and <sup>1</sup>H-NMR, whereas deionized water has been used in the surface tension, fluorescence and Electron paramagnetic resonance (EPR) measurements. Acetone and ethanol were used as solvents for the pyrene and 16-DSE stock solutions respectively; d-CHCl<sub>3</sub> has been used to measure NMR samples.

#### 2.5.2. Surface tension

Surface tension measurements have been performed on the aqueous solutions of CTAB, FSN-100, as well as their mixture solutions in order to determine the critical micelle concentration (CMC) for each case.

##### 2.5.2.1 CTAB and FSN-100 solutions

Stock CTAB solutions were prepared by dissolving the appropriate mass of CTAB in deionized water to produce a stock solution with a CTAB concentration of 10 mM, from

which a range of concentrations were derived. Serial dilutions were prepared to make different CTAB concentrations ranging from 0.01 to 4.0 mM.

FSN-100 stock solutions were prepared by dissolving the appropriate mass of FSN-100 in distilled water to produce a total concentration of 150 mM. Serial dilutions were prepared to make different FSN-100 concentrations ranging from 100 to 0.01 mM.

#### **2.5.2.2. CTAB/FSN-100 mixtures**

Surface tension measurements have also been performed for a number of mixtures between CTAB and FSN-100. A series of CTAB mole fraction mixtures have been prepared to cover a range of compositions in terms of CTAB mole fraction (0.15- 0.9).

### **2.5.3. Fluorescence**

Fluorescence measurements have also been performed to determine the CMC of the pure surfactant solutions and mixtures using pyrene as fluorescent probe.

#### **2.5.3.1. Pyrene stock solution**

A 2  $\mu$ M of pyrene was prepared by dissolving an appropriate amount of pyrene in 1.0 ml acetone and transferring into 1000 ml volumetric flask, then kept in a dark place. The pyrene stock solution was used to prepare different concentrations of CTAB, FSN-100 and their mixtures.

#### **2.5.3.2. Surfactant solution samples**

Surfactant solutions and surfactant mixtures were prepared in distilled water as described in the surface tension case, with 10  $\mu$ L of the pyrene stock solution being transferred to a sample vial to allow acetone to evaporate fully before adding 1.0 ml of the aqueous sample into the vial and mixing for at least 1 h to ensure that the probe has been incorporated into the micelle. Samples have been measured by the fluorescence emission spectrum and by calculating the ratio of the 1<sup>st</sup> and 3<sup>rd</sup> vibronic peak intensities ( $I_3/I_1$ ), which are usually around 373 nm and 384 nm respectively. The CMC for each solution can be estimated from the breakpoint of the curve of ( $I_3/I_1$ ) vs the concentration.

### **2.5.4. Small angle neutron scattering (SANS)**

Small angle neutron scattering measurements have been performed for the pure surfactants and their mixtures. The solutions have also been measured in the presence of 2 % PFH or 2 % hexane as an oil phase.

#### **2.5.4.1. Pure surfactant solutions**

50 mM of CTAB solution and 50 mM of FSN-100 solutions have been prepared in D<sub>2</sub>O and measured by SANS. The same concentration of each surfactant has been mixed with 2 % of PFH or hexane to do the measurements in the presence of oil.

#### **2.5.4.2. Surfactant mixture solutions**

0.2, 0.4, 0.6, and 0.8 CTAB mole fraction solutions have been prepared in D<sub>2</sub>O for SANS measurements. The same mole fractions except 0.4 have also been measured after mixing with 2 % of hexane or PFH.

### **2.5.5. Pulsed-gradient spin-echo NMR spectroscopy (PGSE-NMR)**

PGSE-NMR measurements have been performed in both cases with the oil and without the oil phase for both pure surfactant solutions and the surfactant mixtures.

#### **2.5.5.1. Pure surfactant solutions**

Stock solutions of CTAB, FSN-100 were prepared by dissolving the appropriate mass in deuterium oxide to produce a total concentration of 50 mM. All solutions were prepared from stock solutions using D<sub>2</sub>O as solvent, and 0.6 mL were transferred to 5 mm o.d. NMR tubes (Willmad NMR tubes form Sigma-Aldrich).

#### **2.5.5.2. Surfactant mixture solutions**

0.2, 0.5 and 0.8 CTAB mole fraction solutions have been prepared in D<sub>2</sub>O and mixed with 2 % of hexane and only 0.5 mole fraction was measured with PFH by the NMR spectroscopy before and after adding the oil.

### 2.5.6. Electron paramagnetic resonance spectroscopy (EPR)

EPR spectroscopy measurements have been performed for the aqueous solutions of the pure surfactants and mixtures using 16-DSE as a spin probe.

#### 2.5.6.1. 16-DSE stock solution

The spin probe has been prepared by adding the appropriate amount in 2 ml of ethanol to produce 0.01 M. Figure 2.8 shows the structure of the spin probe 16-DSE.

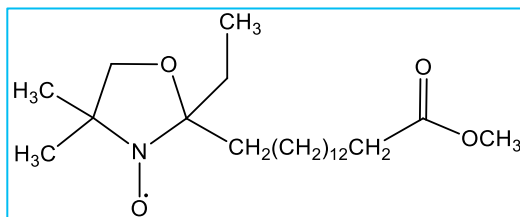


**Figure 2.8 The chemical structure of 16-DSE spin probe.**

#### 2.5.6.1. Surfactant solution samples

To prepare surfactant samples for EPR, 0.02 ml of the probe solution (0.01 M) was transferred into a separate glass vial. After allowing for the ethanol evaporate, 1.0 ml of the surfactant sample was added to the vial and mixed for at least 1 h to give a final spin-probe concentration at  $2 \times 10^{-4}$  M, and to ensure that the probe has been incorporated into the micelle solutions.

### 2.5.7. Scanning Electron Microscopy (SEM)

SEM microscopy has been performed for the synthesized nanoporous materials. The solid sample was ground and held on an aluminium stub holder using carbon tape. Samples were then placed into SEM instruments for scanning.

### 2.5.8. Transmission Electron Microscopy (TEM)

TEM microscopy technique has been performed for the synthesized nanoporous materials. For the analysis, the powder sample was dispersed in hexane as a dispersant to avoid dissolution of the particles in the samples, and a drop of this suspension deposited on a carbon film copper grid.

### **2.5.9. X-ray diffraction (XRD)**

XRD measurements have been performed for the synthesized nanoporous materials. The solid sample was ground and then placed on a plastic, aluminium or glass sample holder avoiding vertical loading before being connected to the instrument.

### **2.5.10. Nitrogen porosimetry**

Nitrogen porosimetry measurements have been performed for the synthesized nanoporous materials. Solid samples were degassed at 120 °C for 2 h before the analysis by N<sub>2</sub> adsorption at –196 °C, with equilibration times of 150 seconds for each data point. The sample has to be extensively degassed, since any tiny amount of water can affect the quantity of adsorbed N<sub>2</sub> molecules by its partial pressure.

### **2.5.11. Thermal gravimetric analysis (TGA)**

TGA measurements have been performed to characterize the catalysts. 1.0 mg of the solid sample was placed on a sample pan, and then a survey scan was run at 20 °C per minute, which began and ended 100 °C below and above the transition of the sample to adjust the beginning and ending temperatures.

### **2.5.12. X-ray photoelectron spectroscopy (XPS)**

XPS measurements have been performed to analyse the prepared catalysts. The sample bar used to accommodate samples is available with an area of 8 cm x1.5 cm, and the maximum sample depth is 4 mm.



## 2.6. References

1. Eastoe, J. and J.S. Dalton, Dynamic surface tension and adsorption mechanisms of surfactants at the air-water interface. *Advances in Colloid and Interface Science*, 2000. **85**(2-3): p. 103-144.
2. A.M. Ovrutsky, A.S.P., M.S. Rasshchupkyna, 5 – Adsorption. The Gibbs Adsorption Equation. *Surfaces, Interfaces, Crystallization*, 2014: p. 127-149.
3. Bermudez-Salguero, C. and J. Gracia-Fadrique, Analysis of Gibbs adsorption equation and thermodynamic relation between Gibbs standard energies of adsorption and micellization through a surface equation of state. *Journal of Colloid and Interface Science*, 2011. **355**(2): p. 518-519.
4. Gunde, R., et al., Surface-Tension of Waste-Water Samples Measured by the Drop Volume Method. *Environmental Science & Technology*, 1992. **26**(5): p. 1036-1040.
5. Royer, C.A., Approaches to Teaching Fluorescence Spectroscopy. *Biophysical Journal*, 1995. **68**(3): p. 1191-1195.
6. do Canto, A.M.T.M., et al., Behavior of pyrene as a polarity probe in palmitoylsphingomyelin and palmitoylsphingomyelin/cholesterol bilayers: A molecular dynamics simulation study. *Colloids and Surfaces a-Physicochemical and Engineering Aspects*, 2015. **480**: p. 296-306.
7. Ray, G.B., I. Chakraborty, and S.P. Moulik, Pyrene absorption can be a convenient method for probing critical micellar concentration (cmc) and indexing micellar polarity. *Journal of Colloid and Interface Science*, 2006. **294**(1): p. 248-254.
8. Aguiar, J., et al., On the determination of the critical micelle concentration by the pyrene 1 : 3 ratio method. *Journal of Colloid and Interface Science*, 2003. **258**(1): p. 116-122.
9. Bacon, G.E., *Neutron Scattering in Chemistry*. 1977, London: Butterworth & Co Publishers Ltd.
10. Bragg, W.L. and J.J. Thomson, The diffraction of short electromagnetic waves by a crystal. *Proceedings of the Cambridge Philosophical Society*, 1914. **17**: p. 43-57.

11. Barnes, I.S., et al., Small-Angle X-Ray-Scattering from Ternary Microemulsions Determines Microstructure. *Journal of Physical Chemistry*, 1988. **92**(8): p. 2286-2293.
12. Heenan, R.K., J. Penfold, and S.M. King, SANS at pulsed neutron sources: Present and future prospects. *Journal of Applied Crystallography*, 1997. **30**: p. 1140-1147.
13. Bales, B.L. and C. Stenland, Statistical Distributions and Collision Rates of Additive Molecules in Compartmentalized Liquids Studied by Epr Spectroscopy .1. Sodium Dodecyl-Sulfate Micelles, 5-Doxylstearic Acid Ester, and Cobalt(II). *Journal of Physical Chemistry*, 1993. **97**(13): p. 3418-3433.
14. Noda, A., K. Hayamizu, and M. Watanabe, Pulsed-gradient spin-echo H-1 and F-19 NMR ionic diffusion coefficient, viscosity, and ionic conductivity of non-chloroaluminate room-temperature ionic liquids. *Journal of Physical Chemistry B*, 2001. **105**(20): p. 4603-4610.
15. Griffiths, P.C., et al., FT-PGSE NMR study of mixed micellization of an anionic and a sugar-based nonionic surfactant. *Journal of Physical Chemistry B*, 1997. **101**(6): p. 915-918.
16. Griffiths, P.C., et al., Role of counterion concentration in determining micelle aggregation: Evaluation of the combination of constraints from small-angle neutron scattering, electron paramagnetic resonance, and time-resolved fluorescence quenching. *Journal of Physical Chemistry B*, 2004. **108**(12): p. 3810-3816.
17. Peric, M. and B.L. Bales, Lineshapes of spin exchange broadened EPR spectra. *Journal of Magnetic Resonance*, 2004. **169**(1): p. 27-29.
18. Abragam, A.B., B, *Electron paramagnetic resonance of transition ions*. 2012, Oxford: Oxford University Press.
19. Bales, B.L., Inhomogeneously Broadened Spin-Label Spectra, In *Biological Magnetic Resonance*. *Biological Magnetic Resonance* 1989. **8**: p. 77.
20. Schindler, B., H. Kohl, and L. Reimer, Low-voltage energy filtering scanning transmission electron microscopy with a 'simulated' spherical deflection analyzer. *Electron Microscopy 1998, Vol 1*, 1998: p. 487-488.

21. Reimer, L., Scanning Electron Microscopy Physics of Image Formation and Microanalysis. Vol. 12. 2000: T Mulvey, Measurement Science and Technology.
22. Fultz, B., Howe, James M., Transmission Electron Microscopy and Diffractometry of Materials 2012: Springer Science & Business Media.
23. Barrett, E.P., L.G. Joyner, and P.P. Halenda, The Determination of Pore Volume and Area Distributions in Porous Substances .1. Computations from Nitrogen Isotherms. Journal of the American Chemical Society, 1951. **73**(1): p. 373-380.
24. Joyner, L.G., E.P. Barrett, and R. Skold, The Determination of Pore Volume and Area Distributions in Porous Substances .2. Comparison between Nitrogen Isotherm and Mercury Porosimeter Methods. Journal of the American Chemical Society, 1951. **73**(7): p. 3155-3158.
25. Makowski, W. and P. Kustrowski, Probing pore structure of microporous and mesoporous molecular sieves by quasi-equilibrated temperature programmed desorption and adsorption of n-nonane. Microporous and Mesoporous Materials, 2007. **102**(1-3): p. 283-289.
26. Skoog, D.H., F. Grouch, S. , Principles of instrumental analysis sixth ed. 2007, USA: Thomson higher education, Daivid Harris.
27. Sastre, E.P.-P., J. Mohino, F. D'íaz, I, Synthesis, characterization and catalytic activity of MCM-41-type mesoporous silicas functionalized with sulfonic acid. Applied Catalysis a-General, 2001. **205**: p. 19-30.
28. Wilson, K.E. and C.J. Baddeley, XPS studies of the effects of modification pH on the interaction of methylacetoacetate with (S)-aspartic acid-modified Ni surfaces. Journal of Catalysis, 2011. **278**(1): p. 41-49.
29. G.A. Somorjai, Y.L., Introduction to Surface Chemistry and Catalysis. Second Edition ed. 2010: John Wiley & Sons.
30. Venezia, A.M., X-ray photoelectron spectroscopy (XPS) for catalysts characterization. Catalysis Today, 2003. **77**(4): p. 359-370.
31. Dilillo, M., et al., GC/MS investigations of the total lipid fraction of wool: A new approach for modelling the ageing processes induced by iron-gallic dyestuffs on historical and archaeological textiles. Microchemical Journal, 2015. **118**: p. 131-140.

32. Criado-Garcia, L., et al., Potential of ion mobility spectrometry versus FT-MIR and GC-MS to study the evolution of a heat transfer fluid after its heating process in a thermosolar plant. *Microchemical Journal*, 2015. **121**: p. 163-171.
33. Kresge, C.T., et al., Ordered Mesoporous Molecular-Sieves Synthesized by a Liquid-Crystal Template Mechanism. *Nature*, 1992. **359**(6397): p. 710-712.
34. Grun, M., et al., Novel pathways for the preparation of mesoporous MCM-41 materials: control of porosity and morphology. *Microporous and Mesoporous Materials*, 1999. **27**(2-3): p. 207-216.
35. Dhainaut, J., et al., Hierarchical macroporous-mesoporous SBA-15 sulfonic acid catalysts for biodiesel synthesis. *Green Chemistry*, 2010. **12**(2): p. 296-303.

## **Chapter Three**

# **Phase Behaviour of Mixed Surfactant Systems**

### 3.1. Introduction

The aim of this chapter is to establish an experimental approach to study the mixture of the hydrocarbon surfactant cetyltrimethylammonium bromide (CTAB) and the fluorocarbon surfactant, Zonyl-FSN-100 which has an average chemical structure of  $\text{C}_8\text{F}_{17}\text{C}_2\text{H}_4(\text{OC}_2\text{H}_4)_9\text{OH}$ . The main aim was to determine the size and shape of the micelles and critical micelle concentration at different surfactant ratios.

Different techniques have been used to analyse the single components and their mixtures including surface tension and fluorescence measurements, small-angle neutron scattering (SANS), electron paramagnetic resonance spectroscopy (EPR), pulsed gradient spin-echo nuclear magnetic resonance (PGSE-NMR),  $^1\text{H}$ -NMR and  $^{19}\text{F}$ -NMR. The characterized data from each technique will provide more information about the micellization processes in both single component solutions and mixtures in order to explain the whole picture of the surfactant micelles.

Surface tension and fluorescence measurements have been used to estimate the critical micelle concentration (CMC) values for surfactant solutions and define the relationship between these values and the compositions as a function of CTAB mole fraction. SANS is a good method to estimate the size-shape and structure of the micelles and that is essential to determine micelle compositions especially in the mixed micelle systems. EPR data characterization will help to describe the hydration of micelle headgroup regions and surfactant solution polarity and viscosity, which provide a good measure of the micelle dynamics. The interaction between surfactant micelles and mixed micelles was studied using PGSE-NMR, which measures the diffusion mobility of each component in the solution.  $^1\text{H}$ -NMR and  $^{19}\text{F}$ -NMR have been used to investigate the presence of each surfactant in the mixture.

### 3.2. Surface tension

In this section, surface tension measurements have been carried out for the pure surfactant solution as well as the surfactant mixture solutions in order to estimate the CMC in each case.

#### 3.2.1. Surfactant solutions

Surface tension measurements have been performed to estimate the CMC of CTAB and FSN-100 solutions. Figure 3.1 shows the surface tension of CTAB and FSN-100 aqueous solutions as a function of the solution total concentration. The range of

concentrations in FSN-100 is larger than that in CTAB, since the FSN-100 has two breaking points in the surface tension curve with the concentration.

In the CTAB curve, surface tension values decrease with increasing the total concentration of CTAB aqueous solution up to  $8.0 \times 10^{-4}$  M, which indicates the critical micelle concentration of CTAB. The determined CMC of CTAB is in a good agreement with the literature value [1]. The FSN-100 shows two break points ( $6.8 \times 10^{-5}$  M,  $1.0 \times 10^{-3}$  M) again in agreement with literature values [2], these have previously been explained as pre-association and micellization processes [2, 3]. In addition, the hydrophobicity of FSN-100 is much greater than CTAB, So different micelle structures could be recognised over a range of different concentrations of FSN-100 in the solution.

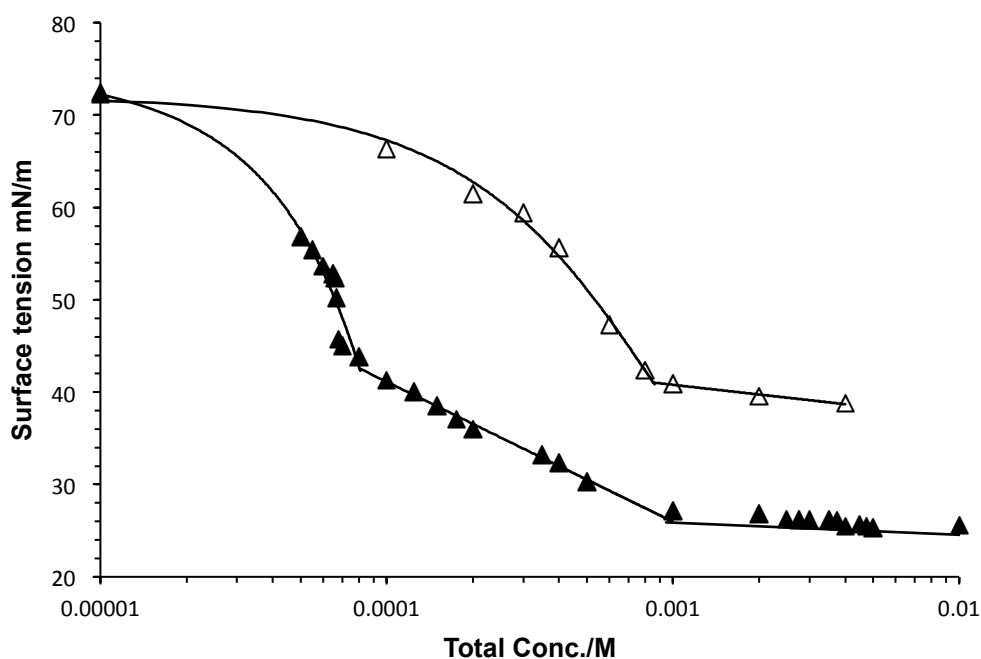


**Figure 3.1** Surface tension measurements as a function of total concentration for CTAB (open triangles) and FSN-100 (closed triangles).

### 3.2.2. Surfactant mixture solutions

Surface tension measurements have been carried out for a range of compositions in terms of CTAB mole fraction and due to the difference in the patterns, data have been divided into two groups of CTAB mole fractions (figures 3.2 and 3.3). In figure 3.2, it is clearly that the CMC increases with increasing CTAB mole fraction up to the CMC of the CTAB solution. However in the other group of mole fractions (figure 3.3), the CMC values do not follow a monotonic relationship with the compositions, suggesting an unusual micellization process over a range of compositions between the two surfactants. This pattern is investigated further in the next section of the chapter.

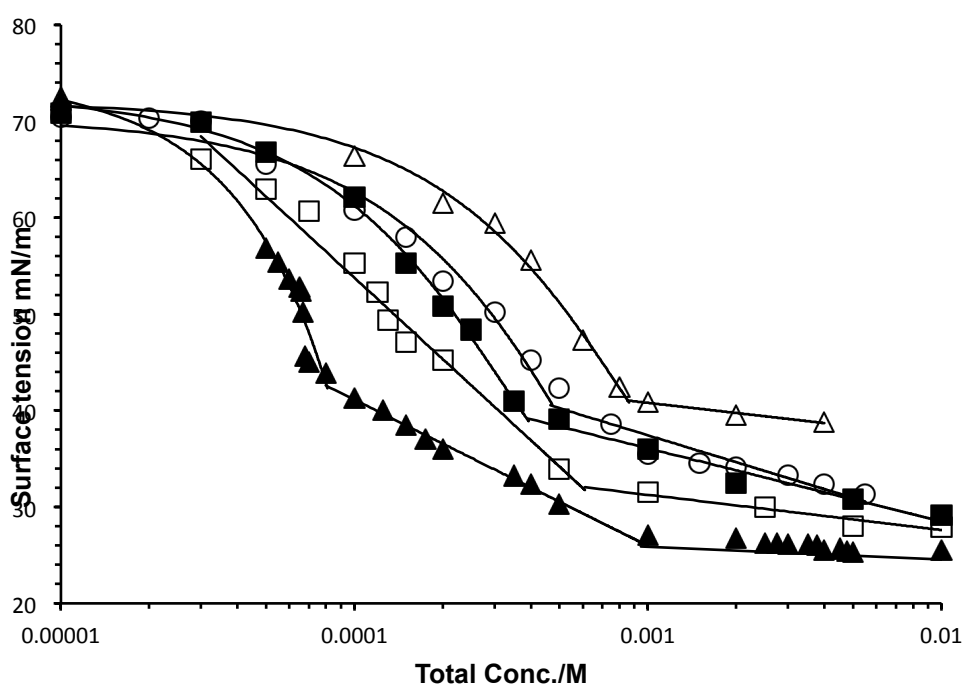


**Figure 3.2** Surface tension measurements as a function of total concentration for CTAB (open triangles), FSN-100 (closed triangles), 0.2 CTAB mole fraction (open square), 0.5 CTAB mole fraction (closed squares) and 0.9 CTAB mole fraction (open circles).



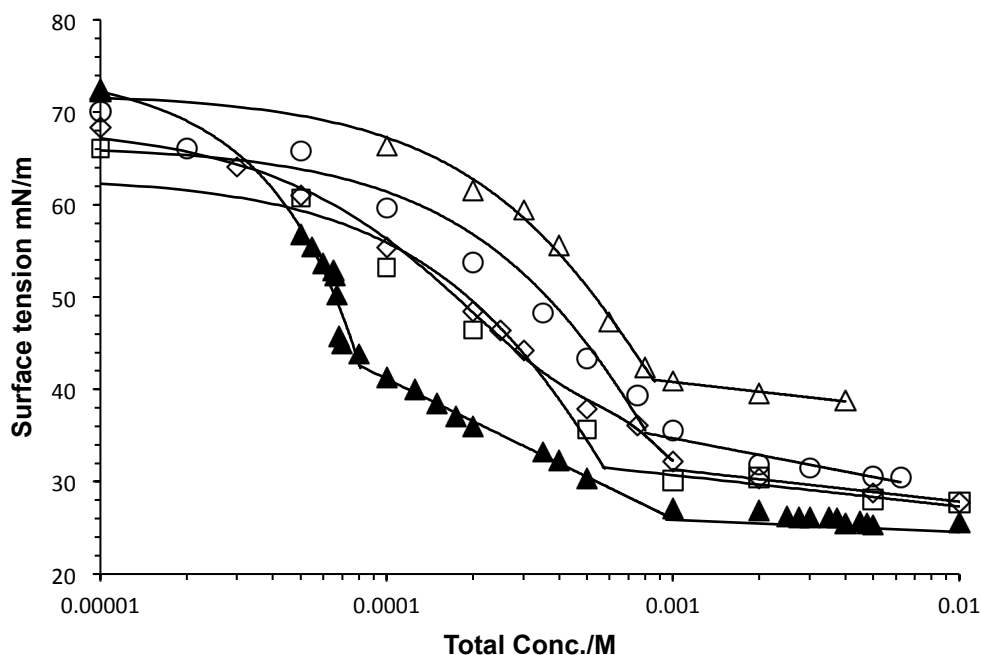


**Figure 3.3** Surface tension measurements as a function of total concentration for CTAB (open triangles), FSN-100 (closed triangles), 0.15 CTAB mole fraction (open squares), 0.33 CTAB mole fraction (open diamonds) and 0.8 CTAB mole fraction (open circles).

### 3.2.3. CMC determination

Surface tension measurements for a range of surfactant compositions have also been used to determine the relationship between CMC values and the CTAB mole fraction (figure 3.4). The two limits correspond to the single component species, for which the CMC values ( $\text{FSN-100} = 6.8 \times 10^{-5} \text{ M}$ ,  $\text{CTAB} = 0.8 \times 10^{-4} \text{ M}$ ) are in excellent agreement with the literature values [1, 2]. In figure 3.4, the first CMC value of FSN-100 has been plotted instead of the second one, because of the micellisation process has been started at this point and then micelles have changed their structures at the second one, so the first CMC represents the actual CMC value in terms of its definition and should not be ignored.

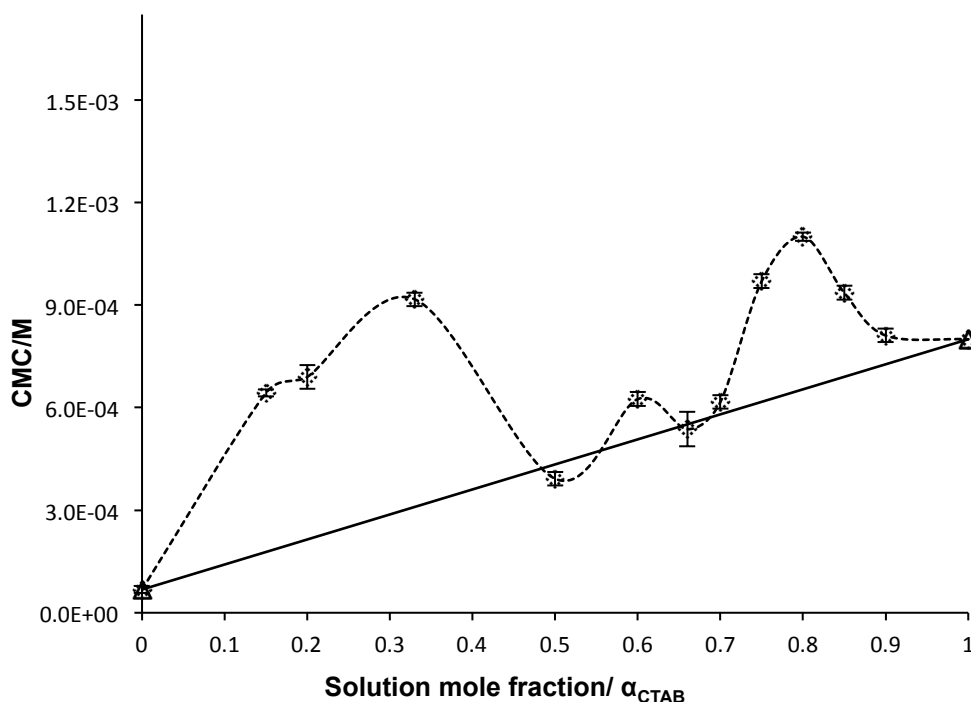


**Figure 3.4** The critical micelle concentration, CMC, as a function of CTAB solution mole fraction determined by surface tension. The solid line corresponds to the ideal mixing prediction; the dotted line is a guide to the eye.

The CMC vs  $\alpha_{CTAB}$  behaviour in figure (3.4) shows a number of distinct features. Particularly, significant regions where the CMC is greater than would be predicted by an ideal mixing approach. Therefore, there are specific interactions between the two molecules, and these are strongly antagonistic, surprisingly, this system includes a region apparent ideality around  $0.5 > \alpha_{CTAB} > 0.7$ . The increases in CMC in the mixtures to a value greater than its single component CMC, confirm a loss of surfactant activity and the presence of a strongly different micellization process. Clearly, further analysis of the micelle composition and size-shape is required.

### 3.2.4. Surface area of surfactant per molecule calculations

From the surface tension curves, surface area per molecule can be calculated using  $\gamma$  vs  $\ln C$ . The slope of the curve is proportional to the excess absorbed amount of the surfactant at the air water interface per unit area.

The maximum surface excess concentration ( $\Gamma$ ) and the minimum area per molecule  $A_{min}$  have been calculated using equation 3.1 and 3.2, for the single component surfactant solutions and a range of compositions of the mixture as a function of CTAB mole fraction.

$$\Gamma = -(\partial\gamma/\partial\ln C)/nRT \quad (3.1)$$

where  $n$  is the number of species formed by surfactant dissociation (e.g. for non-ionic surfactants  $n = 1$ ),  $R$  is the gas constant and  $T$  is the temperature.

$$A_{min} = 10^{20} / N \cdot \Gamma \quad (3.2)$$

where  $N$  is Avogadro's number and  $A_{min}$  is expressed in  $\text{\AA}^2/\text{molecule}$ .

All calculated parameters from surface tension data have been listed in table 3.1. For CTAB solution,  $\Gamma$  is  $3.4 \times 10^{-6} \text{ mol m}^{-2}$ , and the surface area is  $49 \text{ \AA}^2$ , which agree with the literature values [4]. However, it was not easy to calculate surface area per molecule for the surfactant FSN-100 due to the coexistence of the first and second CMC, but by taking the higher concentration break (0.001M) as the CMC of the surfactant, the fit provides the value of  $4.6 \times 10^{-6} \text{ mol m}^{-2}$  as a maximum surface excess concentration for the FSN-100 and corresponding to the surface area of  $36 \text{ \AA}^2$ , which are in a good agreement with the literature value at the same CMC point [2].

CTAB/mole fraction	CMC $\times 10^4/\text{M}$	$\gamma_{CMC} / \text{mNm}^{-1}$	$\Gamma \times 10^6 / \text{mol m}^{-2}$	$n$	$A_{CMC} / \text{\AA}^2$
0	0.68, 10	56, 30	0.1, 5.0	1.0	1582,36
0.15	6.4	31	5.4	1.1	31
0.20	6.9	33	8.5	1.2	20
0.33	9.1	32	3.8	1.3	44
0.50	3.9	39	4.6	1.5	36
0.60	6.4	35	4.2	1.6	40
0.66	6.1	39	3.4	1.7	47
0.70	6.7	34	3.3	1.7	50
0.75	8.0	34	3.6	1.7	46
0.80	10.6	32	2.9	1.8	57
0.85	11.3	33	3.4	1.8	49
0.9	7.8	35	3.4	1.9	50
1	8.0	42	3.4	2.0	49

**Table 3.1 Values of the CMC, surface tension value at the CMC, maximum surface excess concentration and minimum area per molecule parameters for CTAB, FSN-100, 0.15, 0.2, 0.33, 0.5, 0.6, 0.66, 0.7, 0.75, 0.8, 0.85, and 0.9 CTAB mole fraction solutions,  $n$  for mixtures were calculated as a simple weighted value of CTAB and FSN-100.**

### 3.3. Fluorescence

Surface tension detects changes in the surface composition, which generally reflects the general solution structure. To provide a contrasting measure of the CMC, pyrene solubilisation has also been used. This technique has been used for CTAB, FSN-100 single component solutions as well as a range of compositions of mixtures in terms of CTAB mole fraction.

#### 3.3.1. CTAB and FSN-100 single component aqueous solutions

In the case of the aqueous surfactant solutions of CTAB and FSN-100 the  $I_1/I_3$  values decrease with increasing the surfactant total concentration up to the CMC. In CTAB solutions the break point of the curve (figure 3.5) confirms the estimated CMC value from the surface tension measurements.

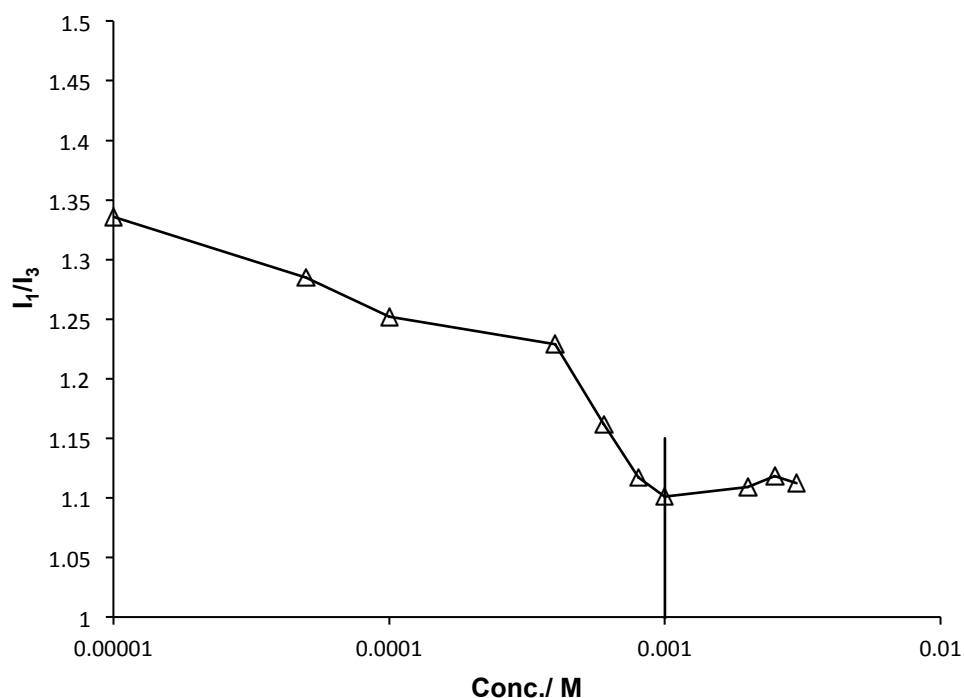


**Figure 3.5** Fluorescence measurements for CTAB aqueous solution. Lines are guide to the eye.

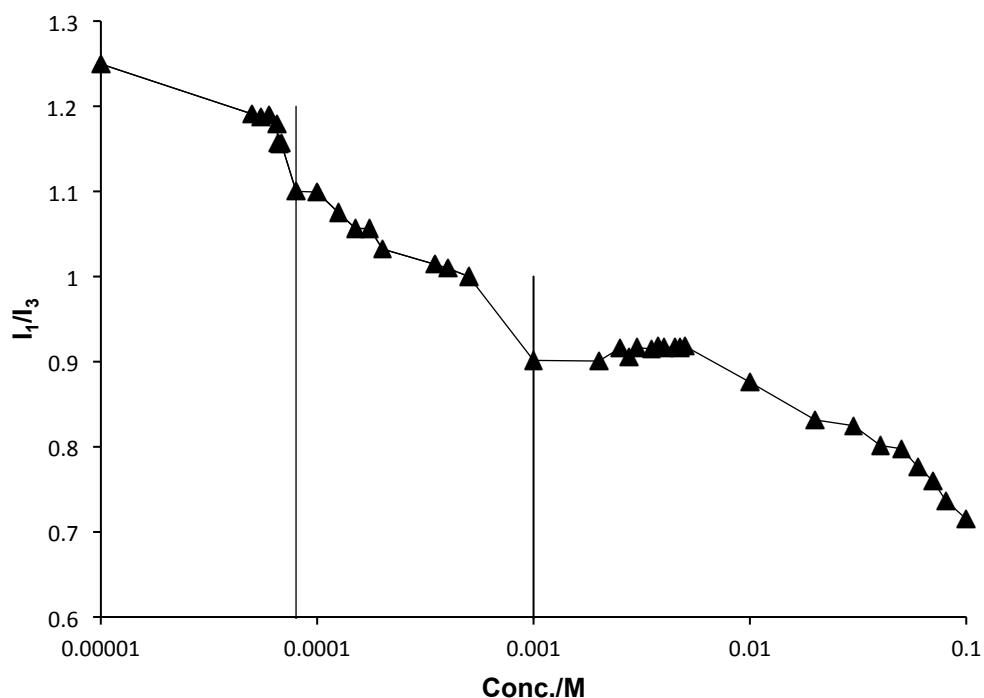


**Figure 3.6** Fluorescence measurements for FSN-100 aqueous solution. Lines are guide to the eye.

Again, two break points have been observed from the FSN-100 curve (figure 3.6), which confirm the type of the micellization process in this surfactant solution. The higher break concentration is exactly the same to that one from the surface tension measurement, whereas the lower one is slightly different.

### 3.3.2. CMC determination

Pyrene probe has been used in the fluorescence measurements to estimate the CMC for different CTAB mole fraction solutions and study the interaction of micelles with low-polar-mass compounds. The curve pattern is similar to the surface tension curve, as the same structure of micelles has been observed through the different concentration regions.

From figure 3.7, the two curves show remarkable similarity, indicating that there is indeed some unusual micellization process occurring in this system and further investigations are required.

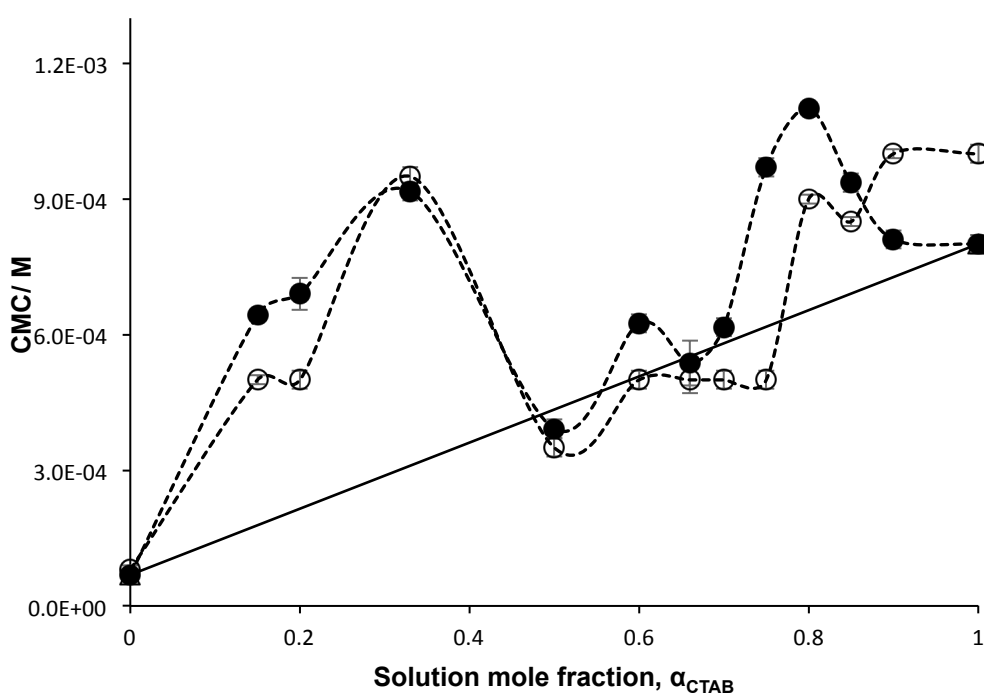


**Figure 3.7** The critical micelle concentration, CMC, as a function of CTAB mole fraction determined by pyrene solubilisation (open circles) and surface tension (closed circles). The dotted lines are guides to the eye. Literature CMC values for the pure surfactants are also plotted, (open triangles).

### 3.4. Small-angle neutron scattering (SANS)

SANS was carried out to quantify the size-shape of the micelles and to investigate the micellisation process in terms of the coexistence of multiple type of micelles. SANS experiment has been carried out for the single component solutions as well as the mixtures as a function of CTAB mole fraction. The scattering intensity,  $I$ , is measured as a function of the scattering vector  $Q$  according to the equation 3.3.

$$I(Q) = n_p V_p^2 (\Delta \epsilon^2) P(Q) S(Q) + B_{inc} \quad (3.3)$$

where,  $n_p$  is the number of scattering bodies within the sample solution,  $V_p$  is the volume of scattering bodies.  $\Delta \epsilon$  is the scattering contrast,  $P(Q)$  is the form factor,  $S(Q)$  is the structure factor and  $B_{inc}$  is the incoherent background.

#### 3.4.1. Model used to fit the data

Equation 3.4 gives the intensity of scattered radiation,  $I(Q)$ , as a function of the wave-vector,  $Q$ .

$$I_{sur.}(Q) = n [S(Q) \langle |F(Q)|^2 \rangle + \langle |F(Q)|^2 \rangle - \langle |F(Q)|^2 \rangle] + B_{inc} \quad (3.4)$$

$S(Q)$  represents the spatial arrangement of the micelles in solution and  $n$  is the micelle number density. In the case of core-shell morphology  $F(Q)$  is represented by equation 3.5.

$$F(Q) = V_1(\rho_1 - \rho_2)F_0(QR_1) + V_2(\rho_2 - \rho_0)F_0(QR_2) \quad (3.5)$$

The subscript 1 represents the scattering from the core and the subscript 2 is for the polar shell  $V_i = \frac{4}{3}\pi R_i^3$  and  $F_0(QR) = \frac{3j_1(QR)}{QR}$  ( $j_i$  is the first-order spherical Bessel function), so,  $\rho_i$  is the neutron scattering length density of the micellar core (subscript 1), the polar shell (subscript 2) and the solvent (subscript 0),

Constants are combined into a single fittable parameter used to “scale” the model intensity to the absolute value. Post-fitting, this scalar is recalculated using the parameters describing the micelle morphology/composition and the molar concentration of micelles to validate the fit. The calculated and observed values should lie within ~10%.

For both surfactants, a charged particle with an elliptical core-shell morphology is the adopted model of the micelle. The average volume per headgroup, average tail volume

and their average scattering length densities are input as constants. These were calculated assuming the composition of the micelle is the same as the solution composition.

#### 3.4.1.1. CTAB parameters

For the head group,  $\rho_{CTAB\ head} = 2.4 \times 10^{-6} \text{ \AA}^{-2}$  and the volume is  $412 \text{ \AA}^3$ . The bromide ion dissociation in the CTAB significantly affect the charge on the micelle and hence the structure factor  $S(Q)$ . For the tail, the average core scattering length density is  $\rho_{CTAB\ tail} = -0.4 \times 10^{-6} \text{ \AA}^{-2}$  and the volume is  $460 \text{ \AA}^3$ .

#### 3.4.1.2. FSN-100 parameters

For the head group,  $\rho_{FSN\ head} = 0.6 \times 10^{-6} \text{ \AA}^{-2}$  and the volume is  $2000 \text{ \AA}^3$ . For the tail, the average core scattering length density is calculated  $\rho_{FSN\ tail} = 2.0 \times 10^{-6} \text{ \AA}^{-2}$  and the volume is  $295 \text{ \AA}^3$ .

In both cases, the structure factor  $S(Q)$  was calculated using the Hayter and Penfold model [5] for spheres of a given micellar concentration, charge and ionic strength, incorporating refinements for low volume fractions and a penetrating ionic background. Various approaches to parameterising the structure factor were adopted based on known or measured estimates of the micelle size and surfactant concentration to calculate the hard sphere volume fraction, charge and Debye length. This method of calculating the structure factor, which assumes spherical particles, remains valid for dilute, isotropic samples of micelles with small degrees of Ellipticity, as same as the case here [6].

The headgroup region, the shell comprising the various headgroups and associated water do not affect the SANS data fitting. The shell scattering length density is calculated from the average headgroup scattering length density and their hydration using equation 3.6.

$$\bar{\rho} = \phi_{water} \rho_{water} + (1 - \phi_{water}) \bar{\rho}_{headgroups} \quad (3.6)$$

Since  $\phi_{water} = \frac{V_{water}}{V_{shell}}$ ,  $V_{water}$  and  $V_{shell}$  parameters are strongly coupled and not amenable to fitting. From EPR calculations (next section (3.5)), the approach of fixing  $\phi_{water}$  value has been adopted and to define the shell volume (thickness). The scattering length density of the hydrated shell region is then (re-)calculated within the analysis software, based on  $\phi_{water}$ , so, that helps to eliminate the trial-and-error aspects which



have been required in previous work to find the overall “best fit” value of  $\phi_{water}$  due to local minima in the least-squares fits [5].

### 3.4.2. Surfactant solutions

Considering the fit for the single component surfactant solutions, the data have been fitted to a model describing the micelle morphology as globular, with a varying degree of ionic character. In both surfactant fittings, constants have been applied to the analysis. Specifically, the known chemical structure, concentration molar volumes, dimensions and scattering length densities, also, the known concentrations and the experimental values of the degree of hydration from EPR (section 3.5) (table 3.3). The ellipticity, the charge and the incoherent background are the only fitting parameters that have not been varied. Figures 3.8 and 3.9 show the scattering curves with the fitting of CTAB and FSN-100 solutions respectively, and the fitting parameters for both surfactants are compared to those from mixtures in the next section, table 3.2.

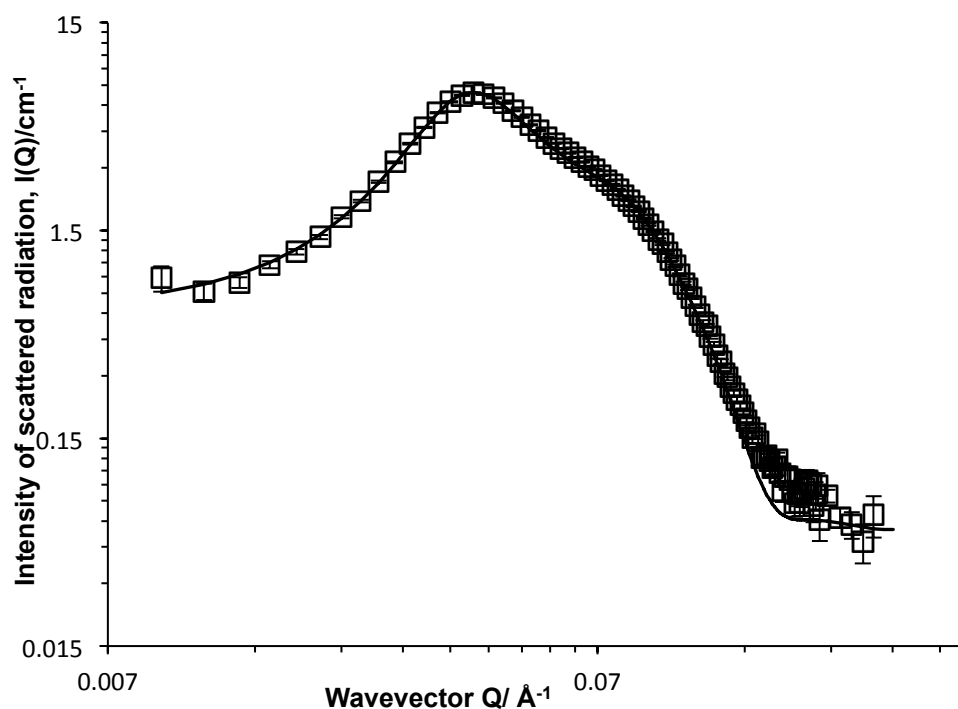


**Figure 3.8** Small angle neutron scattering of 50mM CTAB aqueous solution (open squares) with fit (solid line).

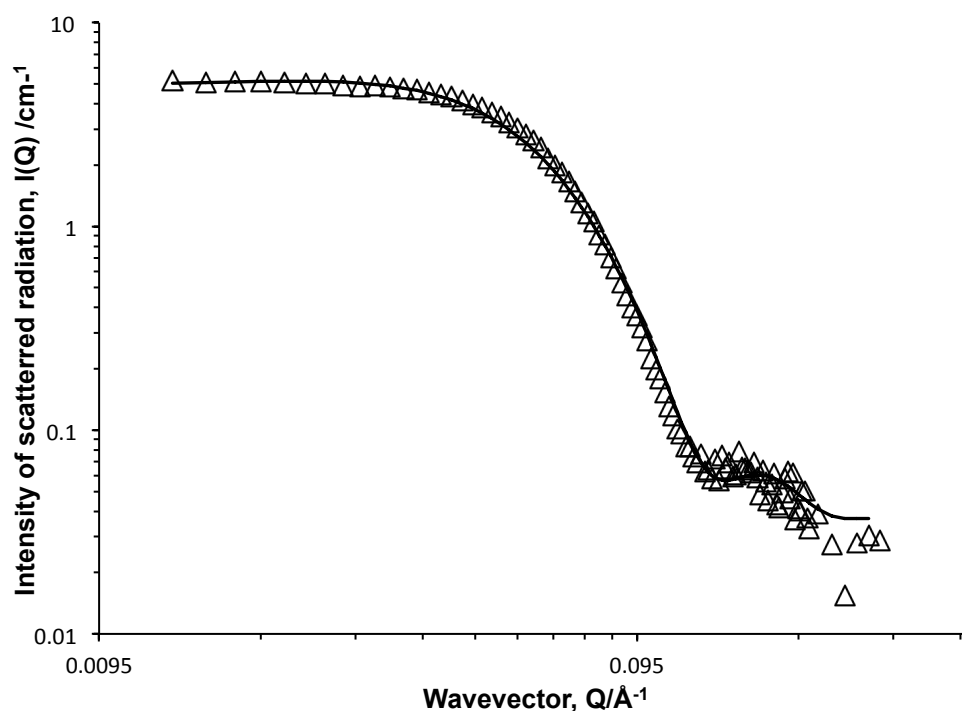


**Figure 3.9** Small angle neutron scattering of 50mM FSN-100 aqueous solution (open triangles) with fit (solid line).

### 3.4.3. Surfactant mixture solutions

SANS measurements were performed on a single component CTAB and FSN-100 as well as selected CTAB/FSN-100 mixtures at specific CTAB mole fractions, in order to detect micelle shape and size corresponding to the features in the CMC plot.

Figures from 3.10 to 3.13 show the SANS curves for each mixture solution. In figure 3.14, SANS data for the single components have been compared to the four studied mixtures. The scattering curves are a composite of the form factor describing the size and the shape, and the structure factor describing the electrostatic interaction between micelles.

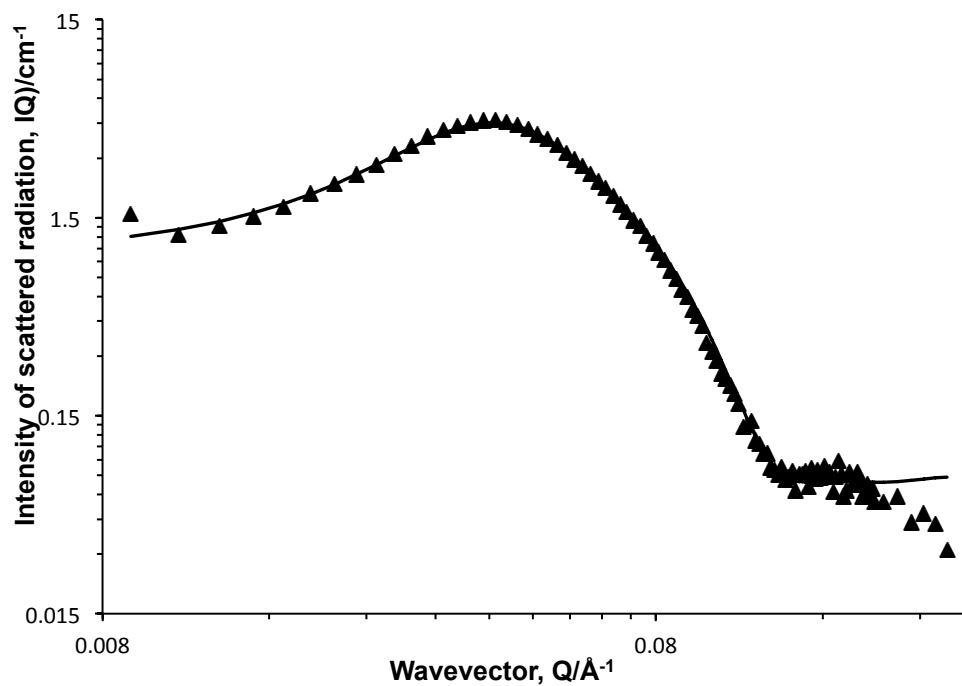


Figure 3.10 Small angle neutron scattering of 50mM of 0.2 CTAB mole fraction aqueous solution (closed triangles) with fit (solid line).

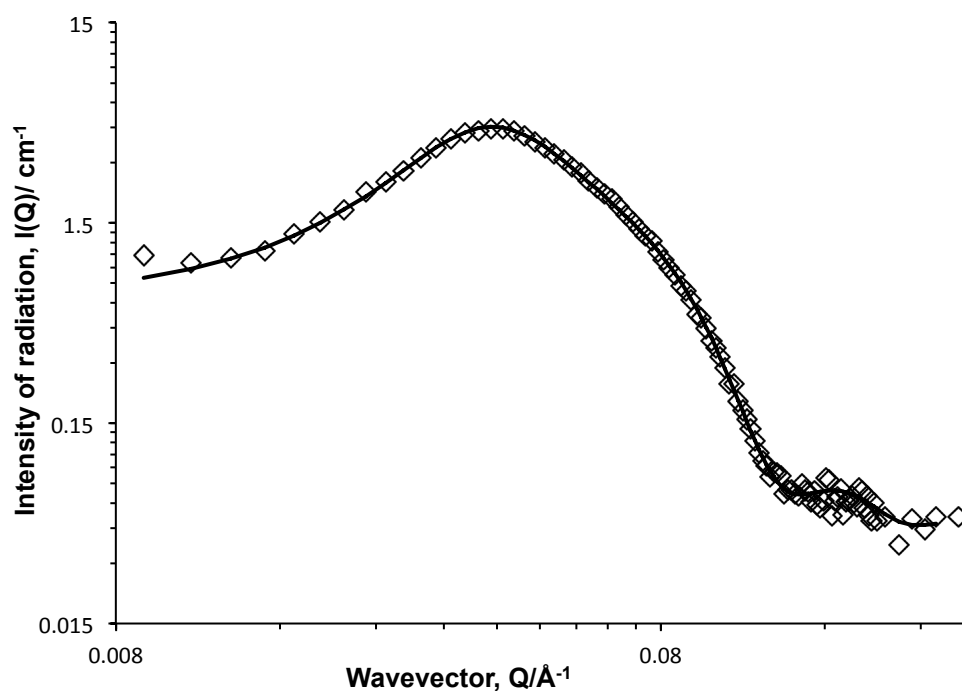


Figure 3.11 Small angle neutron scattering of 50mM of 0.4 CTAB mole fraction aqueous solution (closed squares) with fit (solid line).

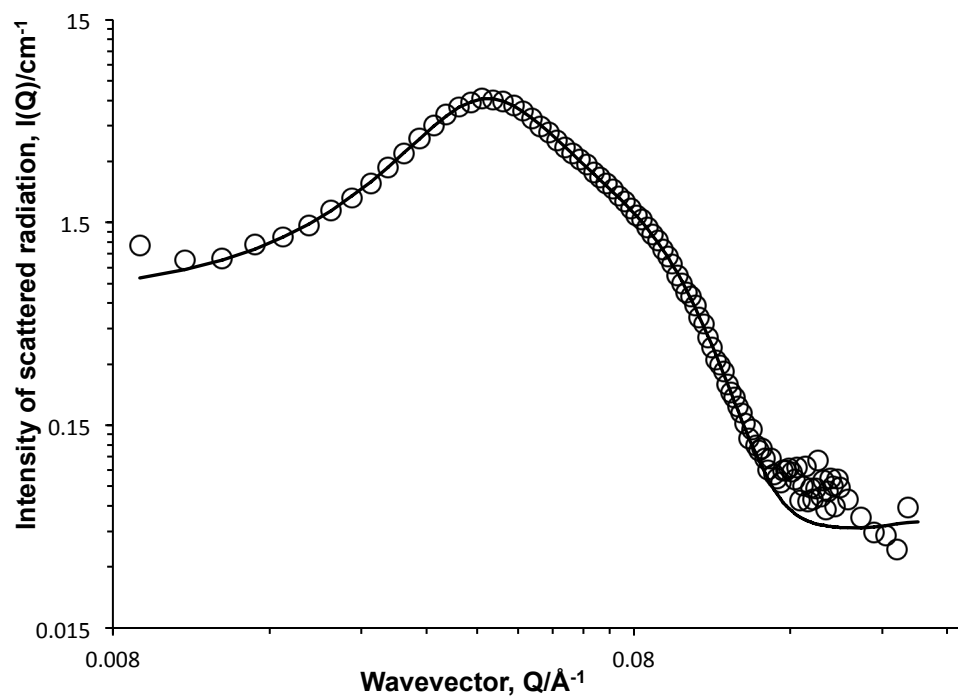


Figure 3.12 Small angle neutron scattering of 50mM of 0.6 CTAB mole fraction aqueous solution (open circles) with fit (solid line).

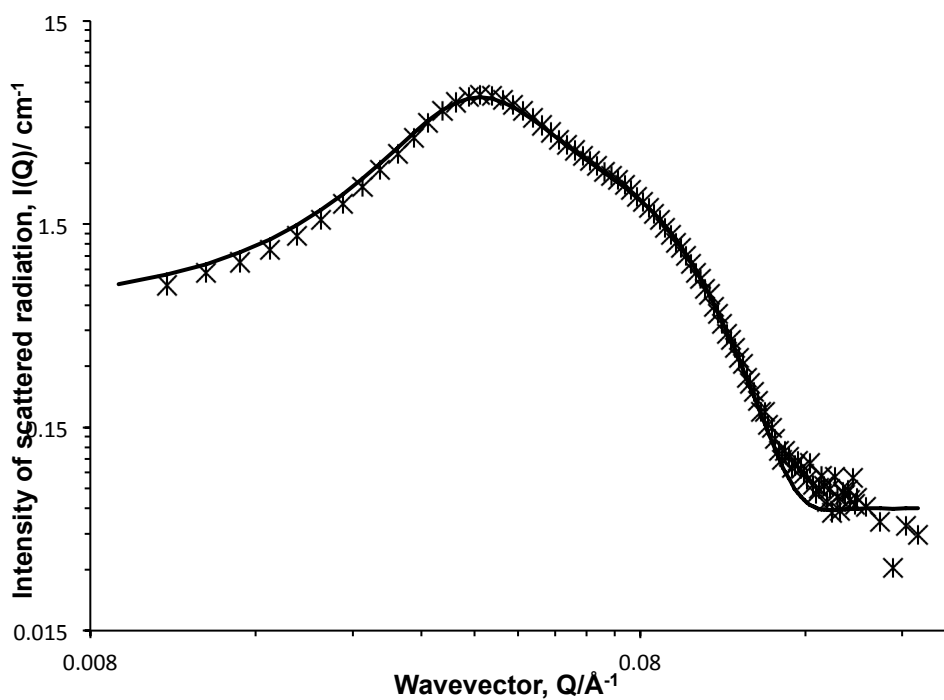
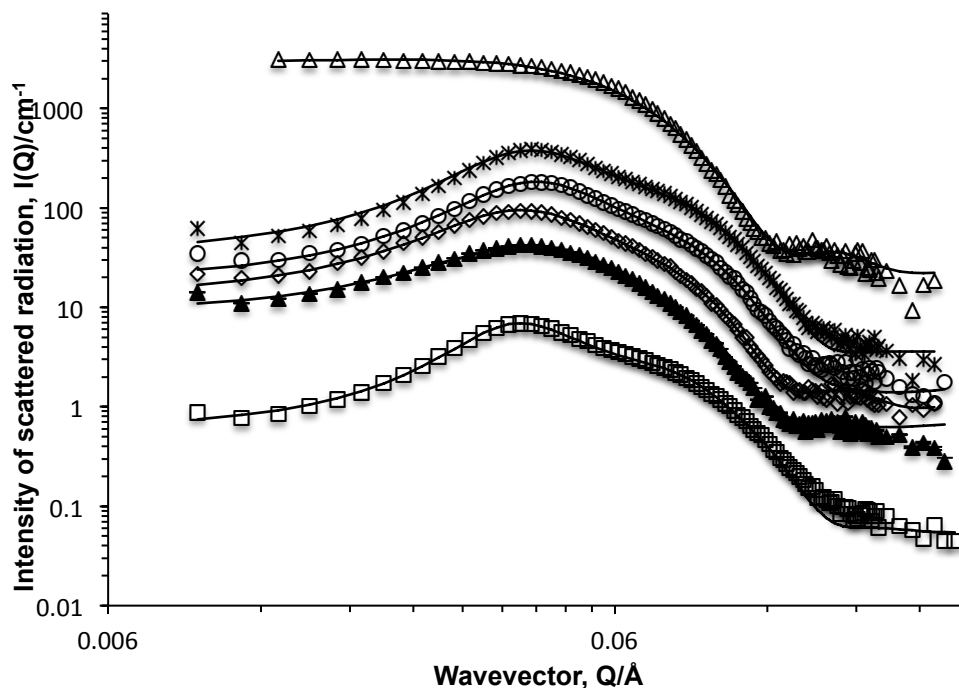


Figure 3.13 Small angle neutron scattering of 50mM of 0.8 CTAB mole fraction aqueous solution (star) with fit (solid line).



**Figure 3.14** Small angle neutron scattering as a function of CTAB mole fraction, (open square)  $\alpha_{\text{CTAB}}=1$ , (open triangle)  $\alpha_{\text{CTAB}}=0$ , (closed triangle)  $\alpha_{\text{CTAB}}=0.2$ , (open diamond)  $\alpha_{\text{CTAB}}=0.4$ , (open circle)  $\alpha_{\text{CTAB}}=0.6$ , (star)  $\alpha_{\text{CTAB}}=0.8$ . Fits are included as solid line. Data are offset by a factor of 3 for clarity.

Ionic surfactant micelles have an oscillatory structure factor in the scattering curve, which is responsible for reduction in intensity at low  $Q$  and “bumps” at higher  $Q$ . However, the scattering from non-ionic micelles does not have these features. This concept clearly occurs for many of the overall features in the data, particularly, the most obvious difference in the curve from FSN-100 compared with all other mixtures. Therefore, once CTAB is added to the solution, the micelles show less variance in structure. As predicted, the scattering intensity decreases at low  $Q$  as the CTAB mole fraction increases, with shoulders around  $Q=0.06 \text{ \AA}^{-1}$  becoming more pronounced. Fitting parameters for the pure surfactants and the mixtures are listed in table 3.2.

CTAB mole fraction	$R_{Core}$ /Å	Shell thickness ( $\pm 5$ ) / Å	Ellipticity, $X$	$V_{s(dry)}/V_{Core}$	$N_{agg.}$ ( $\pm 10$ )
0	13.2	23	1.5	0.8	51
0.2	27.8	12	1.1	0.9	310
0.4	27.8	11	1.0	0.9	250
0.6	26.2	10	1.0	0.9	190
0.8	21.6	10	1.1	1.0	140
1.0	25.7	8	0.85	0.9	135

**Table 3.2 Parameters describing the fits of SANS data from CTAB, FSN-100, 0.2, 0.4, 0.6, 0.8 CTAB mole fraction solutions using a model that describes the micelle as a globular elliptical with some ionic character.**

Table 3.2 describes the fit for the single components and the mixtures parameters. Obviously, the mixtures are strongly characterised by the ionic CTAB component. The aggregation numbers have been calculated via equation (3.7), the ratio of the core volume divided by a simple weighted value of the effective tail volume, this assumes that the micelle composition is identical to the solution one. In addition, the aggregation number of FSN-100 micelles is smaller than the literature value [ $N_{agg}=102$ ] [3]], whereas CTAB micelle aggregation number is in a good agreement with the literature one considering the same concentration [7].

$$N_{agg.} = \frac{V_{core}}{V_{tail}} = \frac{\frac{4}{3}\pi R_{core}^3 X}{\alpha_{CTAB} V_{CTAB}^{tail} + (1-\alpha)_{CTAB} V_{FSN-100}^{tail}} \quad (3.7)$$

where,  $N_{agg.}$  is the aggregation number,  $X$  is the ellipticity,  $R_{Core}$  is the core radius,  $V_{tail}$  is the surfactant tail volume,  $V_{Core}$  is the surfactant core volume.

### 3.5. Electron paramagnetic resonance spectroscopy (EPR)

Electron paramagnetic resonance (EPR) spectroscopy has been used to study the hyperfine coupling constant and rotational correlation times of the spin probe, 16-doxyl-stearic acid methyl ester (16-DSE) solubilized in hydrocarbon surfactant aqueous solution (CTAB), fluorocarbon surfactant aqueous solution (FSN-100), and a range of compositions of hydrocarbon/fluorocarbon surfactant mixtures (HC/CF) as a function of CTAB mole fraction. The data in this experiment were also conducted at two different total surfactant concentrations (20 mM and 50 mM) to assess whether the micelle structure undergoes a significant change with the total concentration.

#### 3.5.1. The choice of spin-probe

The EPR technique introduces a very small amount ( $2 \times 10^{-4}$  M) of nitroxide free radical as a spin probe (in this case, 16-DSE) into the micelle and by measuring the hyperfine coupling constant and rotational correlation times of the probe, the micelle structure can be estimated. These particles have limited solubility in water, so associate closely with the micelles of any charge. Micelles also can accommodate a small number of these particles and no EPR signal is detected from the probe containing surfactant solutions below the critical micelle concentration (CMC). The structure of the spin probe 16-DSE has been shown previously in Chapter Two, section 2.5.6.1.

#### 3.5.2. Hyperfine coupling constant

The hyperfine coupling constant is affected by several factors, which contribute the behaviour of this parameter. These factors include the nature of the micelle headgroup and the replacement of some water molecules, which were in contact with the outer regions of the micelle core adsorbed by the surfactant [6, 8].

In order to limit the analysis of the scattering from the mixtures, EPR was used in SANS data analysis to quantify the hydration of the micelle headgroup region by measuring the hyperfine coupling constant ( $A^+$ ) as a function of polarity index  $H$  (25 °C) defined as the molar ratio of OH groups in a given volume relative to water. Thus, the polarity index corresponds to the volume fraction of water in the polar shell,  $\phi_{water}$ , (hydration) and may be used to constrain the SANS fitting. The volume fraction of the solvent in the headgroup region (hydration) has been estimated using equation 3.8.

$$H (25^\circ\text{C}) = (A^+ - 14.21) / 1.52 \quad (3.8)$$

The hyperfine coupling constant from the two different measurements (20 mM & 50 mM) are plotted versus CTAB mole fraction in figure (3.15). It is obvious that there is a greater degree of water (52%) associated with the FSN-100 headgroup, presumably because of the larger headgroup providing a greater volume for water penetration. The CTAB is a smaller, spherical structure and the predicted value for  $\phi_{H_2O}$  at 50 mM would be calculated from equation (3.9) is  $0.30 \text{ \AA}^3$  and it is in a fair agreement with the experimental value (0.32) (table 3.3). In this equation SANS fitted parameters have been used. Calculation of the estimate for FSN-100 ( $\phi_{H_2O}^{FSN-100}$ ) is less precise due to the uncertainty in the headgroup structure, but again the calculated value (0.53) is in a good agreement with the experimental one (0.52). Table 3.3 also includes the experimental data of water volume fraction in the headgroup region for all mixtures calculated from the hyperfine coupling constants and using equation 3.9.

$$\phi_{H_2O} = \frac{V_{\text{shell}} - V_{\text{headgroups}}}{V_{\text{shell}}} = \frac{\left(\frac{4}{3}\pi (R + \sigma)^3 X - \frac{4}{3}\pi R^3 X\right) - N_{agg} \cdot V_{CTAB}}{\left(\frac{4}{3}\pi (R + \sigma)^3 X - \frac{4}{3}\pi R^3 X\right)} \quad (3.9)$$

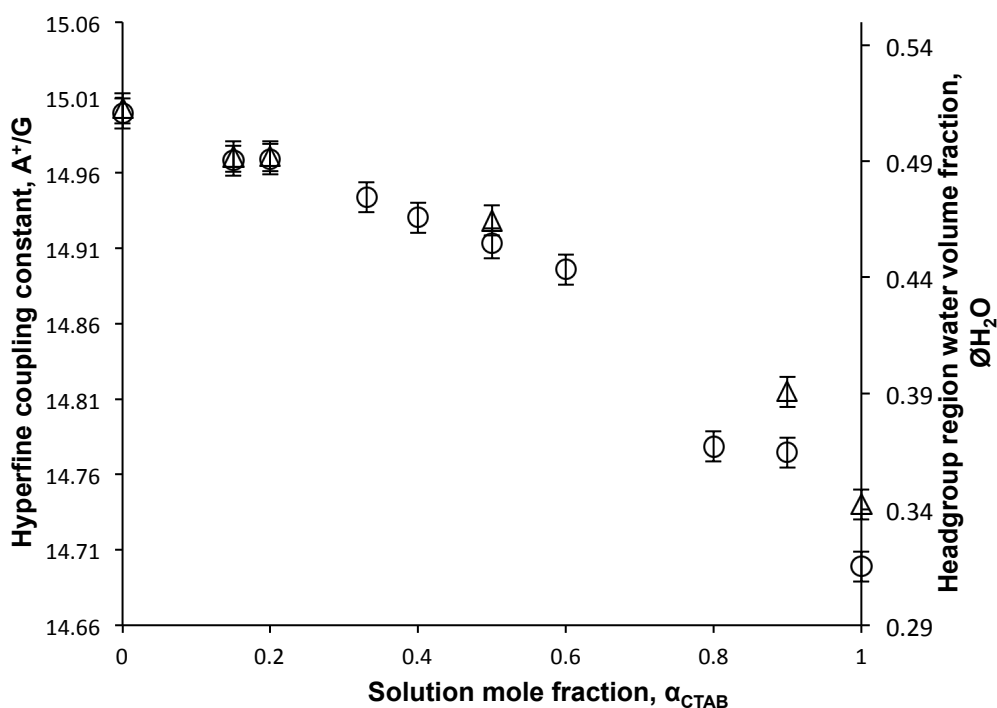


**Figure 3.15** Hyperfine coupling constant of CTAB/FSN-100 mixtures, as a function of CTAB solution mole fraction at a total surfactant concentration of 20 mM (open triangles) and 50 mM (open circles). The corresponding volume fraction of water in the headgroup region is indicated on the secondary axis.



From figure 3.15, the hyperfine coupling constant ( $A_o$ ) decreases with increasing the CTAB mole fraction in both measurements due to the decrease in water molecules around the hydrophobic core of the micelles so the micellar surface will be less polar.

$\alpha_{\text{CTAB}}$	$\alpha_{\text{FSN-100}}$	Exp. $\phi_{\text{H}_2\text{O}}^{\text{shell}}$	Exp. $\phi_{\text{H}_2\text{O}}^{\text{shell}}$
		50 mM/ ( $\pm 0.2$ )	20 mM/ ( $\pm 0.2$ )
0	1	0.52	0.52
0.15	0.85	0.50	0.50
0.2	0.8	0.50	0.50
0.33	0.67	0.48	-
0.4	0.6	0.47	-
0.5	0.5	0.46	0.47
0.6	0.4	0.45	-
0.8	0.2	0.37	-
0.9	0.1	0.37	0.40
1	0	0.32	0.35

**Table 3.3 Experimental values for volume fraction of water in the polar shell ( $\phi_{\text{H}_2\text{O}}$ ) using EPR, in the single surfactant solutions and mixtures at two different total surfactant concentration.**

### 3.5.3. Rotational correlation time

The EPR experiment provides an additional characterisation of the micelle via the rotational correlation time ( $\tau_c$ ), which is a measure of the dynamics with the micelle and the micelle tumbling itself and indicates the time taken for the probe to rotate through an angle one radian around its axis [6]. Determining the rotational correlation time from EPR analysis assesses the mobility of the spin probe inside surfactant micelles. Figure 3.16, shows the rotational correlation times for 16-DSE solubilized in CTAB micelles, FSN-100 micelles and in a range of compositions in terms of CTAB mole fraction at the two different total concentration.

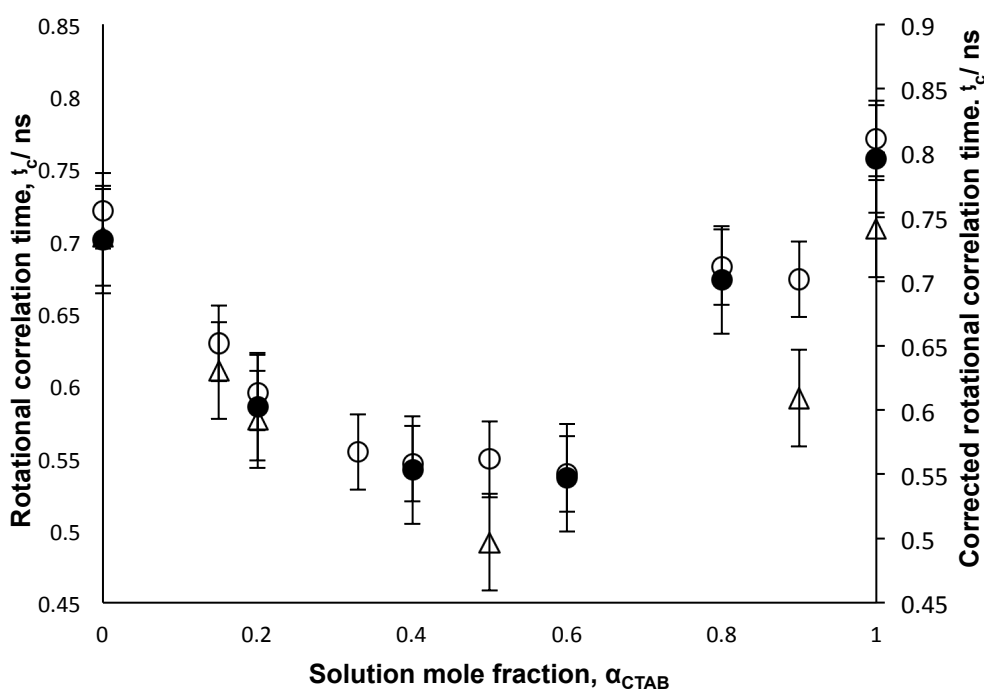


**Figure 3.16** Rotational correlation time of 16-DSE in CTAB/FSN-100 mixtures, as a function of CTAB solution mole fraction at a total surfactant concentration of 20 mM (open triangles) and 50 mM (open circles). The rotational correlation time corrected using SANS data are over-plotted (closed circles).

The two single component micelles have a similar microviscosity and there is a pronounced minimum in  $\tau_c$  across the entire mole fraction range, consistent with a decrease in local viscosity experienced by the probe. At low CTAB mole fractions up to 0.5 the rotational correlation times decrease as the mobility of the spin probe can rotate easily and spin faster. Less viscos system also is presented once CTAB mole fraction reaching the mole fraction of 0.5, after the point of 0.5, the rotational correlation times and viscosity increase with increasing CTAB mole fraction.

As a usual procedure in the rotational correlation time studies, the separation of the dynamics of the spin probe within the micelle  $\tau_{Relative}$  to that of the micelle itself  $\tau_{micelle}$  is required in order to comment on the microviscosity of the headgroup region. In the concentration of 50 mM, the estimation of the size using SANS data has been used to obtain  $\tau_{micelle}$  to arrive at  $\tau_{Relative}$ , which is over-plotted in figure 3.16, for selected data points, [9]. Clearly, as expected, the  $\tau$  correction has little impact on the appearance and the pronounced minimum in microviscosity as a function of CTAB mole fraction is still obvious.

Moreover, the microviscosity does not show any obvious dependence of  $N_{agg.}$  as curvature being largely defined by the numbers and bulkiness of the headgroups and the degree of hydration. It is also obvious that there is an opposite influence of the smaller TAB headgroup and the bulky but hydrated ethylene oxide headgroup of FSN-100.

### 3.6. PGSE- NMR spectroscopy studies

As a complementary approach, pulsed gradient spin-echo nuclear magnetic resonance (PGSE-NMR) spectroscopy was employed to provide more information about micelle structures.

PGSE-NMR spectroscopy has been used to measure the self-diffusion coefficient of the single component of CTAB and FSN-100 aqueous solutions and mixtures of both surfactants as a function of CTAB mole fraction. The measured self-diffusion coefficient is a weighted value of the non-micellised and micellised components. Basically, if a coexisting micelle population were present, coupled with varying levels of non-micellised surfactant, the diffusion coefficient of the CTAB and FSN-100 should be quite different. However, Figure 3.17 shows similar diffusion coefficient values for both surfactants, and that again, consistent with the SANS conclusion that these two surfactants mix, further, the diffusion coefficient values are mutually comparable consistent with the relative volumes of the respective micelles, which have been calculated using SANS data ( $V_{micelle} = \frac{4}{3} \pi R_m^3$ ,  $V_{micelle}$  were calculated from known volumes of constituent groups of CH<sub>2</sub>, CO, .....

$$R = (V_{CTAB})^{1/3} = (1.4 \times 10^5 \text{ \AA}^3)^{1/3} \sim 32 \text{ \AA}$$

$$R = (V_{FSN-100})^{1/3} = (2.4 \times 10^5 \text{ \AA}^3)^{1/3} \sim 39 \text{ \AA}$$

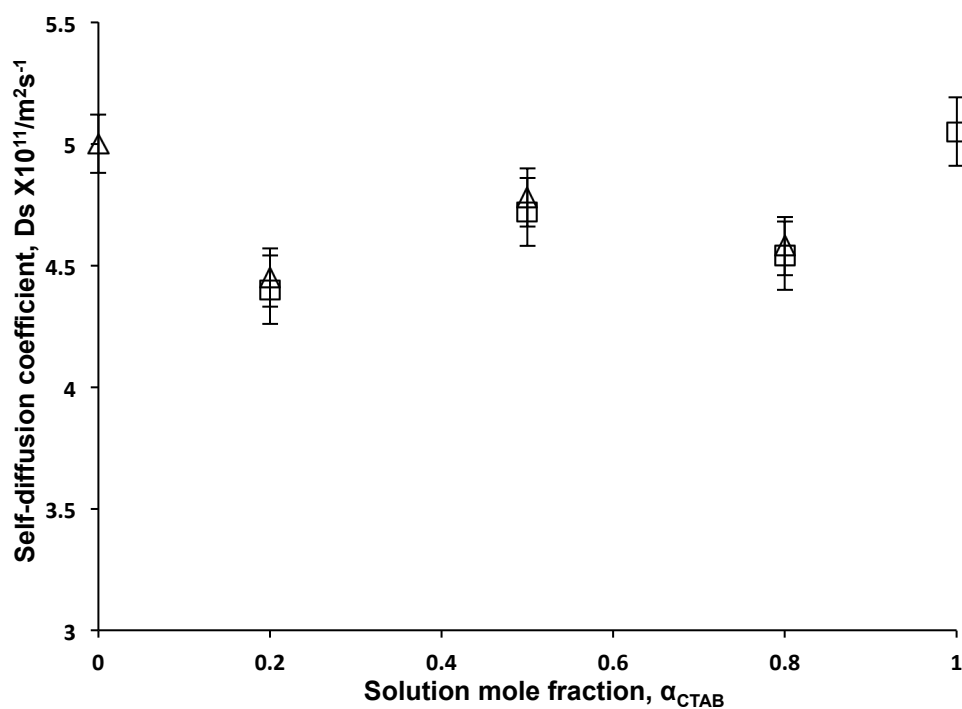


Figure 3.17 Self-diffusion coefficients as a function of CTAB mole fraction, (open squares)  $\alpha_{\text{CTAB}} = 1$ , (open triangles)  $\alpha_{\text{CTAB}} = 0$ .

### 3.7. $^1\text{H}$ -NMR

NMR spectroscopy provides an efficient tool for studying micelle formation and mixing of various surfactants. In this part of the project, micelles in the hydrocarbon/fluorocarbon surfactant mixtures as well as in the single component solutions have been studied.  $^1\text{H}$ -NMR spectroscopy has been measured for 50 mM CTAB aqueous solution, 50 mM FSN-100 aqueous solution and the mixture of both surfactants at the ratio of 1:1. The concentrations are selected to be above the CMC of each surfactant in order to confirm the presence of micelles in all solutions.

#### 3.7.1. 50 mM CTAB solution

Figure 3.18 shows the  $^1\text{H}$ -NMR spectrum of 50 mM CTAB solution. Signals from the main hydrophobic chain protons, terminal methylene group and methylene group from attached to head group nitrogen can be identified. For instance, it is clear that  $\text{CH}_3$  is at a chemical shift of 0.75 ppm and signals from protons around nitrogen are at a chemical shift of 3.06 ppm.

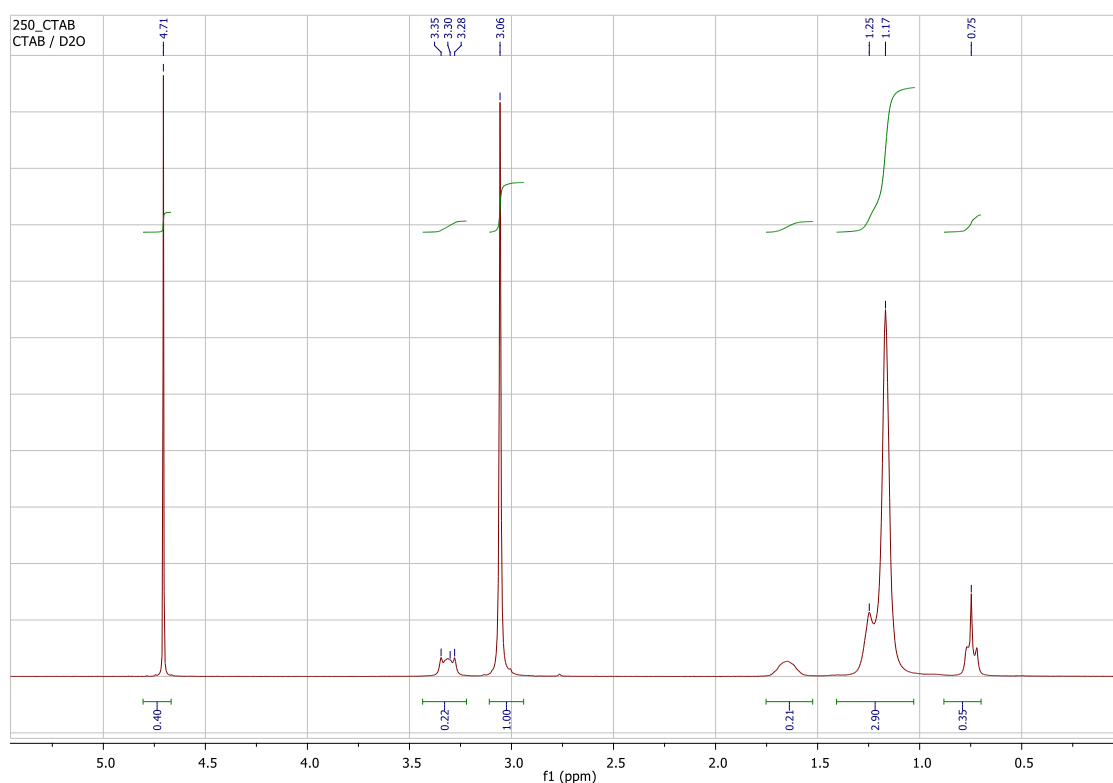


Figure 3.18  $^1\text{H}$  High resolution-NMR data from 50 mM of CTAB in  $\text{D}_2\text{O}$ .

### 3.7.2. 50 mM FSN-100 solution

Figure 3.19 shows the  $^1\text{H}$ -NMR spectrum of the solution 50 mM FSN-100. Two signals from hydrophobic chain protons and hydroxyl group at 3.54 ppm and 2.23 ppm are observed respectively.

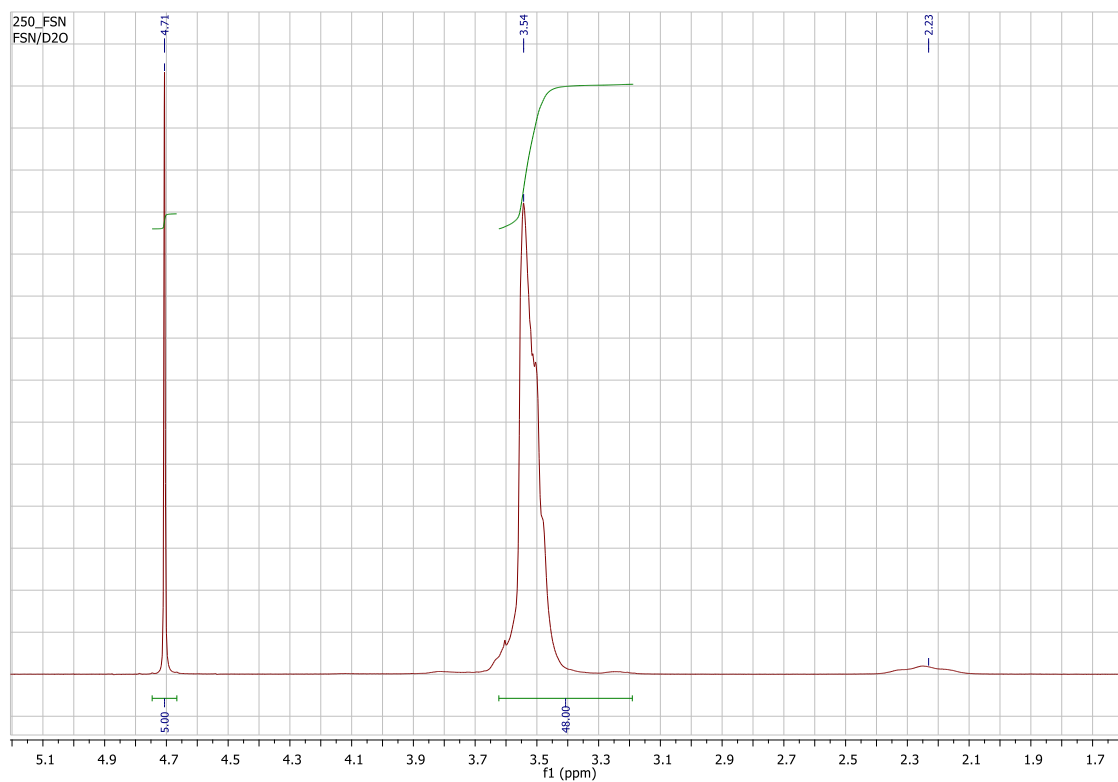
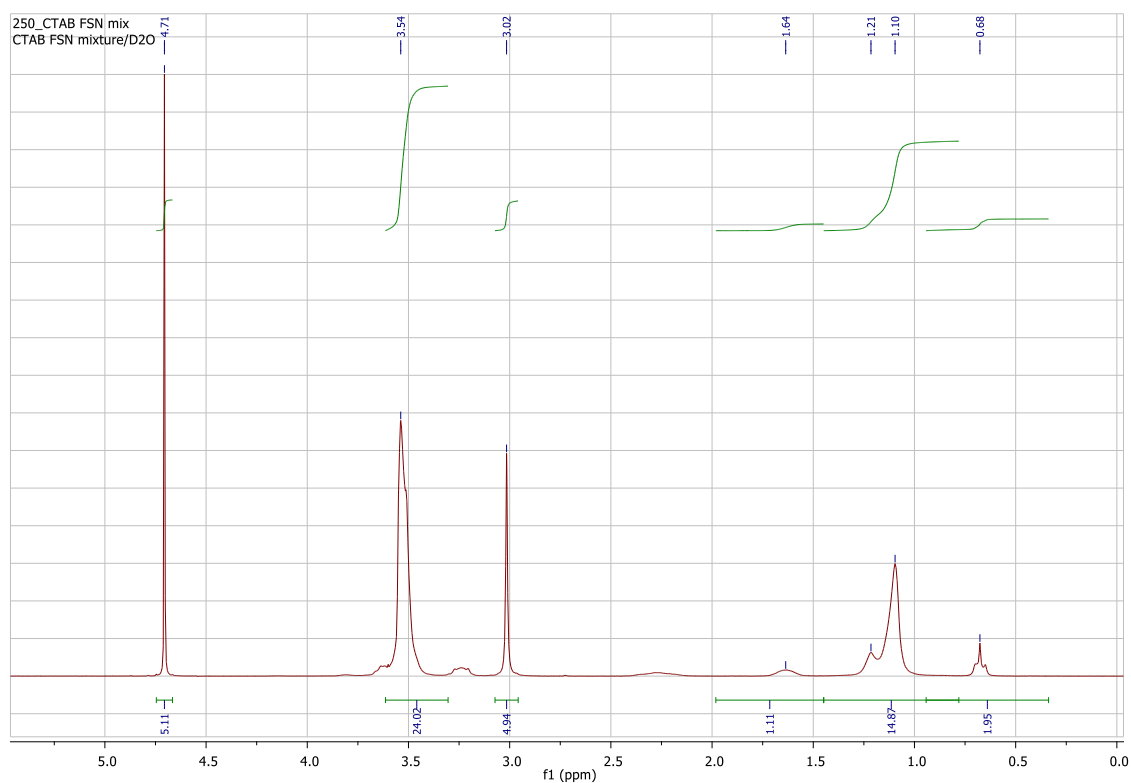


Figure 3.19  $^1\text{H}$  High resolution-NMR data from 50 mM of FSN-100 in  $\text{D}_2\text{O}$ .

### 3.7.3. CTAB/FSN-100 (50 mM, 50 mM) mixture solution

In figure 3.20, the presence of both surfactant micelles are confirmed from proton chemical shifts related to both surfactants. It is one phase mixture and from the intensities of peaks at 0.75 ppm CH<sub>3</sub> in CTAB spectrum and 3.54 ppm CH<sub>2</sub> in FSN-100 spectrum (0.18 CTAB becomes 0.09 in the mixture) (0.30 FSN becomes 0.18 in the mixture).



**Figure 3.20** <sup>1</sup>H High resolution-NMR data from the mixture of CTAB and FSN-100 in D<sub>2</sub>O.

In the table 3.4, the signal of CH<sub>3</sub> was shifted from 0.75 ppm in CTAB to 0.68 ppm in the mixture, which may indicate that there is a degree of mixing between the two surfactants.

Surfactant solution	Signals	Single component sol. Chemical shift/ (ppm)	Mixture chemical shift/ (ppm)
CTAB	CH <sub>3</sub>	0.75	0.68
FSN-100	(CH <sub>2</sub> ) O	3.54	3.54

**Table 3.4 Chemical shifts of CH<sub>3</sub> (CTAB) and CH<sub>2</sub> (FSN-100) signals in the single surfactant solution and the mixture.**



### 3.8. $^{19}\text{F}$ -NMR

In order to study the system of fluorinated surfactant FSN-100 and its mixture with the hydrocarbon surfactant CTAB,  $^{19}\text{F}$ -NMR spectroscopy is required. The measurement was performed for the solutions of 50 mM FSN-100 and the mixture with CTAB. From a previous study [3], the  $^{19}\text{F}$ -NMR spectrum of FSN-100 in  $\text{D}_2\text{O}$  was observed in the region from -116 to -112 ppm.

#### 3.8.1. 50 mM FSN-100 and FSN-100/CTAB mixture

From figure 3.21, six signals from 7  $\text{CF}_2$  and the terminal  $\text{CF}_3$  group were observed. One of the environment sensitive  $\text{CF}_2$  signals appears at 114.15 ppm for the solution. This signal are at the same chemical shift in the case of the mixture (figure 3.22). As CTAB has no fluorine, it cannot be shown by  $^{19}\text{F}$ -NMR.

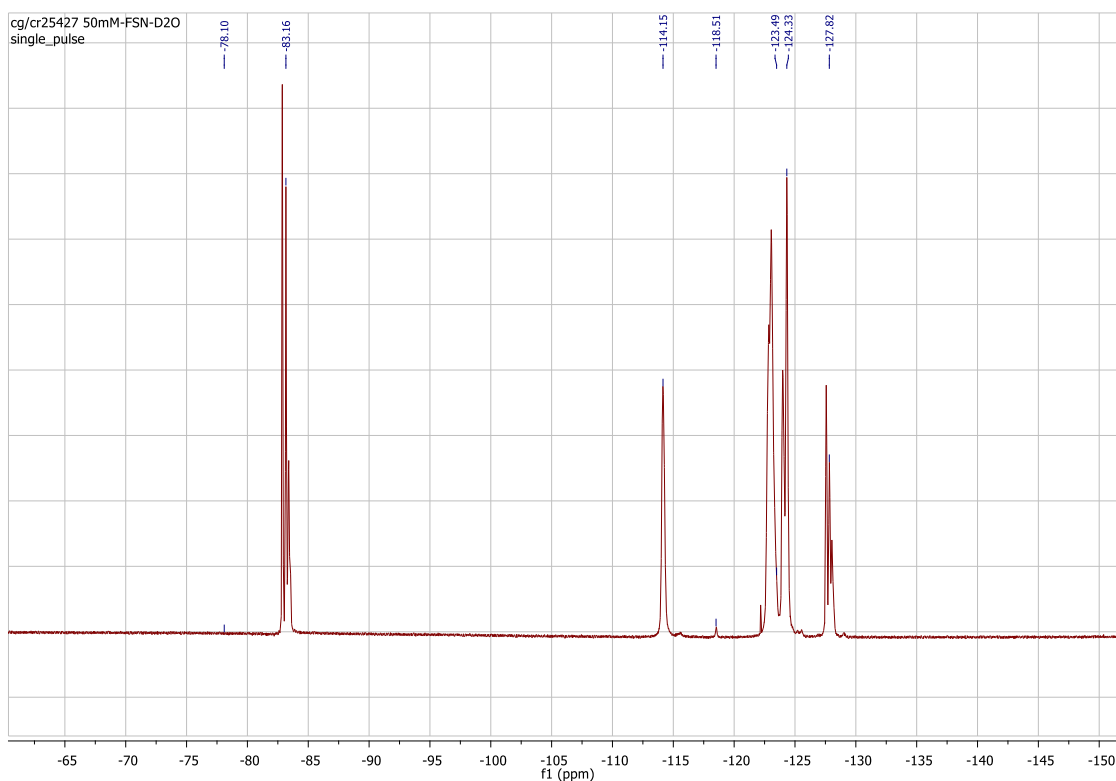
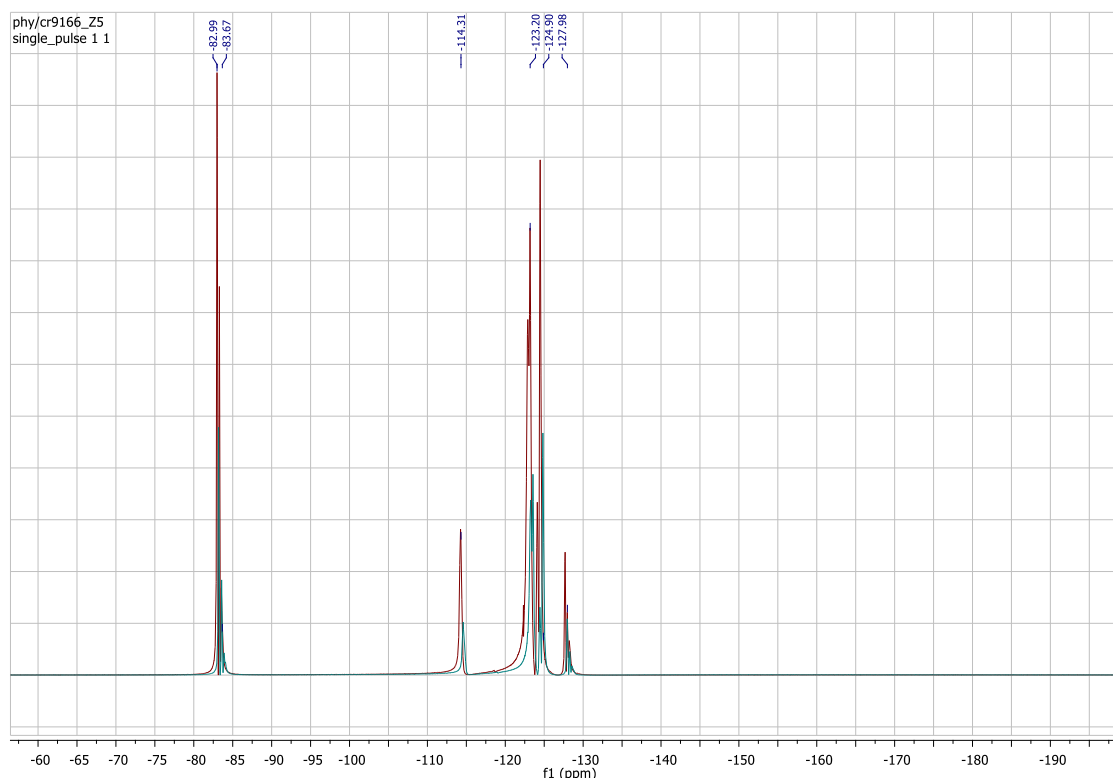


Figure 3.21  $^{19}\text{F}$  High resolution-NMR data from 50 mM of FSN-100 in  $\text{D}_2\text{O}$ .



**Figure 3.22**  $^{19}\text{F}$  High resolution-NMR data from 50 mM of FSN-100 in  $\text{D}_2\text{O}$  (red) and the mixture of CTAB and FSN-100 in  $\text{D}_2\text{O}$  (blue).

From NMR analysis, the structure of each surfactant has been investigated, and the  $^1\text{H}$ -NMR spectrum for the mixture indicates the presence of each surfactant. This confirms the mixing behaviour between CTAB and FSN-100 in the aqueous solutions.

### 3.9. Conclusions

Mixed micelles of the cationic surfactant CTAB and the non-ionic surfactant FSN-100 have been studied by various techniques. The data show that the two surfactants mix nonideally with CMCs higher than predicted for the ideal mixing except some concentrations ( $0.5 > \alpha_{\text{CTAB}} > 0.7$ ), which show a degree of ideality. The mixing between the two surfactants has been confirmed using the NMR technique. This behaviour ensures that there is a substantially different micellization process along a range of compositions and that depends on how the micellization process is dominated by which surfactant. It is clearly that from SANS data the mixtures are strongly characterised by the CTAB component, and micelles are less variable in structure when different amounts of CTAB were added to the solution. With increasing the CTAB mole fraction a reduction in the amount of water presented in the head group region, as smaller CTAB micelles being more characterized in the mixture, so less polar system is presenting as CTAB mole fraction is increased. To conclude, the combination of data

from all mentioned techniques can present a more detailed picture of the CTAB/FSN-100 mixed micelle system, which provides information that would not be extracted from any technique alone.

### 3.10. References

1. Aguiar, J., et al., *On the determination of the critical micelle concentration by the pyrene 1 : 3 ratio method*. Journal of Colloid and Interface Science, 2003. **258**(1): p. 116-122.
2. Szymczyk, K., *Behaviour of the fluorocarbon surfactants in the monolayer at the water-air interface and in the bulk phase*. Journal of Fluorine Chemistry, 2013. **150**: p. 109-116.
3. Skvarla, J., et al., *Micellization of Zonyl FSN-100 fluorosurfactant in aqueous solutions*. Colloids and Surfaces a-Physicochemical and Engineering Aspects, 2014. **443**: p. 209-215.
4. Szymczyk, K. and B. Janczuk, *The adsorption at solution-air interface and volumetric properties of mixtures of cationic and nonionic surfactants*. Colloids and Surfaces a-Physicochemical and Engineering Aspects, 2007. **293**(1-3): p. 39-50.
5. Bales, B.L., et al., *Precision relative aggregation number determinations of SDS micelles using a spin probe. A model of micelle surface hydration*. Journal of Physical Chemistry B, 1998. **102**(50): p. 10347-10358.
6. Bales, B.L., *Inhomogeneously Broadened Spin-Label Spectra, In Biological Magnetic Resonance*. Biological Magnetic Resonance 1989. **8**: p. 77.
7. Haldar, J., et al., *Molecular modulation of surfactant aggregation in water: Effect of the incorporation of multiple headgroups on micellar properties*. Angewandte Chemie-International Edition, 2001. **40**(7): p. 1228-+.
8. Bales, B.L. and C. Stenland, *Statistical Distributions and Collision Rates of Additive Molecules in Compartmentalized Liquids Studied by Epr Spectroscopy .1. Sodium Dodecyl-Sulfate Micelles, 5-Doxylstearic Acid Ester, and Cobalt(II)*. Journal of Physical Chemistry, 1993. **97**(13): p. 3418-3433.
9. Bales, B.L., R. Ranganathan, and P.C. Griffiths, *Characterization of mixed micelles of SDS and a sugar-based nonionic surfactant as a variable reaction medium*. Journal of Physical Chemistry B, 2001. **105**(31): p. 7465-7473.

**Chapter Four**  
**The Solution Behaviour of the Oil Swollen**  
**Micelles**

## 4.1. Introduction

It has been shown in Chapter Three that there is a considerable nonideality of mixing in the system of CTAB/FSN mixtures. Due to the well-known nonideality of mixing in such systems, it was hypothesised that this nonideality might be harnessed to permit the preferential solubilisation of specific oils into fluorocarbon or hydrocarbon phases where fluorocarbon or hydrocarbon are involved. Moreover, it is well known that surfactants increase the solubility of hydrophobic organic compounds by partitioning it in the hydrophobic core of the micelles and this behaviour is highly dependent on the surfactant concentration [1].

The hydrocarbon chain in CTAB and fluorocarbon chain in FSN-100 and their interactions have been generally studied in terms of their different specific properties (e.g. the hydrophobicity) [2-5]. It can be concluded that fluorine is more electronegative and has larger size than hydrogen, so stable fluorocarbon chains are more bulky and rigid than hydrocarbon chains [6]. Fluorocarbon surfactants have lower CMCs, stronger ability to reduce the surface tension and higher chemical and thermal stability comparing to hydrocarbon surfactants. Due to their low CMCs, many more micelles can be formed from fluorocarbon surfactants at the same concentration of hydrocarbon surfactants. Thus they are expected to be more suitable for solubilisation of volatile organic compounds compared to hydrocarbon surfactants [7].

On the other hand, ethoxylated nonionic surfactants such as FSN-100 have different solubilisation effect on hydrophobic organic compounds depending on the length of ethoxy chain. The greater ethoxy chain length will decrease the solubilisation on the hydrophobic organic compounds such as hexane [8]. However, there are few studies about the use of fluorocarbon surfactant in the solubilisation of hexane [7]. As a consequence, different phase behaviour is expected from the CTAB and FSN-100 in hexane and perfluorohexane (PFH).

It is also strongly recommended to use a multi-technique approach to characterise surfactant/oil systems as each technique provides different results, which may be compared. Therefore, here is surfactant/oil solutions have been investigated by  $^1\text{H}$ -NMR,  $^{19}\text{F}$ -NMR, small-angle neutron scattering (SANS) and pulsed gradient spin-echo NMR (PGSE-NMR). In order to prepare for these studies, a good point to start with is the visibly determined phase behaviour of surfactant/oil solutions. In this part of the thesis, some findings for the surfactants CTAB and FSN-100 and their mixtures with and without oil will be presented and discussed.

## 4.2. Phase behaviour of surfactant/oil solutions

In principle, CTAB and FSN-100 associate into micelles above the CMC in water and form different phases at higher concentrations. Since all surfactant solutions were prepared at concentrations of 50 mM, which are above the CMC of both surfactants, the surfactant phase behaviour at the molecular level of the aggregates in the system will be discussed. A fixed amount of oil (hexane or PFH) has been added to the single surfactant solution as well as to the surfactant mixtures and then photos for the resulted emulsions have been taken in each case.

### 4.2.1. Surfactant/W/O systems

Figure 4.1 represents 50 mM of CTAB and 50 mM of FSN-100 aqueous solutions before and after the addition of 2 % of hexane. Both surfactants have a good solubility in water at 25 °C as shown in the figure, but once hexane is added to the surfactant solution, the solution splits into two phases. This experiment was repeated over a range of different oil amounts and in all cases the hexane was split to the top of the solution.

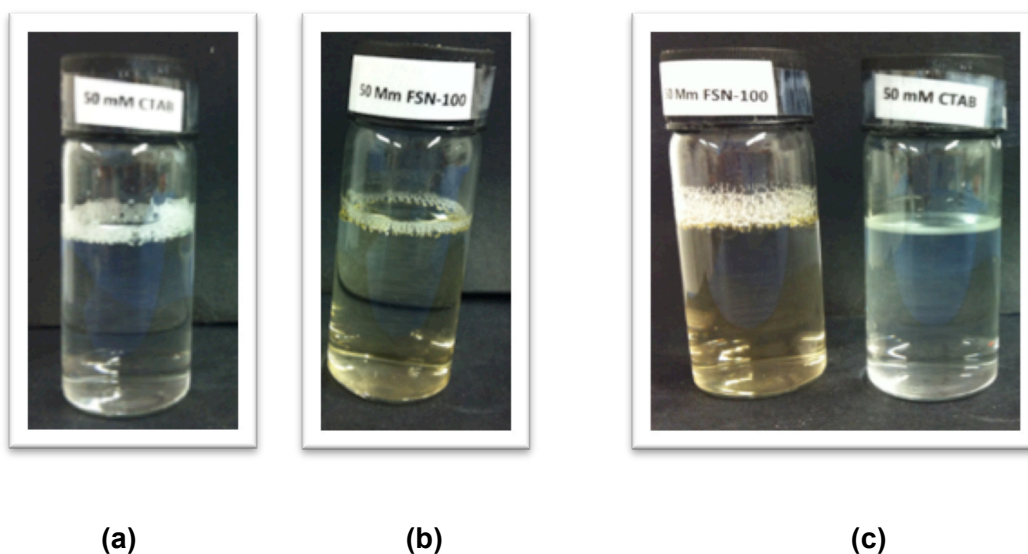


**Figure 4.1** Surfactant aqueous solutions for both CTAB and FSN-100 before (a), (b) and after adding 2 % of hexane (c).

The same procedure has been performed with the PFH and two-phase solutions have been collected but in this case PFH was at the bottom of the vial ( $d = 1.669 \text{ g/ml}$  at 25 °C). Photos of the PFH case have been excluded to avoid repetition.

The question here is how much of the 2 % hexane or PFH goes into the aqueous phase, existing in the micelles of each surfactant. In order to know whether a degree of

mixing might be investigated,  $^1\text{H}$ -NMR and  $^{19}\text{F}$ -NMR were performed for the two phases separately for each sample. The results of these measurements will be discussed in the next two sections of this chapter.

#### 4.2.2. Surfactant mixtures/W/O systems

Three mixtures have been prepared (0.2, 0.6 and 0.8 CTAB mole fraction) and then 2 % of oil has been added to the solutions. Figure 4.2 represents those solutions with hexane, and it is clear that hexane is at the top of the solution in all cases. However, PFH separated to the bottom.

Again photos with the PFH case have been excluded to avoid the repetition. Further,  $^1\text{H}$ -NMR and  $^{19}\text{F}$ -NMR were performed for the two phases separately for the 50 mM of a mixture of the two surfactants with the two oils, which will be also discussed in the next two sections of this chapter.

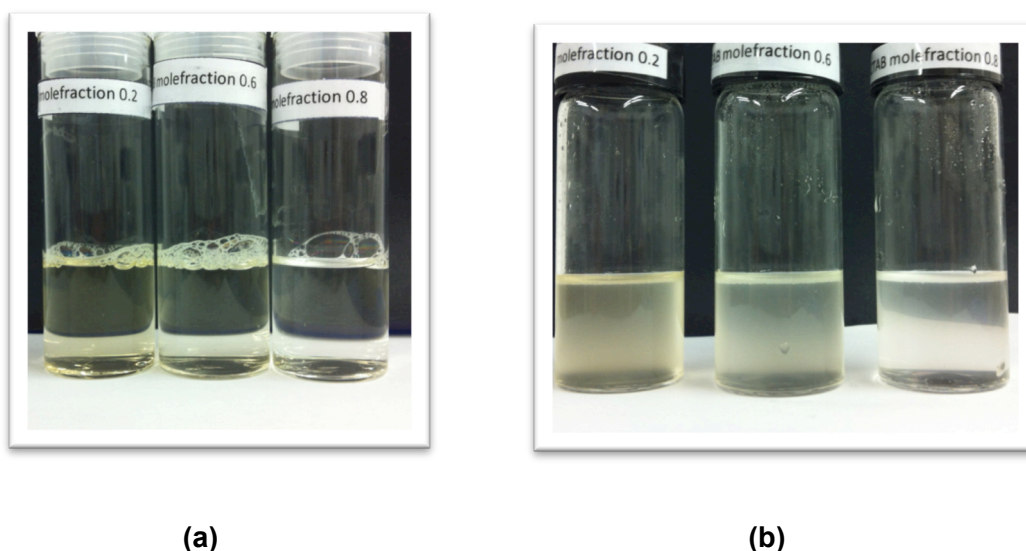


**Figure 4.2** Surfactant mixture aqueous solutions of 0.2, 0.6 and 0.8 in terms of CTAB mole fraction before (a) and after adding 2 % of hexane (b).

#### 4.3. $^1\text{H}$ -NMR measurements

This section will focus on investigating whether hexane or PFH as oil phases mix or do not mix with the surfactant mixture as well as with the single component solutions.  $^1\text{H}$ -NMR spectroscopy has been measured for 50 mM CTAB aqueous solution, 50 mM FSN-100 aqueous solution and the mixture of both surfactants at the ratio of 1:1 in the presence of 2 % hexane or PFH. The concentrations are selected to be above the CMC of each surfactant in order to ensure the presence of micelles in all solutions.



From section 4.2 of this chapter, phase separation of the oil has been noticed in all surfactant/oil solutions from the aqueous phases resulting in two components. Thus, the main question is whether the oil has some solubilisation in the surfactant solution? Analysing both layers in each surfactant-oil solution and studying chemical shifts in the  $^1\text{H}$ -NMR spectroscopy should resolve this issue.

### 4.3.1. CTAB/hexane

The system is a two-phase solution and each phase has been analysed by the  $^1\text{H}$ -NMR spectroscopy. Figure 4.3 shows  $^1\text{H}$ -NMR spectrum of the CTAB solution in  $\text{D}_2\text{O}$  (red) and the lower phase of CTAB/hexane solution in  $\text{D}_2\text{O}$  (blue) spectra as hexane splits to the top of the solution. Both spectra are identical, and protons from hexane should have chemical shifts at (0.91-0.86 ppm,  $\text{CH}_3$ ) and (1.35-1.23 ppm,  $\text{CH}_2$ ) [9]. However all signals from CTAB protons, which have been discussed in Chapter Three, can be identified in the lower phase spectrum. There is no much difference between the spectra of the pure CTAB solution and the lower phase of CTAB/ hexane solution suggesting that there is no mixing between CTAB and hexane and no hexane goes into CTAB micelles.

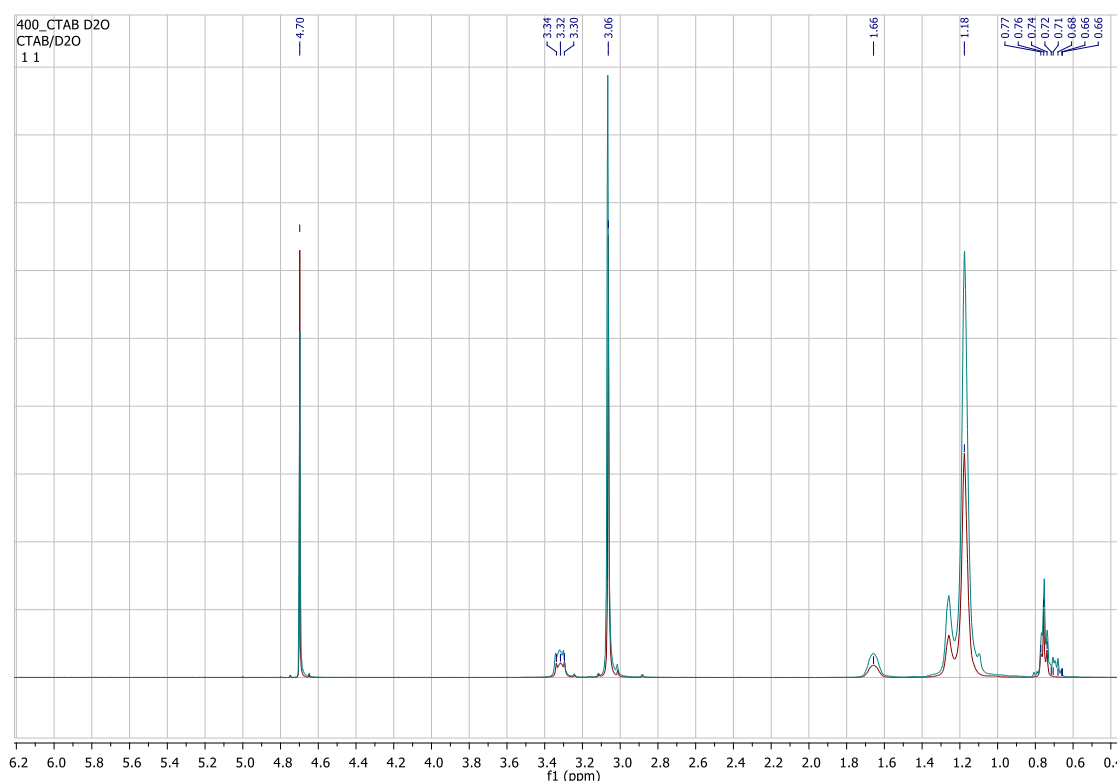


**Figure 4.3**  $^1\text{H}$  High resolution-NMR data from 50 mM of CTAB in  $\text{D}_2\text{O}$  (red) and the lower phase of CTAB/ hexane solution (blue).

On the other hand, in order to investigate whether some surfactant goes to the top of the solution (oil phase),  $^1\text{H}$ -NMR spectra of the top phase compared to the CTAB spectra is required.

Figure 4.4 shows spectra from CTAB in  $\text{CDCl}_3$  (blue) and the top phase of CTAB/hexane in  $\text{CDCl}_3$  solution (red). Peaks from CTAB do not exist in the spectrum of the top phase CTAB/hexane solution. However, comparing the hexane in  $\text{CDCl}_3$  spectrum to that from the top phase of CTAB/hexane (figure 4.5), spectra are identical, which suggests that there is no CTAB in the top phase of the solution and the whole phase is only hexane as the hexane signals at chemical shifts of 0.8-0.9 ppm for  $\text{CH}_3$  and 1.2-1.4 ppm for  $\text{CH}_2$  which are consistent with the literature in  $\text{CDCl}_3$  [9].

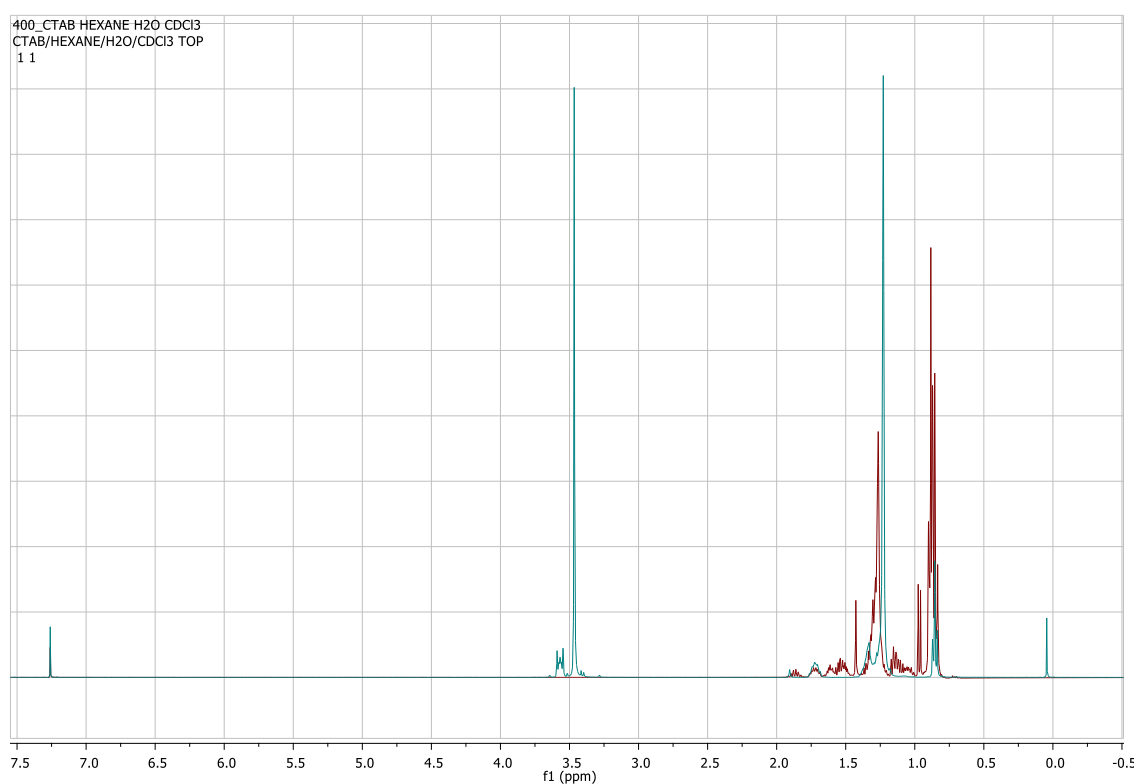


**Figure 4.4**  $^1\text{H}$  High resolution-NMR data from 50 mM of CTAB in  $\text{CDCl}_3$  (blue) and the top phase of CTAB/hexane in  $\text{CDCl}_3$  solution (red).

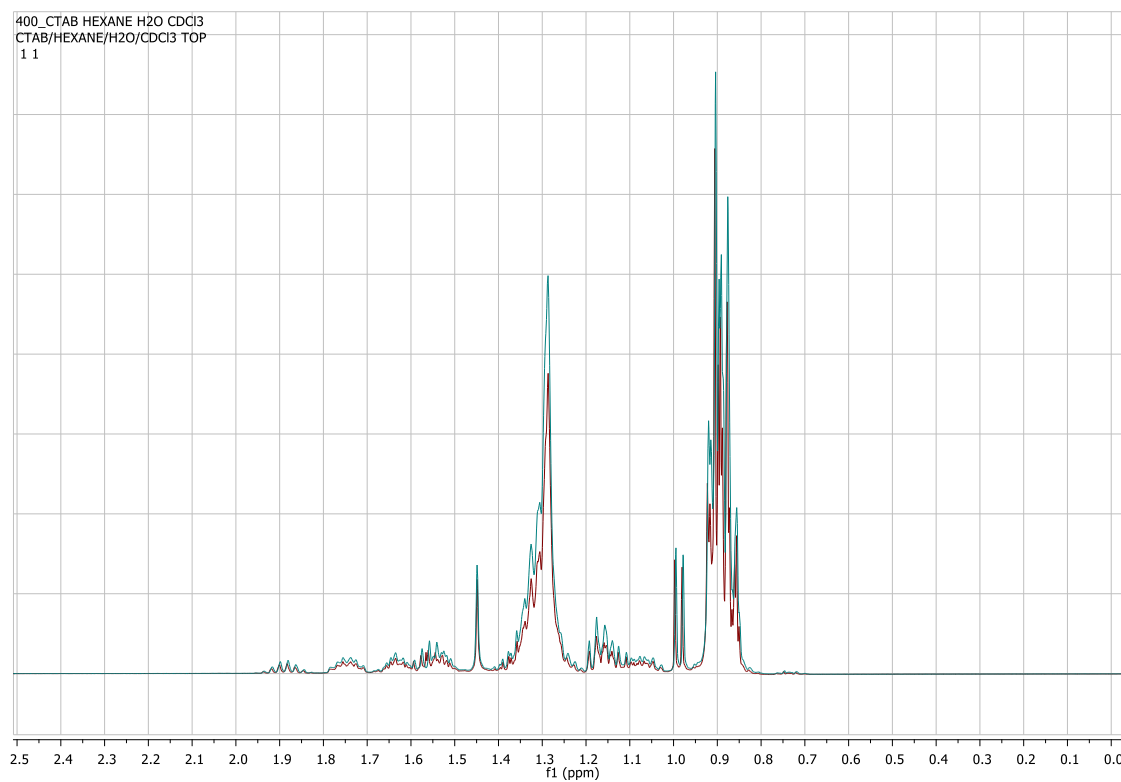


**Figure 4.5**  $^1\text{H}$  High resolution-NMR data from the top phase of CTAB/ hexane in  $\text{CDCl}_3$  (red) and hexane in  $\text{CDCl}_3$  solution (blue).

### 4.3.2. CTAB/PFH

As the PFH goes to the bottom of the vial after mixing with the surfactant solution, the top phase (the surfactant phase) this time is more important to be analysed in order to investigate whether some PFH goes into CTAB micelles or not.

Figure 4.6 shows the spectra of CTAB solution (red) and the top phase of CTAB/PFH solution (blue). Again all signals in the spectrum of the top phase are from CTAB. However, since there are no protons in the PFH structure that can be detected by  $^1\text{H}$ -NMR,  $^{19}\text{F}$ -NMR has been used to detect any PFH in the surfactant phase, the results of which will be studied in the next section (4.4) of this chapter.

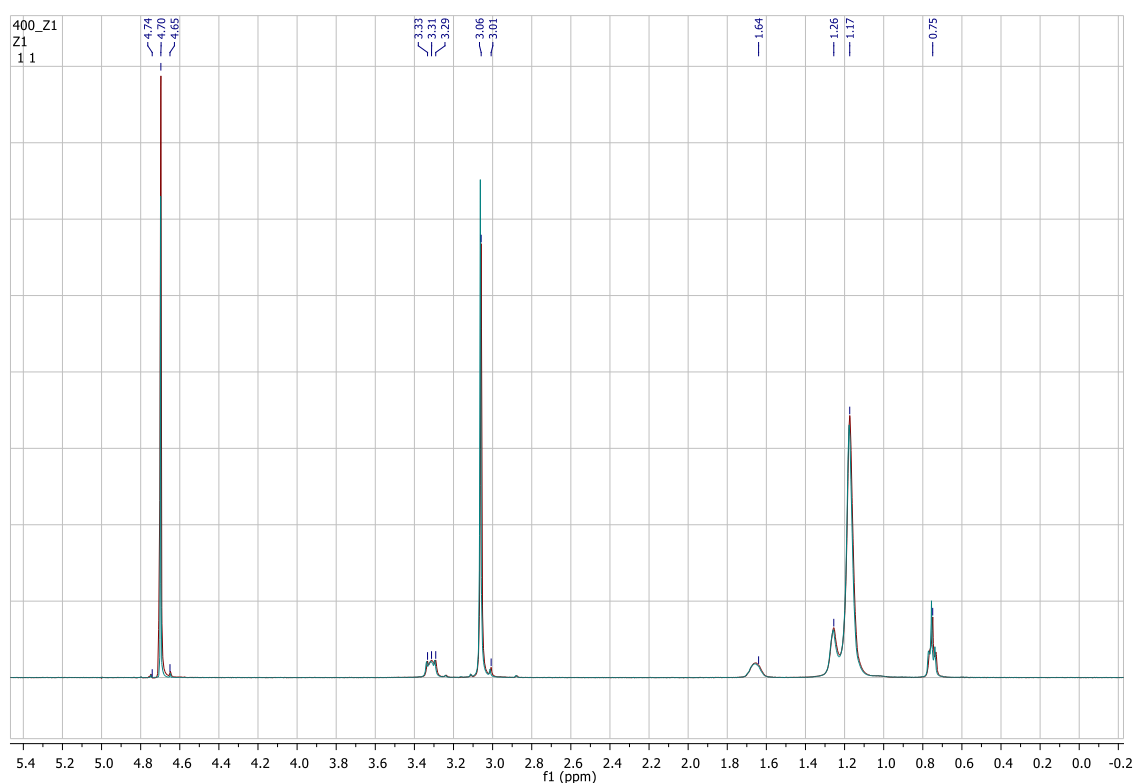


**Figure 4.6**  $^1\text{H}$  High resolution-NMR data from the top phase of 50 mM CTAB solution with 2 % PFH in  $\text{D}_2\text{O}$  (red) and the solution of CTAB in  $\text{D}_2\text{O}$  (blue).

### 4.3.3. FSN-100/hexane

This solution is also two phases and each one has been analysed by  $^1\text{H}$ -NMR. Figure 4.7 shows the  $^1\text{H}$ -NMR spectra of the lower phase of the solution FSN-100 with 2 % of hexane (red) and the solution of 50 mM of FSN-100 in  $\text{D}_2\text{O}$ . It was discussed in Chapter Three that two signals from hydrophobic chain protons and hydroxyl group at 3.54 ppm and 2.24 ppm were observed respectively in the  $^1\text{H}$ -NMR spectra of FSN-100 solution, and the same peaks have also been observed in the mixture with hexane. The spectra do not include any hexane signals suggesting that there is no mixing between the surfactant FSN-100 and hexane.

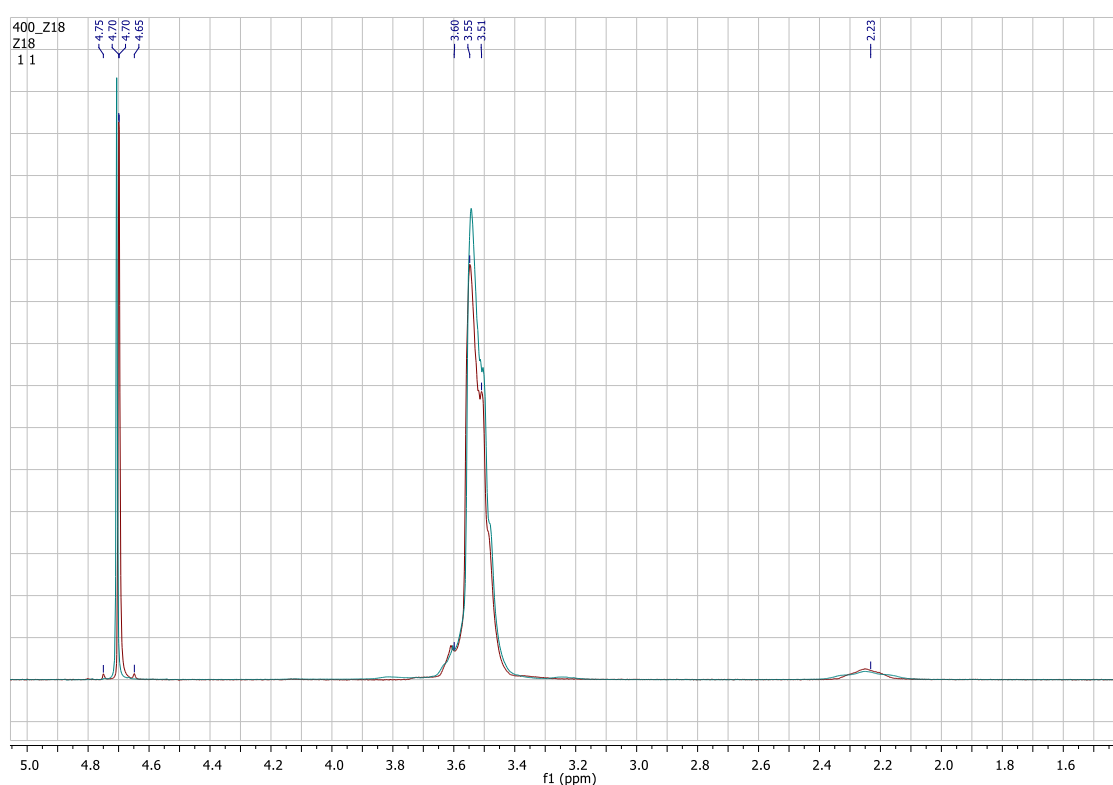


**Figure 4.7**  $^1\text{H}$  High resolution-NMR data from the lower phase of 50mM FSN-100 solution with 2% hexane in  $\text{D}_2\text{O}$  (red) and the solution of FSN-100 in  $\text{D}_2\text{O}$  (blue).

#### 4.3.4. FSN-100/PFH

Similarly, PFH as an oil phase cannot be detected by the  $^1\text{H}$ -NMR spectroscopy, as the oil has no protons in the structure. Figure 4.8 represents the top phase spectrum (blue) comparing to the FSN-100 spectrum of the solution and they are identical. The lower phase is only the oil PFH as no  $^1\text{H}$ -NMR spectrum of this phase is observed (data not shown).

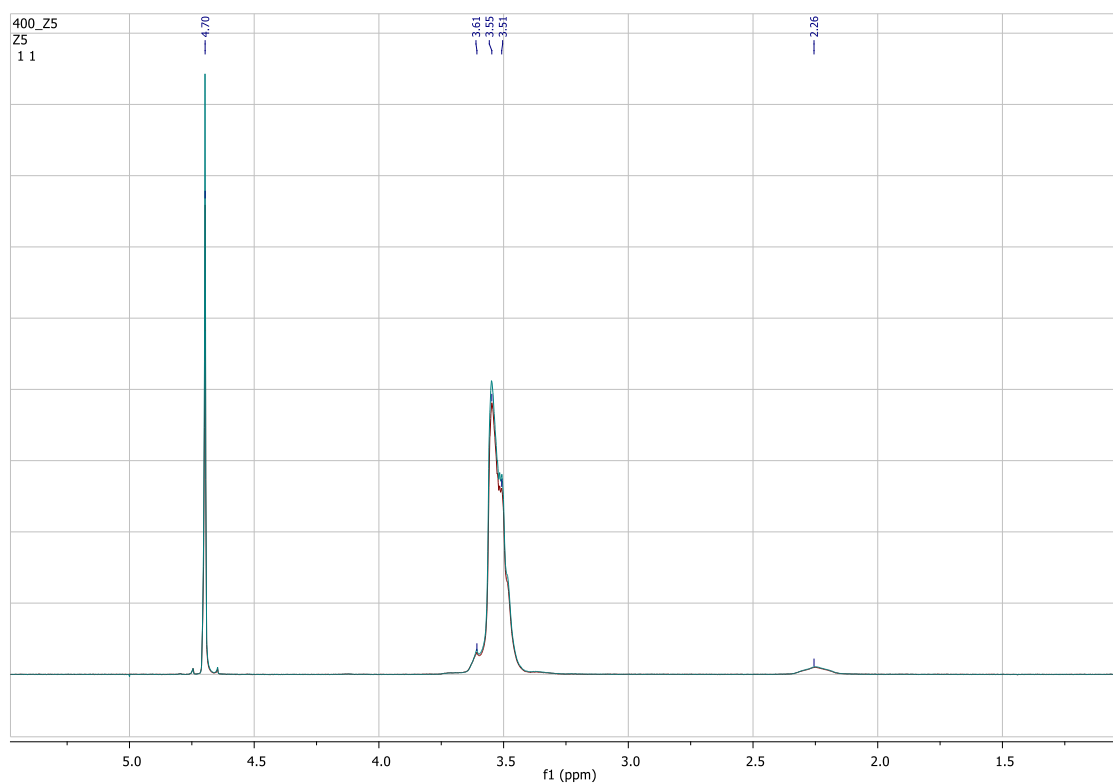


**Figure 4.8  $^1\text{H}$  High resolution-NMR data from the top phase of 50mM FSN-100 solution with 2% PFH in  $\text{D}_2\text{O}$  (red) and the solution of FSN-100 in  $\text{D}_2\text{O}$  (blue).**

### 4.3.5. The mixture/hexane

From the previously analysed spectra, it has been concluded that neither CTAB nor FSN-100 mixes with hexane. Thus, the question is whether the mixture of both surfactants accommodates some oil in the mixed micelles or not?

The mixture was also separated into two phases and each layer was analysed by  $^1\text{H}$ -NMR spectroscopy. As hexane goes to the top layer so the surfactant aqueous solution (at the bottom) should be considered to investigate whether the mixed micelles mix with hexane or not. Figure 4.9 shows the spectra from the lower phase (red) and it is exactly the same as the spectra from CTAB/FSN-100 mixture (blue) suggesting that there is no mixing between hexane and the surfactant mixture as well. Further, the top phase of the mixture is only hexane as no surfactant peaks are observed in the spectra. The spectra are similar to that one in the figure 4.5, and excluded to avoid repetition.

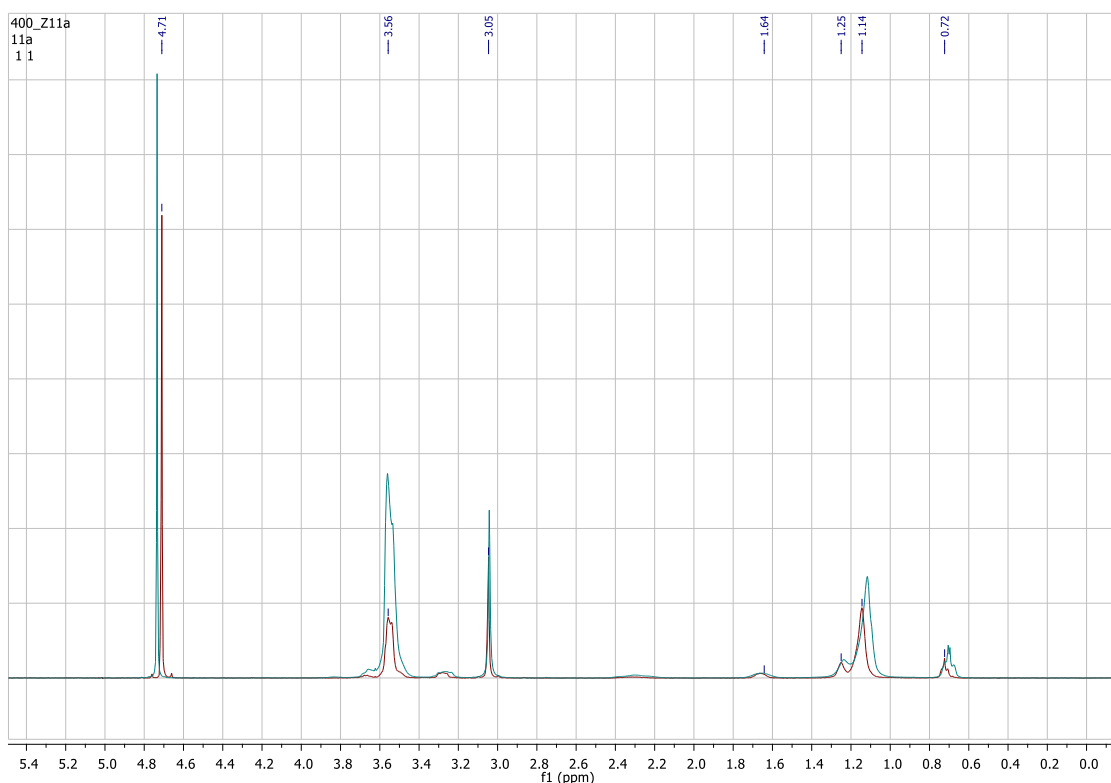


**Figure 4.9**  $^1\text{H}$  High resolution-NMR data from the lower phase of CTAB/FSN-100 mixture solution with 2 % hexane in  $\text{D}_2\text{O}$  (red) and the solution of CTAB/FSN-100 in  $\text{D}_2\text{O}$  (blue).

### 4.3.6. The mixture/PFH

Again, since neither of the pure surfactants mix with PFH, does the mixture of both surfactants mix?

Figure 4.10 shows the  $^1\text{H}$ -NMR spectrum of the top phase of the mixture solution of 50 mM CTAB/FSN-100 with 2 % of PFH, which clearly has the same spectrum to that from the mixture without oil. This shows that the spectrum of CTAB/FSN-100 mixture is not changed by adding PFH, (cannot tell if PFH is there or not by  $^1\text{H}$ -NMR).

The lower phase of this solution has no observed signals by the  $^1\text{H}$ -NMR and is therefore confirmed to be only the oil PFH.

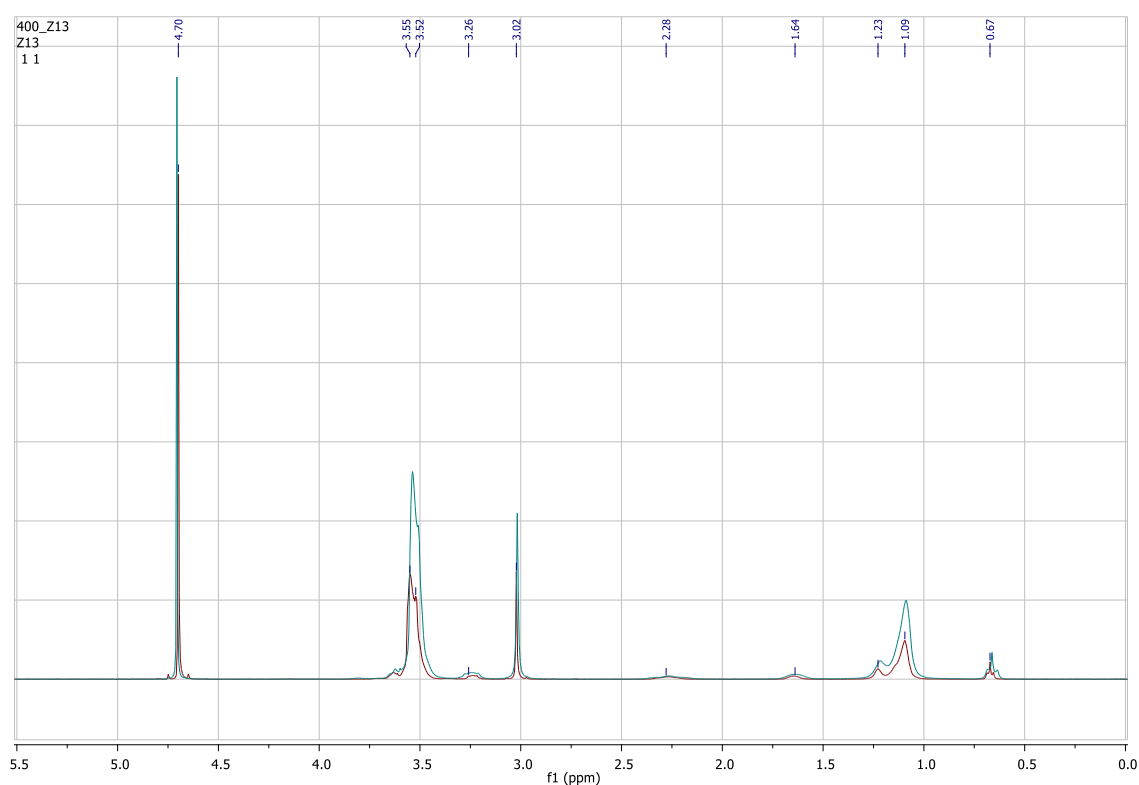


**Figure 4.10  $^1\text{H}$  High resolution-NMR data from the top phase of CTAB/FSN-100 mixture solution with 2 % PFH in  $\text{D}_2\text{O}$  (red) and the solution of CTAB/FSN-100 in  $\text{D}_2\text{O}$  (blue).**



## 4.4. $^{19}\text{F}$ -NMR measurements

$^{19}\text{F}$ -NMR has been used to study the solutions of CTAB/PFH, FSN-100/hexane, FSN-100/PFH, the surfactant mixture with hexane and the surfactant mixture with PFH, as other systems do not include fluorine in their structures (e.g. CTAB/hexane).

As all solutions are two phases, the  $^{19}\text{F}$ -NMR analysis has been performed for each phase.

### 4.4.1. CTAB/PFH

The top phase of the solution of 50 mM CTAB with 2 % PFH has been analysed by  $^{19}\text{F}$ -NMR and the spectrum was essentially only noise, this observation means that no fluorine is detected in this phase. As  $^1\text{H}$ -NMR has shown the CTAB to reside in the upper phase, this suggests that there is no mixing between the CTAB surfactant and the PFH. Figure 4.11 shows the lower phase spectrum of the solution (red) and it is similar to the spectra of the PFH (blue).  $^1\text{H}$ -NMR of the lower phase confirmed that there is no mixing of CTAB into the oil, (only noise detected).

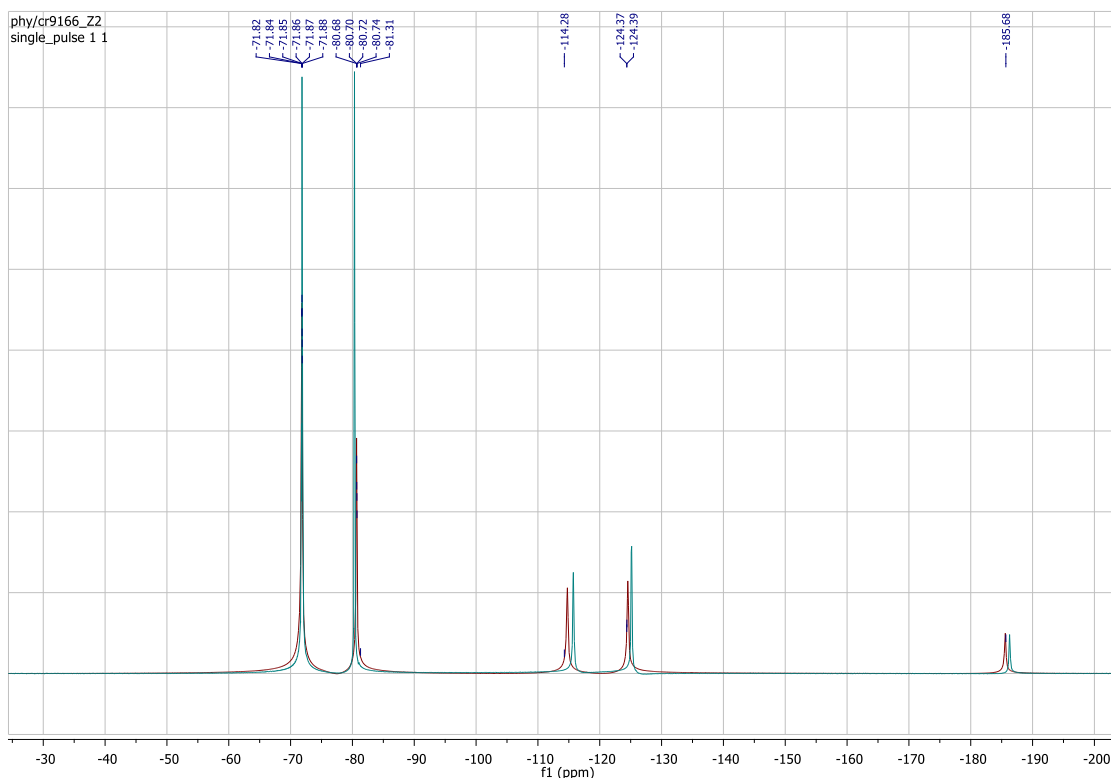


**Figure 4.11**  $^{19}\text{F}$  High resolution-NMR data from the lower phase of CTAB solution with 2 % PFH in  $\text{CDCl}_3$  (red) and the solution of PFH in  $\text{CDCl}_3$  (blue).

### 4.4.2. FSN-100/ hexane

The solution is also two phases and hexane is located on the top. The  $^{19}\text{F}$ -NMR spectrum for the top phase is only a noise as no fluorine is detected suggesting that the surfactant does not exist in the top phase (oil phase).

The lower phase is only the surfactant, and from  $^1\text{H}$ -NMR there is no hexane in this phase. This confirms that hexane does not dissolve with the surfactant. Figure 4.12 shows the lower phase of the solution of FSN-100 with 2 % hexane and the spectra of the pure surfactant FSN-100, clearly both spectra are identical.

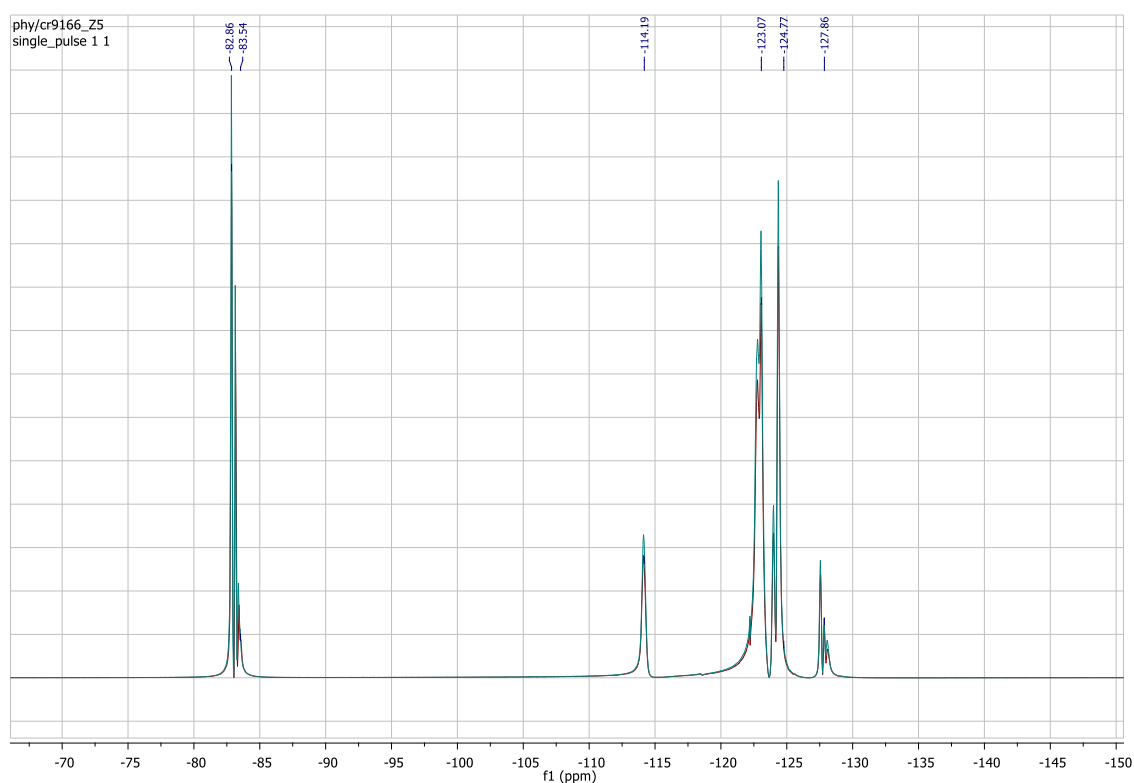


**Figure 4.12**  $^{19}\text{F}$  High resolution-NMR data from the lower phase of FSN-100 solution with 2 % hexane in  $\text{D}_2\text{O}$  (blue) and the solution of 50 mM FSN-100 in  $\text{D}_2\text{O}$  (red).

### 4.4.3. FSN-100/PFH

The question here is whether the fluorosurfactant mix with the fluorocarbon oil? Figure 4.13 shows the spectra of the top phase of 50 mM FSN-100 with 2 % of PFH solution compared to the pure FSN-100 solution spectra. Clearly, there are no signals from PFH in the surfactant phase and both spectra are similar suggesting that PFH does not exist in the surfactant phase and both spectra are similar suggesting that PFH does not exist in the aqueous FSN-100 solution, thus the surfactant does not mix with the PFH.

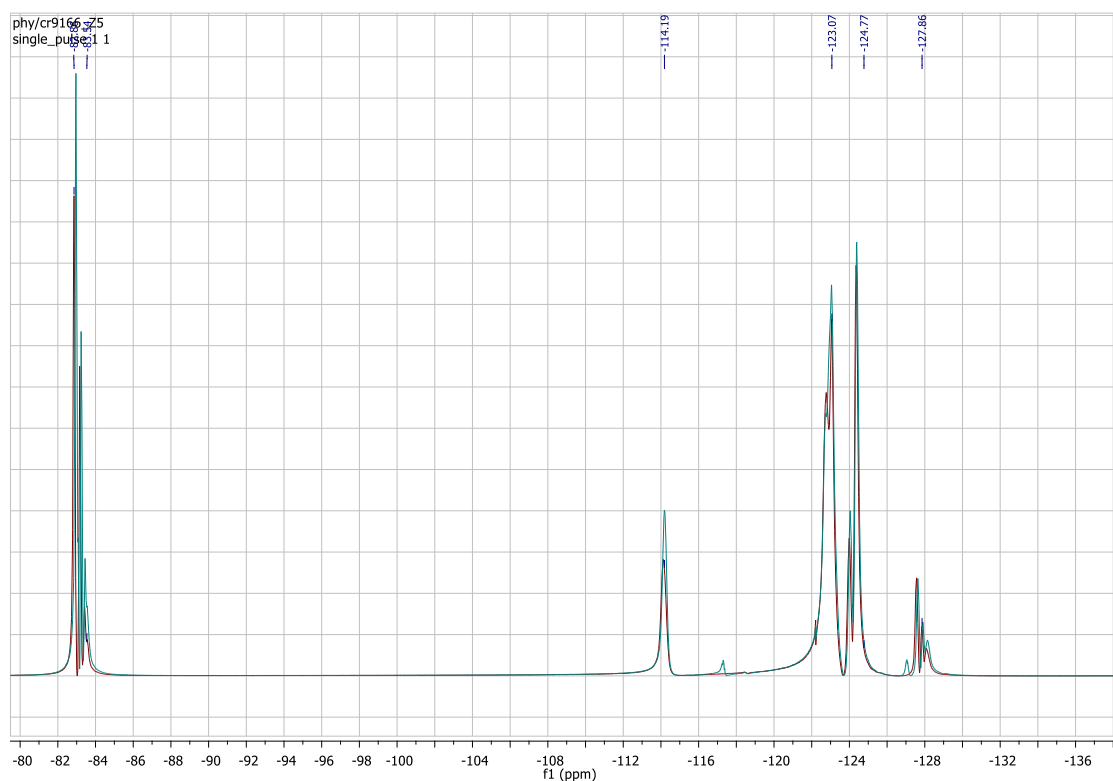


**Figure 4.13**  $^{19}\text{F}$  High resolution-NMR data from the top phase of FSN-100 solution with 2 % PFH in  $\text{D}_2\text{O}$  (blue) and the solution of 50 mM FSN-100 in  $\text{D}_2\text{O}$  (red).

#### 4.4.4. The surfactant mixture /hexane

Figure 4.14 shows the  $^{19}\text{F}$ -NMR of the lower phase of the mixture with hexane and the mixture without oil. Both spectra are identical suggesting that there is also no mixing between the mixture and hexane, which has been confirmed by  $^1\text{H}$ -NMR.

The spectrum of the top phase is only noise as the whole phase is hexane.

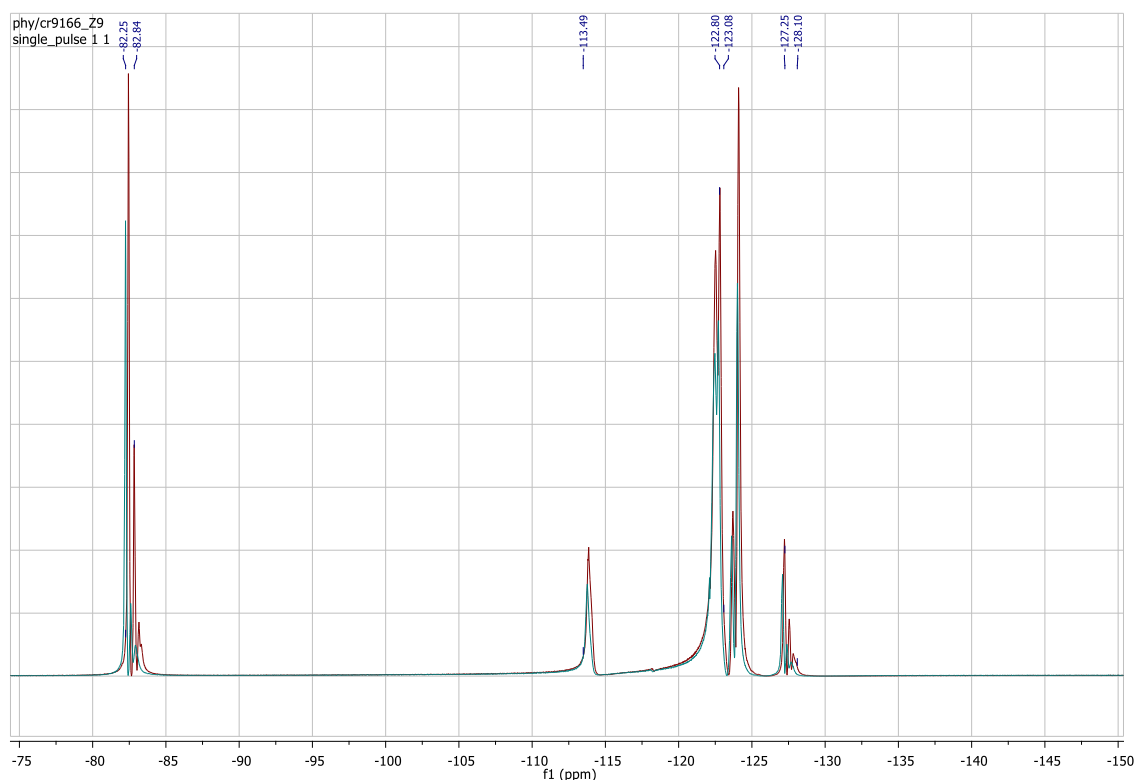


**Figure 4.14**  $^{19}\text{F}$  High resolution-NMR data from the lower phase of the CTAB/FSN-100 mixture solution with 2 % hexane in  $\text{D}_2\text{O}$  (red) and the mixture solution of 50 mM CTAB/FSN-100 in  $\text{D}_2\text{O}$  (blue).

#### 4.4.5. The surfactant mixture/PFH

Figure 4.15 shows that spectra from the top phase of surfactant mixture with 2 % PFH (blue) and the mixture without oil (red). Spectra are identical except the small signal at 117.18 ppm in the case of mixture with oil which does not exist in the oil spectrum indicating that this signal may be an impurity.

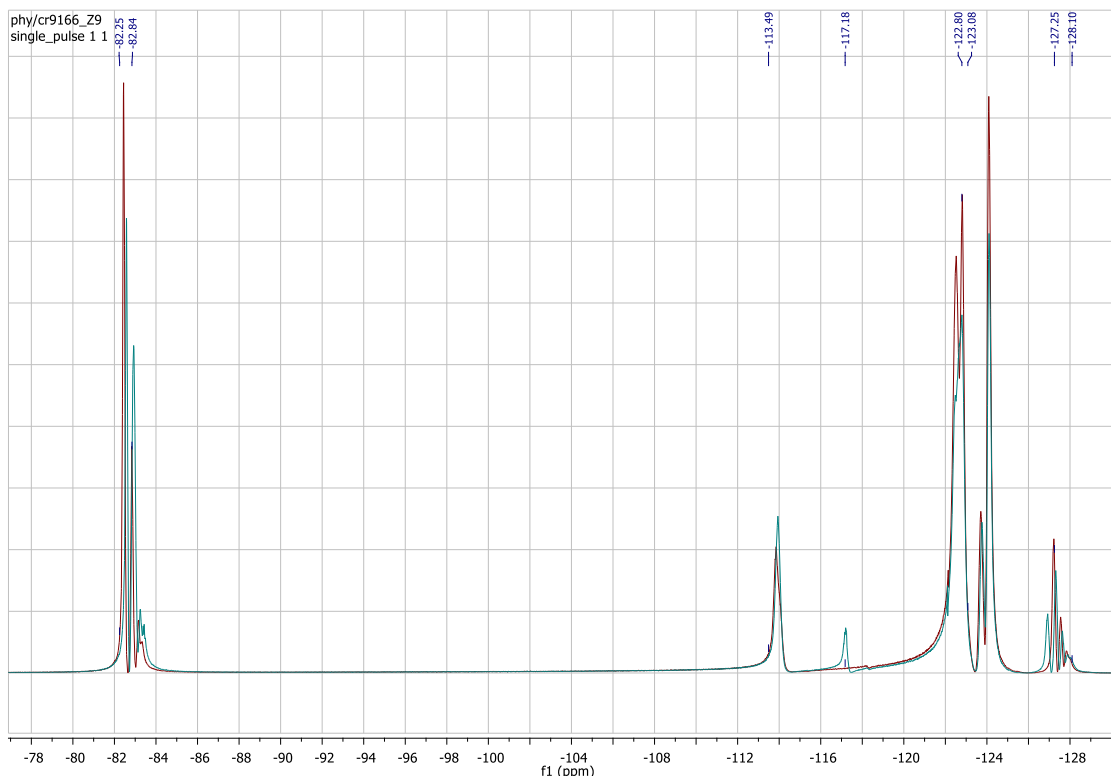


**Figure 4.15**  $^{19}\text{F}$  High resolution-NMR data from the top phase of the CTAB/FSN-100 mixture solution with 2 % PFH in  $\text{D}_2\text{O}$  (blue) and the mixture solution of 50 mM the CTAB/FSN-100 in  $\text{D}_2\text{O}$  without PFH (red).

#### 4.5. PGSE- NMR spectroscopy

The determination of the self-diffusion coefficient of each component in the surfactant/oil solutions is required in order to have a complete characterization. This part deals with the characterization at the molecular level of the aggregates in the surfactant/water/oil systems through pulsed gradient spin-echo NMR experiments. The technique has been used to measure the self-diffusion coefficients of CTAB (ionic surfactant) and FSN-100 (non-ionic surfactant) in the absence and presence of hydrocarbon oil (hexane) and fluorocarbon oil (PFH). All data were fitted to (single + single stretched), double (two components) fits using the CORE (Component REsolved PGSE NMR) method of data analysis. From the CORE outcomes, effective

spectra for all fitted components have been collected and used to calculate the self-diffusion coefficients. Figure 4.16 shows the results of PGSE-NMR measurements for the single component of 50 mM CTAB and 50 mM FSN-100 aqueous solutions and three mixtures of both surfactants (0.2, 0.5 and 0.8 CTAB mole fraction) with and without a fixed amount of oil (2 % hexane or 2 % PFH). For each system, the diffusion coefficient of CTAB and FSN-100 were reported. The systems without oils have been included in Chapter Three.

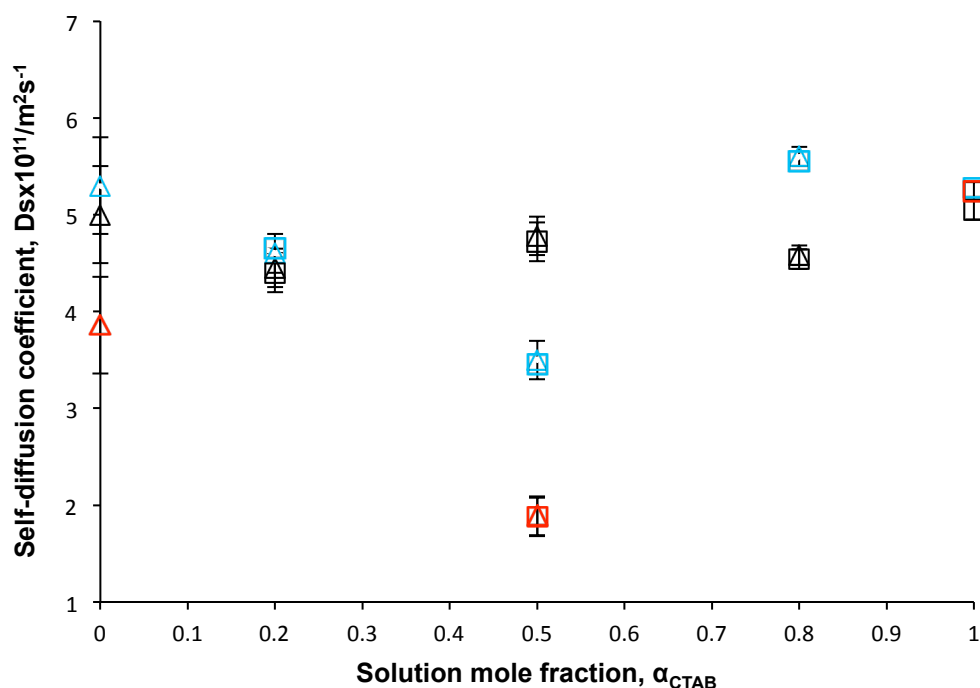


**Figure 4.16** Self-diffusion coefficients of CTAB and FSN-100 and the mixtures with hexane and PFH as a function of CTAB mole fraction.  $\alpha_{\text{CTAB}} = 1$  (open squares),  $\alpha_{\text{CTAB}} = 0$  (open triangles), CTAB/hexane (open blue squares), FSN/hexane (open blue triangles), CTAB/PFH (open red squares), FSN/PFH (open red triangles).

For better understanding of these systems, it is useful to review the interaction of oils and single surfactant systems before discussing what happens when oil is added to a mixture containing hydrocarbon and fluorocarbon surfactants.

#### 4.5.1 CTAB with hexane or PFH solutions ( $\alpha_{\text{CTAB}} = 1$ )

In figure 4.16, the self-diffusion coefficients are plotted vs CTAB mole fraction. From the diffusion coefficient values, it is obvious that adding hexane or PFH to the CTAB solution does not make any difference in the mobility of CTAB micelles and similar micelle sizes would be presented in all cases, which confirms that CTAB aqueous

solution does not mix with both hexane and PFH consistent with results from  $^1\text{H}$ -NMR and  $^{19}\text{F}$ -NMR. This means that the mixing of hexane or PFH and CTAB in the core is not applicable since CTAB as a hydrophilic surfactant has a low solubility in hexane or PFH as discussed above (sections 4.2.1).

#### 4.5.2 FSN-100 with hexane or PFH solutions ( $\alpha_{\text{CTAB}} = 0$ )

From figure 4.16 the self-diffusion coefficient of FSN-100 is slightly changed after adding hexane and PFH to the surfactant solution but these values are still within the experimental errors. This is evident that FSN-100 micelle diffusion does not change in the hexane case as well as the PFH case, indicating that FSN micelle size and mobility are similar to that in the pure surfactant micelles indicating the low efficiency of hexane to mix with the surfactant. It is also obvious from  $^1\text{H}$ -NMR and  $^{19}\text{F}$ -NMR that both oils are not at all soluble in the surfactant solution. This is not in agreement with the literature [1, 7] which suggests that there is a great solubilisation between hexane and FSN-100. However, these two studies involve different surfactant concentrations and different techniques used to investigate this solubility.

#### 4.5.3 Surfactant mixtures with oils

Figure 4.16 shows that the changes in the self-diffusion coefficients of each surfactant are more pronounced when oils added to the mixture of 0.5 CTAB mole fractions. However, both surfactants have similar diffusion in all cases, which confirms the mixing behaviour between the two surfactants, which has been studied in Chapter Three. Both surfactant diffusions are becoming slightly higher once hexane is added to 0.2 and 0.8 CTAB mole fractions although these changes are almost within the experimental errors. Adding PFH to the mixtures 0.2 and 0.8 has not been studied to measure the self-diffusion coefficients due to the limited time to do these measurements.

The mixture of  $\alpha=0.5$  shows larger changes in the diffusion coefficient than at  $\alpha=0.2$ , and  $\alpha=0.8$ . Both oils apparently lower  $D_s$  for the surfactant/PFH more so than hexane. This is currently difficult to explain given the data at  $\alpha=0.2$  and  $\alpha=0.8$ . However, the mixture of  $\alpha=0.5$  has not been measured by other techniques, so these values are not comparable and further investigations including repeating this measurement is highly required. At this point, possible explanations are due to the micelle shape change. Table 4.1 includes the self-diffusion coefficients for the measured solutions.

CTAB/mole fraction	Self-diffusion coefficient/ ( $10^{-11} \pm 0.5$ )/ $\text{m}^2\text{s}^{-1}$					
	Hexane				PFH	
	CTAB	FSN	CTAB	FSN	CTAB	FSN
0.0		5.00		5.30		3.86
0.2	4.40	4.45	4.65	4.60	-	-
0.5	4.72	4.78	3.45	3.50	1.88	1.89
0.8	4.54	4.58	5.55	5.60	-	-
1.0	5.05		5.28		5.24	

**Table 4.1 Self-diffusion coefficients of CTAB, FSN-100 and mixtures of 0.2, 0.5, 0.8 CTAB mole fractions in the presence of hexane or PFH at 25 °C.**

## 4.6. Small-angle neutron scattering (SANS)

The complete characterization of the surfactant/oil systems requires the determination of size and shape of the aggregates in solutions. Such details can be obtained using SANS analysis techniques.

All measurements were performed on the fixed-geometry, time of flight LOQ diffractometer (ISIS Spallation Neutron Source, Oxfordshire UK). Surfactant concentrations were 50 mM and 2 % of the oil (hexane or PFH) has been added to the single surfactant solutions as well as to the mixtures of 0.2, 0.6 and 0.8 CTAB mole fraction. Excess oil was removed before starting the measurements. All data were fitted to a model describing the globular micelle morphology.

### 4.6.1 Surfactants with oils

In this part of the discussion, the scattering of the single surfactant in the presence of the two different oils will be presented first and compared to that for the surfactant in the absence of oil, which have been discussed in Chapter Three. In all cases samples were prepared by adding of excess oil (2%) and removal of aqueous phase for study by SANS.

#### 4.6.1.1. CTAB /hexane solutions

From figure 4.17, the scattering from the ionic CTAB surfactant micelles shows the form expected for a charged micelle with a reduction in the intensity at low  $Q$  due to the structure factor. In the curve from the presence of hexane and without hexane, there is no difference in the scattering of both cases suggesting that there is no much hexane goes into the core of CTAB micelles, and there is no change in the shape of micelles. Figure 4.18, describes the fit for CTAB with hexane solution and all parameters are listed in table 4.2, and compared to those for the pure CTAB aqueous solution.



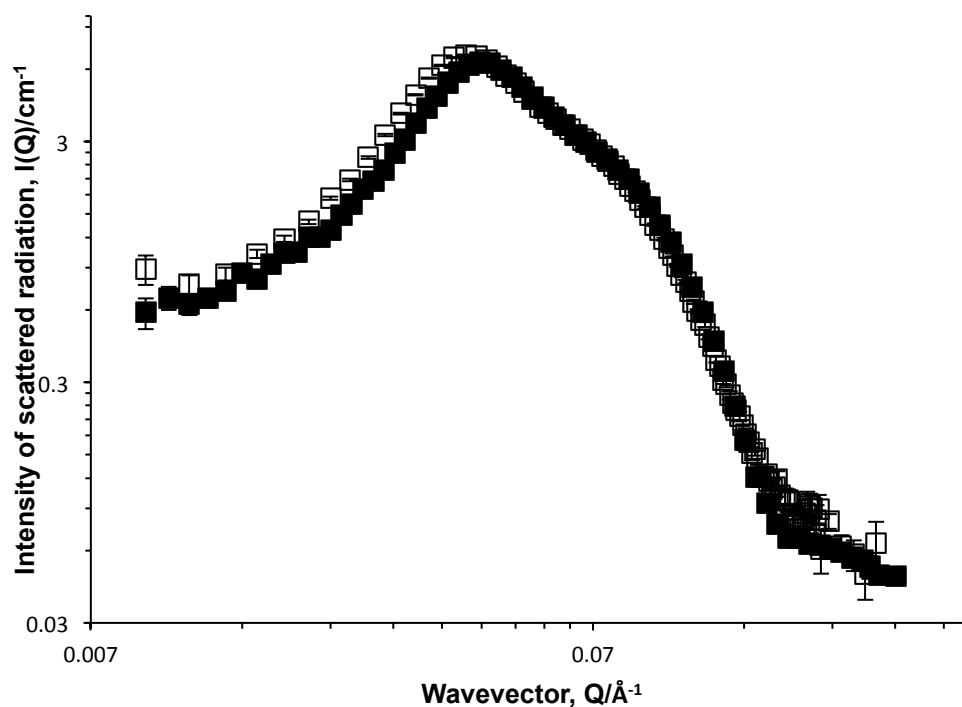


Figure 4.17 Small angle neutron scattering of 50 mM CTAB aqueous solution (open square) in  $\text{D}_2\text{O}$  and 50 mM CTAB aqueous solution in  $\text{D}_2\text{O}$  saturated with 2 % hexane (closed square).

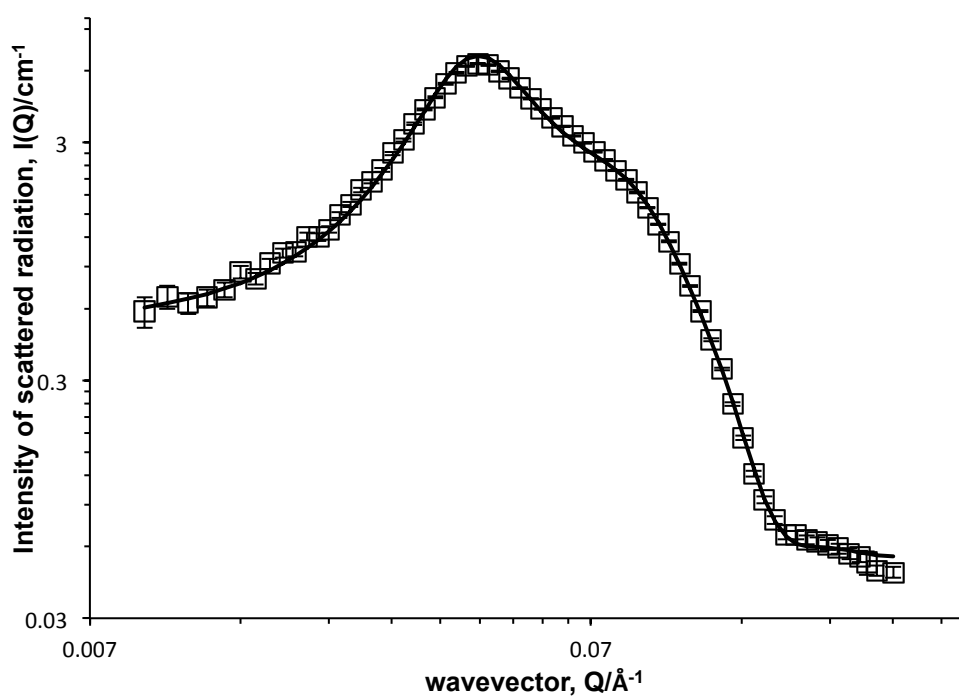


Figure 4.18 Small-angle neutron scattering of 50 mM CTAB aqueous solution in  $\text{D}_2\text{O}$  saturated with 2% hexane (open square) with the fit (solid line).

CTAB / Parameter	Without hexane	With hexane
Aggregation number, $N_{agg.}$ ( $\pm 10$ )	135	-
Volume fraction of solvent in the core, $\phi_{sol} \pm 0.01$	0.02	0.03
“Core” radius, $R_{Core}$ /Å	25.7	25.9
Incoherent background scattering, $B/cm^{-1} \pm 0.01$	0.02	0.03
Ellipticity, $X$	0.85	0.65
$V_{s(dry)}/V_{Core}$	0.9	0.9

**Table 4.2 Parameters describing the fits of SANS data from CTAB solutions in D<sub>2</sub>O saturated with 2 % hexane and compared to the pure surfactant parameters, using a model that describes the micelle as a globular elliptical with some ionic character.**

From table 4.2, parameters of both solutions with hexane and without hexane are similar and this is in a good agreement with the shape of both curves in figure 4.17. The core radius is about the same with a little change in the ellipticity suggesting that either hexane does not exist in the core of the micelle and thus the aggregation number does not change, or a tiny amount of hexane exists in the core and in this case the aggregation number can not be calculated as this amount is unknown.

#### 4.6.1.2. FSN-100 /hexane solutions

Figure 4.19 shows the scattering from the non-ionic surfactant FSN-100 micelles, there is now a noticeable “bump” around  $Q = 0.1 \text{ Å}^{-1}$ , (higher  $Q$  values) and no reduction in the intensity at low  $Q$  as the micelle is uncharged. Little difference is observable between the hexane and no-hexane samples. There is also no difference between the scattering curves at low  $Q$  values, whereas at higher  $Q$  values FSN-100 with hexane have lower intensity associated with different levels of incoherent background.

Figure 4.20, describes the fit for FSN-100 with hexane solution and all parameters are listed in table 4.3 and compared to those for the pure FSN-100 aqueous solution.

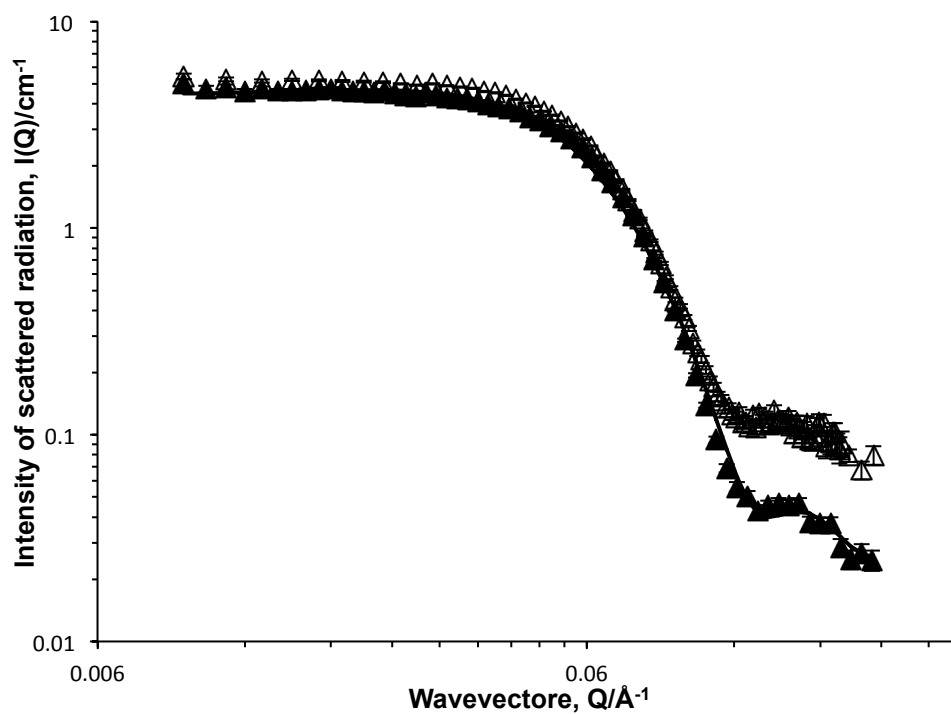


Figure 4.19 Small-angle neutron scattering of 50 mM FSN-100 aqueous solution in  $\text{D}_2\text{O}$  (open triangle), and the solution in  $\text{D}_2\text{O}$  saturated with 2 % hexane (closed triangle).

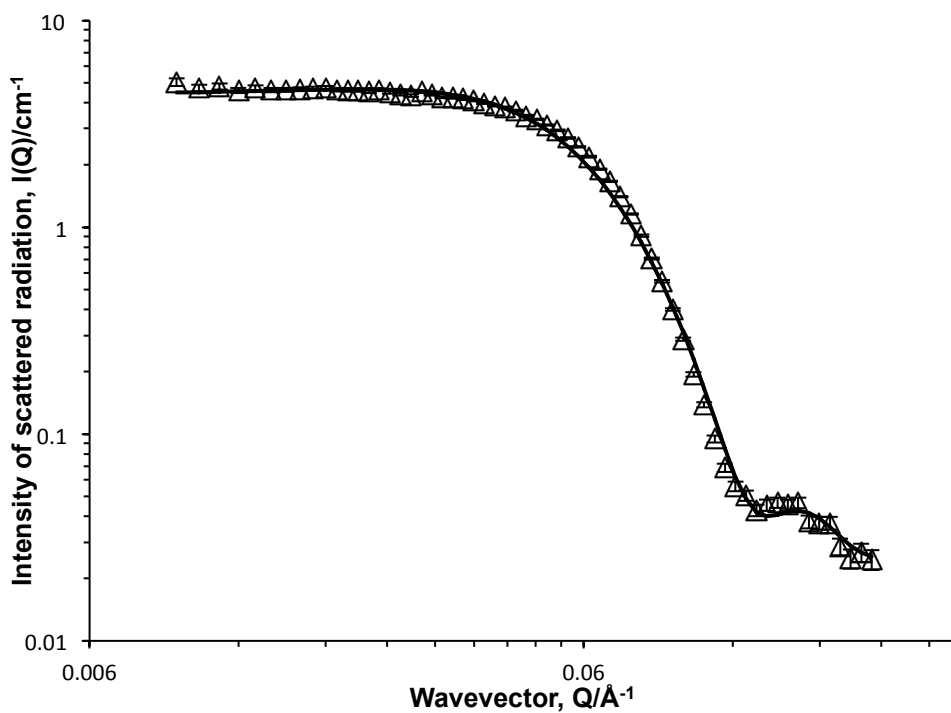


Figure 4.20 Small-angle neutron scattering of 50 mM FSN-100 aqueous solution in  $\text{D}_2\text{O}$  saturated with 2 % hexane (open triangle) with the fit (solid line).

FSN-100 /Parameter	Without hexane	With hexane
Aggregation number, $N_{agg.} (\pm 10)$	50	-
Volume fraction of solvent in the core, $\phi_{sol} \pm 0.01$	0.02	0.02
“Core” radius, $R_{Core} / \text{\AA}$	13.2	13.3
Incoherent background scattering $B/\text{cm}^{-1} \pm 0.01$	0.05	0.02
Ellipticity, $X$	1.5	1.6
$V_{s(dry)}/V_{Core}$	0.8	0.8

**Table 4.3 Parameters describing the fits of SANS data from FSN-100 solutions in D<sub>2</sub>O saturated with 2 % hexane and compared to the pure surfactant parameters, using a model that describes the micelle as a globular elliptical with some ionic character.**

Again parameters are similar in both cases except the incoherent background scattering parameter as described in figure 4.19. The aggregation number in the FSN-100/hexane solution is not expected to change from the pure surfactant. FSN-100/hexane solution has been fitted as a solid object due to the small difference in the scattering length density between the head group and the tail in the FSN-100 micelles, and the module used considered the interface between the micelle and the solvent, so the shell thickness is excluded from the calculations. Thus, the module has been forced to calculate the radius based only on the core of the micelle to be comparable to the parameters of the pure surfactant estimated in Chapter Three. This situation is different from CTAB case since the core and shell in the spherical CTAB micelles is more pronounced.

#### 4.6.1.3. CTAB/PFH solutions

This section shows the scattering curves obtained for CTAB and CTAB with PFH. From figure 4.21, it is clear that the intensity from CTAB aqueous solution is stronger than that with the PFH particularly at low Q values suggesting a slight difference in the concentrations due to either the experimental errors as both experiments have been

performed in different measurements or losing some surfactant aqueous solution when removing the oil phase in the preparation of the samples for scattering. This is obvious also from the collected parameters in the table 4.4 as they are similar. The reduction in the intensity at low  $Q$  values, which characterizes the ionic surfactants, is clearly noticeable in both cases.

Figure 4.22, describes the fit for CTAB solution in the presence of PFH and all collected parameters from the fit are listed in table 4.4, and compared to those for the CTAB aqueous solution.

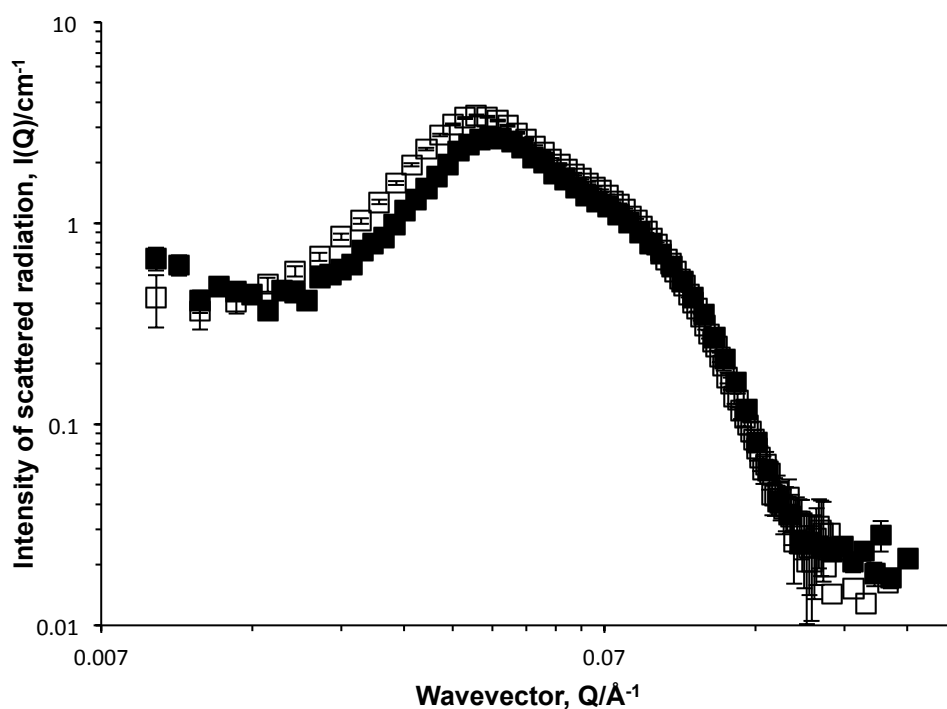


**Figure 4.21** Small angle neutron scattering of 50 mM CTAB aqueous solution (open square) in  $D_2O$  and 50 mM CTAB aqueous solution in  $D_2O$  saturated with 2 % Perfluorohexane (closed square).

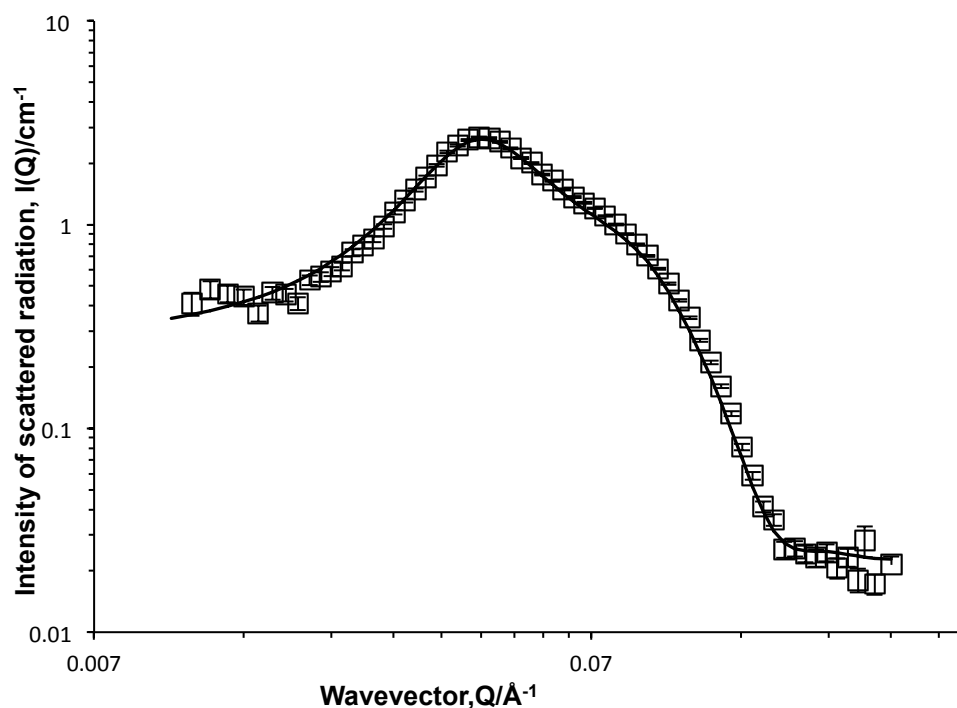


**Figure 4.22** Small-angle neutron scattering of 50 mM CTAB aqueous solution in D<sub>2</sub>O saturated with 2 % PFH (open square) with the fit (solid line).

CTAB / Parameter	Without PFH	With PFH
Aggregation number, $N_{agg.}$ ( $\pm 10$ )	135	-
Volume fraction of solvent in the core, $\phi_{sol} \pm 0.01$	0.02	0.03
“Core” radius, $R_{Core}$ /Å	25.7	25.9
Incoherent background scattering B/cm <sup>-1</sup> $\pm 0.01$	0.02	0.02
Ellipticity, $X$	0.85	0.75
$V_{s(dry)}/V_{Core}$	0.9	0.9

**Table 4.4** Parameters describing the fits of SANS data from CTAB solutions in D<sub>2</sub>O saturated with 2 % hexane and compared to the pure surfactant parameters, using a model that describes the micelle as a globular elliptical with some ionic character.

#### 4.6.1.4. FSN-100/PFH solutions

From figure 4.23, similar scattering from the FSN aqueous solution and the FSN with PFH at low  $Q$  values is introduced. The “bump” around  $Q = 0.1 \text{ \AA}^{-1}$  is more pronounced in the surfactant/oil case suggesting a little more  $\text{H}_2\text{O}$  floating in  $\text{D}_2\text{O}$  solvent. There is no difference between the scattering curves at low  $Q$  values, whereas at higher  $Q$  values FSN-100 with oil solution has lower intensity. Figure 4.24, describes the fit for FSN with PFH solution and all parameters are listed in table 4.5 and compared to those for the FSN aqueous solution.

Again, the model used to fit the FSN-100/PFH data has been forced to calculate the radius based only on the core of the micelle in order to compare these parameters to those from the pure surfactant estimated in Chapter Three. From table 4.5 parameters are about the same suggesting that PFH does not mix with surfactant, which agrees with other techniques used in this chapter.

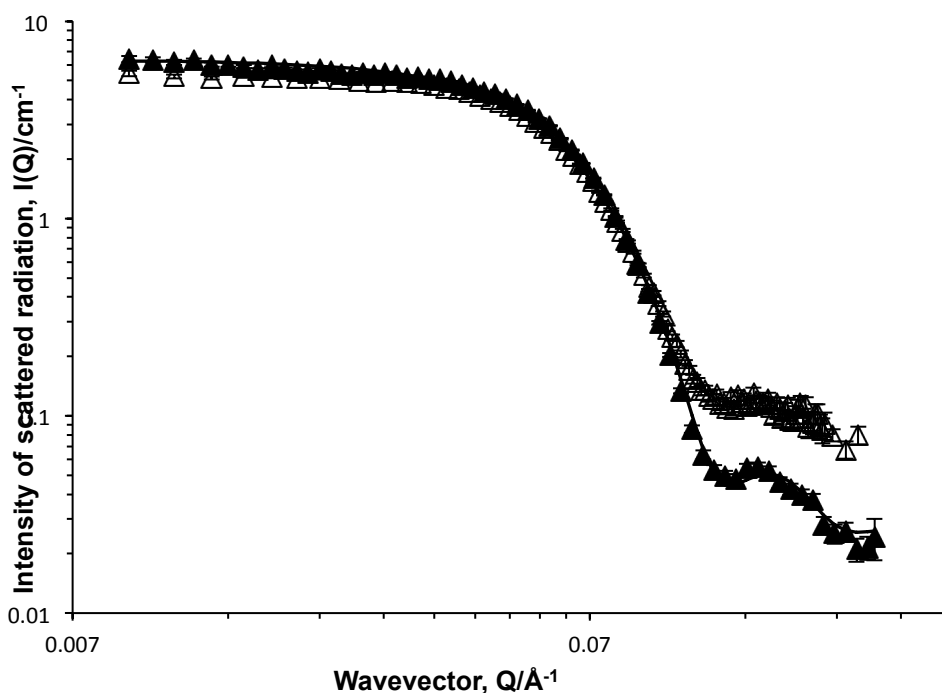


**Figure 4.23** Small angle neutron scattering of 50 mM FSN-100 aqueous solution (open triangle) with fit (solid line), 50 mM FSN-100 in  $\text{D}_2\text{O}$  saturated with 2 % perfluorohexane (closed triangle).

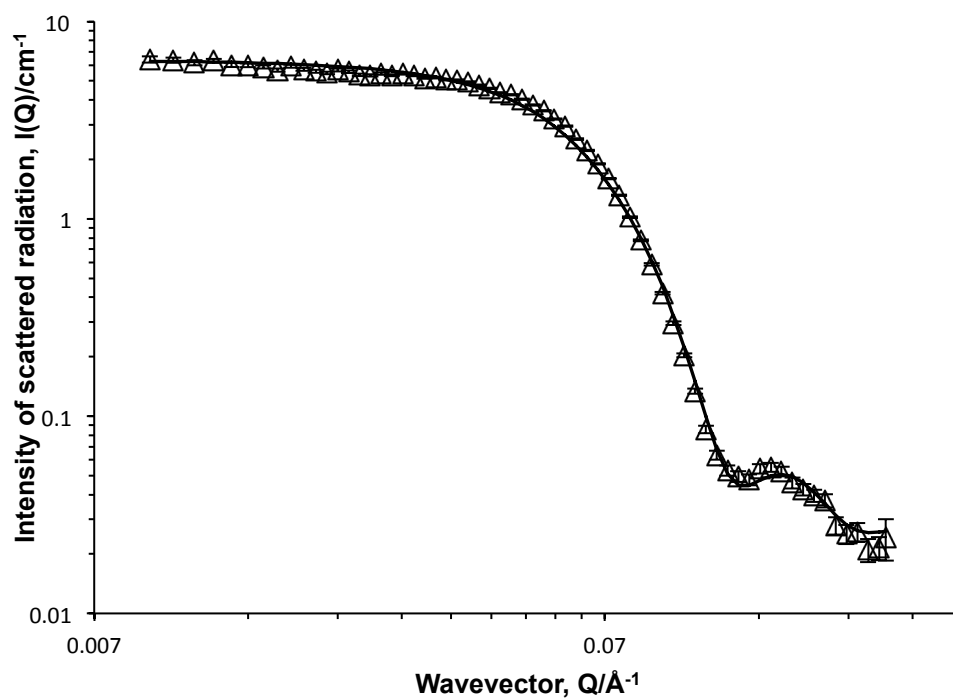


**Figure 4.24** Small-angle neutron scattering of 50 mM FSN-100 aqueous solution in D<sub>2</sub>O saturated with 2 % PFH (open triangle) with the fit (solid line).

FSN-100 / Parameter	Without PFH	With PFH
Aggregation number, $N_{agg.}$ ( $\pm 10$ )	50	-
Volume fraction of solvent in the core, $\phi_{sol} \pm 0.01$	0.02	0.01
“Core” radius, $R_{Core}$ / Å	13.2	13.4
Incoherent background scattering B/cm <sup>-1</sup> $\pm 0.01$	0.05	0.03
Ellipticity, $X$	1.5	1.6
$V_{s(dry)}/V_{Core}$	0.8	0.8

**Table 4.5** Parameters describing the fits of SANS data from FSN-100 solutions in D<sub>2</sub>O saturated with 2 % hexane and compared to the pure surfactant parameters, using a model that describes the micelle as a globular elliptical with some ionic character.



### 4.6.2. Surfactant mixture /oil solutions

The neutron scattering measurements have been performed for three different surfactant mixtures (0.2, 0.6, and 0.8 CTAB mole fraction) in the presence of hexane or PFH. All solutions are at total concentration of 50 mM and 2 % of hexane or PFH was added to the mixture and stirred for a while before measuring the saturated solution. In this section data will be discussed separately, once with the hexane and then with the PFH.

#### 4.6.2.1. Mixture/hexane solutions

As discussed in Chapter Three for the mixtures without oils, the scattering intensity in the figure 4.25, decreases at low  $Q$  as the CTAB mole fraction increases, with shoulders around  $Q=0.06 \text{ \AA}^{-1}$ . However, the “bump” at high  $Q$  values is more pronounced at the mixture of 0.2 and that is similar to what has been noticed in the FSN-100/hexane scattering, which suggests that this bump is more characterized by the FSN-100 surfactant.

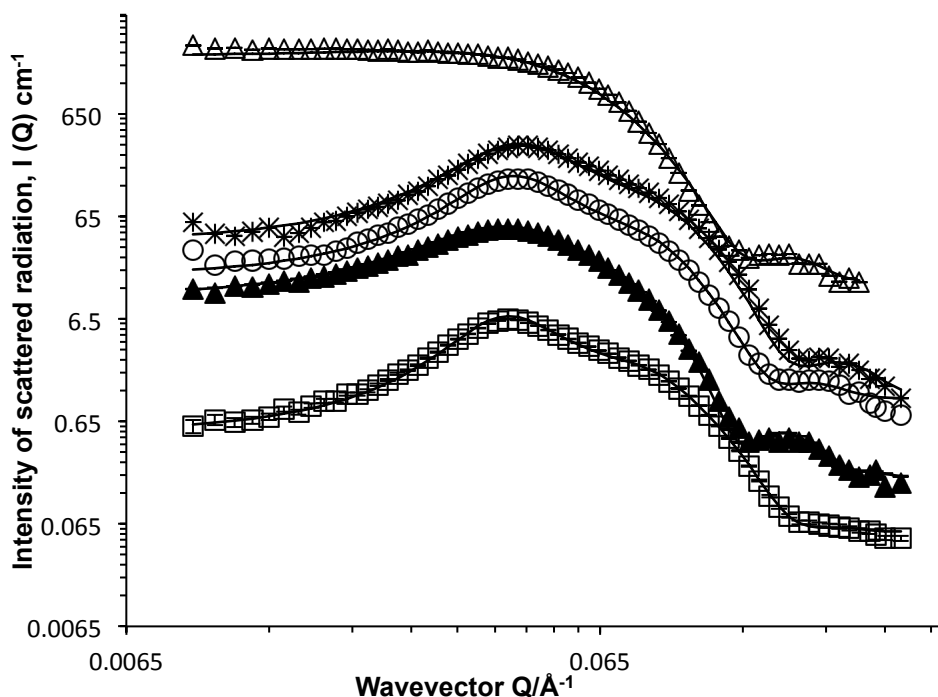


**Figure 4.25** Small angle neutron scattering as a function of CTAB mole fraction, (open square)  $\alpha_{\text{CTAB}} = 1$ , (open triangle)  $\alpha_{\text{CTAB}} = 0$ , (closed triangle)  $\alpha_{\text{CTAB}} = 0.2$ , (open circle)  $\alpha_{\text{CTAB}} = 0.6$ , (star)  $\alpha_{\text{CTAB}} = 0.8$ , and 2 % Hexane. Fits are included as solid line. Data are offset by a factor of 3 for clarity.

Table 4.6, describes the fit of the mixtures with hexane parameters, and the only parameter has changed mostly is the core radius which decreases with increasing the CTAB mole fraction. In this table parameters from mixture/hexane solutions have been compared to those from the mixtures without hexane (values between brackets) and it is obvious that both are similar suggesting that mixtures do not mix with hexane as same as the pure surfactant solutions.

Mixtures with hexane, (CTAB mole fraction) / parameters	0.2	0.6	0.8
Volume fraction of solvent in the core, $\phi_{sol}$ $\pm 0.01$	0.02	0.05	0.03
“Core” radius, $R_{Core}$ /Å	27.9 (27.8)	26.5 (26.2)	21.8 (21.6)
Incoherent background scattering $B/cm^{-1}$ $\pm 0.01$	0.02	0.03	0.02
Ellipticity, $X$	1.2 (1.1)	1.1 (1.0)	1.2 (1.1)
$V_s (dry)/V_{Core}$	0.8 (0.9)	0.8 (0.9)	0.8 (1.0)

**Table 4.6 Parameters describing the fits of SANS data from the mixtures with hexane of 0.2, 0.6, 0.8 CTAB mole fraction solutions using a model that describes the micelle as a globular elliptical with some ionic character. Parameters between brackets are for the mixtures without oil.**

#### 4.6.2.2. Mixture/PFHH solutions

From figure 4.26, similar pattern to the hexane case in the scattering of the mixtures with a noticeable higher intensity at high  $Q$  in the mixture of 0.8 CTAB mole fractions. It is also similar to the mixtures without oil; mixtures are strongly characterized by the CTAB component as micelles in the emulsions show similar structure with increasing CTAB concentration.

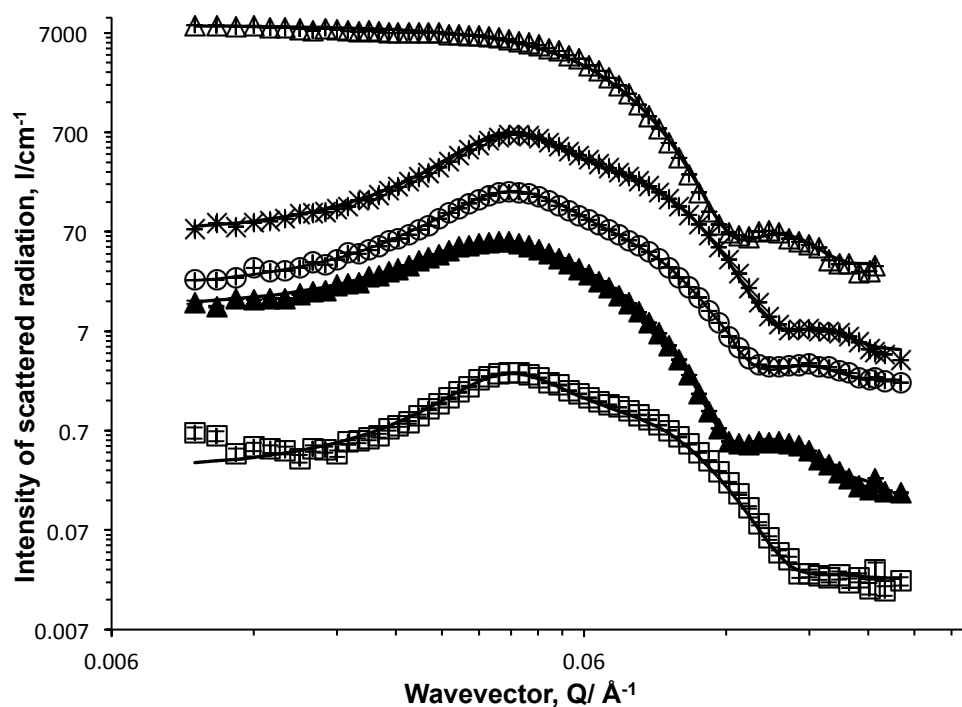


Figure 4.26 Small angle neutron scattering as a function of CTAB mole fraction, (open square)  $\alpha_{\text{CTAB}} = 1$ , (open triangle)  $\alpha_{\text{CTAB}} = 0$ , (closed triangle)  $\alpha_{\text{CTAB}} = 0.2$ , (open circle)  $\alpha_{\text{CTAB}} = 0.6$ , (star)  $\alpha_{\text{CTAB}} = 0.8$ , and 2 % perfluorohexane. Fits are included as solid line. Data are offset by a factor of 3 for clarity.

Mixtures with PFH (CTAB mole fraction)/ Parameters	0.2	0.6	0.8
Volume fraction of solvent in the core, $\phi_{sol}$ $\pm 0.01$	0.02	0.03	0.03
“Core” radius, $R_{core}$ /Å	27.9 (27.8)	26.6 (26.2)	21.9 (21.6)
Incoherent background scattering $B/cm^{-1}$ $\pm 0.01$	0.04	0.08	0.04
Ellipticity, $X$	1.2 (1.1)	1.0 (1.0)	1.2 (1.1)
$V_{s(dry)}/V_{Core}$	0.9	0.8	0.9

**Table 4.7 Parameters describing the fits of SANS data from the mixtures with PFH of 0.2, 0.6, 0.8 CTAB mole fraction solutions using a model that describes the micelle as a globular elliptical with some ionic character. Parameters between brackets are for the mixtures without oil.**

From table 4.7, parameters are similar to those from mixtures without oils (between brackets). Similar shapes of micelles are introduced and the core radius decreases with increasing the CTAB mole fraction consistent to the pattern from mixtures with no oil.

## 4.7. Conclusions

The cationic CTAB and non-ionic FSN-100 surfactants and their phase behaviour in the presence of hydrocarbon oil (hexane) and fluorocarbon oil (PFH) have been studied in this chapter by  $^1H$ -NMR,  $^{19}F$ -NMR, PGSE-NMR and SANS. The data show that both surfactants (CTAB & FSN-100) mix with neither hexane nor PFH and that has been shown consistently by all used techniques. This conclusion does not agree with the data in a very recent literature publication [7], which suggested that there is a great solubilisation between hexane and FSN-100. However, different surfactant concentrations and techniques have been used in the reference and that may suggest that the amount of oil used in the project here is not enough to be detected. This approach has been confirmed from all techniques used and all data are consistent indicating that at the surfactant concentration of 50 mM and 2 % of oil, there is no solubilisation of both oils with both surfactants.

From the mixing surfactant systems, which have been studied in Chapter Three, it was concluded that a different micellization process along a range of compositions has been investigated, and from SANS data the mixtures are strongly characterised by the CTAB component, and micelles have similar structure once different amounts of CTAB was added to the solution. The same behaviour is noticeable in the surfactant/oil solutions for the surfactant mixtures and in the presence of oil; mixed micelles are not able to accommodate hexane or PFH. This is noticeable from the similar micelle shapes of both mixtures with and without oils.

## 4.8. References

1. Yang, C.P., et al., *Effects of surfactants and salt on Henry's constant of n-hexane*. Journal of Hazardous Materials, 2010. **175**(1-3): p. 187-192.
2. Krafft, M.P., *Fluorocarbons and fluorinated amphiphiles in drug delivery and biomedical research*. Advanced Drug Delivery Reviews, 2001. **47**(2-3): p. 209-228.
3. Krafft, M.P. and J.G. Riess, *Chemistry, Physical Chemistry, and Uses of Molecular Fluorocarbon-Hydrocarbon Diblocks, Triblocks, and Related Compounds-Unique "Apblar" Components for Self-Assembled Colloid and Interface Engineering*. Chemical Reviews, 2009. **109**(5): p. 1714-1792.
4. Kissa, E., *Fluorinated surfactants and repellents*. Surfactant science series (2nd ed.). Vol. 97. 2001, New York: 97Marcel Dekker, Inc, New York. 607.
5. Kovalchuk, N.M., et al., *Fluoro- vs hydrocarbon surfactants: why do they differ in wetting performance?* Adv Colloid Interface Sci, 2014. **210**: p. 65-71.
6. Mukerjee, P. and T. Handa, *Adsorption of Fluorocarbon and Hydrocarbon Surfactants to Air-Water, Hexane-Water, and Perfluorohexane-Water Interfaces - Relative Affinities and Fluorocarbon-Hydrocarbon Nonideality Effects*. Journal of Physical Chemistry, 1981. **85**(15): p. 2298-2303.
7. Xiao Xiao, X.B.Y.J.F.X.X., *Absorption and recovery of n-hexane in aqueous solutions of fluorocarbon surfactants* Available online at [www.sciencedirect.com](http://www.sciencedirect.com). Journal of environmental sciences, 2015: p. 1-9.
8. Yeom, I.T., M.M. Ghosh, and C.D. Cox, *Kinetic aspects of surfactant solubilization of soil-bound polycyclic aromatic hydrocarbons*. Environmental Science & Technology, 1996. **30**(5): p. 1589-1595.
9. Fulmer, G.R., et al., *NMR Chemical Shifts of Trace Impurities: Common Laboratory Solvents, Organics, and Gases in Deuterated Solvents Relevant to the Organometallic Chemist*. Organometallics, 2010. **29**(9): p. 2176-2179.

## **Chapter Five**

### **The Application of Mixed Surfactant Systems to Template Hierarchical Nanoporous Materials**

## 5.1. Introduction

The synthesis of templated porous materials can be carried out using surfactant molecules dispersed in a solvent which are aggregated to form micelles and direct the pore structure when combined with the inorganic precursor (e.g.  $\text{Si}(\text{OEt})_4$ ). This can occur by one of the two methods described previously in Chapter One, A common example is when surfactant micelles form micellar rods and then aggregate together to form a hexagonal array in solution as an initial step in a liquid crystal templating mechanism [1], whereas in emulsion templating, oils are added to swell the micelles and provide an environment for the precursor molecules to condense around the template [2]. This work utilises both mechanisms as a hybrid, in which a swollen liquid crystalline template is used, or at least that was the hypothesis we explored.

In general, the shape and size of a micelle are controlled by the molecular geometry of the surfactant molecules and the solution conditions such as surfactant concentration, pH and temperature [3]. Various surfactants with different properties are used to introduce different porosity into materials [4-6]. For example, increasing the length of the alkyl chain in the surfactant can be used to increase pore diameter. In addition, the use of fluorinated surfactants can be used as templates to produce various mesostructures [7].

This part of the thesis will report the synthesis of hierarchical porous materials using mixed surfactant micelles (CTAB & FSN-100) based on their solution phase behaviour, which is covered in Chapters Three and Four. In this work, different amounts of oil (PFH) have been added to the mixed micelle surfactant solutions to examine whether structural differences in the synthesized materials in terms of their porosity and morphology may be induced. The volume percentage (V %) of PFH in the solution starts from 0 %, to 33 %. After calcination, the organic template has been removed and then different techniques have been used to characterize these materials including scanning electron microscopy (SEM), transmission electron microscopy (TEM), porosimetry and X-ray diffraction (XRD).

This chapter is laid out as follows; the scoping experiments are first presented, to outline the strategy taken in selecting further systems to explore.



## 5.2. System screening experiments

Two surfactants and two oils have been examined here. The hydrocarbon surfactant CTAB and Zonyl FSN-100, where the supplier literature suggests a structure of  $C_8F_{17}C_2H_4(OC_2H_4)_9OH$  or FSO-100,  $(CF_3(CF_2)_4-(EO)_{10})$  as fluorocarbon surfactants have been used. Hexane has been used as hydrocarbon oil combined with the fluorocarbon oil perfluorohexane (PFH). Samples here were characterized by, TEM and XRD following calcination to remove the organic template.

### 5.2.1. Using CTAB with Zonyl FSO-100 (FSO sample)

The surfactant FSO-100 has been used with the hydrocarbon surfactant CTAB with both oils hexane and PFH as a template. The characterization was based on TEM and X-ray diffraction. For an ordered hexagonal structure, three distinguished peaks are expected in the XRD pattern. For this sample no peaks were observed, (the curve is not included) suggesting the formation of disordered structure in this attempt. TEM image in figure (A1) in the Appendix gives further evidence of disordered structure that might describe foam structure. Further, it was not clear which component was the responsible of the disordered structure. However, a decision of not using the surfactant of FSO-100 was taken and another fluorocarbon surfactant was sourced.

### 5.2.2. Using FSN-100 surfactant (FSN sample)

FSN sample has been synthesized using only the fluorocarbon surfactant FSN-100. The TEM image for the FSN sample (figure A2 in the Appendix) shows obviously that the sample has neither clear morphology, nor disordered system. This experiment has been carried out to investigate the morphology of the material when the template is only FSN-100. Thus, the FSN-100 does not support formation of nanoparticles on its own and adding another surfactant is highly needed.

### 5.2.3. Using FSN-100 surfactant and PFH (FSN/PFH sample)

The template in this case is the fluorocarbon surfactant FSN-100 aqueous solution and PFH as an oil phase. Again, there is no obvious structure after calcination and removing the template as shown in the TEM image for FSN/PFH sample (figure A3 in the Appendix). This experiment was conceived to investigate the type of pores resulted from the template including the fluorocarbon surfactant and the oil but without using the hydrocarbon surfactant of CTAB.

#### 5.2.4. Using the template of FSN-100/ CTAB/PFH/hexane

This experiment represents the two surfactants and the two oils in the template, (CTAB, FSN-100) (PFH, hexane). Figure 5.1 shows TEM images of the sample at two different scales. Some regions describe ordered pores (figure 5.1 (a)), whereas foam structure (figure 5.1 (b)) is observed in some areas of the sample after calcination. It has been suggested that hexane expands the pores and makes foams, and higher surface area material ( $920 \text{ m}^2/\text{g}$ ) was produced. Excluding hexane from the template was the next step to see whether the foam structure was from hexane or not.

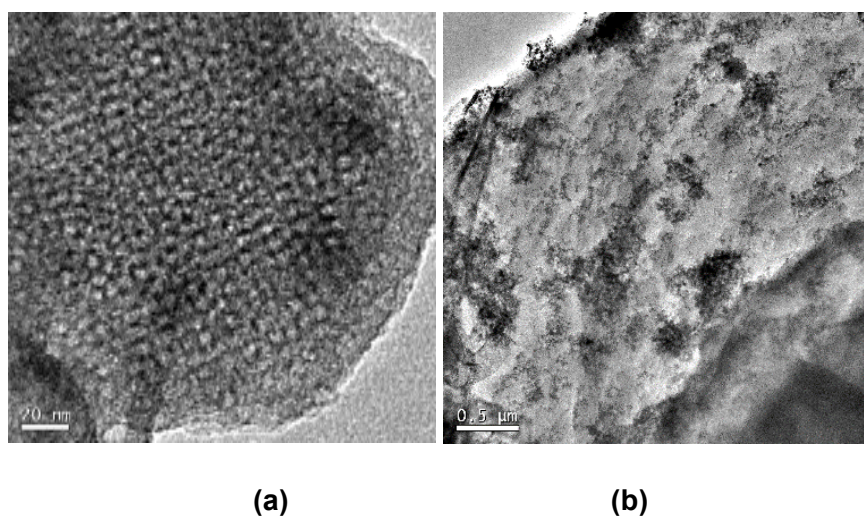


Figure 5.1 TEM images (a, b) of the sample FSN/ CTAB/PFH/ hexane.

#### 5.2.5. Using the template of FSN-100/CTAB/PFH

Figure 5.2 shows TEM image of the calcined material using the template of CTAB/ FSN-100/PFH and explains that micelles in the template are well organised to produce such pores. This image is the representative for the material as the material has stable solid structure. The material also possesses high surface area and well-ordered pores using various characterizations, which are going to be more focused in next sections.

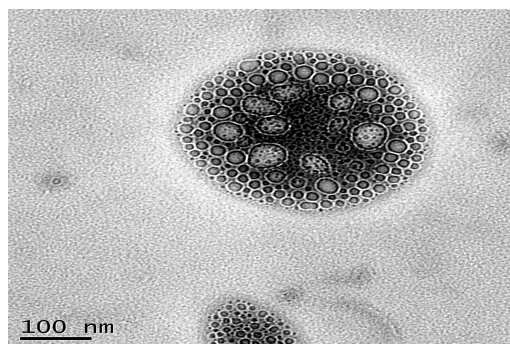


Figure 5.2 TEM image of the sample FSN/ CTAB/PFH.

Thus, from the last attempt, using the two surfactants (CTAB/FSN-100) and the oil PFH to template the materials has been considered and this template is taken further.

### 5.3. The synthesis of the comparator MCM-41

The last experiment to test the surfactant templating was the synthesis of MCM-41 as a comparator for the targeted materials. The experiment was based on the MCM-41 synthesis pathway presented previously [8].

The adsorption and desorption isotherms of nitrogen were performed at 77 K for MCM-41. Figure 5.3 shows the  $N_2$  isotherm and pore size distribution of the MCM-41. The isotherm is typically a type IV isotherm with gas adsorbed amount uptake between  $\sim 0.2$  and 0.4. The amount of adsorbed nitrogen increased gradually with an increase in relative pressure. The specific surface area according to the Brunauer, Emmett and Teller model (BET) and the average pore diameter according to the Barrett, Joyner and Halenda method (BJH) are  $1020.210 \text{ m}^2/\text{g}$  and  $3.01 \text{ nm}$  respectively, which are in a good agreement to the literature values [8].

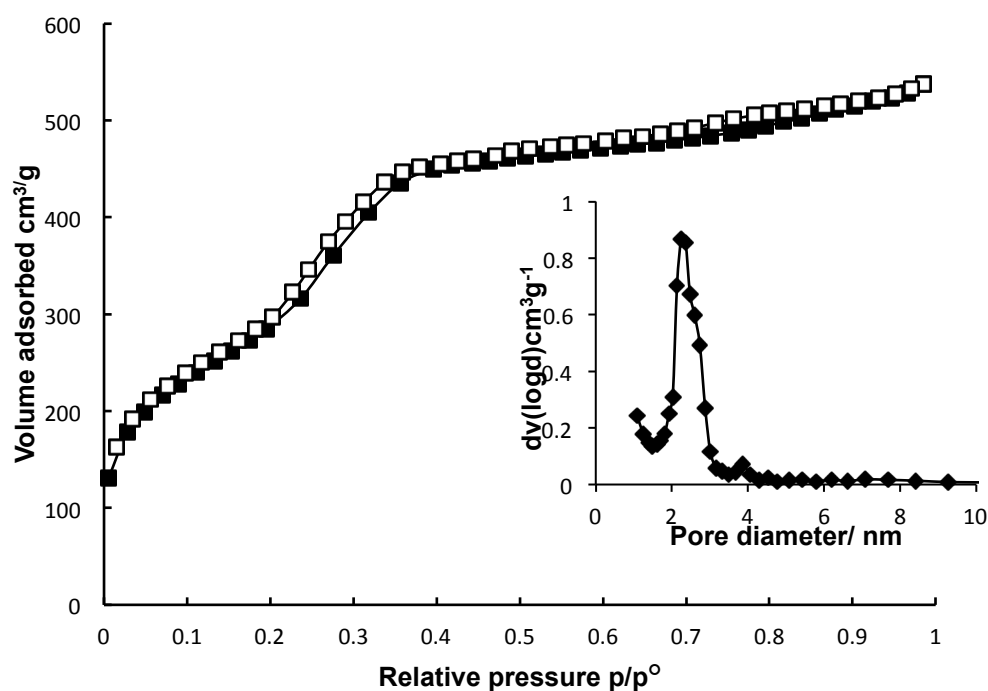


**Figure 5.3**  $N_2$  adsorption (closed square)-desorption (open square) isotherms and BJH pore size distribution (figure inside) of MCM-41 comparator.

Scanning electron microscopy has also been performed for MCM-41 to determine the particle size and morphology. It is clear that most of the particles are spherical in form and the particle size ranges from 400 to 1000 nm (figure 5.4).

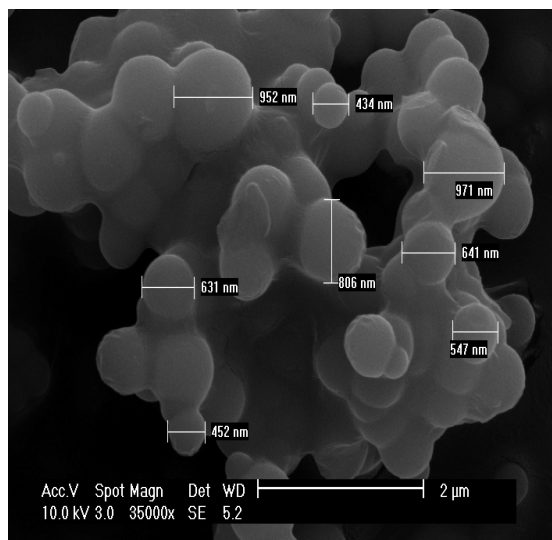


**Figure 5.4 Scanning electron microscopy image of MCM-14 comparator.**

From these results, the MCM-41 synthesis pathway [8] was adjusted to include the fluorocarbon surfactant FSN-100 and perfluorohexane as an oil phase in order to create an additional type of pores in a hierarchical material pore structure.

## 5.4. CTAB/FSN/PFH based systems

Due to the previous findings, the system of two surfactants FSN-100 and CTAB with the fluorocarbon oil (PFH) has been adopted to template different porous materials. Different amounts of oil in the surfactant mixture were used to investigate how that affects the porosity system of the synthesized materials.

Six samples have been prepared due to the different oil amounts in the template, starting from no oil sample 0 % and then 1 %, 11 %, 20 %, 27 % and 33 % (oil V/ V%). All samples have been characterized and studied individually to discuss the porosity in terms of the material surface area and pore size distribution as well as the morphology of ordered structures. Table 5.1 includes sample details, which represent the template components.

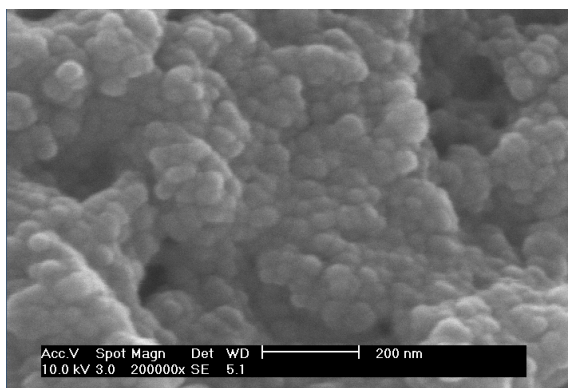
Sample (V%)	Sample details
0 %	CTAB/FSN-100/H <sub>2</sub> O
1 %	CTAB/FSN-100/H <sub>2</sub> O/ (0.4 ml) PFH
11 %	CTAB/FSN-100/H <sub>2</sub> O/ (5 ml) PFH
20 %	CTAB/FSN-100/H <sub>2</sub> O/ (10 ml) PFH
27 %	CTAB/FSN-100/H <sub>2</sub> O/ (15 ml) PFH
33 %	CTAB/FSN-100/H <sub>2</sub> O/ (20 ml) PFH

**Table 5.1 Sample details and abbreviations.**

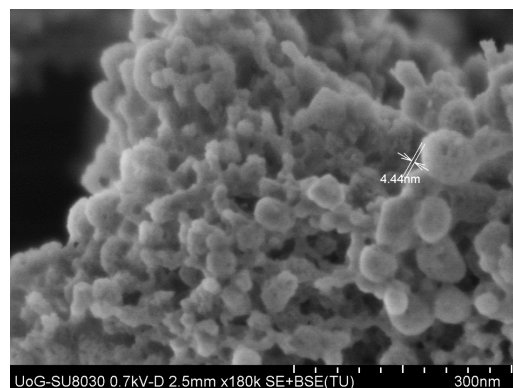
## 5.5. Scanning electron microscopy (SEM)

Scanning electron microscopy has been used to have an idea about the particle size, particle morphology and the particle size distribution of the synthesized materials. The particle size for all measured samples are in the same range and only three samples will be shown in this section as examples.

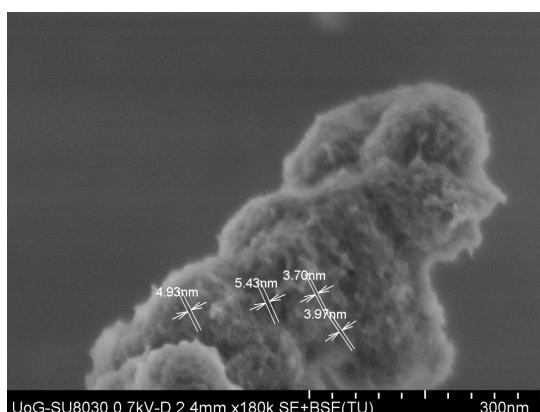
Figures 5.5 shows SEM images for particles prepared using 0 %, 20 % and 33 % (PFH) after calcination. It is clear that most particles are spherical with different diameters but some agglomerates are associated with the 33 % sample. Hollow silica spheres are also visible in 20 % sample (figure 5.5 (b)) and more irregular arrangements like sponge are connected to 33 % sample indicating different material pore morphology varying with oil content (figure 5.5 (c)). This confirms that oil amount has an influence on particle morphology.



(a) 0 % sample



(b) 20 % sample



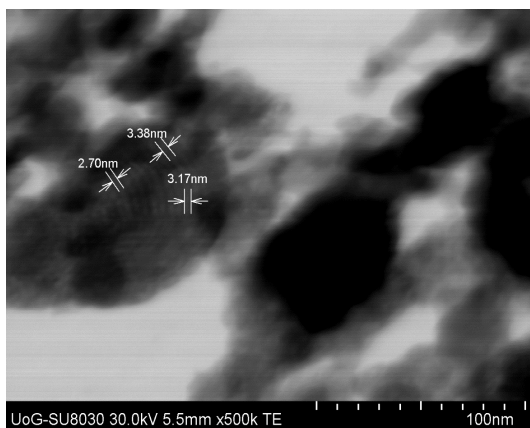
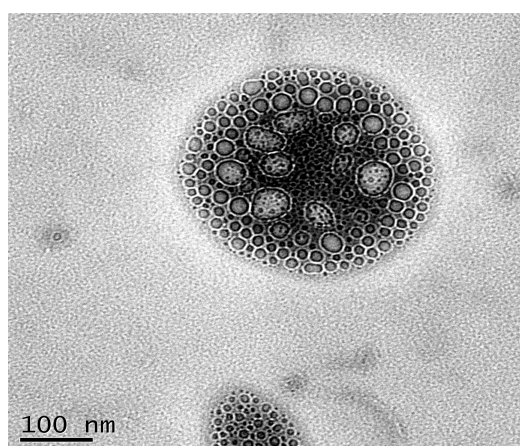
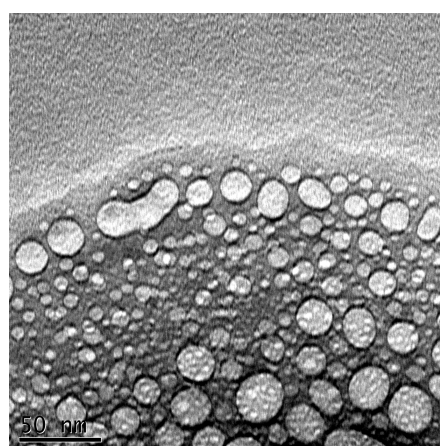
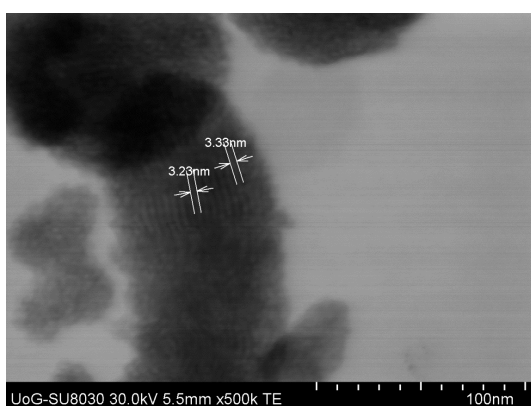
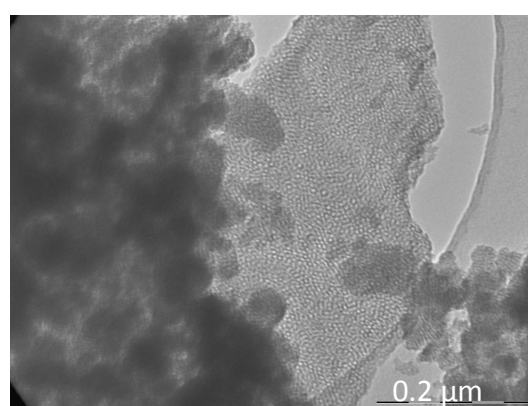
(c) 33 % sample

Figure 5.5 SEM images of the samples, 0 % (a), 20 % (b) and 33 % (c).

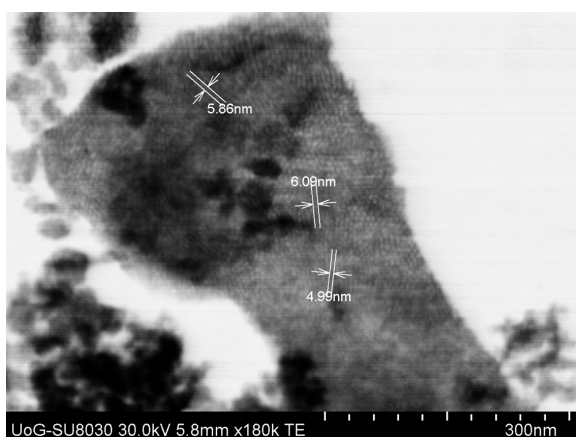
## 5.6. Transmission electron microscopy (TEM)

Pore arrangements have been evaluated using transmission electron microscopy (TEM), which shows that the typical hexagonal structure and channels of mesoporous materials are retained in most cases.

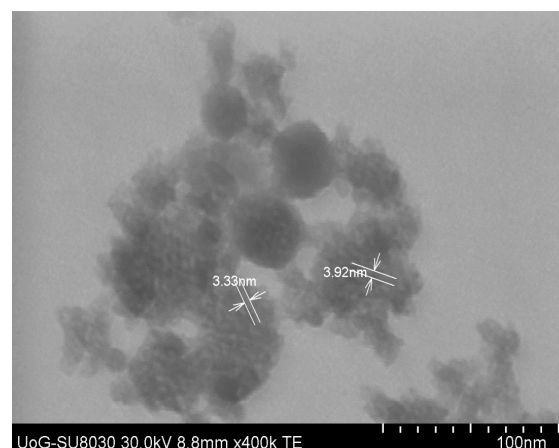
All TEM images of synthesized materials will be shown in this section, as different pore arrangements are visible over the range of template compositions. Long order and well-defined structure have been achieved in most samples with few differences in pore sizes. Most interesting TEM images have been collected from the 1 % sample (figure 5.6 (b & b')), and clearly that surfactant micelles in the template are well organised to produce such pores with a high organised morphology. Further, once oil is added to the template pores become more regular and the surfactant mixtures can make more regular micelles to make such pores at this specific phase composition. Similar regularity continues over the range of compositions in the rest of samples (see images c', d, f and f' in figure 5.6). However, two types of pores are produced in 1 % and 33 % samples, which may suggest the bimodal pore size distribution as small and large mesoporous material or as meso-macro pores which is going to be tested by N<sub>2</sub> isotherm measurements (see b & f in figure 5.6).

**(a) 0 % sample****(b) 1 % sample****(b') 1 % sample****(c) 11 % sample****(c') (scale 0.2 μm), 11 % sample**

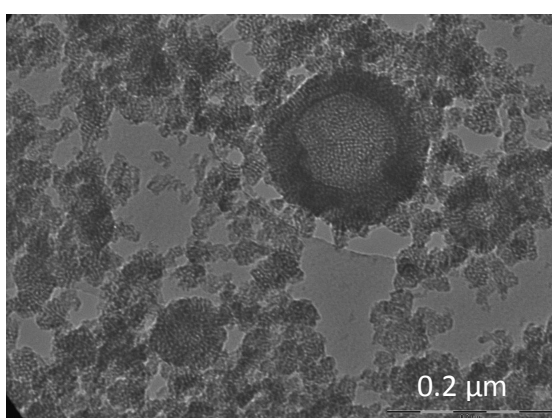




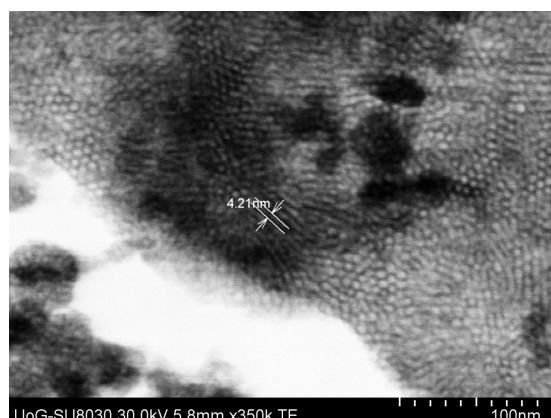
(d) 20 % sample



(e), 27 % sample



(f) 33 % sample



(f') 33 % sample

**Figure 5.6** TEM images of the samples, 0 % (a), 1 % (b) & (b'), 11 % (c) & (c'), 20 % (d), 27 % (e) and 33 % (f) & (f').

## 5.7. Porosimetry characterization

Gas adsorption is one of the most important measurements to characterize nanoporous materials. Nitrogen adsorption-desorption isotherms were used to estimate the specific surface areas using Brunauer, Emmett and Teller method (BET), and the use of nitrogen adsorption to analyse the pore size distributions using the Barrett, Joyner and Halenda (BJH) method, which is based on the Kelvin equation [9, 10].

### 5.7.1. N<sub>2</sub> adsorption- desorption isotherms

Nitrogen adsorption-desorption isotherms have been obtained for each sample to investigate the porosity system of the materials. All samples were outgassed before measurements were performed. The gas adsorption starts to form a monolayer on the surface and then multilayer and then the capillary condensation occur. This procedure

is strongly related to the porosity type as micropores filling occurs at low pressure at ( $P/P^\circ < 10^{-4}$ ), whereas high pressure is required to fill mesopores and start the capillary condensation and macropores ( $> 50$  nm) filling occurs only at very high  $P/P^\circ$ . Thus, the shape of the plot of adsorbed amount of  $N_2$  versus the relative pressure indicates the porosity system.

In addition, based on  $N_2$  isotherm types presented previously in the introduction (Chapter One), different types of  $N_2$  isotherms with an observed hysteresis loop have been collected from the six materials (figures 5.7 - 5.10). The observations confirm the gas capillary condensation in the pores from 2 and 50 nm (mesopores) [11]. Each isotherm will be discussed individually in the next sections.

### 5.7.1.1. N<sub>2</sub> isotherm of 0 % sample

Figure 5.7 shows a typical N<sub>2</sub> isotherm of the 0.0 % sample. The adsorption branch coincides with the desorption branch until about  $P/P^\circ = 0.9$ , and then the isotherm is slightly broadened to provide a hysteresis loop which appears in the multilayer range of isotherms. This type of isotherm suggests type II isotherm and it is closer to the type V hysteresis loop, suggesting mesopore filling and capillary condensation presenting a different type of porosity compared to the other samples.

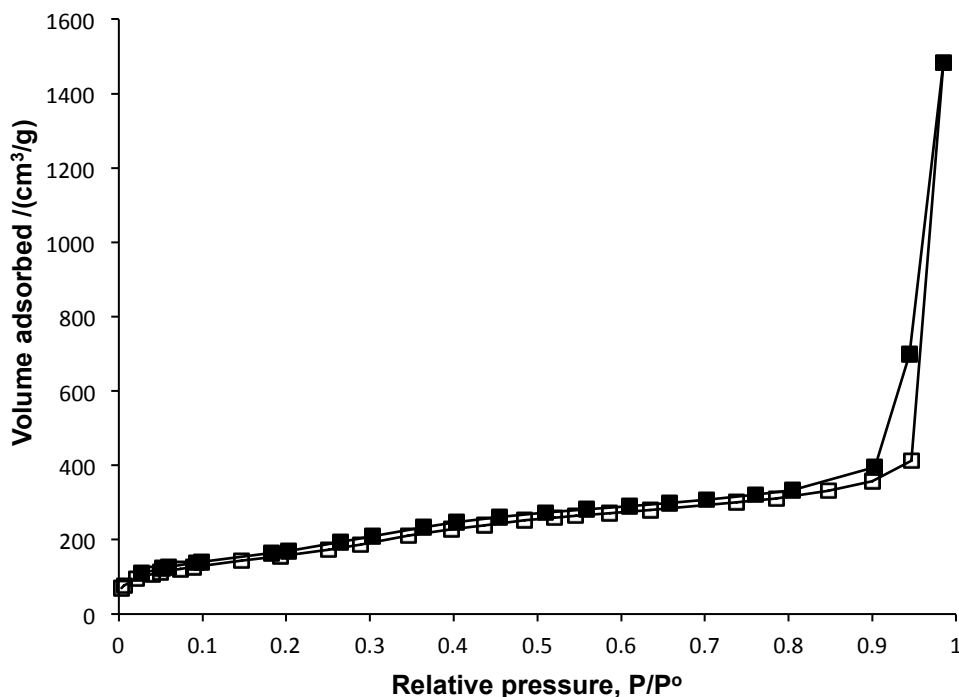
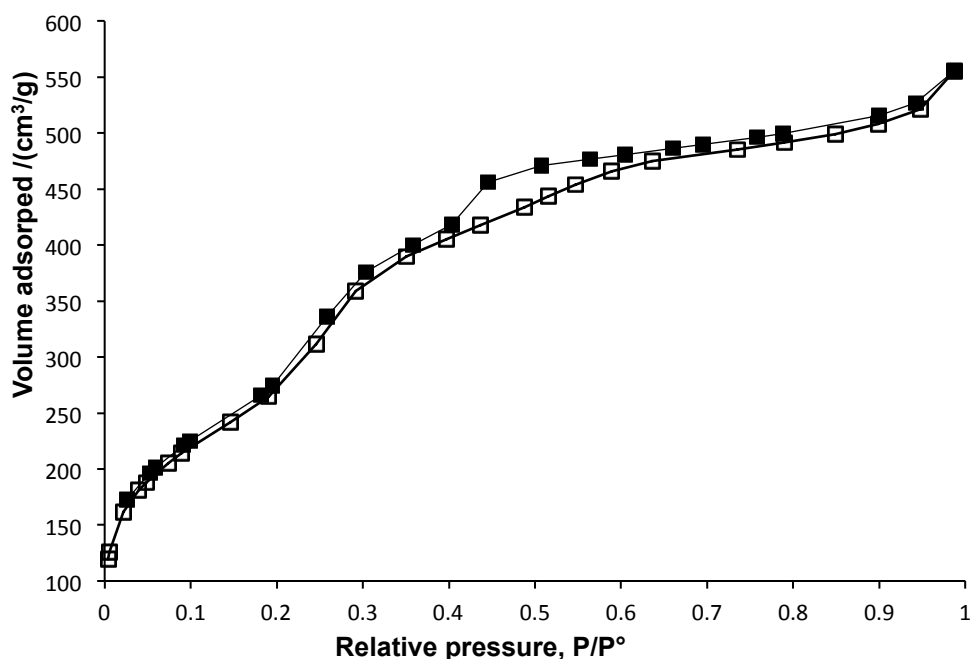


Figure 5.7 N<sub>2</sub> adsorption (open square)-desorption (closed square) isotherms for 0 % mesoporous sample.

### 5.7.1.2. N<sub>2</sub> isotherm of 1 % sample

A different type of isotherm is observed from 1 % sample suggesting a different type of porosity from the previously discussed sample. Figure 5.8 shows type IV isotherm, which indicates the capillary condensation in meso and macropores. In the isotherm, the closure of  $P/P^\circ$  is at about 0.4 which therefore corresponds to the lower limit of capillary condensation hysteresis.



**Figure 5.8** N<sub>2</sub> adsorption (open square)-desorption (closed square) isotherms for 1 % mesoporous sample.

### 5.7.1.3. N<sub>2</sub> isotherm of 11 %, 20 % and 27 % samples

Similar shape of isotherms has been collected from samples 11 %, 20 % and 27 %. The adsorption branch in these samples coincides with the desorption branch until about 0.8 and then the isotherm is broad. Type V isotherm is presented from these three materials suggesting a different pore order and regularity. Figure 5.9 shows the isotherm of 11 % samples as an example for the three materials.

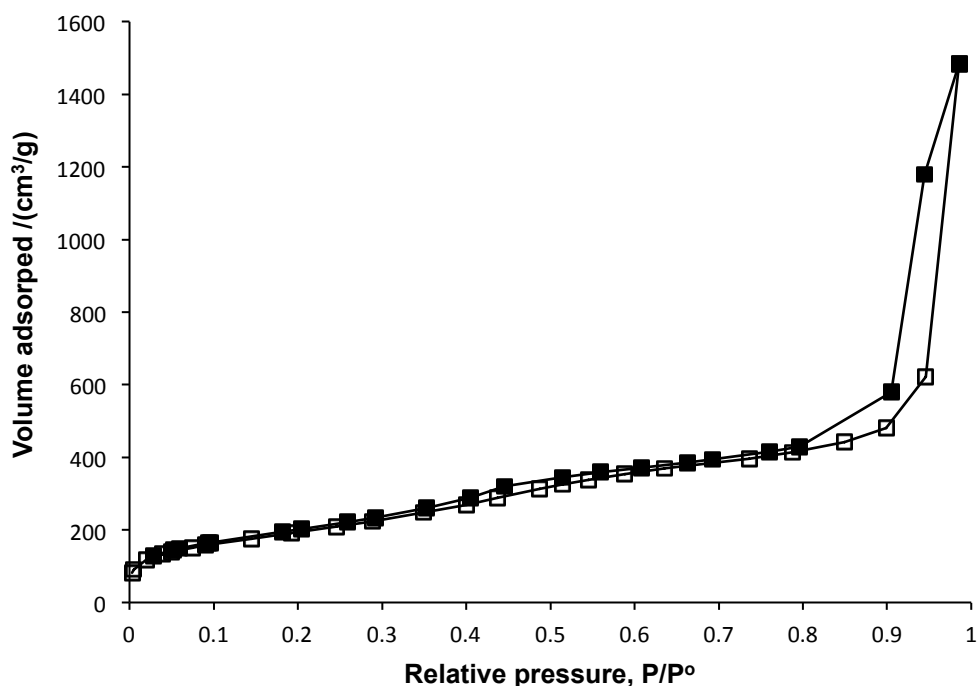
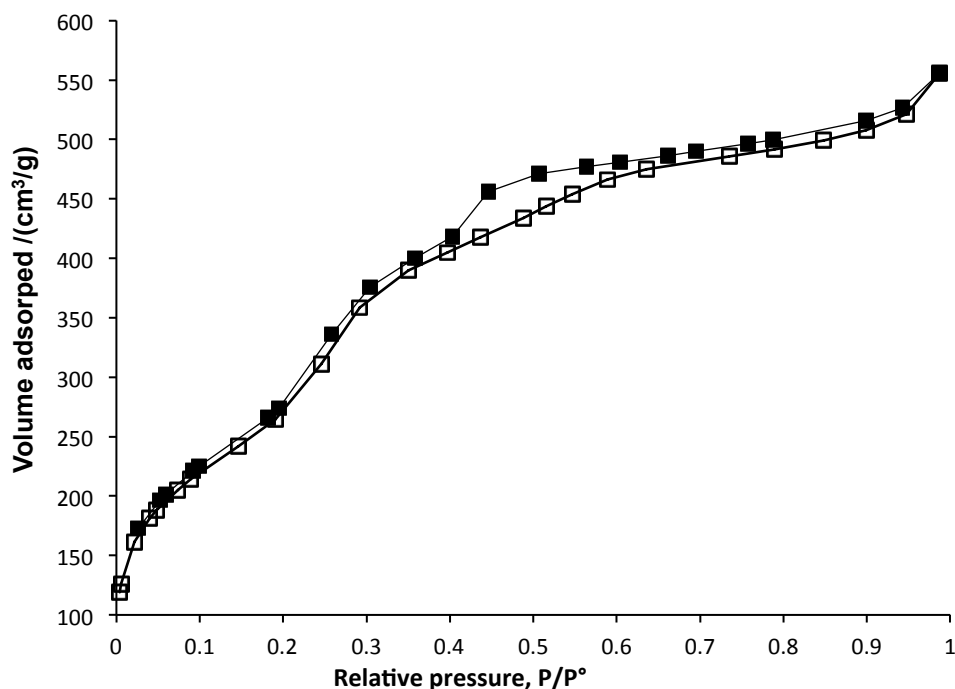


Figure 5.9 N<sub>2</sub> adsorption (open square)-desorption (closed square) isotherms for 11 % mesoporous sample.

#### 5.7.1.4. N<sub>2</sub> isotherm for 33 % sample

Again due to specific features, the two templates of 1 % and 33 %, produced materials after calcination that exhibit similar pore structure and regularity and are quite different from all the other samples. Figure 5.10 shows N<sub>2</sub> isotherm from the 33 % sample, and the adsorbed amount of N<sub>2</sub> increased gradually with increasing the relative pressure by multilayer adsorption. The uptake of the adsorbed amount was also around the relative pressure of 0.4, which provides a similar hysteresis to that one in 1 % sample.



**Figure 5.10** N<sub>2</sub> adsorption (open square)-desorption (closed square) isotherms for 33 % mesoporous sample.

Considering the data for the samples overall, 1 % and 33 % show similar adsorption behaviour and porosity system and they are different from other materials as will be obvious in all measured parameters over the next sections.

### 5.7.2. BET specific surface area

The specific surface area according to the BET equation has been estimated for all synthesized materials using the  $N_2$  isotherms. Figure 5.11 shows a comparison of the BET specific surface areas of all samples. Lower surface area is related to the 0 % sample (577  $m^2/g$ ) and once oil is added to the template, specific surface area of materials has increased.

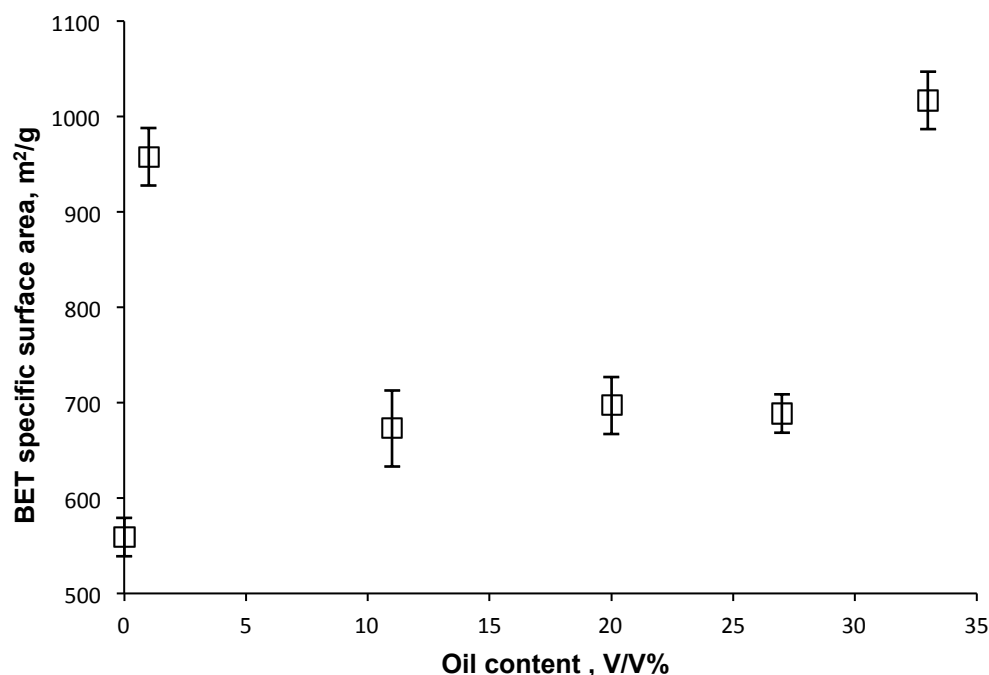


**Figure 5.11** BET surface area vs oil volume in the template of samples 0 %, 1 %, 11 %, 20 %, 27 % and 33 %.

It is also clear that the highest surface area is for 1 % and 33 % samples (969 and 1090  $cm^2/g$  respectively) (see table 5.2). Further, the three samples in the middle (11 %, 20 % and 27 %) of the oil phase structured have almost the same surface area value suggesting that increasing the oil volume over this range, it does not affect the surface area, the isotherm shape or the pore structure at these three samples. These differences between the samples (1 %, 33 %) and the rest have been confirmed by the isotherm and TEM images as well as by X-ray diffraction as will be shown in the next sections.

### 5.7.3. Pore size determination

The average pore diameter has also been estimated from desorption isotherms using the BJH method. From table 5.2, it is observed that the pore diameter increases slightly from 2.5 nm to 3.3 nm when only 1 % of oil has been added to the template and for the rest of samples pore diameters are in the same range.

Oil volume in the template/ V%	Surface area/ m <sup>2</sup> /g ( $\pm 10$ )	Pore diameter/ nm ( $\pm 0.1$ )	Pore volume/ cm <sup>3</sup> /g ( $\pm 0.1$ )
0	577	2.49	2.32
1	969	3.27	2.24
11	702	3.40	2.34
20	716	3.39	2.33
27	707	3.42	2.38
33	1090	2.78	1.12

**Table 5.2 N<sub>2</sub> porosimetry parameters for synthesized materials obtained at different oil volume ratios.**

From table 5.2, comparing samples templated with oil, samples, which have high surface area have also the lowest pore diameter and pore volume and they are different from the rest of samples. Since, all materials have been prepared in the same conditions, and the difference is only in the quantity of the oil added to the template, the variety of porosity systems is strongly related to the amount of oil raised in each experiment.

The values of pore diameter and pore volume for all synthesized materials and how that relates to the oil content in templates are shown in figure 5.12. Values are not in a linear relationship, but they explain the differences in the intermediate materials from the samples 1 % and 33 %.



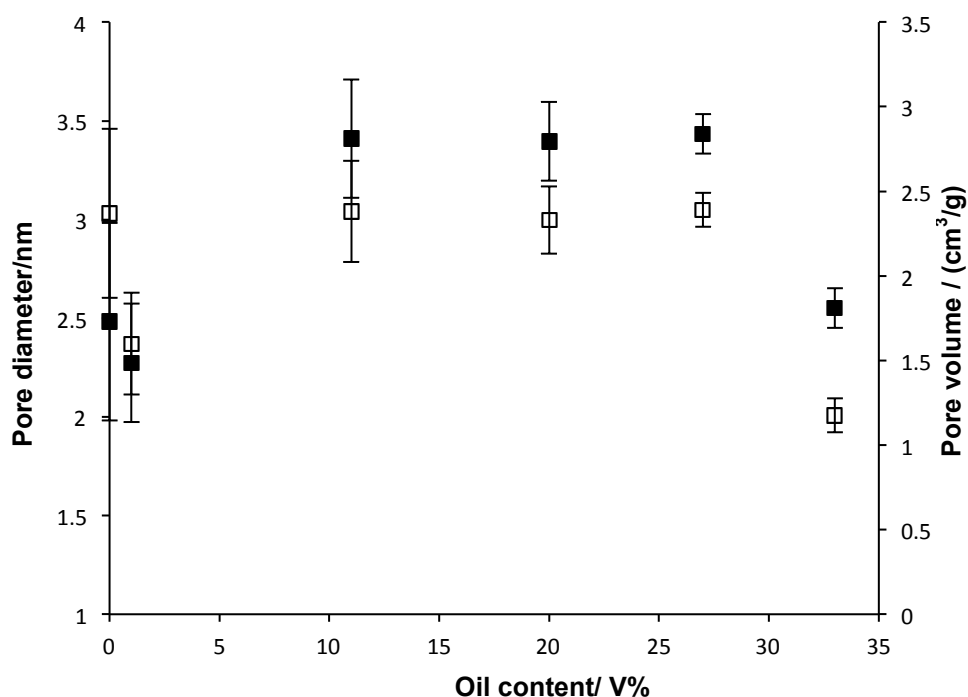


**Figure 5.12** Pore diameter (closed square) and pore volume (open square) vs oil content in the template of samples 0 %, 1 %, 11 %, 20 %, 27 % and 33 %.

From figure 5.12, the lowest pore diameter and pore volume were found for 1 % and 33 % samples, whereas 11 %, 20 % and 27 % have similar values to each other consistent with the BET surface area differences.

In terms of the BJH pore size distribution of each sample, different distributions have been collected from the six materials. Figure 5.13 shows the BJH pore size distribution of the sample synthesized from the template without oil (0 % sample). The figure shows one peak as one type of pores is presented in this sample.

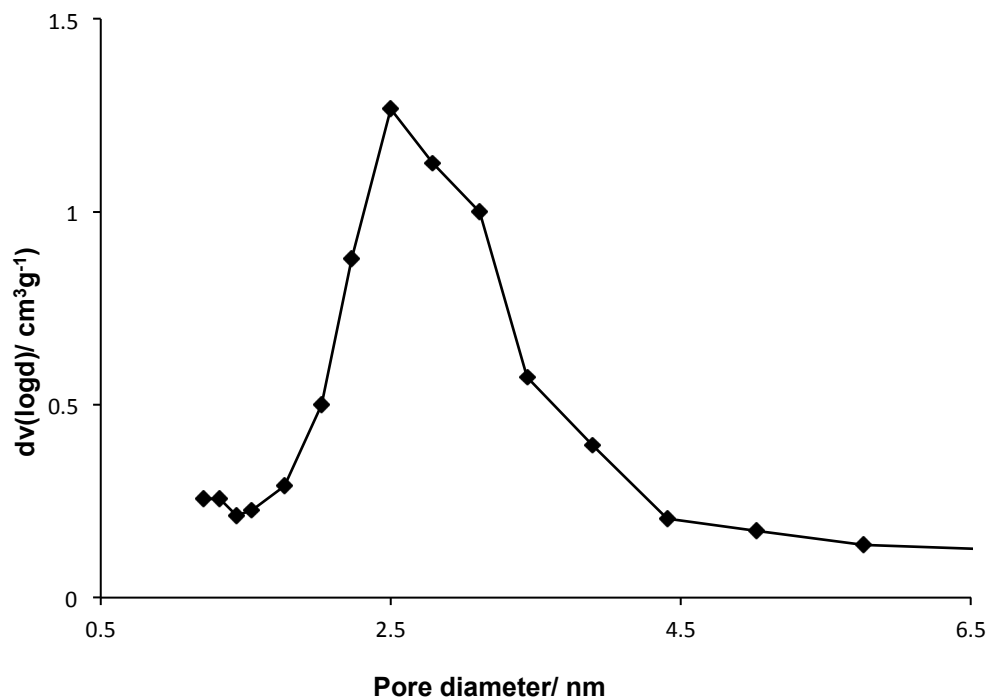


Figure 5.13 BJH pore size distribution of 0 % sample.

Further, the quantity of oil has similar effect on the pore size distribution in samples 11 %, 20 % and 27 %, one type of pores are presented in these samples. Again, this is consistent with their TEM images, surface areas and pore diameters. Figure 5.14 represents the pore size distribution of 18.5 % sample as an example, which is similar to that in the other two samples (11 %, 27 %) (Figures are not shown to avoid repeating).

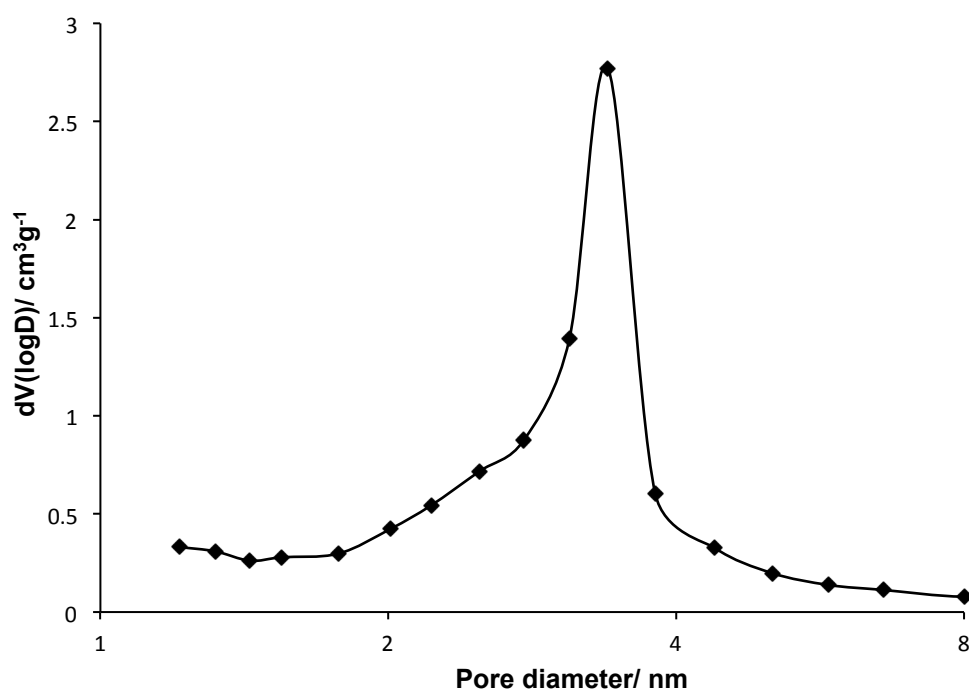


Figure 5.14 BJH pore size distribution of 20 % sample.

However, the BJH pore diameter distribution of 1 % and 33 % samples exhibit two well-defined maxima for the material suggesting formation of bimodal mesoporous silica (figures 5.15 & 5.16).

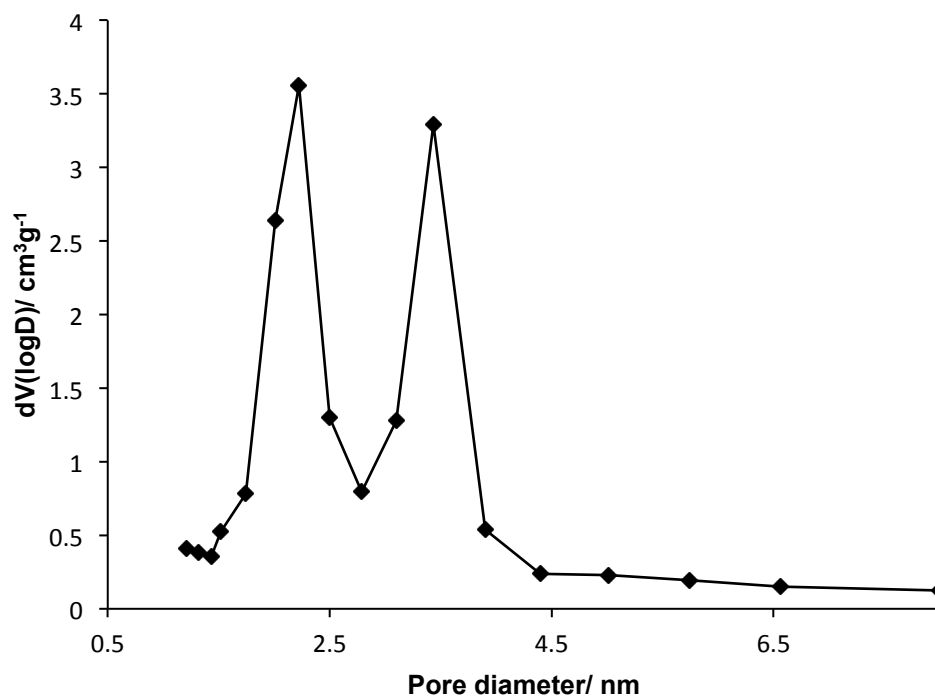


Figure 5.15 BJH pore size distribution of 1 % sample.

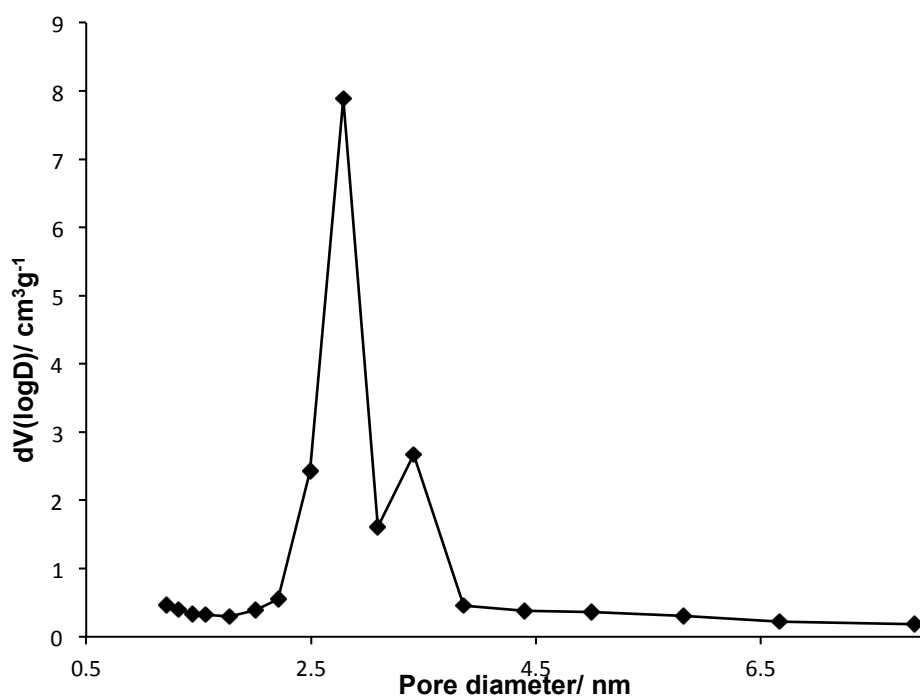
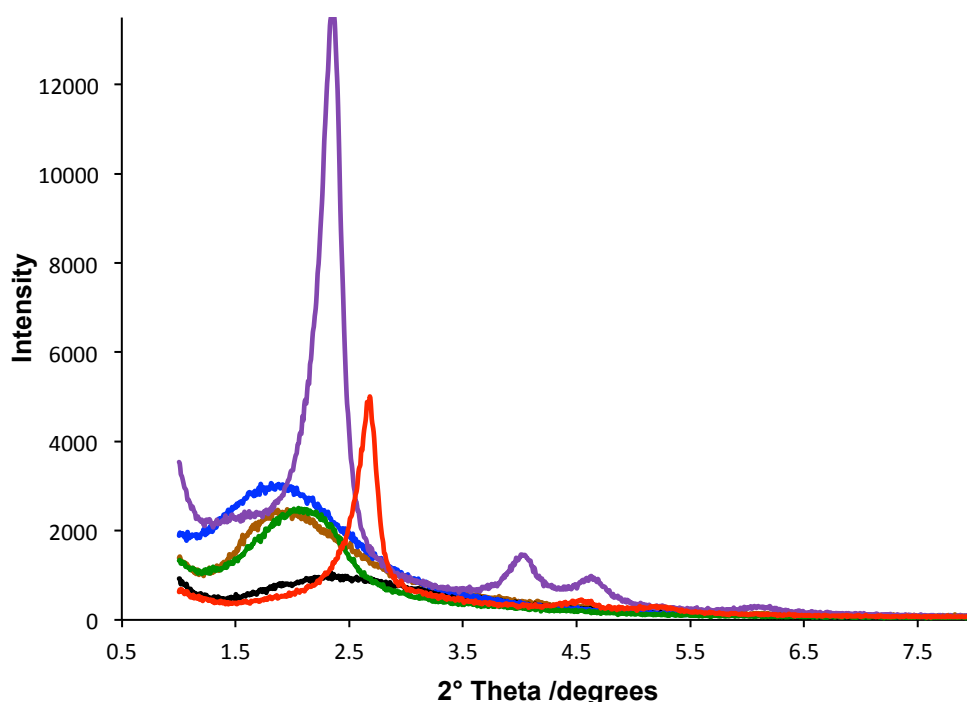


Figure 5.16 BJH pore size distribution of 33 % sample.

To conclude the porosimetry findings, samples 1 % and 33 % have similar isotherms, and higher specific surface areas comparing to other materials. This is consistent with the collected TEM images, which described more homogeneous and ordered porosity system in both cases. Samples of 11 %, 20 % and 27 % showed similar values of surface area, pore volume and pore diameter.

## 5.8. X-ray Diffraction (XRD)

XRD patterns for all synthesized materials are compared in figure 5.17. Interestingly, once oil is added to the mixed surfactant template the intensity of the first peak becomes stronger in XRD curves, so using the template without oil does not indicate a strong long structural order from the XRD curve of the 0 % sample (black line in figure 5.17). The figure shows that 33 % and 1 % have well-ordered structures and the oil volume in these samples suggests a favourable phase composition for the formation of the target structure. This was indicated by the three obvious Bragg peaks at low angle ( $2\theta$ ) between 2-7°. These three distinct reflections suggest the lattice parameters of 100, 110 and 200, which are strongly related to the hexagonal structure of pore morphology.



**Figure 5.17** XRD patterns of samples 0 % (black), 1 % (red), 11 % (brown), 20 % (green), 27 % (blue) and 33 % (purple).

From XRD curves,  $d$ -spacing or the Layer spacing and pore spacing of the first reflection have been calculated using Braggs Law, and the values of diffraction angle  $\theta$  have been estimated from each curve (table 5.3). The table shows that the samples 11 %, 20 % and 27 % have  $d$ -spacing and pore spacing values in the same range as each other. However, 1 % and 33 % samples, which have more regular pores based on their XRD curves, have also lower pore parameters.

Oil volume in the template/V%	$2^\circ\theta$ , $d$ spacing, nm ( $\pm 0.01$ )	Pore spacing, a/nm ( $\pm 0.02$ )
0	2.36, 3.73	4.31
1	2.66, 3.32	3.84
11	1.95, 4.52	5.22
20	2.01, 4.40	5.09
27	1.92, 4.58	5.29
33	2.34, 3.77	4.36

**Table 5.3 Pore structure parameters from XRD measurements.**

To summarize XRD findings, the well-ordered structures have been observed in the samples of 1 % and 33 % due to the obvious peaks collected from such hexagonal structures. The peak intensity of 0 % sample is the lowest comparing to other samples templated with the oil whereas the intensity of the first peak has increased with increasing the amount of oil in the template. This suggests the importance of oil in the template to possess well-ordered porosity system with regular morphology.

## 5.9. Conclusions

To conclude, the concept of fabricating hierarchically bimodal mesopore structures using surfactant mixtures templating approach was investigated in this chapter. To summarize the observations of measured techniques, long range ordering and porosity were observed in most prepared samples particularly at the 1 % and 33 % templates. Both of these materials possess bimodal pore diameter distribution, high surface areas resulted from N<sub>2</sub> porosimetry, and more regular pore systems based on XRD curve patterns. That was also consistent with the collected TEM images from the two samples since, the pores with different sizes and well-organized porosity with a higher degree of regularity can be observed from their images.

Further, these data indicate the importance of the role of PFH in surfactant mixture systems to template nanoporous silica. This was the hypothesis needed to explore since the PFH was added to make swollen liquid crystalline template. Once the oil is added to the template, the resulting materials had higher BET surface areas and more regular pores. All intermediate oil contents (11 %, 20 % and 27 %) have similar conclusion in each characterization, suggesting similar pore structures are connected to these samples. However, the samples 1 % and 33 % possess high pore order regularity and high surface areas comparing to the rest of the samples.

Both surfactants did not show a clear mixing behaviour with the oil PFH as studied in Chapter Four. The shape and size of the mixed micelles were presented in the presence of PFH are similar to those in the case of absence of oil suggesting that there is no evidence of the solubility of PFH in the mixed micelles too with exception of the mixture of 0.5 CTAB mole fraction which possessed different behaviour with the oil in the PGSE data analysis. Thus, the swollen micelles behaviour is not able to explain the difference in the structure of the templated materials once PFH is added to the template. However, since materials with more regular porosity systems and higher surface areas were associated to the use of surfactant/oil template, the system after adding the TEOS needs to be analysed. This will help to investigate how adding TEOS to the templating makes such changes associated to the amount of oil. In addition, the variety of the porosity systems within the samples formed in oil is not yet justified and that may require the synthesis of more materials to expand the range of surfactant/oil compositions. That also helps to understand the advantage of the template in 1 % and 33 % samples as they have higher surface areas and more regular pores than other materials.

Nonetheless, all synthesized porous materials obtained can be used further to form catalysts, and in the next chapter grafting approaches will be considered to obtain this in a suggesting future work of the application of these materials. `

## 5.10. References

1. Pal, N. and A. Bhaumik, *Soft templating strategies for the synthesis of mesoporous materials: Inorganic, organic-inorganic hybrid and purely organic solids*. Advances in Colloid and Interface Science, 2013. **189**: p. 21-41.
2. Imhof, A. and D.J. Pine, *Ordered macroporous materials by emulsion templating*. Nature, 1997. **389**(6654): p. 948-951.
3. Attard, G.S., J.C. Glyde, and C.G. Goltner, *LIQUID-CRYSTALLINE PHASES AS TEMPLATES FOR THE SYNTHESIS OF MESOPOROUS SILICA*. Nature, 1995. **378**(6555): p. 366-368.
4. Gao, F., et al., *Phase Separation of Mixed Micelles and Synthesis of Hierarchical Porous Materials*. Langmuir, 2014. **30**(38): p. 11284-11291.
5. Jana, S.K., A. Mochizuki, and S. Namba, *Progress in pore-size control of mesoporous MCM-41 molecular sieve using surfactant having different alkyl chain lengths and various organic auxiliary chemicals*. Catalysis Surveys from Asia, 2004. **8**(1): p. 1-13.
6. Sel, O., et al., *Principles of hierarchical meso- and macropore architectures by liquid crystalline and polymer colloid templating*. Langmuir, 2006. **22**(5): p. 2311-2322.
7. Rankin, S.E., et al., *Fluorinated surfactant templating of ordered nanoporous silica*. Self-Assembled Nanostructured Materials, 2003. **775**: p. 47-52.
8. Grun, M., et al., *Novel pathways for the preparation of mesoporous MCM-41 materials: control of porosity and morphology*. Microporous and Mesoporous Materials, 1999. **27**(2-3): p. 207-216.
9. Barrett, E.P., L.G. Joyner, and P.P. Halenda, *The Determination of Pore Volume and Area Distributions in Porous Substances .1. Computations from Nitrogen Isotherms*. Journal of the American Chemical Society, 1951. **73**(1): p. 373-380.
10. Joyner, L.G., E.P. Barrett, and R. Skold, *The Determination of Pore Volume and Area Distributions in Porous Substances .2. Comparison between Nitrogen Isotherm and Mercury Porosimeter Methods*. Journal of the American Chemical Society, 1951. **73**(7): p. 3155-3158.



11. Wang, X., Bu, X. and Feng, P. , *Porous Inorganic Materials.* , in *Encyclopedia of Inorganic Chemistry.* . 2006. p. 1-21.

## **Chapter Six**

### **Further studies and Future Work**

## 6.1. Introduction

Catalysis - an essential application for nanoporous materials - has been studied to describe their efficiency. This chapter includes some further studies and suggestions of future work for the materials synthesized in Chapter Five, as well as a preliminary assessment to these materials as catalysts.

Having synthesized a series of mesoporous materials, the next step was to assess their suitability as catalytic supports. The first reaction was to functionalize their surface structure by grafting of alkoxysilanes followed by an oxidation reaction to attach organic functional groups to the surface. Active sites are created at the surface of the catalyst for use in heterogeneous catalysis reactions. This method also generates a new class of ordered hierarchical sulfonic acid functionalized silicas without the risk of pore blockage [1]. Grafting reactions and their subsequent oxidations have been evaluated by the thermal gravimetric analysis (TGA) and X-ray photoelectron spectroscopy (XPS) techniques. Further, the sulfonic acid functionalized silicas (grafted materials) have been used to enhance the rate of esterification of palmitic acid ( $C_{16}$ FFA) with methanol. The conversion rate and the catalytic reactivity have been characterized by gas chromatography (GC). Overall, this chapter will focus on the efficiency of the synthesized nanoporous materials as catalysts. Four materials (0%, 1%, 11% and 33%) synthesized in Chapter Five were used as catalyst support here and studied in this application part of the thesis to see whether the difference in the amount of the oil PFH (perfluorohexane) has affected the ability of the catalyst.

## 6.2. Grafting materials

Sulfonic acid functionalization was performed via post- synthesis grafting reaction on four samples of the nanoporous materials. Grafting of mercaptopropyl thiol groups has been performed on the synthesized materials, and their subsequent oxidation to produce tethered sulfonic acid centres ( $RSO_3H$ ) attached to the surface [2] (figure 6.1). Grafting reactions were evaluated by TGA and XPS techniques. Each technique provides the quantity of sulfonic acid loading, thermal stability and calculated the sulfur content (S content) attached to the surface of the material.

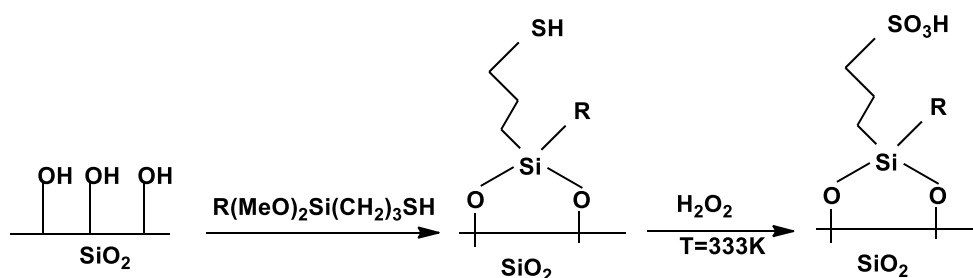


**Figure 6.1** A schematic representation of the sulfonic acid functionalization reaction.

### 6.2.1. Thermal gravimetric analysis (TGA)

TGA experiments have been used to test the thermal stability of the grafted materials as well as to calculate the S content across the series. Figure 6.2 shows TGA curves for [0 %, 1 %, 11 % and 33 %] grafted materials. It is obvious that the weight loss percentages increased with increasing the oil content (PFH) in the mesoporous material series. The first loss at temperatures less than 200 °C (not shown) characterises the desorption of water from the pores or material surfaces [3]. Water loss has been excluded from figure 6.2, to clarify the other loss, which is more important in order to calculate the decomposition of the organic components.

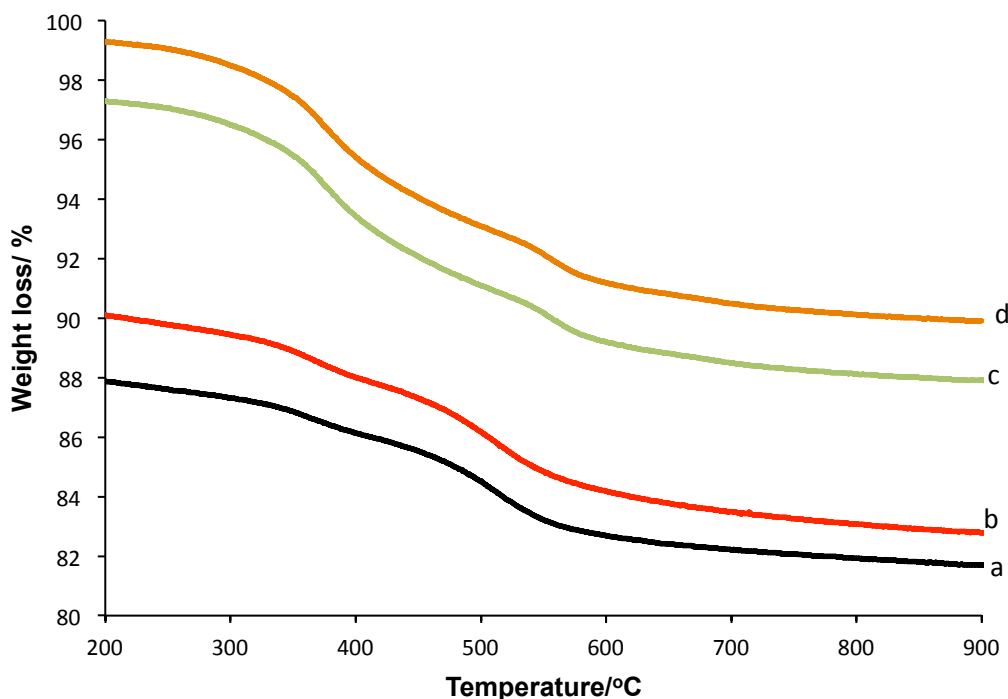


**Figure 6.2** The thermal analysis curves (TGA) of (a) 0 % (black line), (b) 1 % (red line), (c) 11 % (green line) and (d) 33 % (orange line) sulfonic acid functionalized mesoporous silicas.

The loss above 200 °C is due to organic component decompositions including surfactant decomposition at 200-250 °C, organosulfonic acid decomposition at about 460 °C and propylthiol decomposition at 350 °C [4, 5].

From figure 6.2, it is clear that there is no significant weight loss observed after 550 °C. Comparing to a previous study [6] which has a similar TGA curve shape, it showed that weight loss occurring between 350 °C and 550 °C can be referred to the removal of tethered mercaptopropyl groups which decomposed by 350 °C, and propylsulfonic acid moieties which are stable until 450 °C and then decompose to give as follows, C<sub>3</sub>H<sub>6</sub>, SO<sub>2</sub> and H<sub>2</sub>O. Therefore, the weight loss in figure 6.2 between the temperatures 350 °C and 550 °C was used to determine the experimental S content per cent values in all samples (table 6.1).

Sample	Weight loss/% 350-550 °C	Estimated S content/wt % (± 0.1) 350-550 °C
0 %	0.308	0.82
1 %	0.203	0.49
11 %	0.223	0.61
33 %	0.242	0.76

**Table 6.1 the weight percentages of sulfur content of functionalized materials evaluated by TGA technique.**

Table 6.1 shows the weight loss percentages of the particles over this temperature range and the calculated sulfur content percentages, which were obtained from the decomposition of each grafted material. With exception of the 0 % sample (no oil in the template), the weight percent of sulfur estimated from TGA increases with increasing the volume of oil in the surfactant template used to synthesize the nanoporous support material.

The weight loss between 350 and 550 °C was calculated from the TGA data, and was assumed to be due to C<sub>3</sub>H<sub>6</sub>, SO<sub>2</sub> and H<sub>2</sub>O in the ratio of 1:1:1 as described in previous calculations [6]. This gives a theoretical weight per cent of S content of this mixture of 25 %. This value was used to estimate the S content in the mixture decomposed from

each material. However, S content weight % estimated here is lower than that in similar materials studied previously (sulfonic acid functionalized SBA-15 [6] and sulfonic acid functionalized MCM-41 [7]).

### 6.2.2. X-ray photoelectron spectroscopy (XPS)

As a complementary technique, XPS has been performed to provide quantitative and qualitative information for the grafted materials. Analysis of the peak intensities and peak positions determines the specific elements related to the binding energy (BE) and the relation between the intensity of the photoelectron peaks and the concentration of the element [3]. Thus, the peak intensity measures how much of the element at the surface and the peak position indicates the chemical composition and the element.

The sulfur is the most important element, and defines whether the surface has been grafted with sulfur or not. It also shows the level of loading of sulfur on the grafted material which may be compared to the findings from TGA. Figure 6.3 shows the sulfur (2S) spectrum close to the surface region for one of grafted materials as an example.

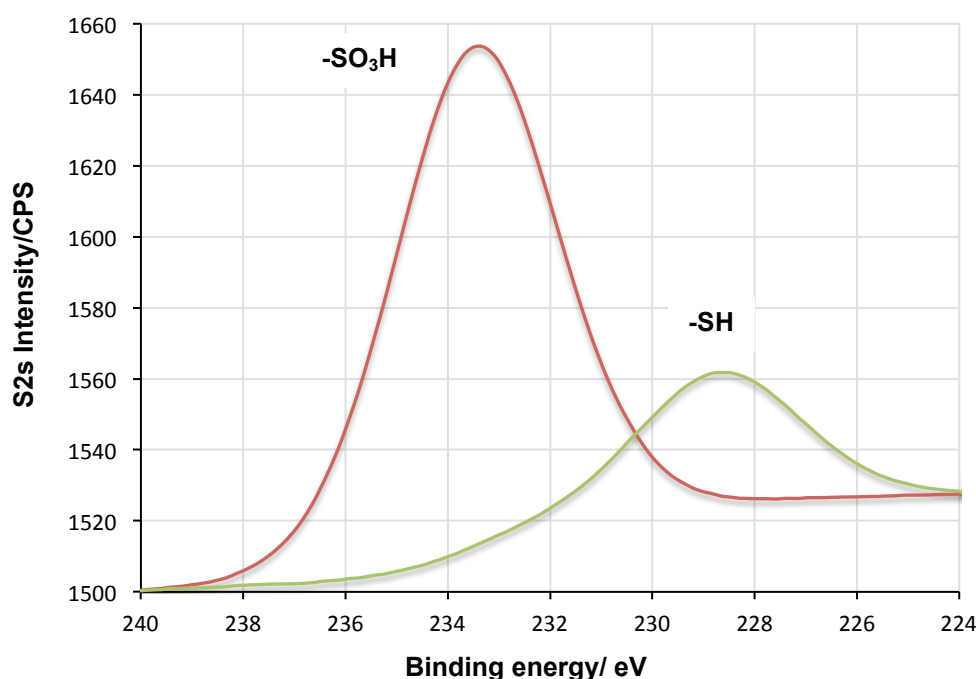


**Figure 6.3 XPS spectrum (S 2s ) of functionalized 0 % sample showing peaks for sulfur as thiol (228.0 eV) and in the oxidized sulfonic acid form (233.0 eV).**

High-resolution spectra of the S 2s core-level and very low-resolution spectra of the S 2p have been observed in all samples. In figure 6.3, the S 2s spectra indicate the

existence of two types of sulfur species, one at low BE (228 eV) associated to –SH groups and the other at higher BE (233 eV) corresponds to –SO<sub>3</sub>H groups [2, 8].

XPS is only sensitive to the region near the material surface and the level of grafting process and the percentages of sulfur on the surfaces can be determined. Since, –SH and –SO<sub>3</sub>H are the two possible forms of sulfur near the surface, MCM-41-SH is the form for the material before the oxidation and the MCM-41-SO<sub>3</sub>H form is after oxidation [9] in the grafting process of MCM-41 as an example.

Figure 6.3 shows that XPS spectra analysis has revealed the presence of two sulfur chemical environments at the two different binding energies 233.0 eV for the oxidized sulfur form (SO<sub>4</sub>) or SO<sub>3</sub>H and 228.0 eV for the element S or the thiol form (–SH), indicating an incomplete thiol oxidation to sulfonic acid in the oxidation step.

Table 6.2, shows the proportion of both sulfur oxidized to –SO<sub>3</sub>H and the thiol form –SH, and very low percentages associated to the thiol form in all samples in terms of the measured element concentration.

Sample, oil content/ V/V%	Element conc. % SO <sub>4</sub> & -SO <sub>3</sub> H (233 eV)	Element conc. % S & -SH (228 eV)
0	80	20
1	80	20
11	70	30
33	86	14

**Table 6.2 Binding energy and element concentrations from XPS analysis for grafted materials.**

In addition, the sulfur content percentages have been estimated from the peaks and listed in table 6.3. Values from XPS agree with the literature for similar materials (sulfonic acid functionalized SBA-15, 1.2-1.8 wt %) [6].

Sample, oil content/ V/V%	S content, TGA/ wt %	S content, XPS/ wt %
0	0.82	1.35
1	0.49	1.31
11	0.61	1.61
33	0.76	2.18

**Table 6.3 Sulfur content in weight percent of functionalized materials evaluated by XPS and TGA techniques.**

To compare results from TGA and XPS, table 6.3 shows the weight percent of sulfur estimated at the surface of the material across the series. It is clear that figures are not consistent, but in both cases the weight percent of sulfur increases with increasing the oil volume in the template in the samples of 1 %, 11 % and 33 %. However the disagreement between both values from TGA and XPS needs further investigations.

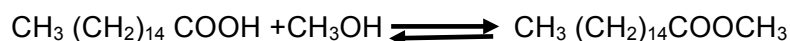
### 6.3. Catalytic activity

To investigate the properties of the porous materials prepared in Chapter Five as catalyst support, the catalytic performance of sulfonic acid functionalized porous silica at 60 °C was assessed the esterification of palmitic acid with methanol. Despite their incomplete oxidation in the synthesis of catalyst (grafting reaction), the palmitic acid esterification reaction occurred with comparable conversion rate.

#### 6.3.1. Palmitic acid esterification reaction

Sulfonic acid silica catalysts were evaluated using esterification of palmitic acid (C<sub>16</sub> saturated fatty acid) with methanol reaction.

Palmitic acid esterification was performed using the same grafted materials (0 %, 1 %, 11 %, and 33 %) to produce methyl palmitate as shown in the next reaction.





Products were quantified using GC analysis and figure 6.4 shows conversions of palmitic acid to palmitate after 6 h in each reaction as well as the conversion in a similar palmitic acid reaction used mesoporous functionalized silica [6]. The sample 0 % has the lowest conversion of ~7.7 % after 6 h, whereas higher conversions have been considered in samples 1 %, 11 % and 33 % (sample numbers 2,3 and 4 in the figure respectively). The conversion also has been increased with increase the oil volume in the template used to synthesis the material support.

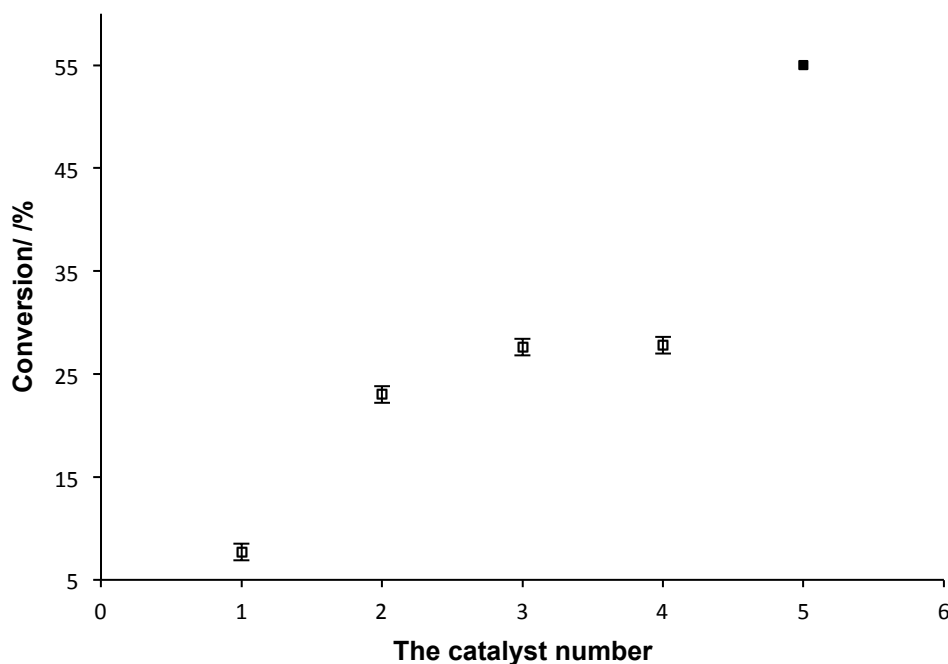


**Figure 6.4 Palmitic acid conversions after 6 h at 60 °C using sulfonic acid functionalized porous silica catalysts of samples 1, 2, 3 and 4 ( 0 %, 1 %, 11 %, and 33 % (open squares) respectively), and the conversion from the literature (sample 5, (closed square)).**

Comparing to the conversion in the literature [6], catalysts synthesized in this project have lower conversions. They are also very low compared to the palmitic acid conversion with methanol observed by using the catalyst of Al-MCM-41 (79 %) [10]. This was expected due to the low sulfur loading estimated from TGA. However, the conversions are consistent with the TGA and XPS findings in terms of the increase of the conversion with increasing the weight percent of sulfur.

## 6.4. Conclusions

There are two main conclusions about the functionalized sulfonic acid catalysts. First, the activity of catalysts used depends on sulfonic acid loading at all reactions, since the catalyst that has higher sulfur loading possesses higher palmitic acid conversion. Data from XPS showed very similar spectra patterns with slight differences in sulfur wt % values for all sulfonic functionalized catalysts prepared in this work. However, lower sulfur weight percentages have been estimated from TGA for the same materials, which may need further investigations including repeating TGA measurements or grafting more nanoporous materials. The highest conversion (~28 %) was observed using the sample of 33 %, whereas very low conversion (7.7 %) was associated to the sample 0 %.

The second is there appears to be a relationship between the activity of the functionalized material as catalysts and material template compositions, which has been clearly shown from conversion figures across the series. Increasing oil volume in the template used to synthesize the catalyst support has a direct influence on the conversion reaction of palmitic acid with methanol. However, due to the structure of the materials synthesized, it was expected that higher loading of sulfur and higher palmitic acid conversions would be associated to the samples 1 % and 33 % as they have the highest surface areas and more organized and well-ordered porosity systems, but this was not. This unexpected behaviour needs more investigations including the synthesis of more materials with a wider range of surfactant/oil compositions or repeating the grafting and esterification reactions. Further characterizations on the catalysts might be required in terms of studying their structure using X-ray diffractions, SEM, or TEM. Due to the limited time, such investigations have not been carried out in the catalysis part of the project, suggesting that the preliminary assessment in this chapter might be a starting point in further studies in this field.

## 6.5. References

1. Parlett, C.M.A., K. Wilson, and A.F. Lee, *Hierarchical porous materials: catalytic applications*. Chemical Society Reviews, 2013. **42**(9): p. 3876-3893.
2. Farrukh, A., et al., *Surface-functionalized silica gel adsorbents for efficient remediation of cationic dyes*. Pure and Applied Chemistry, 2014. **86**(7): p. 1177-1188.
3. Venezia, A.M., *X-ray photoelectron spectroscopy (XPS) for catalysts characterization*. Catalysis Today, 2003. **77**(4): p. 359-370.
4. Diaz, I., et al., *Synthesis of MCM-41 materials functionalised with dialkylsilane groups and their catalytic activity in the esterification of glycerol with fatty acids*. Applied Catalysis a-General, 2003. **242**(1): p. 161-169.
5. Mbaraka, I.K. and B.H. Shanks, *Design of multifunctionalized mesoporous silicas for esterification of fatty acid*. Journal of Catalysis, 2005. **229**(2): p. 365-373.
6. Dhainaut, J., et al., *Hierarchical macroporous-mesoporous SBA-15 sulfonic acid catalysts for biodiesel synthesis*. Green Chemistry, 2010. **12**(2): p. 296-303.
7. Diaz, I., et al., *Synthesis, characterization and catalytic activity of MCM-41-type mesoporous silicas functionalized with sulfonic acid*. Applied Catalysis a-General, 2001. **205**(1-2): p. 19-30.
8. Cano-Serrano, E., J.M. Campos-Martin, and J.L.G. Fierro, *Sulfonic acid-functionalized silica through quantitative oxidation of thiol groups*. Chemical Communications, 2003(2): p. 246-247.
9. Siril, P.F., et al., *Optimising catalytic properties of supported sulfonic acid catalysts*. Applied Catalysis a-General, 2009. **364**(1-2): p. 95-100.
10. Carmo, A.C., et al., *Production of biodiesel by esterification of palmitic acid over mesoporous aluminosilicate Al-MCM-41*. Fuel, 2009. **88**(3): p. 461-468.

## **Chapter Seven**

### **Conclusions**

## 7.1. Project conclusions

In order to establish whether this approach would generate a hierarchical porous silica, mixtures of hydrocarbon and fluorocarbon surfactants (CTAB/FSN-100) in the presence of perfluorohexane (PFH) have been used to template nanoporous silicas. The morphology of synthesized materials have been studied in terms of the specific surface area and pore size distribution. The role of surfactants in the templating process has also been investigated by studying the surfactant phase behaviour in the pure surfactant solution as well as the mixture. The study of surfactant phase behaviour was considered in terms of determining the surfactant critical micelle concentration since the templating process is based on the surfactant self-assembly approach and how the inorganic species condense around the micelles, and create pores after removing the surfactant aggregates.

The surfactant critical micelle concentration has been obtained using two different techniques, surface tension and fluorescence measurements. Different micellization processes have been observed across the studied range of compositions. For example, the two surfactants (CTAB and FSN-100) mix nonideally except for a degree of ideality at some CTAB mole fractions ( $0.5 > \alpha_{\text{CTAB}} > 0.7$ ). The well-known nonideal behaviour of such mixture has been used to study the systems of surfactant mixture with hydrocarbon oil (hexane) or fluorocarbon oil (PFH) in order to investigate the role of adding the oil PFH in the surfactant template as swelling agent, and how that affects the porosity arrangements. The structure of CTAB micelles, FSN-100 micelles, CTAB/FSN-100 mixed micelles and mixtures with hexane or PFH have been determined focusing on their size and shape. The main conclusion in the CTAB/FSN-100 systems over a range of CTAB mole fractions is that these mixtures are strongly characterized by the hydrocarbon surfactant, both in the presence of oil and without.

The hierarchical porous materials synthesized here from the mixture of CTAB/FSN-100 and different amounts of PFH have different morphologies over the composition range. Higher specific BET surface areas and more regular pores result once the oil has been added to the surfactant template with different porosity being observed as the PFH volume is raised in the template. Since the CTAB dominates the micellization process and micelles retain similar structures in a range of CTAB/FSN-100 compositions, the hexagonal porosity system observed in the synthesized materials is strongly related to the CTAB micellar structure. However, the relationship between the surfactant phase behaviour in the presence of PFH and the templated materials can be seen from the data collected in Chapter Four. The insolubility of PFH in the core of each surfactant

may explain the similar structure from most of the synthesized materials, except the 1 % and 33 %, which have a slightly different porosity system. These materials were studied in more details. The key finding here is the increase of the material specific surface area once PFH is added to the template, even with the insolubility of the oil with the two surfactants.

The catalytic activity of the synthesized nanoporous materials has been measured to study the potential of the materials as catalysts. The focus was to find out the relationship between the activity of the catalyst in the reaction and the phase composition of the template. The catalyst was able to convert palmitic acid to palmitate in spite of the low loading of sulfonic acid on the surface introduced by the grafting reaction. However, these results are preliminary and many further investigations are required in order to build up a clearer description of this relationship.

To conclude CTAB and FSN-100 mixtures have been studied as an example of hydrocarbon-fluorocarbon surfactant blends. The mixed micelles have extensively characterized in terms of their structure and dynamics, using a range of techniques. There is no obvious correlation that relate the surfactant solution structures to the final catalyst morphology, though it should be noted that the synthesis was carried out in the presence of a solvent other than a simple aqueous one.

The future work should focus on the application of the porous materials produced from such surfactant templating, in the presence of more representative solution conditions. This should allow a closer match between the final catalyst structure and the mixed micellar structure, and the porosity. This may necessitate more investigations including the use of different fluorocarbon surfactants in the surfactant phase or different fluorocarbon oils added to the template.

## **Appendix**

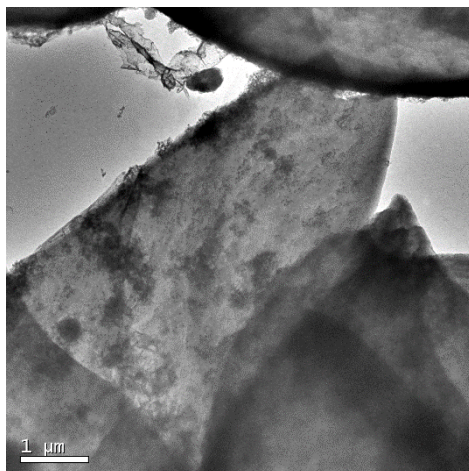


**Figure A1 TEM image of sample FSO as described in Chapter Five, section 5.2.1.**

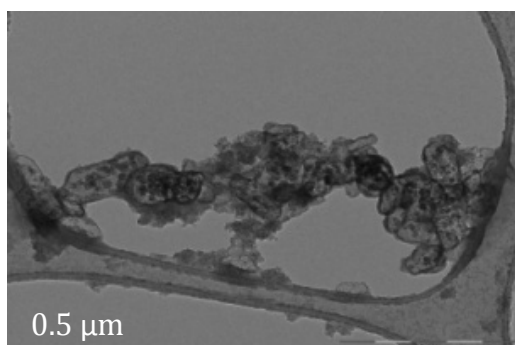


**Figure A2 TEM image of the sample FSN as described in Chapter Five, section 5.2.2.**

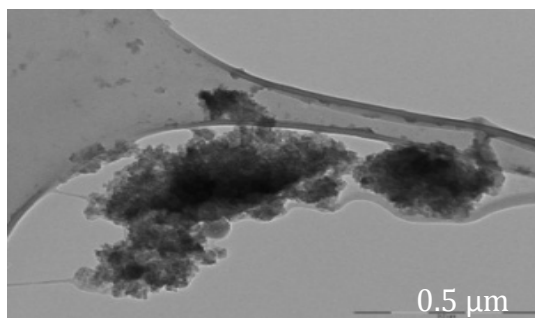
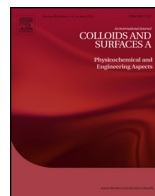


**Figure A3 TEM image of the sample FSN/ PFH as described in Chapter Five, section 5.2.3.**





## Quantifying the micellar structure formed from hydrocarbon-fluorocarbon surfactants

Zaineb O. Et-Tarhouni<sup>a,\*</sup>, Emma Carter<sup>a</sup>, Damien M. Murphy<sup>a</sup>, Peter C. Griffiths<sup>b</sup>, Omar T. Mansour<sup>b</sup>, Stephen M. King<sup>c</sup>, Alison Paul<sup>a,\*\*</sup>

<sup>a</sup> School of Chemistry, Cardiff University, Main Building, Park Place, Cardiff CF10 3TB, UK

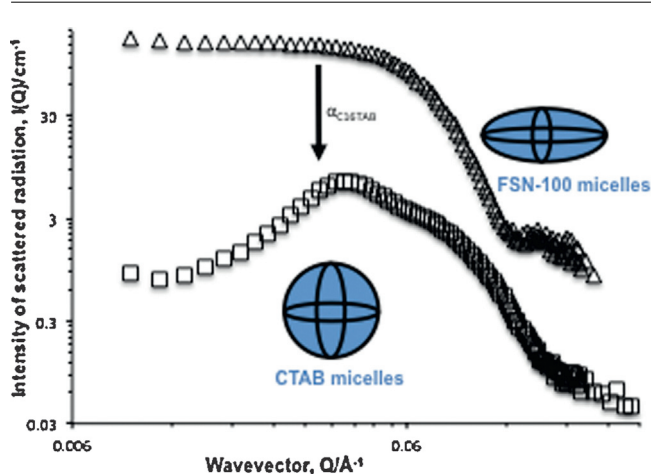
<sup>b</sup> Department of Pharmaceutical, Chemical and Environmental Sciences, Faculty of Engineering and Science, University of Greenwich, Medway Campus, Central Avenue, Chatham Maritime, Kent, ME4 4TB, UK

<sup>c</sup> Rutherford Appleton Laboratory, Science and Technology Facilities Council, Didcot, Oxfordshire, OX11 0QX, UK

### HIGHLIGHTS

- Unusual micellisation process occurs in the system C<sub>16</sub>TAB/FSN-100 mixture solutions.
- FSN-100 forms disc-like micelles with aggregation number of 65.
- C<sub>16</sub>TAB forms globular, charged micelles with a larger aggregation number than FSN-100.

### GRAPHICAL ABSTRACT



### ARTICLE INFO

#### Article history:

Received 5 June 2015

Received in revised form 6 December 2015

Accepted 14 December 2015

Available online 30 December 2015

#### Keywords:

Critical micelle concentration (CMC)

Micelle shape and size

Mixed micelles

### ABSTRACT

Many technological formulations contain mixtures of surfactants, each contributing some distinct property. Characteristics of each surfactant are often modulated in the mixture, based on the interactions between the various components present. Here, the mixing of the hydrocarbon surfactant cetyltrimethyl ammonium bromide (C<sub>16</sub>TAB) and the fluorocarbon surfactant, Zonyl-FSN-100 with average chemical structure of C<sub>8</sub>F<sub>17</sub>C<sub>2</sub>H<sub>4</sub> (OC<sub>2</sub>H<sub>4</sub>)<sub>9</sub>OH, is quantified, in particular, the size and shape of the micelles and their critical micelle concentration (CMC). The CMC data suggest there are specific interactions between the two components which are strongly antagonistic. Small-angle neutron scattering (SANS) has been used to quantify the size and shape of the micelle, and these data indicate that the single component FSN-100 forms disc-like micelles with a small aggregation number (~65) and the C<sub>16</sub>TAB forms globular, charged micelles with a larger aggregation number (135). The aggregation number of the mixed micelle is substantially greater than either of the pure species. Overall, a detailed study of CTAB, FSN-100 and their mixture systems will be presented in this paper.

© 2015 Elsevier B.V. All rights reserved.

\* Corresponding author.

\*\* Corresponding author.

E-mail addresses: [zeltarhouni@yahoo.com](mailto:zeltarhouni@yahoo.com) (Z.O. Et-Tarhouni), [paula3@cardiff.ac.uk](mailto:paula3@cardiff.ac.uk) (A. Paul).

<http://dx.doi.org/10.1016/j.colsurfa.2015.12.015>

0927-7757/© 2015 Elsevier B.V. All rights reserved.

## 1. Introduction

Surfactant solutions have been a subject of many investigations [1–7]. Surfactants self-assemble in aqueous solutions to form a wide variety of aggregated structures and many techniques have been developed to study these structures, most based on determining the shape/size of the micelles formed, and their critical micelle concentration. The latter gives an idea of the strength and nature of the interaction between the surfactants in the solution. Here, surface tension, fluorescence, small-angle neutron scattering (SANS), pulsed-gradient spin-echo NMR (PGSE-NMR) spectroscopy and

electron paramagnetic resonance spectroscopy (EPR) have been employed to provide a detailed insight into one interesting system, a mixture of a charged, hydrocarbon surfactant and a non-charged, fluorocarbon surfactant.

Hydrocarbon surfactant micelle systems have been extensively studied [3–6], however there are far fewer studies on fluorinated and partially fluorinated surfactant micelles, even though the latter material possess many unique features, especially increased surface activity and hydrophobicity [7–10]. The miscibility of fluorocarbon and hydrocarbon surfactants often presents a challenge to formulation. In this study, we are concerned with the

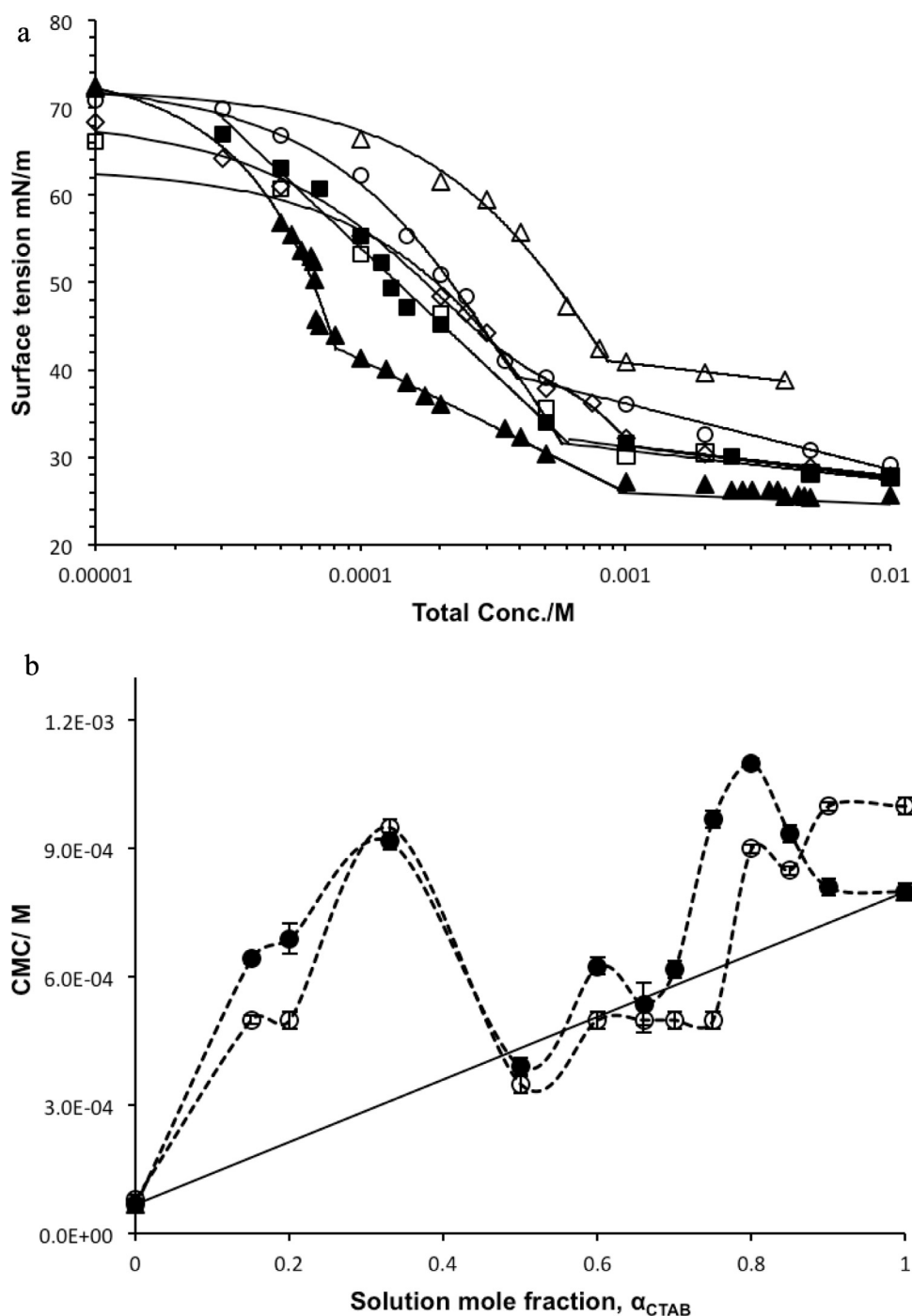


**Fig. 1.** (a) Surface tension measurements as a function of total concentration for (open triangles)  $\alpha_{\text{C}_{16}\text{TAB}} = 1$ , (closed triangles)  $\alpha_{\text{C}_{16}\text{TAB}} = 0$ , (open squares)  $\alpha_{\text{C}_{16}\text{TAB}} = 0.15$ , (open diamonds)  $\alpha_{\text{C}_{16}\text{TAB}} = 0.33$ , (closed squares)  $\alpha_{\text{C}_{16}\text{TAB}} = 0.2$ , and (open circles)  $\alpha_{\text{C}_{16}\text{TAB}} = 0.5$ . (b) The critical micelle concentration, CMC, as a function of C<sub>16</sub>TAB mole fraction determined by pyrene solubilisation (open circles) and surface tension (closed circles). Literature CMC values for the pure surfactants are also plotted, (open triangles).

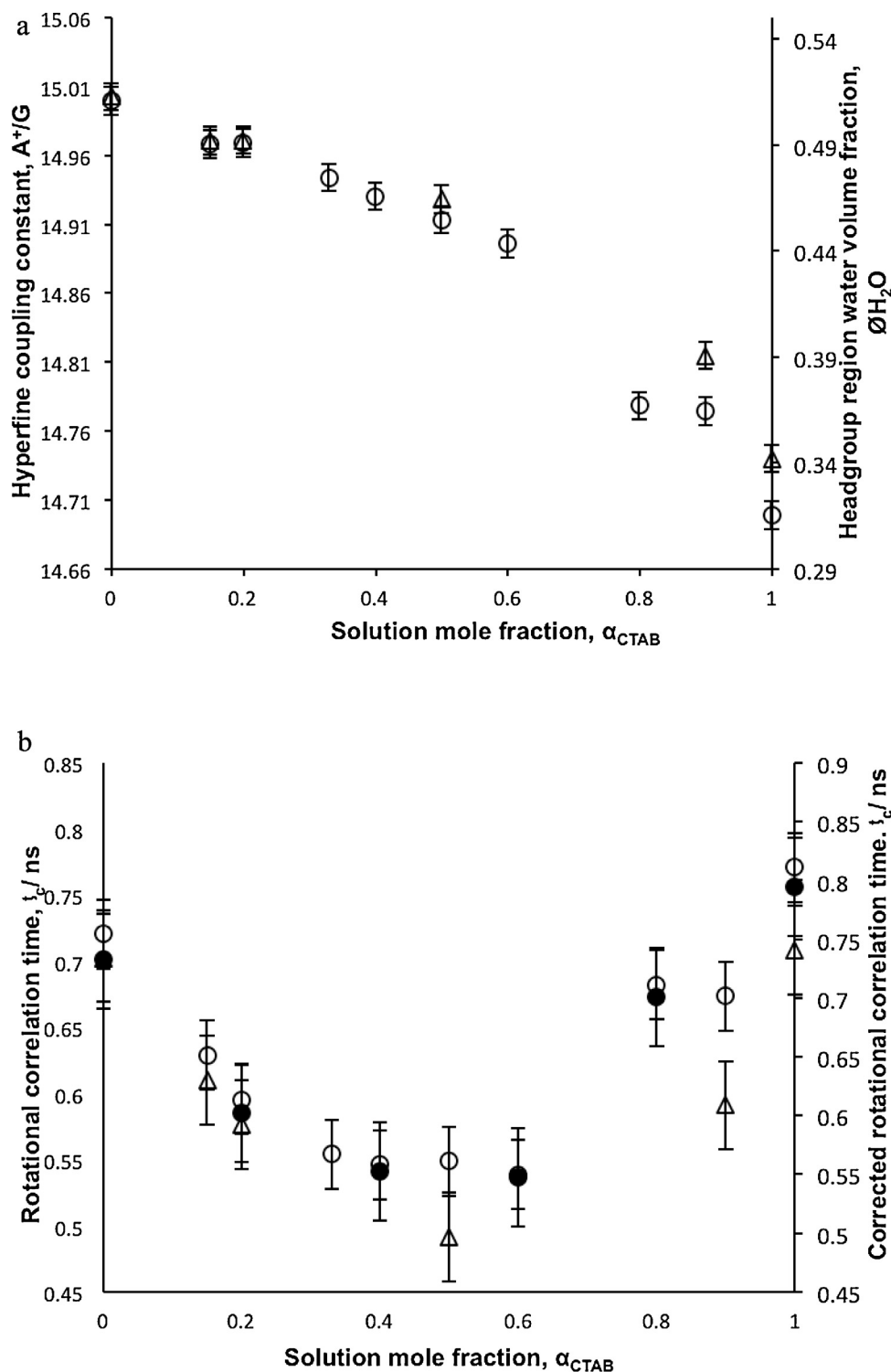


**Fig. 2.** (a) Hyperfine coupling constant of  $C_{16}TAB$ /FSN-100 mixtures, as a function of  $C_{16}TAB$  solution mole fraction at a total surfactant concentration of 20 mM (open triangles) and 50 mM (open circles). The corresponding volume fraction of water in the headgroup region is indicated on the secondary axis. (b) Rotational correlation time of 16-DSE in  $C_{16}TAB$ /FSN-100 mixtures, as a function of  $C_{16}TAB$  solution mole fraction at a total surfactant concentration of 20 mM (open triangles) and 50 mM (open circles).

aggregation of  $C_{16}TAB$  as the model hydrocarbon surfactant and FSN-100 as a model fluorocarbon surfactant;  $C_{16}TAB$  has been well-characterised [3,11], whereas FSN-100 has been less well studied, but interestingly, it exhibits two CMC values in aqueous solution, indicating a rather more complex micellisation process [8,10].

## 2. Materials and methods

### 2.1. Materials

Cetyltrimethyl ammonium bromide ( $C_{16}TAB$ ) and Zonyl FSN-100 fluorosurfactant, 16-doxyl stearic acid methyl ester (16-DSE)

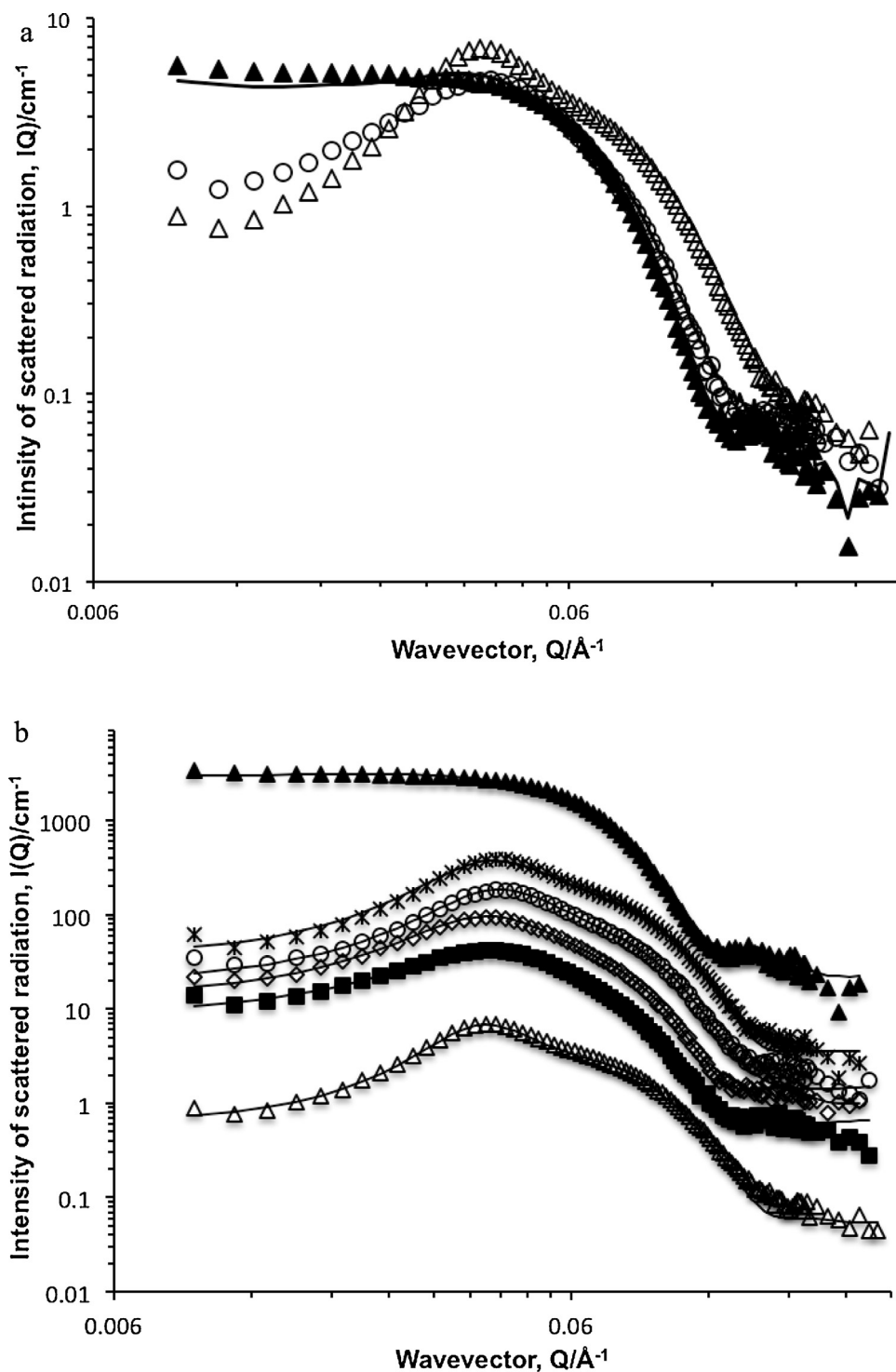


**Fig. 3.** (a) Small angle neutron scattering as a function of C<sub>16</sub>TAB mole fraction, (open triangles)  $\alpha_{\text{C}_{16}\text{TAB}} = 1$ , (closed triangles)  $\alpha_{\text{C}_{16}\text{TAB}} = 0$ , (open circles)  $\alpha_{\text{C}_{16}\text{TAB}} = 0.2$ . The solid line represents the calculated numerical average of the two pure surfactant data sets, scaled to an appropriate concentration. (b) Small angle neutron scattering as a function of C<sub>16</sub>TAB mole fraction, (open triangles)  $\alpha_{\text{C}_{16}\text{TAB}} = 1$ , (closed triangles)  $\alpha_{\text{C}_{16}\text{TAB}} = 0$ , (closed squares)  $\alpha_{\text{C}_{16}\text{TAB}} = 0.2$ , (open diamonds)  $\alpha_{\text{C}_{16}\text{TAB}} = 0.4$ , (open circles)  $\alpha_{\text{C}_{16}\text{TAB}} = 0.6$ , (stars)  $\alpha_{\text{C}_{16}\text{TAB}} = 0.8$ . Fits are included as solid line. Data are offset by a factor of 3 for clarity.

spin-probe and pyrene fluorescent probe were purchased from Sigma-Aldrich and used as received. The solvent was D<sub>2</sub>O in the SANS and PGSE-NMR, and deionized water in the surface tension, fluorescence and EPR measurements. Acetone (Aldrich) and ethanol (Aldrich) were used as solvents for the stock pyrene and 16-DSE solutions.

## 2.2. Surface tension

Surface tension measurements were carried out at room temperature and using LAUDA Drop Volume Tensiometer (TVT1). In this instrument, the volume of a drop that detaches from a capillary is determined. By increasing the volume of the drop, its weight increases until it reaches a critical value at which it cannot be coun-

terbalanced by the surface tension. The force balance at the drop results in the following relation for the surface tension, Eq. (1).

$$\sigma = Vg\Delta\rho F/2\pi r_{\text{cap}} \quad (1)$$

where  $\sigma$  = interfacial tension,  $V$  = drop volume,  $g$  = acceleration constant,  $\Delta\rho$  = difference of the densities of both adjacent phases,  $F$  = correlation factor, and  $r_{\text{cap}}$  = radius of the capillary.

### 2.3. Fluorescence

All solutions have been prepared from stock solutions by addition of surfactant stock solutions in distilled water to vials containing the pyrene probe. The pyrene concentration was kept constant at  $2 \times 10^{-6}$  M by addition of 0.01 ml of acetone containing pyrene stock solution to empty glass vials and subsequent evaporation of the acetone before addition of the aqueous surfactant solution. Photophysical data were obtained on a JobinYvon–Horiba Fluorolog spectrometer fitted with a JY TBX photodetection module. All spectra were recorded using an excitation wavelength of 340 nm. All samples have been measured at room temperature. CMCs were determined by the breakpoints in the concentration dependent ratio of the third to first vibronic peak, known as the  $I_3/I_1$  ratio.

### 2.4. Small-angle neutron scattering

The SANS measurements were performed as detailed previously [12] on the fixed-geometry, time-of-flight LOQ diffractometer (ISIS Spallation Neutron Source, Oxfordshire, UK). All measurements were carried out at 25 °C. Experimental measuring times were between 40 and 80 min. All scattering data were normalised for the sample transmission and incident wavelength distribution, corrected for instrumental and sample backgrounds using an empty quartz cell, and for the linearity and efficiency of the detector response. The data were put onto an absolute scale using a well-characterised partially-deuterated polystyrene-blend standard sample.

#### 2.4.1. SANS data fitting and analysis

The intensity of scattered radiation,  $I(Q)$ , as a function of the wave-vector,  $Q$ , is given by;

$$I_{\text{sur.}}(Q) = n [S(Q)|F(Q)|^2 + |F(Q)|^2 - |F(Q)|^2] + B_{\text{inc}} \quad (2)$$

where in the case of a core-shell morphology  $F(Q)$  is represented as,

$F(Q) = V_1(\rho_1 - \rho_2)F_0(QR_1) + V_2(\rho_2 - \rho_0)F_0(QR_2)$ . The first term represents the scattering from the core (subscript 1) and the second, the polar shell (subscript 2).  $V_i = 4/3\pi R_i^3$  and  $F_0(QR) = 3j_1(QR)/QR$ , ( $j_i$  is the first-order spherical Bessel function).  $S(Q)$  represents the spatial arrangement of the micelles in solution and  $n$  the micelle number density.  $\rho_i$  is the neutron scattering length density of the micellar core (subscript 1), the polar shell (subscript 2) and the solvent (subscript 0). These constants are combined into a single fittable parameter used to “scale” the model intensity to the absolute value. Post-fitting, this scalar is recalculated using the parameters describing the micelle morphology/composition and the molar concentration of micelles to validate the fit. The calculated and observed values should lie within ~10%.

The model of the micelle adopted here is that of a charged particle with an elliptical core-shell morphology. In the model the average volume per headgroup average tail volume and their average scattering length densities are input as constants, calculated assuming the composition of the micelle is the same as the solution composition. For C<sub>16</sub>TAB,  $\rho_{\text{C16TABhead}} = 2.4 \times 10^{-6} \text{ \AA}^{-2}$  and

volume  $412 \text{ \AA}^3$ . For the FSN-100,  $\rho_{\text{FSNhead}} = 0.6 \times 10^{-6} \text{ \AA}^{-2}$  and volume  $2000 \text{ \AA}^3$ . The bromide ion dissociation in the C<sub>16</sub>TAB case does however, significantly affect the charge on the micelle and hence the structure factor  $S(Q)$ , a point we return to later in the discussion. The average core scattering length density is also similarly calculated, with  $\rho_{\text{C16TABtail}} = -0.4 \times 10^{-6} \text{ \AA}^{-2}$  and volume  $460 \text{ \AA}^3$  whereas  $\rho_{\text{FSNtail}} = 2.0 \times 10^{-6} \text{ \AA}^{-2}$  and volume  $295 \text{ \AA}^3$ .

The structure factor  $S(Q)$  was calculated using the Hayter and Penfold [13] for spheres of a given micellar concentration, charge and ionic strength, incorporating refinements for low volume fractions and a penetrating ionic background. Various approaches to parameterising the structure factor were adopted based on known or measured estimates of the micelle size and surfactant concentration to calculate the hard sphere volume fraction, charge and Debye length. We have shown that this method of calculating the structure factor, which assumes spherical particles, remains valid for dilute, isotropic samples of micelles with small degrees of ellipticity, as is the case here [14,15].

For the SANS analysis, the hard sphere volume fraction was fixed at 0.02, calculated from the total surfactant concentration (assuming a mass density of  $1 \text{ g cm}^{-3}$ ). Starting values for the charge (20) and Debye length were estimated based on typical values for ionic surfactants [14], and scaled according to C<sub>16</sub>TAB mole fraction. The  $S(Q)$  parameters were refined during the fitting process to obtain the best fit parameters for  $P(Q)$ .

The fitting of SANS data is insensitive to the headgroup region, the shell comprising the various headgroups and associated water. The prevailing shell scattering length density is calculated from the average headgroup scattering length density and their hydration, given  $\bar{\rho} = \phi_{\text{water}}\rho_{\text{water}} + (1 - \phi_{\text{water}})\bar{\rho}_{\text{headgroups}}$ . Since  $\phi_{\text{water}} = V_{\text{water}}/V_{\text{shell}}$ , the parameters  $V_{\text{water}}$  and  $V_{\text{shell}}$  are strongly coupled and not amenable to fitting. We adopt the approach of fixing  $\phi_{\text{water}}$  at the EPR determined value that inter alia, defines the shell volume (thickness). The scattering length density of the hydrated shell region is then (re-) calculated within the analysis software, based on  $\phi_{\text{water}}f_{\text{water}}$ . Hence, constraining this value eliminates the trial-and-error aspects required in previous work to find the overall “best fit” value of  $\phi_{\text{water}}f_{\text{water}}$  due to local minima in the least-squares fits [14].

### 2.5. PGSE-NMR spectroscopy

Pulsed-Gradient Spin-Echo (PGSE-) NMR measurements were performed on a Bruker AMX400 NMR spectrometer operating at 400 MHz (<sup>1</sup>H) using a stimulated echo sequence. All the experiments were run at 25 °C using the standard heating/cooling system of the spectrometer to an accuracy of  $\pm 0.3$  °C. All solutions were prepared from stock solutions using D<sub>2</sub>O, and 0.6 ml were transferred to 5 mm o.d. NMR tubes (Willmad NMR tubes form Sigma-Aldrich).

The self-diffusion coefficient,  $D_s$ , was deduced by fitting the attenuation of the integral for a chosen peak to Eq. (3).

$$A(\delta, G, \Delta) = A_0 \exp(-k \times D_s) \quad (3)$$

where  $A$  is the signal intensity in the presence and absence (0) of the field gradients, and  $k = -\gamma^2 G^2 \delta^2 (\Delta - \delta/3)$ , where  $\gamma$  is the magnetogyric ratio,  $\Delta$  the diffusion time,  $\delta$  the gradient pulse length, and  $\sigma$  the ramp time, and  $G$  is the gradient field strength [16].

Association and complexation processes can both be extracted from an analysis of the self-diffusion coefficients  $D_s$ . In case of micellization studies, the attenuation function observed in the <sup>1</sup>H NMR spectra corresponded to the methylene resonance associated to  $-(\text{CH}_2)_x-$  of the inner part of the hydrocarbon chains related to the broad peak between  $\delta = 1.11$ – $1.20$  ppm and thus, reflects the time-average population-weighted average mobility of the monomeric

and micellized surfactant. In case of complexation, the attenuation function was recorded from the peak corresponding to the methylene in the spacer (singlet at  $d = 5.36$  ppm) and again, reflected the time-average population-weighted average mobility of monomeric and micellised surfactant.

## 2.6. EPR spectroscopy

To prepare samples for EPR, 16-DSE (0.01 M) was prepared by dissolving the appropriate amount in 2 ml of ethanol and then 0.02 ml of the solution transferred into a separate glass vial. After allowing for ethanol evaporation, 1.0 ml of the sample was added to the vial and mixed for at least 1 h to give a final spin-probe concentration at  $2 \times 10^{-4}$  M and to ensure that the probe has been incorporated into the micelle solutions.

Experimental details for the EPR measurements are also identical to those described previously [15] and only brief details are repeated here. These non-degassed samples were sealed with a gas-oxygen torch into melting point capillaries, which were housed within a quartz EPR tube for the measurements. The temperature was controlled to  $\pm 0.2$  K by a Bruker Variable Temperature Unit BVT 2000. Five spectra were taken at X-band on a Bruker ESP-300 spectrometer.

### 2.6.1. EPR lineshape fitting and analysis

The lineshapes were fitted to a Voigt approximation to separate the Gaussian and Lorentzian components of the spectral lines and to locate the resonance fields of the three EPR lines arising from the nitroxide radical to a precision of a few mG. Rotational correlation times are computed from the overall linewidth of the centre line and the peak-to-peak heights of the three lines and corrected for inhomogeneous broadening using the procedure outlined by Bales [12,15].

The separation  $A+$  of the low and centre lines ( $M_I = +1$  and  $M_I = 0$ ) is directly related to the polarity index  $H$  ( $25^\circ\text{C}$ ), defined as the molar ratio of OH groups in a given volume relative to water (Eq. (4)).  $H$  ( $25^\circ\text{C}$ ) therefore corresponds to the volume fraction of water in the polar shell,  $f_{\text{water}}$ , and may be used to constrain the SANS fitting.

$$H(25^\circ\text{C}) = (A+ - 14.21) / 1.52 \quad (4)$$

## 3. Results and discussion

### 3.1. Critical micelle concentration (CMC) determinations

Surface tension measurements have been carried out for a range of solution compositions expressed as a function of  $C_{16}\text{TAB}$  (solution) mole fraction. The raw are included in Supplemental section (Figs. S1 and S2), but representative data are included in Fig. 1a. The two limits correspond to the single component species, for which our CMC values ( $C_{16}\text{TAB} = 0.8 \times 10^{-4}$  M, FSN-100 =  $6.8 \times 10^{-5}$  M) are in excellent agreement with literature ones [6,8], (Supplemental Fig. S1). FSN-100 shows two break points ( $6.8 \times 10^{-5}$  M,  $1.0 \times 10^{-3}$  M) again as observed previously [8], these have previously been ascribed to pre-association and micellization processes. As may be seen for FSN-100 rich mixtures, there are still two break points, but at higher  $\alpha_{C_{16}\text{TAB}}$ , only one prevails.

The CMC vs  $\alpha_{C_{16}\text{TAB}}$  behaviour in Fig. 1b shows a number of distinct features, in particular, significant regions where the CMC is greater than would be predicted by an ideal mixing approach. Therefore, there are specific interactions between the two molecules, and these are strongly antagonistic. What is surprising in this system is the presence of a region of apparent ideality around  $0.5 > \alpha_{C_{16}\text{TAB}} > 0.7$ . Such increases in CMC, crucially to a concentration of one of the species to a value greater than its single

component CMC, as around  $0.2 < \alpha_{C_{16}\text{TAB}} < 0.4$  emphasises a loss of surfactant activity and the presence of a substantially different micellization process. Clearly, further analysis of the micelle composition and size/shape is warranted.

Surface tension detects changes in the surface composition, which generally reflects the prevailing solution structure. To provide a contrasting measure of the CMC, pyrene solubilisation has also been used. The two curves show remarkable similarity (Fig. 1b), indicating that there is indeed some unusual micellization process occurring in this system.

### 3.2. Electron paramagnetic resonance spectroscopy (EPR) measurements

In order to constrain various parameters in the analysis of the scattering data (the next section), EPR was used to quantify the hydration of the micelle headgroup region. The EPR technique introduces a very small amount of nitroxide free radical as a spin probe (in this case, 16-DSE) into the micelle and by measuring the hyperfine coupling constant, the micelle structure can be estimated. The data in this experiment were also recorded at two different total surfactant concentrations (20 mM and 50 mM) to assess whether the micelle structure undergoes a significant change with total concentration.

The hyperfine coupling constant from the EPR measurements are plotted versus  $C_{16}\text{TAB}$  mole fraction in Fig. 2a. It is obvious that there is a greater degree of water (52%) associated with the FSN-100 headgroup, presumably because of the larger headgroup providing a greater volume for water penetration. The  $C_{16}\text{TAB}$  is a smaller, spherical structure and the predicted value for  $\phi_{\text{H}_2\text{O}}$  at 50 mM would be calculated from Eq. (5) is 0.30, in fair agreement with the experimental value (0.32) (Table 1). Calculation of the estimate for FSN-100 is less precise due to the uncertainty in the headgroup structure, but again the calculated value (0.53) is in good agreement with the experimental one (0.52).

$$\phi_{\text{H}_2\text{O}} = \frac{V_{\text{shell}} - V_{\text{headgroups}}}{V_{\text{shell}}} = \frac{\left(\frac{4}{3}\pi(R+\sigma)^3X - \frac{4}{3}\pi R^3X\right) - N_{\text{agg}}V_{\text{CTAB}}}{\left(\frac{4}{3}\pi(R+\sigma)^3X - \frac{4}{3}\pi R^3X\right)} \quad (5)$$

The headgroup region of the cationic micelle is densely populated with the spherical, cationic headgroups and accordingly, the spin-probe will experience a relatively viscous environment (Fig. 2b). By contrast the non-ionic micelle headgroup region will be populated by fairly large, oligomeric sterically hindering headgroups and accordingly, the spin-probe will also experience a viscous environment. These features are not that sensitive to the aggregation number.

For each cationic molecule ( $C_{16}\text{TAB}$ ) that is removed from the mixed headgroup region, by the mixing of the cationic and non-ionic headgroups, there will be a change in amount of water equivalent to the difference in the respective headgroup volumes, consistent with the change in aggregation number. This is seen as the largely linear dependence of hydration (Fig. 2a) as a function of CTAB mole fraction. Interestingly, the spin-probe experiences a more mobile, a less viscous environment (Fig. 2b), between the two single surfactant extremes, as evidenced by the minimum in the rotational correlation time, a minimum in the viscosity.

EPR experiment provides an additional characterisation of the micelle via the rotational correlation time ( $\tau_c$ ) which is a measure of the dynamics with the micelle and the micelle tumbling itself (Fig. 2b).

The two single component micelles have a similar microviscosity and there is a pronounced minimum in  $\tau_c$  cross the entire mole fraction range, consistent with a decrease in local viscosity experienced by the probe.

It is customary to separate the dynamics of the spin probe within the micelle  $\tau_{\text{Relative}}$  to that of the micelle itself  $\tau_{\text{micelle}}$  in



**Table 1**

Experimental values for volume fraction of water in the polar shell ( $\phi_{\text{H}_2\text{O}}$ ) using EPR, in the single surfactant solutions and mixtures at two different total surfactant concentration.

$\text{C}_{16}\text{TAB}/\text{M}$	FSN-100/M	Exp. $\phi_{\text{H}_2\text{O}}^{\text{shell}}$ 50 mM/( $\pm 0.2$ )	Exp. $\phi_{\text{H}_2\text{O}}^{\text{shell}}$ (20 mM/( $\pm 0.2$ ))
0	1	0.52	0.52
0.15	0.85	0.50	0.50
0.2	0.8	0.50	0.50
0.33	0.67	0.48	–
0.4	0.6	0.47	–
0.5	0.5	0.46	0.47
0.6	0.4	0.45	–
0.8	0.2	0.37	–
0.9	0.1	0.37	0.40
1	0	0.32	0.35

order to comment on the microviscosity of the headgroup region. We use the SANS estimate of the size to obtain  $\tau_{\text{micelle}}$  to arrive at  $\tau_{\text{Relative}}$ , which is over-plotted in Fig. 2b, for selected data points [17]. Clearly, as expected, the  $\tau_{\text{corrected}}$  has little impact on the appearance. There is still a pronounced minimum in microviscosity as a function of  $\text{C}_{16}\text{TAB}$  mole fraction.

The microviscosity does not show any obvious dependence of  $N_{\text{agg}}$  as curvature, being largely defined by the numbers, and bulkiness of the headgroups, modulated by the prevailing degree of hydration. There is a clearly an opposite influence of the smaller TAB headgroup and the bulky, but hydrated ethylene oxide headgroup of the FSN-100.

### 3.3. Small-angle neutron scattering (SANS) studies

One mechanism by which apparent antagonistic micellization may occur is the coexistence of multiple types of micelles. Therefore, SANS was carried out to test this hypothesis and to quantify the size/shape of the micelles as a function of solution composition.

SANS measurements were performed on a single component  $\text{C}_{16}\text{TAB}$  and FSN-100 as well as selected  $\text{C}_{16}\text{TAB}/\text{FSN-100}$  mixtures at specific  $\text{C}_{16}\text{TAB}$  mole fractions, in order to detect micelle shape and size corresponding to the features in the CMC plot. Fig. 3a illustrates the approach adopted to test the hypothesis that two micelle types coexist. The figure shows the data from  $\text{C}_{16}\text{TAB}$  and FSN-100 alone, plus the measured data for  $\alpha_{\text{C}_{16}\text{TAB}} = 0.2$ , where the CMC shows a significant departure from ideality. The solid line represents the calculated numerical average of the two pure surfactant data sets, scaled to an appropriate concentration. As can be seen this calculated data set is not in agreement with the experimental data for  $\alpha_{\text{C}_{16}\text{TAB}} = 0.2$ . This clearly shows that we do not have two populations of FSN and  $\text{C}_{16}\text{TAB}$  micelles, and therefore that mixed micelles must be present. This has been demonstrated for other sample compositions in Supplemental section (Figs. S3 and S4).

Fig. 3b shows the SANS data for the single components and four mixtures. The scattering curves are a composite of the form factor describing the size and the shape, and the structure factor describing the electrostatic interaction between micelles.

The scattering from ionic surfactant micelles possess an oscillatory structure factor which will lead to reduction in intensity at low  $Q$  and “bumps” at higher  $Q$ . These features are not expected in

the scattering from a non-ionic micelle, at least at moderate concentrations. This simple interpretation accounts for many of the gross features in the data, in particular, the most striking difference in the curve from FSN-100 compared with all other mixtures. Expressed differently, once  $\text{C}_{16}\text{TAB}$  is added to the solution, the micelles show less variance in structure, and more similarity with the pure  $\text{C}_{16}\text{TAB}$ . As predicted, the scattering intensity decreases at low  $Q$  as the  $\text{C}_{16}\text{TAB}$  mole fraction increases, with shoulders around  $Q = 0.06 \text{ \AA}^{-1}$  becoming more pronounced.

Therefore, we conclude that coexisting population of pure micelles do not exist, and the next challenge is to characterize, in detail, the structure of the mixed micelles formed.

Considering the fit for the single component surfactant solutions, the data have been fitted to a model describing the micelle morphology as globular, with a varying degree of ionic character. In both cases, constants have been applied to the analysis; specifically, using the known chemical structure, concentration molar volumes, dimensions and scattering length densities, in constraining with the known concentrations and the experimental values of the degree of hydration from EPR (Table 1). The fitting parameters that are allowed to freely float are the ellipticity, the charge and the incoherent background.

From Table 2, describing the fit for the single components and the mixtures parameters, reflect what is also evident from the data, namely that the mixtures are strongly characterised by the ionic  $\text{C}_{16}\text{TAB}$  component. The aggregation numbers have been calculated via equation (6), the ratio of the core volume divided by a simple weighted value of the effective tail volume, this assumes that the micelle composition is identical to the solution one. In addition, the aggregation number of FSN-100 micelles is a little smaller than the literature value [10], whereas  $\text{C}_{16}\text{TAB}$  micelle aggregation number is in a good agreement with the literature one [18].

$$N_{\text{agg}} = \frac{V_{\text{core}}}{V_{\text{tail}}} = \frac{\frac{4}{3} \pi R_{\text{core}}^3 X}{\alpha_{\text{CTAB}} V_{\text{CTAB}}^{\text{tail}} + (1 - \alpha)_{\text{CTAB}} V_{\text{FSN-100}}^{\text{tail}}} \quad (6)$$

where,  $N_{\text{agg}}$  is the aggregation number,  $X$  is the ellipticity,  $R_{\text{core}}$  is the core radius,  $V_{\text{tail}}$  is the surfactant tail volume,  $V_{\text{core}}$  is the surfactant core volume.

The model assumes a single micelle type and the success of this approach in describing the data suggests that either a single micelle

**Table 2**

Parameters describing the fits of SANS data from  $\text{C}_{16}\text{TAB}$ , FSN-100, and their mixtures as a function of  $\text{C}_{16}\text{TAB}$  mole fraction using a model that describes the micelle as a globular elliptical with some ionic character.

$\text{C}_{16}\text{TAB}$ mole fraction	$R_{\text{core}}/\text{\AA}$	Shell thickness ( $\pm 5$ )/ $\text{\AA}$	Ellipticity, $X$	$V_{\text{S(dry)}}/V_{\text{core}}$	$N_{\text{agg}} (\pm)$
0	13.3	24	1.5	0.8	65
0.2	27.8	12	1.1	0.9	310
0.4	27.8	11	1.0	0.9	250
0.6	26.2	10	1.0	0.9	190
0.8	21.6	10	1.1	1.0	140
1.0	25.8	8.0	0.85	0.9	135

type is indeed present or any coexisting population of micelles are not substantially different. As a complimentary approach, PGSE-NMR was employed to provide more information about micelle structures.

#### 3.4. PGSE- NMR spectroscopy studies

In this experiment, the measured diffusion coefficient is a weighted value of the non-micellised and micellised components. One would expect that if a coexisting micelle population were present, coupled with varying levels of non-micellised surfactant, the diffusion coefficient of the C<sub>16</sub>TAB and FSN-100 would be quite different. Clearly, they are not (Supplemental Fig. S5), again, consistent with the SANS conclusion that these two surfactants mix, further, the diffusion coefficient values are mutually comparable consistent with the relative volumes of the respective micelles, also suggest that the solution composition is the same as the micellar one.

#### 4. Conclusions

Mixed micelles of cationic C<sub>16</sub>TAB and non-ionic FSN-100 surfactants have been studied by various techniques. The data show that the two surfactants mix nonideally with CMCs higher than predicted for ideal mixtures whilst some concentrations show a degree of ideality. This behaviour confirms that there is a substantially different micellization process across a range of compositions. It is clear that from SANS data the mixed micelles are strongly characterised by the C<sub>16</sub>TAB component, and micelles have less variable in structure when different amount of C<sub>16</sub>TAB was added to the solution. With increasing C<sub>16</sub>TAB mole fraction, there is a reduction in the amount of water present in the headgroup region. Furthermore, combining resulted data from several techniques has been used to conduct a full picture of the micellar system of C<sub>16</sub>TAB, FSN-100 and their mixtures.

#### Acknowledgments

Cardiff University, the University of Greenwich, STFC and Libyan Government are acknowledged for financial support, including a PhD studentship (ZE).

#### Appendix A. Supplementary data

Supplementary data associated with this article can be found, in the online version, at <http://dx.doi.org/10.1016/j.colsurfa.2015.12.015>.

#### References

- [1] H.B. de Aguiar, et al., Surface structure of sodium dodecyl sulfate surfactant and oil at the oil-in-water droplet liquid/liquid interface: a manifestation of a nonequilibrium surface state, *J. Phys. Chem. B* 115 (12) (2011) 2970–2978.
- [2] N.C. Das, et al., Shape and size of highly concentrated micelles in CTAB/NaSal solutions by small angle neutron scattering (SANS), *Langmuir* 28 (33) (2012) 11962–11968.
- [3] A.J. Mills, J. Wilkie, M.M. Britton, NMR and molecular dynamics study of the size, shape, and composition of reverse micelles in a cetyltrimethylammonium bromide (CTAB)/*n*-hexane/pentanol/water microemulsion, *J. Phys. Chem. B* 118 (36) (2014) 10767–10775.
- [4] P.C. Griffiths, et al., Small-angle neutron scattering, electron paramagnetic resonance, electrophoretic NMR, and time-resolved fluorescence quenching studies of sodium dodecyl sulfate and tetra (ethylene oxide) dodecyl ether mixed surfactant micelles, *J. Phys. Chem. B* 108 (4) (2004) 1351–1356.
- [5] P.C. Griffiths, et al., Role of counterion concentration in determining micelle aggregation: evaluation of the combination of constraints from small-angle neutron scattering, electron paramagnetic resonance, and time-resolved fluorescence quenching, *J. Phys. Chem. B* 108 (12) (2004) 3810–3816.
- [6] J. Aguiar, et al., On the determination of the critical micelle concentration by the pyrene 1:3 ratio method, *J. Colloid Interface Sci.* 258 (1) (2003) 116–122.
- [7] J. Eastoe, et al., Fluorinated nonionic surfactants bearing either CF<sub>3</sub>- or H-CF<sub>2</sub>-terminal groups: adsorption at the surface of aqueous solutions, *Langmuir* 17 (25) (2001) 7873–7878.
- [8] K. Szymczyk, Behaviour of the fluorocarbon surfactants in the monolayer at the water–air interface and in the bulk phase, *J. Fluorine Chem.* 150 (2013) 109–116.
- [9] K.V. Schubert, E.W. Kaler, Microemulsifying fluorinated oils with mixtures of fluorinated and hydrogenated surfactants, *Colloids Surf. A: Physicochem. Eng. Aspects* 84 (1) (1994) 97–106.
- [10] J. Skvarla, et al., Micellization of Zonyl FSN-100 fluorosurfactant in aqueous solutions, *Colloids Surf. A: Physicochem. Eng. Aspects* 443 (2014) 209–215.
- [11] M.A. Bahri, et al., Investigation of SDS, DTAB and CTAB micelle microviscosities by electron spin resonance, *Colloids Surf. A: Physicochem. Eng. Aspects* 290 (1–3) (2006) 206–212.
- [12] B.L. Bales, C. Stenland, Statistical distributions and collision rates of additive molecules in compartmentalized liquids studied by EPR spectroscopy.1. Sodium dodecyl-sulfate micelles, 5-doxylosteoric acid ester, and cobalt(II), *J. Phys. Chem.* 97 (13) (1993) 3418–3433.
- [13] J.B. Hayter, J. Penfold, An analytic structure factor for macroion solutions, *Mol. Phys.* 42 (1) (1981) 109–118.
- [14] B.L. Bales, et al., Precision relative aggregation number determinations of SDS micelles using a spin probe. A model of micelle surface hydration, *J. Phys. Chem. B* 102 (50) (1998) 10347–10358.
- [15] B.L. Bales, Inhomogeneously broadened spin-label spectra, in biological magnetic resonance, *Biol. Magnet. Reson.* 8 (1989) 77.
- [16] P.C. Griffiths, et al., FT-PGSE NMR study of mixed micellization of an anionic and a sugar-based nonionic surfactant, *J. Phys. Chem. B* 101 (6) (1997) 915–918.
- [17] B.L. Bales, R. Ranganathan, P.C. Griffiths, Characterization of mixed micelles of SDS and a sugar-based nonionic surfactant as a variable reaction medium, *J. Phys. Chem. B* 105 (31) (2001) 7465–7473.
- [18] J. Haldar, et al., Molecular modulation of surfactant aggregation in water: effect of the incorporation of multiple headgroups on micellar properties, *Angew. Chem. Int. Ed.* 40 (7) (2001), p. 1228–+.